NANYANG TECHNOLOGICAL UNIVERSITY
SINGAPORE

Development and Optimization of Selective Laser Sintered-Polymeric Composites and Structures for Functional Applications

YUAN SHANGQIN

SCHOOL OF MECHANICAL AND AEROSPACE ENGINEERING

2017

Development and Optimization of Selective Laser Sintered-Polymeric Composites and Structures for Functional Applications YUAN SHANGQIN 2017

Development and Optimization of Selective Laser Sintered-Polymeric Composites and Structures for Functional Applications

YUAN SHANGQIN

SCHOOL OF MECHANICAL AND AEROSPACE ENGINEERING

A thesis submitted to the Nanyang Technological University in partial fulfillment of the requirement for the degree of
Doctor of Philosophy

2017

Acknowledgements

It is my pleasure to thank the following people whose advice, guidance and supply are extremely helpful for completing this incredible journey.

"Dream – A passion within me and a given from you."

I would like to express my heartfelt gratitude to my supervisors Professor Chua Chee Kai and Associate Professor Zhou Kun for their guidance and encouragement as well as constant support throughout the PhD study. I appreciate Prof. Chua for leading the exciting research field of 3D printing and making global impacts. He has always provided effective discussion about the novelty of my research and patient guidance whenever I encountered problems. I will also give my sincere thanks to Prof. Zhou who has given me the opportunity to conduct this PhD thesis research. Prof. Zhou has always devoted his resources to supporting my research study and provided precious advice for the writing and presentation of academic reports. I would like to wholeheartedly thank him for giving invaluable guidance and memorable experiences, allowing me to discover the entirely new field with countless supports and unlimited excitement from continuously innovative techniques and inspiring sciences.

"You are my lucky charm in the journal."

My sincere appreciation is extended to my teammate Dr. Bai Jiaming who has always provided experimental assistance and valuable discussions for product design. I also owe a great debt of gratitude to Dr. Shen Fei for his inspiration and assistance in accessing essential information and knowledge that has contributed to the success of

this research work. He has helped me accomplish the toughest task in the study of material and structural mechanics. Special thanks should also go to Dr. Wei Jun whose advice has always inspired me to move forward and target higher.

"Sitting and thinking maybe have much higher priority than a normal researcher, who is a proxy of your seriousness."

I would like to show my gratitude to the people for inspiring and encouraging me to devote into the scientific research and academic path when I was very young. I thank Prof. Wong Chee Chong and Prof. Shu Yang for many insightful discussions and encouragements during my undergraduate study at NTU and my internship at the University of Pennsylvania, USA. I owe my deepest gratitude to Dr. Chin Jia Min, Dr. Eric Ng and Dr. Wu Gaoxiang, who patiently trained and communicated with me for conducting laboratory works. They helped me to have passion in science and engineering rather than just simply work as a researcher.

"Every day, every minute, every breath, every person around me truly is a gift and is precious."

I owe the deepest gratitude to my parents and friends who have been supporting along the way and caring about me. My parents have always educated me to be independent, keep studying and gain wisdom to pursue the dreams. I would like to give special thanks to my close friend Ms. Yang Jing, who was the only one that has known my entire tough and exciting journey over the past four years. My roommates Dr. Tao Kai and Ms. Yang Lixia have also taken care of me. It is a great treasure to establish the precious bonding and relationships with them during my life.

"To get a thorough understanding of oneself is to get a full control of one's life. Then one will find his or her life full of colour and flavour."

It is a meaningful and valuable journey to pursue PhD study with flexible time but self-discipline. This period could be the most memorable experience because of the freedom in the work, life and study. I have had enough space and time to think about business, history, philosophy and even cultures, overwhelmed by the traditional Chinese philosophy and the western culture revolution. It is the period that I have had the mental freedom to look into myself, discover what is inside my heart and listen to my inner voices as well as challenge and overcome myself.

List of Publications

Journal Articles

[1] **Yuan S**, Zheng Y, Chua CK, Yan Q, Zhou K. Electrical and Thermal Conductivities of MWCNT/Polymer Composites Fabricated by Selective Laser Sintering. ***Composites Part A: Applied Science and Manufacturing***. 2018;150:203-213

[2] Shen F, **Yuan S**, Chua CK, Zhou K. Development of process efficiency maps for selective laser sintering of polymeric composite powders: Modeling and experimental testing. ***Journal of Materials Processing Technology***. 2018;254:52-9.

[3] Tian X, Jin J, **Yuan S**, Chua CK, Tor SB, Zhou K. Emerging 3D-Printed Electrochemical Energy Storage Devices: A Critical Review. ***Advanced Energy Materials***. 2017;7:1700127.

[4] Bai J, **Yuan S**, Shen F, Zhang B, Chua CK, Zhou K, et al. Toughening of polyamide 11 with carbon nanotubes for additive manufacturing. ***Virtual and Physical Prototyping***. 2017;12:235-40.

[5] **Yuan S**, Shen F, Bai J, Chua CK, Wei J, Zhou K. 3D soft auxetic lattice structures fabricated by selective laser sintering: TPU powder evaluation and process optimization. ***Materials & Design***. 2017;120:317-27.

[6] **Yuan S**, Bai J, Chua CK, Zhou K, Jun W. Characterization of creeping and shape memory effect in laser sintered thermoplastic polyurethane. ***Journal of Computing and Information Science in Engineering.*** 2016;16:041007.

[7] Shen F, **Yuan S**, Guo Y, Zhao B, Bai J, Qwamizadeh M, et al. Energy absorption of thermoplastic polyurethane lattice structures via 3D printing: modeling and prediction. ***International Journal of Applied Mechanics***. 2016;08:1640006.

[8] **Yuan S**, Bai J, Chua CK, Wei J, Zhou K. Highly enhanced thermal conductivity of thermoplastic nanocomposites with a low mass fraction of MWCNTs by a facilitated latex approach. ***Composites Part A: Applied Science and Manufacturing***. 2016;90:699-710.

[9] **Yuan S**, Bai J, Chua CK, Wei J, Zhou K. Material evaluation and process optimization of CNT-coated polymer powders for selective laser sintering. ***Polymers***. 2016;8:370.

[10] Bai J, **Yuan S**, Chow W, Chua CK, Zhou K, Wei J. Effect of surface orientation on the tribological properties of laser sintered polyamide 12. ***Polymer Testing***. 2015;48:111-4.

[11] Bai J, Goodridge R, **Yuan S**, Zhou K, Chua C, Wei J. Thermal Influence of CNT on the Polyamide 12 Nanocomposite for Selective Laser Sintering. ***Molecules***. 2015;20:19041.

Conference Presentations

[1] **Yuan S**, Bai J, Chuang SL. , Chua CK., Wei J and Zhou K, "Development of an ultra-high thermal conductive MWCNT reinforced polymer nanocomposite" in Proceedings ICMAT & IUMRS-ICA, 28 Jun–3 Jul, 2015, Suntec Singapore

[2] **Yuan S**, Bai J, Chow W, Chua CK, Wei J and Zhou K, "Characterization of creeping and shape memory effect in laser sintered thermoplastic polyurethane," in Proceedings ICIDM, 24 Jan–26 Jan, 2016, University of Auckland, Auckland, New Zealand.

[3] **Yuan S**, Bai J, Chua CK, Wei J and Zhou K, "Dynamic mechanical behaviours of laser sintered polyurethane incorporated with MWCNTs," in Proceeding Pro-AM, 16 May-19 May, 2016, Nanyang Technological Univeristy, Singapore.

[4] **Yuan S**, Chua CK and Zhou K, "3D soft metamaterials fabricated by selective laser sintering of polyurethane," in Proceeding SFF, 8 Aug – 12 Aug, 2016, AT&T Conference Center, Austin, Texas, USA

[5] Bai J, Goodridge RD, **Yuan S**, Chua SL, Zhou K and Wei J, "Effect of carbon nanotubes on the thermal conductivity and laser sintering process of polyamide 12" in Proceedings ICMAT & IUMRS-ICA, 28 Jun–3 Jul, 2015. Suntec Singapore.

Technical Disclosures and Patents

[1] **Yuan S**, Bai J, Zhou K, Chua CK, Wei J, "Method of embedding carbon nanomaterials into/onto polymeric powders for powder-based additive manufacturing" Know-How, 2017

[2] Vastola G, Bai J, **Yuan S**, Zhou K, Chua CK and Wei J, "Method to calculate part shrinkage and distortion in selective laser sintering of polyamide 12 additive manufacturing", Singapore Provisional Patent. Reference NO.: 10201702645S

Abstract

Polymer nanocomposite technology is an emerging field in which nanoscale fillers are embedded into a polymer to produce materials with advanced functionalities. The properties imparted by carbon nanotubes (CNTs) to the polymer can be remarkably good. Thermoplastic polymers such as polyamide 12 (PA12) and thermoplastic polyurethane (TPU) incorporated with CNTs have the potential to create a whole new generation of composites with significantly improved performances through the selective laser sintering (SLS) system instead of the conventional manufacturing processes of nanocomposites. This PhD research aims to develop new polymeric nanocomposite powders, optimize the process parameters of SLS for printing these powders, and investigate the multi-functionality of the printed composite parts and their applications in energy absorption and dissipation.

The development of composite powders is the primary step for the SLS process. A surfactant-facilitated latex technique was developed to prepare multi-walled CNTs (MWCNTs)-coated polymer powders, which possess the desirable microstructures and surface morphologies for the SLS process. This method of embedding nanoparticles into/onto polymeric powders was facile, green, low cost and scalable, providing a universal route for the rational design and engineering of configuration and morphology of composite powders. The thermal conductivity, thermal capacity, optical properties, rheological and viscoelastic properties, and flowability of the new powders were properly characterized for further evaluation.

These powder properties affect the powder deposition, bed temperature control and

sintering performance of the entire laser sintering process. A methodology of process optimization and powder evaluation was proposed, which applied a simplified theoretical model to calculate the energy required for polymer melting and decomposition and then predict the effective range of the input laser energy. This methodology can effectively narrow down the working range of sintering parameters and identify the set of optimal process parameters in the SLS process. Additionally, the established model can be generally applied to the prediction of the effective range of the input laser energy for semi-crystalline and amorphous polymers, such as PA12, TPU and their composites.

To explore the end-use application of laser-sintered composite materials, their multi-functionality was investigated, and the process-structure-property relationship was studied to reveal the reinforcement mechanisms of nanofillers within the polymeric matrix. The laser-sintered MWCNTs-reinforced composites exhibited promising improvements in electrical conductivities and mechanical properties, as well as the slight enhancements in thermal conductivities. The sintering of the MWCNTs-coated polymeric powders could create the composites with segregated microstructures that built the three-dimensional (3D) CNTs-network and formed the continuous conductive pathways for electrons and phonons within polymer matrices. Meanwhile, after laser sintering, the MWCNTs were retained at the powder-boundaries and prohibited the movement of polymer chains upon mechanical forces, thus leading to the enhancements in the mechanical properties.

With the improved mechanical toughness and strength, the CNT/PA12 composites were proposed to be used for the fabrication of the 3D cellular and auxetic lattices for

the destructive energy absorption purpose. Another type of 3D soft auxetic lattices was fabricated by the laser-sintered TPU material, which could be highly flexible and recoverable upon cyclic compressive loading. Meanwhile, the energy absorption capability of 3D lattices could be engineered by tuning the structure designs and controlling the material formulations. Thus, the concept of the digitization and integration of materials and structures was implemented into the SLS system and the newly prepared polymeric nanocomposites was incorporated with complex 3D lattice structures. The multi-scale and multi-functional architectures could be designed and engineered to possess vibration resistance and impact shock absorption.

This PhD dissertation developed a systematic and integrated methodology for material development, process optimization and structure design in the SLS process. This methodology provides an effective guidance for formulating materials and engineering their morphology to match the stringent requirements of the feeding material for the SLS process. The designed 3D auxetic or cellular lattices can be manufactured through the optimized system using the newly developed materials to achieve the desirable performance of energy absorption or dissipation.

Table of Contents

List of Tables

List of Figures

Chapter 1 Introduction

1.1 Background

Additive manufacturing (AM) via three-dimensional (3D) printing is a group of solid freeform fabrication methods to layer-by-layer build up 3D objects based on the computer-added design models and pre-coded slice files [1, 2]. Thus, AM techniques have the capability of fabricating components with complex geometries without the need of any tooling or moulding process. Selective laser sintering (SLS) is one of powder-based AM techniques, introduced to manufacture polymers or polymeric composites into products with improved functionalities and extend their end-use applications as the essential components of automobile, aircraft and aeronautical sectors [3-5]. Polyamides such as PA12 and PA11 are the most common materials used in the SLS system and intensive research works have been conducted on the material development of polyamide composites [6, 7]. In recent years, polyethylene [8-10], polyurethanes (PU) [5, 11-14] and other thermoplastic elastomeric materials have been introduced to the laser sintering to fabricate flexible and smart actuators or dampers for wearable device and automotive applications [5].

The development of a new type of composite materials faces many challenges arising from poor mechanical strength, thermal instability, limited consistency and repeatability [11, 15, 16]. To develop new composite powders, a comprehensive understanding of intrinsic properties of polymeric materials, including physical and chemical properties and thermal kinetics, is needed [15, 17-20]. These intrinsic properties significantly influence the multi-functionality of sintered products. Achieving

great consistency and systematic control is a challenge faced in both industrial and academic researches. Therefore, it is necessary to improve the methodology of systematic material development, covering powder preparation and characterization, sintering process optimization and post-processes [21-28]. However, developing new materials for the SLS system is costly and time-consuming [29].

Carbon nanomaterials such as carbon nanotubes (CNTs), graphene and short carbon nanofibers are an emerging group of materials used as reinforcements of polymeric matrices [30-34]. Lightweight carbon/polymer composites exhibit the promising specific modulus and strength in mechanical aspects and possess highly enhanced electrical and thermal properties as compared with neat polymers [35-39]. Thus, the development of carbon nanomaterials-reinforced polymeric composites with desirable functionalities is strongly required in the numerous usages of electrical packaging, anti-electromagnetic interference (EMI), thermal management in the military, automotive and aerospace industries [40-44].

Compared with the conventional composites, nanofillers such as multi-walled CNTs (MWCNTs)-reinforced polymers can simultaneously achieve great enhancements of mechanical strength and toughness as well as the electrical and thermal conductivities [45-50]. MWCNTs are promising nanofillers for preparation of electrical and thermal conductive polymeric composites through several manufacturing methods. These traditional processes including injection moulding, melt extrusion and hot-sintering exhibit the high productivity and dimensional accuracy of products [45, 51, 52]. However, these hot-forming techniques unfortunately encounter the obstacles of nanofiller agglomerations within the polymer matrices. Such undesirable distributions

of fillers adversely affect the electrical and thermal performance of MWCNTs in polymeric matrices, as the poor interfacial adhesion of CNT-polymer and interconnection of CNT-CNT among the 3D space [34, 53-55]. Additionally, the moulding or *in-situ* polymerization processes are facing a great challenge to effectively manufacture products with complex geometries and customized designs for aerospace and biomedical applications.

1.2 Objectives

The PhD study will focus on the formulation and manufacturing process of composite powders and the optimization of the SLS process for the newly developed powders as well as the investigation of the multi-functionality of laser-sintered composite materials and their application for energy absorption. The main challenge is to make the CNTs/polymer composite powders in a colloidal system, as the mixing methods have several disadvantages and limitations. Moreover, there is inherent constraint on the geometry and architecture of the part that can be fabricated by using the newly developed powders. Therefore, to establish the further capability of designing and fabricating functional graded parts through the newly formulated nanocomposites, the main objectives of this PhD study are set as follows.

(i) Development of a novel process for composite powder manufacturing

The proposed method is able to effectively and uniformly coat MWCNTs onto various polymer-based powders. The prepared powders with sufficient flowability can be deposited onto the powder bed of the SLS system smoothly and uniformly to ensure the subsequent heating and sintering processes to be conducted successfully. Meanwhile,

the morphology, thermal behaviours and rheological properties are conducted to validate the feasibility of powders for laser sintering. The nanocomposite powders possess the qualified intrinsic thermal behaviours including rapid melting, slow recrystallization, and mediate melt viscosity.

(ii) Investigation and optimization of the SLS process for MWCNTs-reinforced PA12 and TPU composite powders

In this study, thermoplastic PA12 and thermoplastic PUs (TPUs) elastomer powders are selected as the fundamental polymer-based materials for composite preparation. Two new groups of CNTs-reinforced polymeric nanocomposite powders (CNT/PA12 and CNT/PU) possess unique mechanical, thermal and electrical properties, and the underlying mechanisms of reinforcements are investigated and interpreted through theoretical and experimental approaches. After the material formulation of composite powders is verified, the laser sintering process is further optimized to consistently deliver reliable and repeatable sintered composite products, with desired thermal, electrical and mechanical performances over currently market available products produced by SLS.

(iii) Exploration of the process-structure-property relationships and study of the underlying mechanisms of thermal, electrical and mechanical enhancements

Furthermore, these two new groups of polymeric composites allow SLS to print 3D lightweight and flexible composites with controlled architectures in multi-scale, carbon-based fibre reinforcements (such as MWCNTs) to create hierarchical structures with integrated functionalities. This basic concept enables an entirely new dimension to hybrid engineering design and optimization, such that material compositions,

mechanical strength and toughness as well as electrical and thermal conductivities. A bulk 3D object can be digitally integrated with component design to achieve a highly-optimized structure.

(iv) Energy absorption and dissipation applications of lightweight structures fabricated by CNTs-reinforced PA12 and TPU composites

The lightweight designs such as auxetic and cellular lattices incorporated with MWCNTs-reinforced PA12 and TPU composites are manufactured by the SLS process. The specific modulus, strength and gravimetric energy of lattice structures are investigated to evaluate the energy-absorption capability and compared with those of 3D-printed metallic lattices and other conventional materials for energy absorptions. The robust CNT/PA12 materials can be good candidates for the applications of protective packaging and impact protection; while the soft TPU materials enable the recoverable deformation upon cyclical compression loading and thus are used for actuation and damping purposes.

Figure 1.1 shows the systematic research methodology of manufacturing digitized products. The novelty of this PhD research is the new manufacturing process of composite powders, which can form their desired configurations. Thus, it offers an opportunity to integrate structural design and material digitization through the layer-by-layer powder sintering process. The powder technology and material formulation are addressed in the current work.

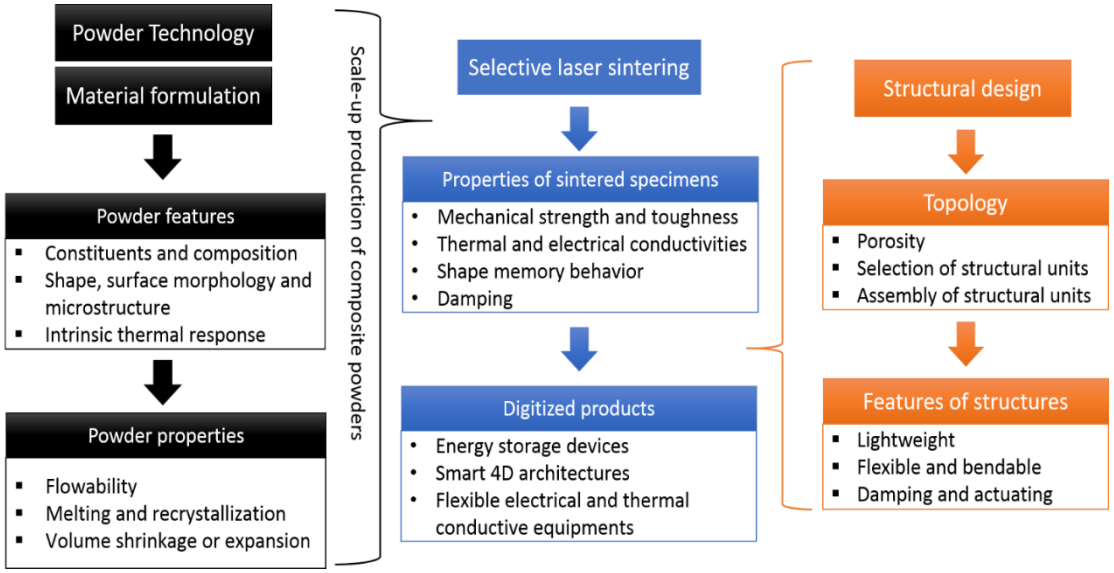

Figure 1.1. Diagram of the research methodology for multi-functional products produced by the SLS system

1.3 Thesis outline

This thesis consists of seven chapters. Following a brief introduction in this chapter, Chapter 2 reviews the state-of-the-art polymeric composite powder manufacturing technologies with a focus on the solution-based processes. Different formulations and additive fillers are reviewed and their merits and limitations are discussed. The mechanical properties and applications of 3D-printed composites are also discussed.

Chapter 3 presents a novel method to embed the functionalized CNTs into/onto the polymeric powders. The fundamental procedures for this powder manufacturing are illustrated. The advantages and achievements of the proposed method are summarized as compared with other approaches of polymeric composite powder manufacturing.

Chapter 4 proposes a systematic and effective method of material evaluation and process optimization, which can be generally applicable for different types of polymers and their composites as well. The critical polymer intrinsic properties and powder

behaviours are characterized to predict the sintering stable range of the SLS process, through which the process optimization can be effectively improved to minimize cost for the process parameter optimization.

Chapter 5 investigates the electrical and thermal conductivities of MWCNTs-reinforced PA12 and TPU composites, which are manufactured by the SLS process. The underlying mechanisms of electrical and thermal enhancements of MWCNTs within the polymeric matrix are investigated through systematic microstructure characterizations.

Chapter 6 focuses on the energy absorption capability of the CNT/PA12 composite lattices and the energy dissipation of laser-sintered TPU lattices. Typical 3D auxetic and cellular lattices are manufactured and their specific compressive strength and gravimetric energy are evaluated through the compression strain-stress relationship and energy-absorption diagram. Additionally, the Ashby charts of specific strength and gravimetric energy are illustrated to compare the laser-sintered composite structures with other available metallic, composite and porous materials.

Finally, major contributions that have been achieved in this thesis research are summarized and future works are recommended in Chapter 7.

Chapter 2 Literature review

In this chapter, a fundamental understanding of the laser sintering system is provided and the principal methodology of new material development is demonstrated. Furthermore, a comprehensive review is provided for the composite materials available to the SLS system. The current available techniques and processes in powder manufacturing are discussed. The solution-based processes are emphasized because these approaches can inspire researchers to further develop a novel method of nanocomposite powder manufacturing with the unique advantages over other types of powder manufacturing.

The functional properties of materials and structures produced by laser sintering or other AM techniques are reviewed in terms of thermal, electrical and mechanical properties. The merits and disadvantages of the functionalities of laser-sintered parts are discussed. Additionally, the potential applications of these laser-sintered structures, such as cellular structures or auxetic structures, are explored.

2.1 Selective laser sintering

SLS, one of AM techniques, offers an opportunity to fabricate products of complex geometries through consolidating powder materials layer-by-layer as illustrated in Fig. 2.1 [56, 57]. Thermoplastic polymer powders are used as building materials or binders to construct 3D objects by a CO_2 laser source [16, 58]. The principal advantages of SLS over other polymer AM techniques are as the follows: i) supporting materials are not necessary for building a complex or hollow structure which can be supported by the

surrounding unfused powders [59-61]; ii) a large number of candidate materials are open to the sintering process [62]; iii) the unfused powders are highly recyclable for subsequent builds [63-65]. For direct laser-sintered products, ceramics, glass beads and carbon fillers can be employed to reinforce the polymeric matrix for end-use applications or rapid prototyping [25, 66-73]. On the other hand, the laser-sintered polymer/metal or polymer/ceramic composite can be utilized for other post-processes such as moulding, casting, and enhanced-sintering for ceramics and refractory metals to improve the processability and reduce the cost of these processes [74-78].

Nowadays, the global market has a strong demand for multifunctional materials in electrical, biological and optical usages. Although most of thermoplastic polymeric powders can be sintered in principle, only a narrow range of polymeric materials are

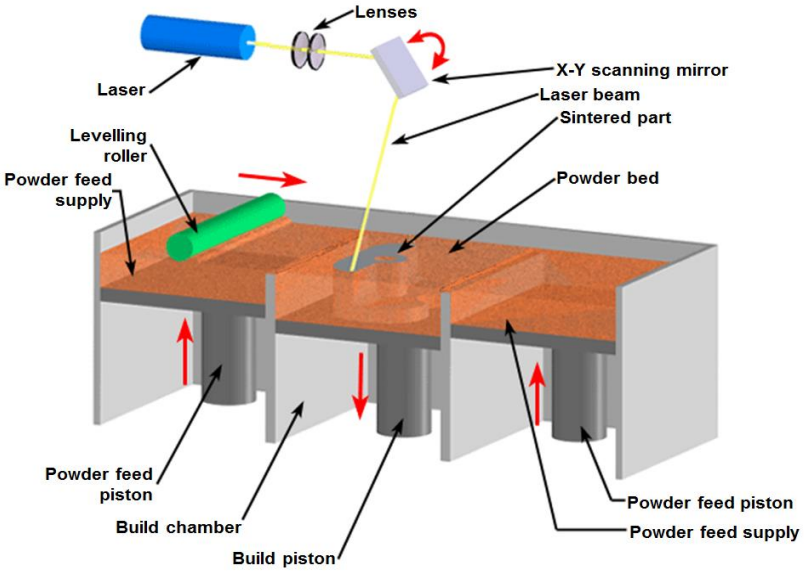

Figure 2.1. Schematic illustration of an SLS system [45].

processed with well-established sets of parameters in the present SLS system, and there are limited functionalities and tunabilities for current commercial polymer resins [62].

In recent decades, intensive attention has been drawn to polymer-based nanocomposites because a pool of nanomaterial candidates can provide large possibilities to broaden the functionalities of polymeric materials and diversify their applications [24, 29, 66, 79]. Therefore, it is desired to develop polymer-based nanocomposites for laser sintering or post-secondary processes to satisfy the current market requirements [80-82]. Unfortunately, the dynamics of nanomaterials in the polymer matrix during sintering is poorly understood, which restricts the development of a new material and the improvement of a manufacturing process [83-86].

2.1.1 Process parameters

The critical factors of the SLS process are indicated in Fig. 2.2 (a), which simultaneously influence the energy input on the specific volume upon laser scanning. The generally applied CO_2 laser follows the double ellipsoidal heat distribution as shown in Fig. 2.2 (b), which was developed from the common model of the Gaussian heat distribution [3, 87, 88]. This heat source is a combination of two half ellipsoids (one in advance of the centre of the heat source and the other at the rear) which considers the asymmetric temperature gradient of the centre of the moving laser heat source [3]. Fig. 2.3 indicates the critical parameters of laser sources, which are directly influencing the energy input upon the scanning process.

The determination of processing parameters for a newly developed polymer or polymer composite to achieve desirable part performance is still challenging in the SLS system because laser sintering is a complex thermal and dynamic process which includes heat absorption, heat transfer, phase change and melt flow manners. The empirical optimization of processing parameters is based on an iteration of trial and error builds,

which is highly time-consuming and extremely expensive depending on the cost per unit of materials, especially for non-recyclable polymers.

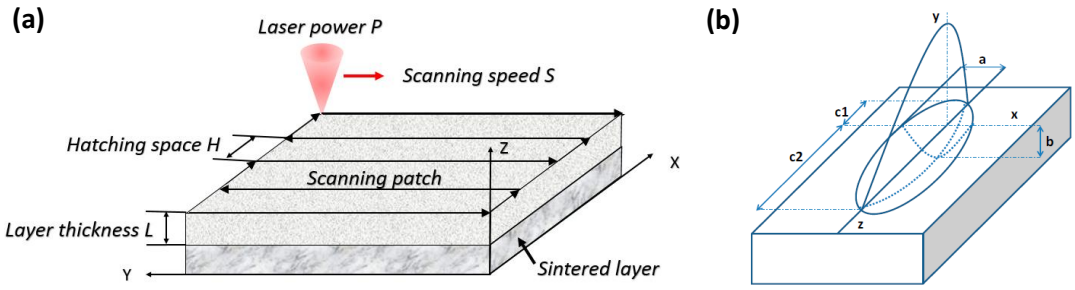

Figure 2.2. Schematic illustrations: (a) key laser scanning factors in the SLS laser process and (b) double ellipsoidal heat source model applied to predict the heat distribution of the CO_2 laser source [3].

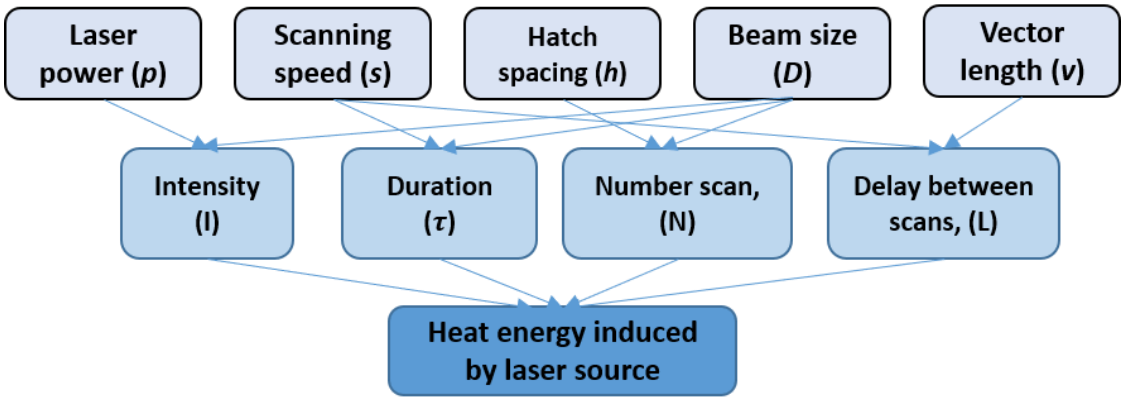

Figure 2.3. The influence of critical laser parameters on the input laser energy.

The theoretical model of heat transfer in the laser sintering process is described by

$$\rho C_P \frac{\partial T}{\partial t} = \frac{\partial}{\partial x}(\kappa \frac{\partial T}{\partial x}) + \frac{\partial}{\partial y}(\kappa \frac{\partial T}{\partial y}) + \frac{\partial}{\partial z}(\kappa \frac{\partial T}{\partial z}) + E\,, \qquad (2.1)$$

where ρ is density κ thermal conductivity, C_p heat capacity of media material, t the time, T the temperature, x, y, and z the coordinates, and E the energy that the polymer absorbs from laser scanning. Eq. (2.1) is applied to predict the temperature distribution in 3D, where the polymer-absorbed energy from laser is strongly dependent on the parameters

of the laser source such as the laser power p, the laser scanning speed s, the hatching space h, the beam size D and the laser vector length v as illustrated in Fig. 2.3. A simplified model is used to predict the energy induced by the laser per unit area E_{area} and unit volume E_{vol}

$$E_{area} = \frac{p}{hs}, \tag{2.2}$$

$$E_{vol} = \frac{p}{hsL}, \tag{2.3}$$

where L is the layer thickness of an individual deposited layer. The energy required for polymer melting is simplified as

$$E_{mv} = \rho\phi[C_p(T_m - T_b) - h_f], \tag{2.4}$$

where ϕ is the packing factor, T_{m} is the melting temperature of polymer, T_{b} is the bed temperature of the building chamber, and h_{f} is the enthalpy of melt [89]. For this model, the polymer absorbed energy E should be higher than the energy required for melting E_{mv}. To quantify the effectiveness of the laser heat for sintering, an energy melt ratio (EMR) is introduced as

$$\text{EMR} = \frac{E_{\text{vol}}}{E_{\text{mv}}}. \tag{2.5}$$

The EMR obtained via a practical method is to compare laser-sintering parameters incorporating the bed temperature and polymer powder properties. Recently, Vasquez *et al.* [16] and Berretta *et al.* [90] employed this model to predict the process parameters, which could numerically calculate the thermal energy to melt the applied powders including the factors of the bed temperature, powder packing density, specific heat, melt temperature and heat of fusion. A stable sintering region (SSR) was investigated to describe the optimal temperature range for a successful sintering process and the estimation of the energy absorption within this range could help to determine the

processing parameters. These polymer powders were melted to coalesce in a liquid phase and then recrystallized to form solid structures upon the superfast heating and cooling cycle. The intrinsic properties of applied powders exhibited temperature and phase-dependent behaviours, but the characterization and calculation for the dynamic influences of thermal properties on laser sintering have not been adequately addressed.

2.1.2 Material development

A schematic flow chart of new material development for the SLS system is shown in Fig. 2.4. The main steps of development involve manufacturing of powders, evaluation of flowability, characterization of powders, laser sintering, characterization of sintered parts and verification of reliability. In the past decade, intensive studies have been conducted to investigate the powder flowability and thermal behaviours of polymers to complete the preliminary steps of material evaluation for laser sintering. The methods of powder manufacturing are introduced in Section 2.2.2.

Powder flowability refers to how a given material flows in a specific equipment, implying that the identical material may perform differently under the different flow conditions. Flowability is the key physical property influencing the decomposition process. Poor homogeneity and uniformity of powders induce uneven layers, leading to porous and weak sintered parts [63]. This property depends on several factors including the particle size distribution, particle shape, surface features, and environmental temperature and moisture. Usually, it is related to the Hamaker constant, which is a force constant used to estimate the interparticle interactions by considering the physic-chemical nature of the materials involved. It can also be directly characterized through

the angle of response (AOR) testing, which quantifies the angle of the cone of a bulk

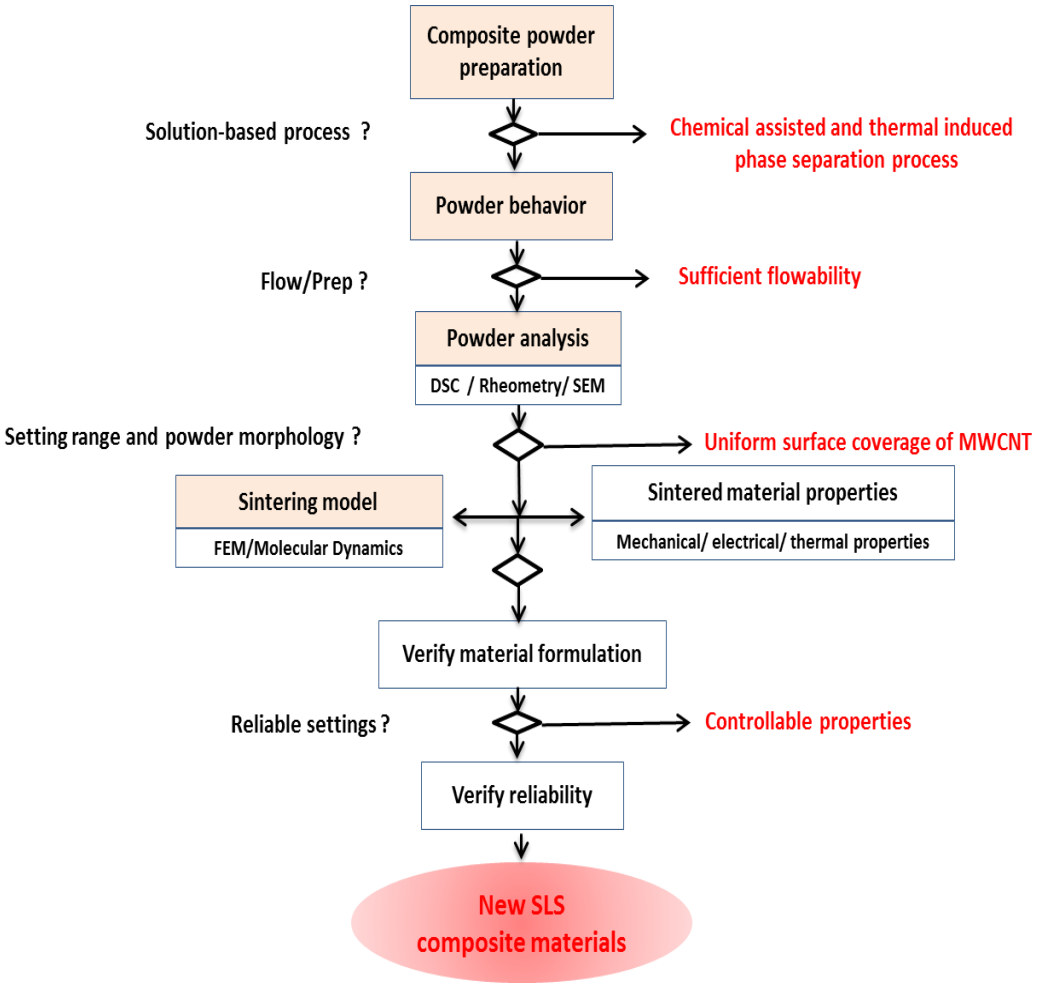

Figure 2.4. Systematic methodology of the composite material development for the SLS system.

material over a flat surface. The testing follows the ASTM C1444 standard [91]. Generally, the AOR is positively correlated to the Hamaker constant; whereas the powder flowability is relatively poor once the AOR is higher than 45°.

Differential scanning calorimetry (DSC) is a technique to characterize the exothermic and endothermic behaviours of polymers upon the heating and cooling process, and it helps to identify the critical temperature transitions such as glass

transition, melting temperature and recrystallization. These transition temperatures are critical to determine the processing window of the specific polymer for sintering, the powder bed temperature and removal chamber temperature. The melt viscosity at the zero-shear rate is usually employed to evaluate the fusion of powders, as the shear viscosity is critical to judging material sinterability as compared with surface tension [92]. Therefore, the rheological characterization is conducted to obtain the complex viscosity, storage and loss modulus of polymer melt in order to investigate the sintering behaviours of polymer powders.

After a parametric control is designed to print parts with respect to different sets of process parameters, the printed parts are usually evaluated by comparing their mechanical properties to verify the material composition and optimize the process parameters. However, the development of a new type of composite materials still faces many challenges arising from poor mechanical strength, thermal instability, and limited consistency and repeatability. To develop new composite powders, a comprehensive understanding of intrinsic properties of polymeric materials, including physical and chemical properties and thermal kinetics, is needed [15, 17-20]. These intrinsic properties significantly influence the multi-functionality of sintered products. Achieving greater consistency and systematic control faces challenges in both industrial and academic researches. Therefore, it is necessary to improve the methodology of systematic material development, covering powder preparation and characterization, sintering process optimization and post-processes [21-28]. However, the development of new materials for the SLS system is costly and time-consuming [29].

2.2 Composite powders

The fundamental materials used in the SLS system are powder-based polymers or polymeric composites, the sizes of which are usually in the range of 50~150 μm [93-95]. The characteristics of these powders significantly influence the sintering process and the properties of sintered products. The critical characteristics of powders often include their size, size distribution, shape, morphology, and composition and configuration if they are composites. These powder features depend on powder manufacturing methods [23, 36, 59, 69, 78, 93, 96, 97]. However, it is still difficult to manufacture polymeric composite powders with desired features for the SLS process. For instance, a proper size range, a uniform size distribution and semi-spherical shape result in a favourable flowability, which is beneficial for the powder deposition process. Desired compositions and configurations of composite powders positively affect the sintering process and can improve the properties of sintered products. The properties of sintered composite products (density, stiffness, modulus, chemical activity, etc.) are often determined by the rule of mixtures in the manufacturing process. Many mechanical failures and defects of composites are attributed to the poor interfacial connection and the unexpected distribution of the fillers in the polymeric matrices [98, 99]. To improve the thermal performances and mechanical properties of powders, the fabrication of polymeric powders generally involves the mechanical mixing and chemical treatments to achieve homogeneous microstructures.

The four states of composite powders can be observed during the sintering process (Fig. 2.5 (a)). Powders are deposited onto a building platform uniformly in the pre-sintering state; powders start to rearrange due to thermal expansion or swelling during

the pre-heating process; when the powders are exposed to laser heat, they immediately melt to form a mixture in the solution precipitation state; the melted composites solidify quickly and then progress to the stage of solid state sintering. Therefore, in such fast heating and quenching processes, the polymer powder may be just partially melted and the filler or secondary grains are glued by the pasty polymer melt. This pressure-free process may induce a unique microstructure in the sintered composite parts as compared with other hot-forming techniques under a high pressure. The polymer phase is interconnected in 3D and the fillers or structural elements are dispersed into the polymer matrix homogeneously.

Based on the configuration of grains within an individual powder, the composite powder systems can be classified into two categories: the separate grain system and the composite grain system [100]. The SLS technique can utilize the separate grain powders as the original building materials, in which the individual powder is of a single material as shown in Fig. 2.5 (c). In this case, two or more separate grains often have distinct reflectivity and radiation absorptions, and thus the laser energy may be predominately adsorbed by one group. In general, one group of these powders acts as a binder material, and another group is a structural material. In contrast, composite grain powders are composed of the polymer matrix and reinforcement in each individual powder. One type of composite grain powders possesses effective and uniform dispersion of reinforcements in polymer matrices as demonstrated in Fig. 2.5 (d). Another type of composite grain powders possess the core-shell configuration (Fig. 2.5 (b)), which can be either polymer-coated ceramic/metallic grains or nanomaterial-coated polymeric grains, ensuring the laser radiation to be preferentially absorbed by the surface coating [76, 101].

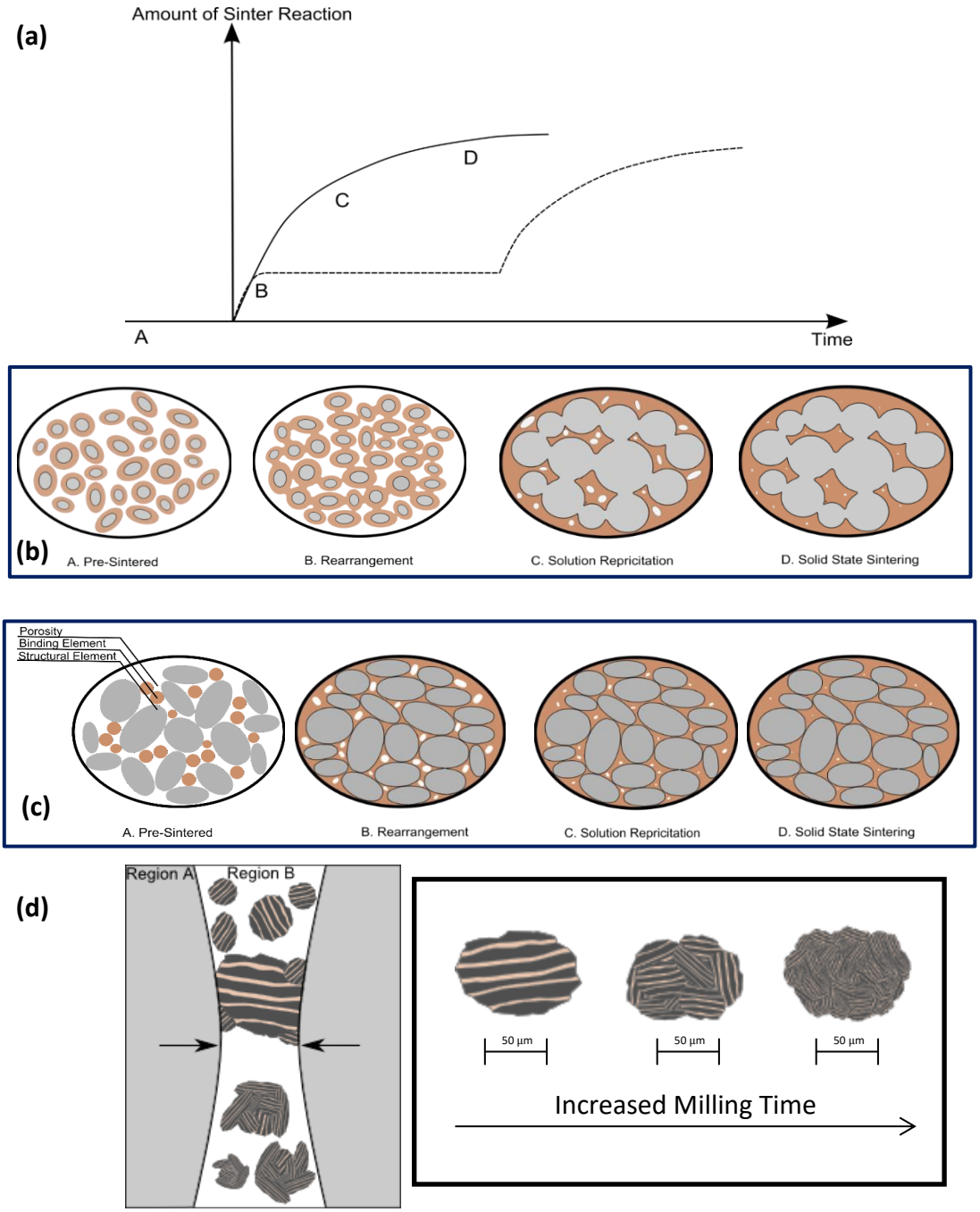

Figure 2.5. Composite powders with different configurations for laser sintering. (a) the stages of powder fusion upon laser heating; (b) sintering of polymer-coated powders; (c) polymer powders used as a binder; (d) embedding fillers intro polymer powders through the milling process [78, 102].

2.2.1 Constituent materials

Polymeric materials are predominately applied in the SLS system. Especially

thermoplastics with a semi-crystalline structure are favourable for the laser sintering process because they exhibit two critical phase transitions from the glassy to the rubbery state and from the rubbery to the melt state, as shown in Fig. 2.6. Meanwhile, thermoplastics can usually blend with a variety of reinforcements to subsequently enhance the functionality of original polymeric matrices. Thus, polymeric composites are emphasized in the SLS system because of their coupling the properties of polymers with the advanced functionalities of reinforcements. A comprehensive understanding of the chemical, mechanical and thermal properties of polymeric materials and reinforcements helps to improve the current sintering techniques and bridges the gap between academic research and market demand. This section discusses the main types of polymeric materials and their composites, with a focus on the chemical and physical behaviours of matrices as well as the functionalities of each group of reinforcements.

2.2.1.1 Polymers

For a successful laser sintering process, polymeric powders generally need to be heated to a pre-heating temperature, namely bed temperature, resulting in a phase change from a glassy to a viscoelastic state, and ultimately to a viscous flowing melt as shown in Fig. 2.6 (a) [103]. The pre-heating temperature of polymeric powders depends on the transition temperature of the polymer matrix, which can be amorphous, semi-crystalline and crystalline polymers. However, few crystalline polymers are present in a powder-based manufacturing system. An amorphous polymer has no defined melting point and gradually softens with an increasing temperature. The transition temperature for an amorphous polymer is the glass transition temperature T_g above which the

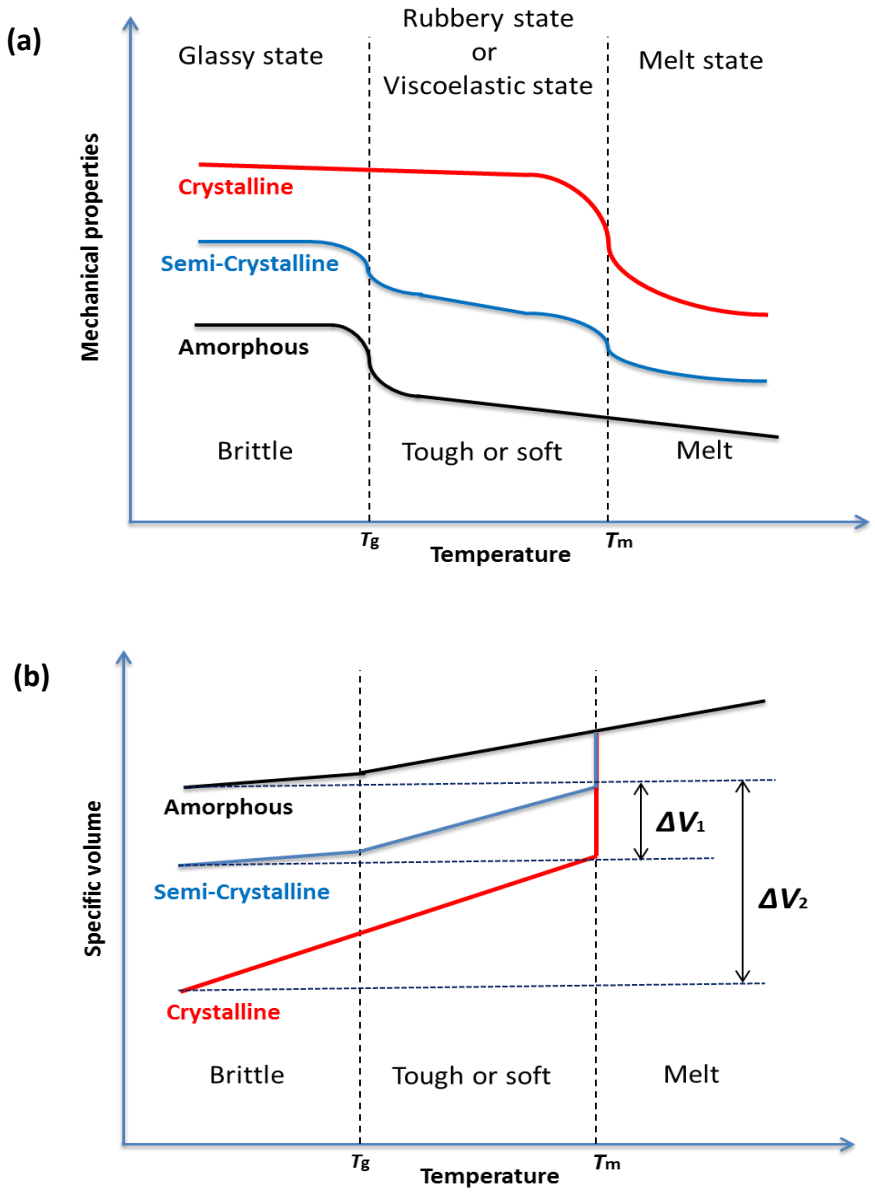

Figure 2.6. (a) Influences of the temperature change on the mechanical properties of amorphous, semi-crystalline and crystalline polymers; (b) the specific volume change caused by temperature drop for amorphous, semi-crystalline and crystalline polymers [62].

amorphous polymer gradually transfers to be a viscous flow. Therefore, the pre-heating temperature of an amorphous polymer in the SLS system is normally equal to or just below its T_g. However, as the amorphous polymer powders experience gradual softening

and have no critical melting point, it is hard to control inter-powder diffusion under an elevated temperature. Thus, to date, amorphous polymers are not preferable in the laser sintering processing.

A semi-crystalline structure in polymers contains both amorphous and crystalline phases. Thus, a semi-crystalline polymer has not only the glass transition temperature T_g, which is usually around or below room temperature, but also a clear melting temperature T_m, normally above 100 °C. This polymer experiences a rapid change from a solid to a viscous flow when sufficient heat is absorbed at T_m (Fig. 2.6). In the SLS system, the pre-heating temperature of a semi-crystalline polymer is often set just below T_m, so that in the sintering process the laser can easily change the polymer into its molten state, allowing it to remain at that temperature for a sufficient period after consolidation. Consequently, large thermal gradient-caused curling can be minimized. Laser heat energy partially melts and fuses the polymer powders, eventually achieving near-fully dense specimens. In this way, the mechanical properties of the sintered specimens are comparable to these of the moulded specimens.

Polymeric materials which are favourable to the SLS process are required to satisfy certain requirements including proper molecular weight, semi-crystalline structure, sharp melting peak, medium melt viscosity, a wide glass temperature window and desired recrystallization behaviour. Firstly, a high average molecular weight is found to improve the mechanical properties, particularly elongation at break. The molecular weight should be above the critical entanglement molecular weight (i.e. the turning point from the viscoelastic to the glassy state), whilst it should also be low enough to reduce the energy input needed for sintering. Secondly, a semi-crystalline polymer exhibits two

critical phase transitions, which significantly affect the specific volume change ΔV_1 and the mechanical properties in the process temperature range as illustrated in Fig. 2.6 (b). A highly crystalline polymer is not recommended for laser sintering because of large volume shrinkage ΔV_2 during solidification and distortion. Thirdly, the semi-crystalline polymer with a sharp melting peak and a low melt viscosity are desirable for laser sintering. In this case, the bed temperature can increase to approach T_m, thus minimizing the laser energy required for consolidation as well as achieving highly dense products. Nevertheless, a high melt viscosity of the polymer is good for its mechanical properties such as tensile strength and elongation at break. Therefore, a medium viscosity of the polymer is preferable to SLS, which can maintain the wetting capability of its powders and yield its desired mechanical properties. Lastly, a proper material candidate should be capable of being processed at a wide range of temperatures, also known as the glass window, which usually falls within the range from recrystallization to melting point. A wide process temperature range allows great processing adjustability, particularly during the optimization of other process conditions; therefore, a small deviation of processing temperature has negligible influences on the dimensional accuracy and mechanical properties. Usually a slow cooling process induces relatively low crystallinity corresponding to the improved ductility of sintered products.

Polyamides PAs or PA-based thermoplastic composites are predominant in the current market mainly because PAs are semi-crystalline thermoplastic polymers with good processability [62, 104, 105]. It was reported that in 2007, 95% of available materials were PA11, PA12 and PA-based composites [62]. Most of PAs have a moderate T_g of 40 °C [7] such as PA11 and PA12, whose T_m falls within 183~190 °C and

176~188 °C, respectively. Their wide temperature differences between T_g and T_m offer a processing advantage to achieve softening and partially melting at relatively low temperatures [100, 103]. As exemplified in Fig. 2.7, the DSC curve of the virgin PA12 powders shows a large temperature difference between the melting and crystallization peaks, which indicates a wide process temperature window for this material.

Allowing for a slow cooling process, delaying and minimizing crystallization during the build process can prevent the accumulation of residual stresses that causes the part to distort [106]. In addition, recrystallization of PA11 or PA12 is sufficiently slow in the consolidation process, resulting in minimal curling [107].

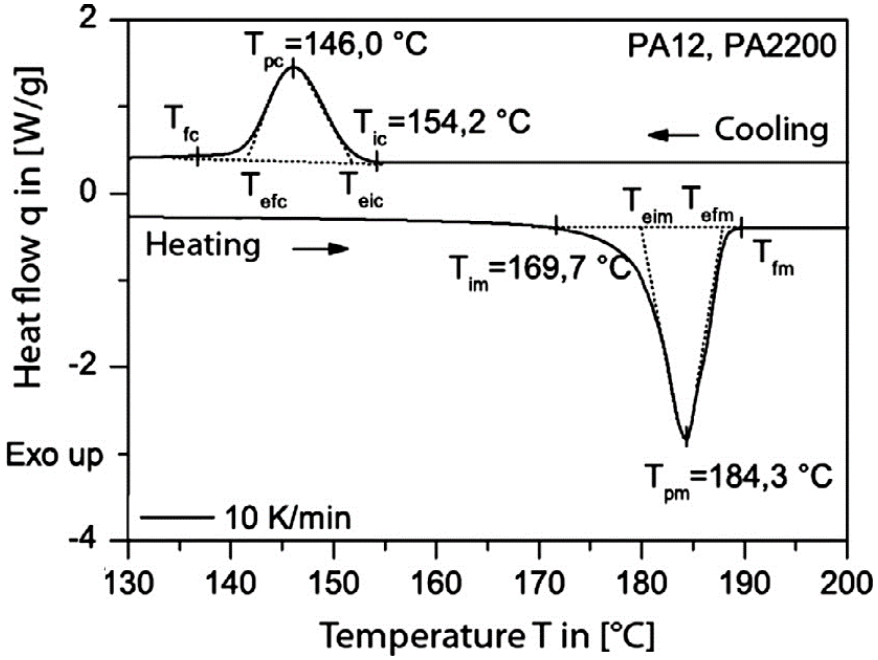

Figure 2.7. DSC curve of virgin PA12 powders which experience a heating and cooling cycle at the rate of 10 °C/min [88].

Commercial PA12 also has a relatively large temperature window, which means that a deviation of several degrees around the optimum process temperature can still yield parts with acceptable mechanical properties. The onset of melting and onset of

recrystallization of PA11 are around 176 °C and 168 °C, respectively [2, 6], and thus PA11, however, has a relative small processing window as compared with PA12. PAs, like other materials, are susceptible to changes in their structures due to thermal processing-induced residual stresses and micro-structural crystalline changes [108].

Amongst SLS powder materials, PAs have relatively high mechanical strength, excellent wear resistance and good sliding properties. However, the degradation of PAs is a function of thermal history of polymer powders. At the pre-heating temperature of ~170 °C within the range of recrystallization of PAs, the active amide groups that exist in aliphatic polyamides form hydrogen bonds between the molecular chains, and then PAs tend to increase the rate of crystallization with highly ordered structures [109]. PA11 experiences rapid re-crystallization and degradation during pre-heating due to the formation of hydrogen bonds between the molecular chains [109]. The induced highly ordered crystalline phase is irreversible upon heating-cooling. Therefore, after a few thermal cycles, PA11 cannot be reused as sintering material. The process inevitably changes the PA melt characteristics and reduces the recyclability of PA powders. Although PA11 has a greater ultimate tensile strength (49.6 MPa) than PA12 (UST- 44 MPa), PA12 is easier to process and recycle, resulting in a greater potential for further usage [7]. Recently, PA6 was also introduced as a material for SLS due to its greater plastic deformation and less elastic recovery under an elevated temperature [110]. Additionally, PA6 and PA12 exhibit similar viscos-dissipative behaviours, and the microstructures of their blends are heterogeneous, with co-continuous or disperse phases [110]. Thus, PA6/PA12 blends are potentially applied for extended commercial applications, particularly in an end-used manufacture scenario. Unfortunately, the

recyclability and reusability of materials must be considered.

Polyurethanes As a new type of SLS materials, thermoplastic PUs (TPUs) were introduced to the market by Bayer MaterialScience and Lehmann & Voss in 2012. More recently, PU-based polymer blends (DuraForm Flex) were launched by 3D Systems. PU-formed products exhibit high wear resistance, good resistance to oils, greases and solvents, and extremely good weather stability as well as high elasticity [18, 55, 111]. In addition, TPU bridges the gap between rubbers and hard plastics, as they possess rubber-liked flexible behaviours with mechanical strengths comparable to those of hard plastics after being re-melted and re-shaped. More importantly, the pre-heating temperature of PUs is as low as ~80 °C, which can minimize warping and maintain a stable sintering process [111]. Plummer and Vasquez reported that un-sintered TPU powders do not experience significant aging effects in the heated build chamber, and therefore can be reused in the next printing job [18]. Therefore, TPUs have the advantages of easy processing, material saving and energy conservation, as compared to other currently available SLS materials. TPUs could also potentially be introduced into biomedical applications, such as E-glass/PU composites [112].Intensive interests have been drawn to TPUs and their composites for tissue engineering and bio-implantation as they are soft and rubbery and possess high ductility and good biocompatibility. However, the thermal properties of TPUs are not perfectly matching the requirements of powders for the SLS system. It is necessary to develop precise process design for TPUs in laser sintering.

2.2.1.2 Reinforcements

Reinforcements can be classified into four categories: i) metallic fillers, ii) ceramic fillers, iii) carbon-based fillers and iv) polymer blends. The enhanced performance of each type of fillers and the constituents of each composite will be elaborated. For the SLS system, reinforcements are often introduced into the polymer matrix for various purposes such as eliminating mechanical and thermal failure of the polymer matrices [113, 114]. The properties of composites are strongly influenced by their constituents and their interfaces often have superior toughness since the filler particles can deflect or prevent nano- and micro-crack propagation [96, 115, 116]. In addition, the reinforcements can have specific functional properties, such as magnetic properties, conductivity, biocompatibility and biodegradability, which broaden the applications of original polymers [117, 118]. Reinforcements can also be introduced to improve the processability of thermoplastics with high melting temperatures. For example, PS (low T_m) blends with PA (high T_m) to assist the thermal melting and diffusion of PA powders in the SLS process [105].

Metallic fillers The addition of metallic fillers in the polymer matrix usually aims at increasing both the thermal and electrical conductivities and enhancing the mechanical properties of the polymer matrix. For instance, aluminium and carbon steel both have such functions to reinforce polymer matrices. However, the chemical affinity and dispersion of metallic particles in the polymer matrix is not easily controlled in the manufacturing process. Most of mechanical failures in metallic polymer composites are attributed to poor interfacial adhesion between metallic and polymeric materials. On the other hand, the metallic phase can also be the functional green part in the metal/polymer

composite. For example, PA12 is used as a binder material to glue metallic powders together so as to form a united body [119]. This method is an energy-saving process used to build metallic green parts at a relatively low temperature, thus significantly reducing the cost of manufacturing refractory metallic materials such as molybdenum [76] and tungsten [120, 121].

Ceramic fillers Ceramic fillers are often used to enhance the mechanical properties of the polymer matrix. Popular ones include oxides and nanoclays which are groups of ceramic fillers known to improve the thermal stability and flame resistance of polymers under elevated temperatures [7, 95, 122, 123]. Additionally, bio-ceramic fillers play an important role in promoting cell attachment and growth in the sintered bio-scaffolds, with hydroxyapatite (HA) and tricalcium phosphate (TCP) which are typical bioactive ceramics utilized to improve functionality of various SLS polymers including PA12, polyether ether ketone (PEEK), polycaprolactone (PCL) and polylactic acid (PLA). The fire-retardant and mechanical properties and the bioactivity of polymeric composites are significantly influenced by the packing density, size, distribution and surface chemistry of fillers, which are usually determined by powder manufacturing processes.

Carbon-based fillers Carbon-based fillers exhibit promising properties, coupling high thermal conductivity and mechanical strength with low mass. Graphite, carbon fibres and carbon black are commonly used carbon-based fillers, blending with PA12 and PA11 to form composite powders. Interestingly, the electrical conductivity of sintered carbon black-reinforced PA can be improved by several orders of magnitude as compared with that of PA alone [124]. Meanwhile, fire-retardant composites made from PA and reinforced with carbon fillers have been successfully produced, which are

suitable for aerospace and military applications [123].

A new generation of carbon-based fillers, including graphene, SWCNTs, MWCNTs and carbon nanofibers, has gained attention in numerous research fields due to impressive electrical, thermal and mechanical properties. Composite products are also possible to exhibit multi-functionalities as compared with the neat polymer matrix. For instance, a small addition of MWCNTs (< 5 wt%) enhances both the mechanical toughness and the electrical conductivity of PA12 simultaneously [104, 115]. However, achieving fair dispensability of nano-reinforcements in the polymer matrix remains a challenge because the carbon nanofibers and the nanotubes with a large surface to volume ratio tend to agglomerate, thus minimizing the interface area with polymer chains.

In general, non-covalent modification and covalent functionalization, e.g. acid oxidation are the main two types of surface treatments for carbon nanomaterials such as CNTs [125]. Herein, the non-covalent functionalization includes polymer warping, surfactant adsorption and endohedral methods [83]. The surfactants treat the CNTs before being fed into the polymer matrices, and the presence of surfactants may facilitate CNTs to compound with polymers. Although non-covalent functionalization could avoid surface defects on the carbon fillers as well as uniformly disperse carbon-based nano-fillers into the polymer matrices, the surfactant molecules are possible to adversely affect the electrical and thermal conductivity at the interface between fillers and polymer matrices [126-128].

Polymer blends Different polymers can be blended together to form composite materials, achieving a synergic effect. The powder materials consisting of one type of

polymer usually have certain constraints for the SLS process, e.g., high melt viscosity, high melting point and non-recyclable characteristic. In contrast, the addition of synthetic polymer chains, such as high-density polyethylene (HDPE), polystyrene (PS) and epoxy, into polymers such as PA11, PA12 and PEEK can ease the processing requirements, minimizing manufacturing cost as well as overcoming the constraints caused by only a polymer. Meanwhile, the thermal behaviours of hybrid polymer powders in the sintering process can be tailored by adjusting the composition of each constituent. Consequently, it is possible to optimize the sintering process and change the performance of sintered products. The new blends are therefore capable of extending the utilization of polymers from prototyping to real functional applications.

2.2.2 Powder manufacturing methods

The compositions of specific composite powders and manufacturing processes are crucial to the functional properties of sintered parts. The composite grains can be obtained through mechanically alloying (e.g. ball milling) two groups of different powders, which are repeatedly milled, ground, fractured and welded together. Meanwhile, chemical treatment-assisted solution-based methods (including dissolution-precipitation, exfoliation-adsorption, emulsion-precipitation, and coating) and melt compounding (melt intercalation, melt extrusion and two-phase melt blending) are widely applied to manufacture composite grain powders. These chemical treatment-assisted approaches have been introduced to bind fillers with polymers and form composite grains. This section mainly discusses the approaches of composite powder preparation, especially solution-based processes.

2.2.2.1 Dissolution precipitation

Dissolution-precipitation is based on a solvent system in which the reinforcements can be dispersed uniformly into a soluble polymer or pre-polymer matrix by ultrasonic oscillation or applying an elevated temperature. The thermodynamic mechanism of dissolution process is illustrated in Fig. 2.8. The polymers and fillers can be dispersed into solvent through exothermic solution or endothermic solution formation, and then the polymer composite precipitates out when the stable state of such solution is disrupted through applying external stimulus such as thermal energy, electrical filed or ionic additives. After a complete precipitation, the obtained precipitants undergo the processes of vacuum dry and ball milling to form composite powders.

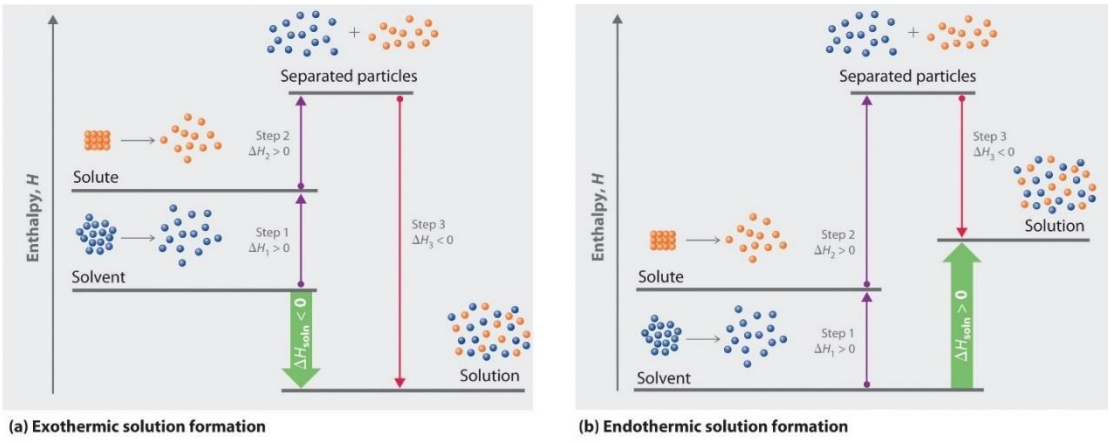

Figure 2.8. Illustration of the mechanism of a dissolution-precipitation process[129]**.**

Ceramics such as oxides, carbides and nitrides can be pre-functionalized by surfactants and subsequently dispersed into the solvent mixture to prepare composites. For instance, the approach used to fabricate nanosilica/PA12 or nanosilica/PA11 composite grains [7, 96] involves the typical dissolution-precipitation and mechanical processes with sequential chemical reactions, composite precipitation, vacuum drying

and ball milling. Titanium dioxide (TiO_2) nanoparticles (0.25 wt%) were also applicable to be dispersed into a PA12/ethanol suspension. During the evaporation of ethanol, the suspended TiO_2 nanoparticles were embedded into PA12 to form TiO_2/PA12 composite that precipitated simultaneously [130]. The sintered specimens consisting of polymeric composites had the improved tensile strength (89%), flexural strength (18%) and tensile modulus (6%), compared with those made by polymers alone [83, 131]. The sintered graphite/PA12 nanocomposite also exhibited much higher thermal stability and had the tensile strength and tensile modulus increased by 20.9% and 39.4%, respectively [96].

2.2.2.2 Emulsion solvent evaporation

Emulsion/solvent evaporation is a process to disperse micro- or nanoparticles into the emulsion system such as a solid-in-oil-water (S/O/W), and then to dry out solvents and precipitate the composite powders simultaneously as shown in Fig. 2.9 [71]. The phase diagram of emulsification is illustrated in Fig. 2.9. The polymer and fillers are usually dispersed in the oil phase, which forms micro-sized spherical droplets within the aqueous solvent. The water-to-oil ratio is tailored to modify the size of droplets with the assistance of amphiphilic surfactants.

For instance, the carbonated hydroxyapatite (CHAp) nanospheres were dispersed in the PLLA-dichloromethane solution by ultrasonication and homogenization to form an S/O nanosuspension [132]. The nano-suspension was mixed with PVA solution to prepare the microspheres of PLLA/CHAp nanocomposites before solvent evaporation. Moreover, silica particles coated with PA12 can be prepared through the emulsion polymerization. The condensation reaction of amide groups occurred in the oil phase of

micelles and subsequently formed polymer shells on the surface of silica particles [71]. Furthermore, an emulsion system could also form when MWCNTs and PA12 were dispersed into chloroform by applying ultra-sonication and magnetic stirring, and

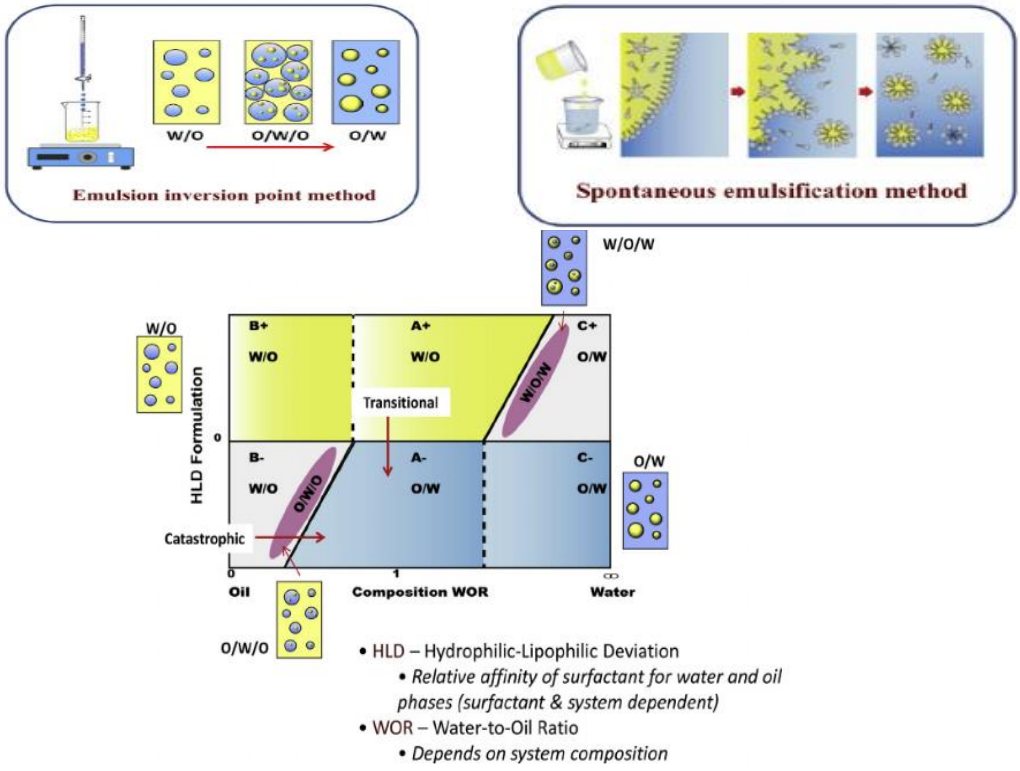

Figure 2.9. The solid-in-oil-water emulsion system uses surfactant and co-surfactant attachments to modify surface properties of solid particles and obtain solid precipitation by the solvent evaporation [133]**.**

eventually the emulsion phase could be separated on a cellulose filter, obtaining a significant particle retention efficiently [67]. The compositions of composites could be tailored by changing the solid phase and the oil phase contents, resulting in different microstructures and thermal behaviours of composite grains. Especially, the nanofillers could be uniformly dispersed into the polymer matrix to enhance the thermal performance of individual composite powders. However, the output of composite micro-particles by emulsion-evaporation is relatively low, which is insufficiently adapted into

a large-scale process for powder manufacturing.

2.2.2.3 Coating

Chemical treatment-assisted coating is usually to coat a binder material onto a structural material, thus forming a core-shell structure in the composite grain powders. This method ensures that the shell material can adsorb the laser radiation efficiently. Thus, more effective bonding can be realized for such a structure is accomplished as the binder material surrounds the constituent core material (Fig. 2.6). Furthermore, a new observation is that carbon-based materials, particularly MWCNTs, are capable of enhancing the thermal energy absorption and accelerating the sintering process, thus achieving condensed sintered parts [134].

Polymer coating Polymers are predominant coating materials owing to their low processing temperatures. Ball milling, dissolution-precipitation and emulsion-evaporation are able to generate composite powders coated with polymeric materials previously discussed. Polymer-coated steel powders (DirectSteel and LaserForm) were commercialized by 3D Systems, formerly DTM Corporation. Another type of commercial polymer-coated powders issand powders produced by DTM-3D System (SandForm) and by EOS GmbH (Direct Croning). The configuration of an individual powder is that a thin phenolic layer is coated as a shell on the surface of Si or Zr sands. In this way, the powders can fuse together and be applied to produce moulds and cores for metal casting. In addition, polymer-coated Mo powders were sintered by IR laser, and the post-processes of laser-sintered parts (including de-binding, high temperature firing and melting infiltration) then assisted in achieving refractory metal parts, in which

Mo wass used as the framework and then impregnated with Cu [21]. SLS offers a possibility to manufacture refractory metal parts by coating metallic powders with a layer of polycrestyne wax. When exposed to the laser beam, low melting point poly (wax) melts completely and induces cohesion as the viscous flow of molten part.

Spray drying coating Spray drying coating is another method to coat ceramic fillers with a polymer shell [102, 122]. As illustrated in Fig. 2.10 the dual feed microencapsulation nozzle can encapsulate two types of liquids, and then the core-shell micro-particles are formed in the atomizing surface.

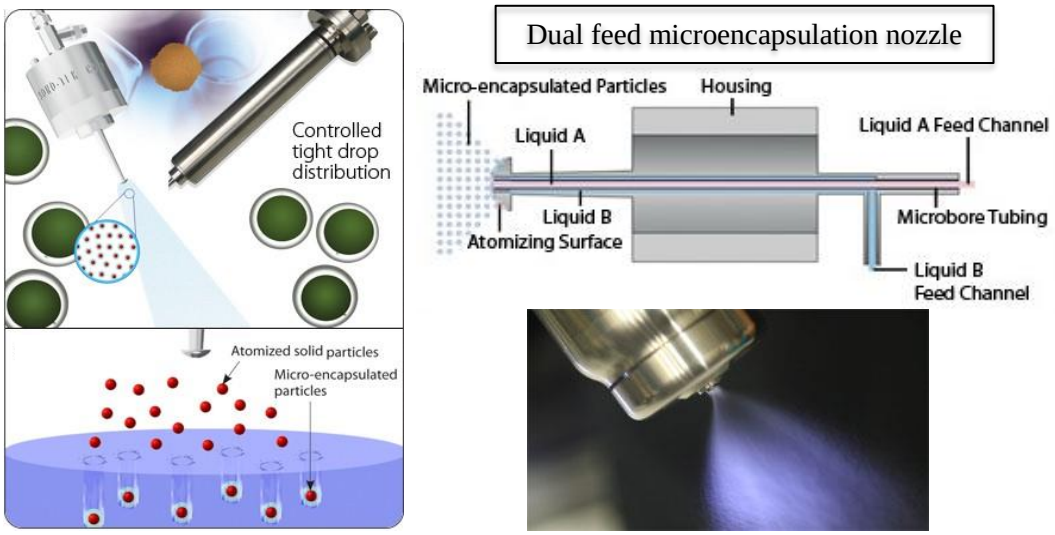

Figure 2.10. Schematic diagram of the ultrasonic spray drying coating process and the dual feed microencapsulation nozzle design [135].

For instance, water-insoluble semi-crystalline polyvinylalcohol (PVA) acts as an organic binder that can effectively bind ceramic particles. Experimentally, the main binder is fully hydrolyzed PVA to be coated on the surface of ceramic, and the powder then undergoes re-crystallization with treatment to further reduce the water solubility of the PVA [122]. Additionally, poly(methy1 methacrylate) (PMMA)-coated silicon carbide (SiC) powders can also be produced through spray drying [102]. These polymer-

coated ceramic or refractory fillers are used to indirect selective laser sintering, and the green part is simply and completely fabricated through post-burning polymeric materials. However, the powders made from spray drying coating usually have large cavity volume as well as high porosity; therefore, these porous powders are not preferable to laser sintering for fabricating dense parts to sustain mechanical loading.

Nanomaterials coating Cai *et al.* [136] invented a process for producing a nanomaterial-treated or -modified polymer to achieve polymer composites. The process comprises three steps: (i) providing a mixture consisting of a solvent, additive and a polymer; (ii) heating the mixture to a desired temperature; (iii) softening the surface of the polymer so that the additive attaches to the polymer. This process usually involves a thermal-induced phase separation method; more specifically, it functions in the region of homogeneous solution in the phase diagram of a polymer solution (Fig. 2.4). This process is also feasible for a wide range of thermoplastic polymers (such as acrylonitrile butadiene styrene (ABS), PA, PS and PE) to be attached by carbon-based additives, ceramic fillers, etc. Nanomaterials have large surface area and surface energy, and tend to attach onto an active surface. For instance, hydrophobic nanoparticles are able to adhere to the soften the polymer surface at an elevated temperature due to van der Waals force. Bai *et al.* [66, 134, 137] applied this process to coat PA12 with a small number of CNTs (0.1~0.2 wt%) for the SLS system and the sintered parts exhibited enhanced flexural, impact and tensile strengths without sacrificing elongation at break. The coated CNTs were able to enhance laser absorption and facilitate polymer melting during the sintering process. Thus, nanomaterials may accelerate the sintering process as well as enhance the functionality of polymers. Consequently, nanomaterial-coated polymeric

composites will have large potential to be further developed as the candidates of SLS materials.

2.3 Functionality of composite materials

Multi-functional materials are emerging in the AM field from upstream academic research to downstream industrial manufacturing, as they exhibit excellent properties for the extended applications. Composite materials are able to improve the functionality of original neat materials with the addition of fibers or other additives. Carbon-based additives such as carbon nanofibers, CNTs and graphite possess impressive thermal, electrical and mechanical properties to reinforce the polymer matrices. This sub-section summarizes the studies on the multi-functionality of carbon/polymer composites and discusses the performance of composites manufactured by the SLS system.

2.3.1 Thermal properties

Thermoplastics are usually thermal and electrical insulators. The thermal conductivity of engineering polymers such as polyamides and polyurethane ranges from 0.1 to 0.4 $Wm^{-1}K^{-1}$, which is much lower than that of metallic or carbon-based materials. The addition of conductive fillers via CNTs is an effective approach to reinforce the thermal and electrical conductivity of polymer. Polymer nanocomposites with CNTs can benefit a variety of applications including electronic thermal management and heat exchange. Individual single-walled CNTs (SWCNTs) have promising thermal conductivities of more than 3000 $Wm^{-1}K^{-1}$, and the non-equilibrium molecular dynamics simulations estimated that the value could be up to 6000 $Wm^{-1}K^{-1}$ [32, 138]. Theoretically, thermal and electrical conductivities of polymers with a small loading fraction of CNTs could

increase substantially; for example, the effective medium theory predicted a factor of 250 enhancement in thermal conductivity when 5 vol% randomly oriented CNTs were loaded [139, 140]. MWCNTs can potentially yield a significant enhancement of thermal conductivities due to the fact that heat transport via inner walls are not adversely affected by the imperfections presenting on outer walls [105, 106]. However, Fig. 2. 11 illustrates that experimentally the enhancement of thermal conductivities in CNT/polymer nanocomposites is usually limited within one order of magnitude, which is only a modest increase compared with theoretical predictions, and the reasons for the relatively low conductivity are still too complex to be understood [105-109].

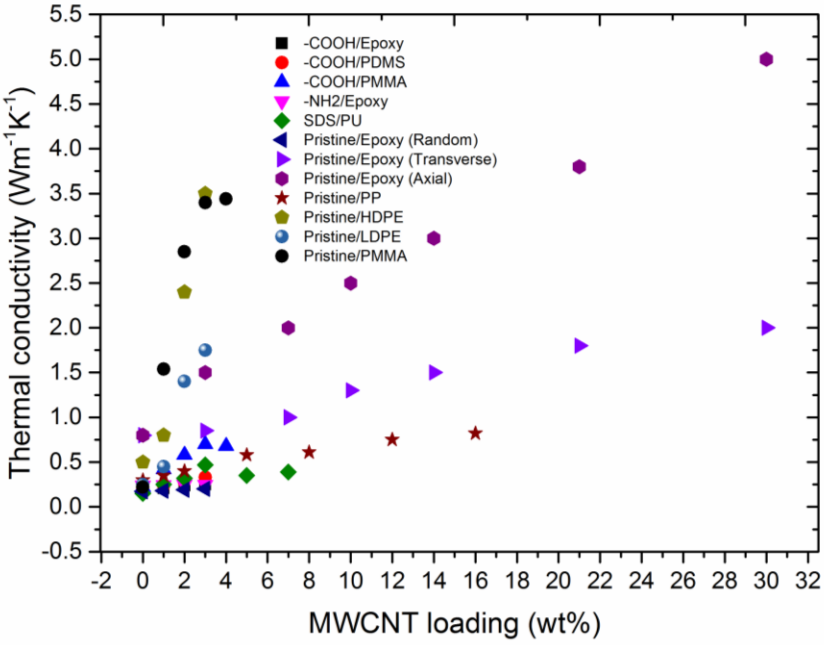

Figure 2.11. Thermal conductivities of MWCNTs-reinforced polymeric nanocomposites through various manufacturing methods (Type of functional group/polymer matrix) [53].

The disparity between theoretical predictions and experimental data might be caused by the distribution of the CNTs within the polymer matrix [52, 141, 142], the influence of CNTs on the crystallinity of polymer [143, 144], interfacial thermal

resistances that impede phonon conduction between the CNTs and the polymer or between the contacting CNTs [141], surface functionalization of the CNTs [126, 145], and impurities and lattice defects within individual CNTs [140, 145, 146]. The distribution of CNTs within polymer matrices through different methods (e.g., melt blending and *in-situ* polymerization) usually faces a challenge to uniformly disperse CNTs into the pasty melted polymers or the precursor solution of polymers, and few techniques could ensure that a 3D interconnected network of CNTs can be formed with the polymers [147]. For 2D problems, Ivanov *et al.* suggested that polymer nanocomposites with aligned CNTs could increase the thermal conductivity by a factor of 20 with the loading of 20 vol% CNTs [148]. Besides, increasing the degree of crystallinity in polymers typically results in a proportional increase in both the elastic modulus and the thermal conductivity, especially in semi-crystalline polymers. Previous studies reported that CNTs could impact on the dynamic recrystallization of semi-crystalline polymers, such as PAs, PU and PE, and change the crystallinity and grain size of crystals [149]. Consequently, the polymer chain orientation and alignment could increase the thermal conductivity of polymer matrix [150, 151]. Furthermore, surface modifications were introduced to the CNT suspensions to improve their dispersion properties and uniformity of CNTs within matrices, but their influence on the thermal and electrical conductivities of polymeric composites has remained unclear [126]. The interfacial resistance of CNT-CNT and tube resistance are illustrated in Fig. 2.12, and the temperature drop is also demonstrated along the tube and the interface of tubes. Surface functionalization is also possible to induce face defects or impurities, which limit the phonon propagations and enhance the scattering, damping of phonon modes,

etc. [145]. The most recent researches demonstrated that covalent bonds or hydrogen bonds are able to enhance the phonon transportation between polymers and carbon lattices or between lateral polymer chains [147, 152, 153].

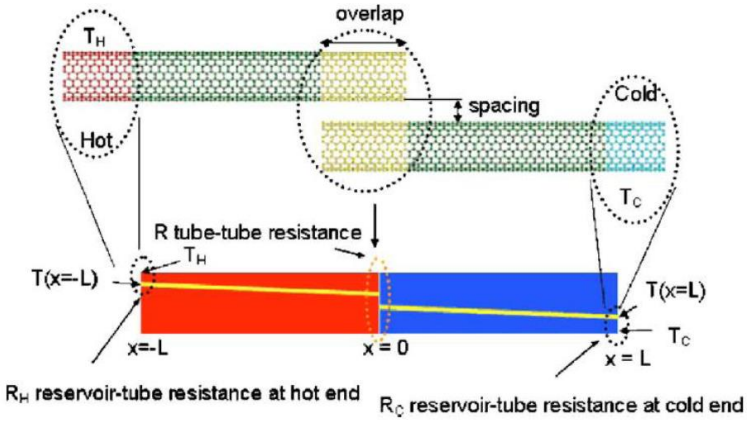

Figure 2.12. 2D scenario for CNT-CNT contact and temperature profile are illustrated along the alignment direction of CNTs. The critical temperature dropped at the interface caused by the effect of thermal contact resistance [149].

2.3.2 Electrical properties

Aerospace and military components contain a large number of parts assembled in small volumes. This increases the total number of interfaces driving both complexity and adjustable electrical conductivity. To date, the enhancement of electrical conductivity is one of the largest barriers to be overcome. Generally, by introducing carbon-based fillers such as graphite, carbon black, CNTs and graphene, the electrical conductivity of polymeric composites in the range of electrostatic dissipation (ESD) or beyond that range can be achieved [25]. The minimum weight loading to induce this conductivity in the insulated polymer matrix is known as the percolation threshold, which strongly depends on the filler orientation, dispersion, inter-particle spacing and the properties of the polymer matrix [137]. The percolation theory can be applied to explain the electrically conducting behaviour of composites consisting of fillers and

insulating matrices (see Fig. 2.13) [154]. However, few physical models about polymeric composites for SLS have been developed to investigate the electrical percolation threshold corresponding to the distribution, concentration and aspect ratio of fillers [155].

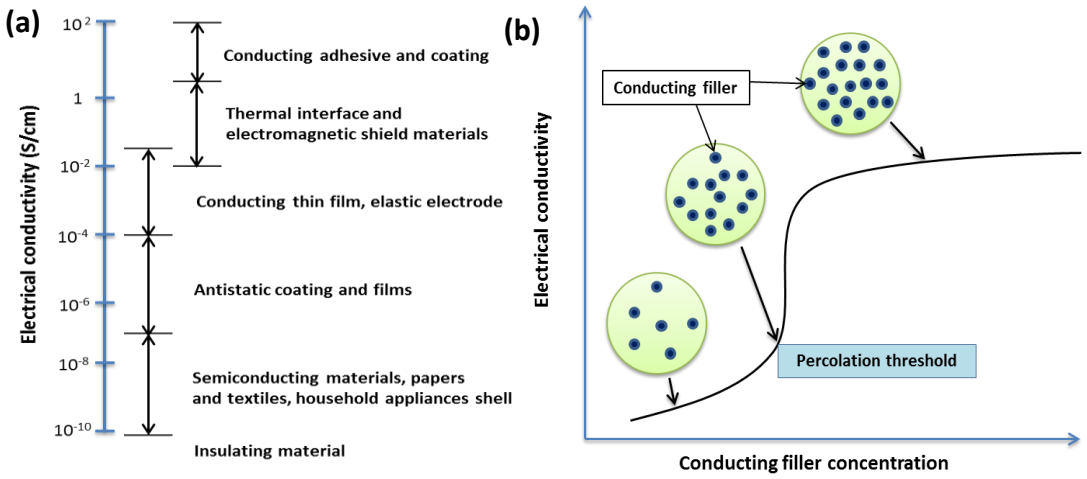

Figure 2.13. (a) Typical applications of conductive polymeric composites and (b) a schematic of percolation phenomenon and conductive network in the composite [46].

Conventional manufacturing techniques involving melt mixing and blending are not suitable for processing CNTs or graphene materials as the high shear forces can break the conductive network and reduce the aspect ratio of the nanomaterials, thus resulting in a high percolation threshold. SLS is desirable to form the network of carbon fillers in polymeric nanocomposites because the shear forces are negligible during powder sintering. In Fig. 2.14 (a), the laser-sintered specimens possessed much higher electrical conductivity than the injection moulded specimens as observed in the carbon black/PA12 composites with the same loading of 4 wt% [101]. This is because the carbon black remained around the powder boundaries to form a network as shown in Fig. 2.14 (c) and the blended carbon-black were embedded into PA12 which prohibited

the electron transfer in the composite structure.

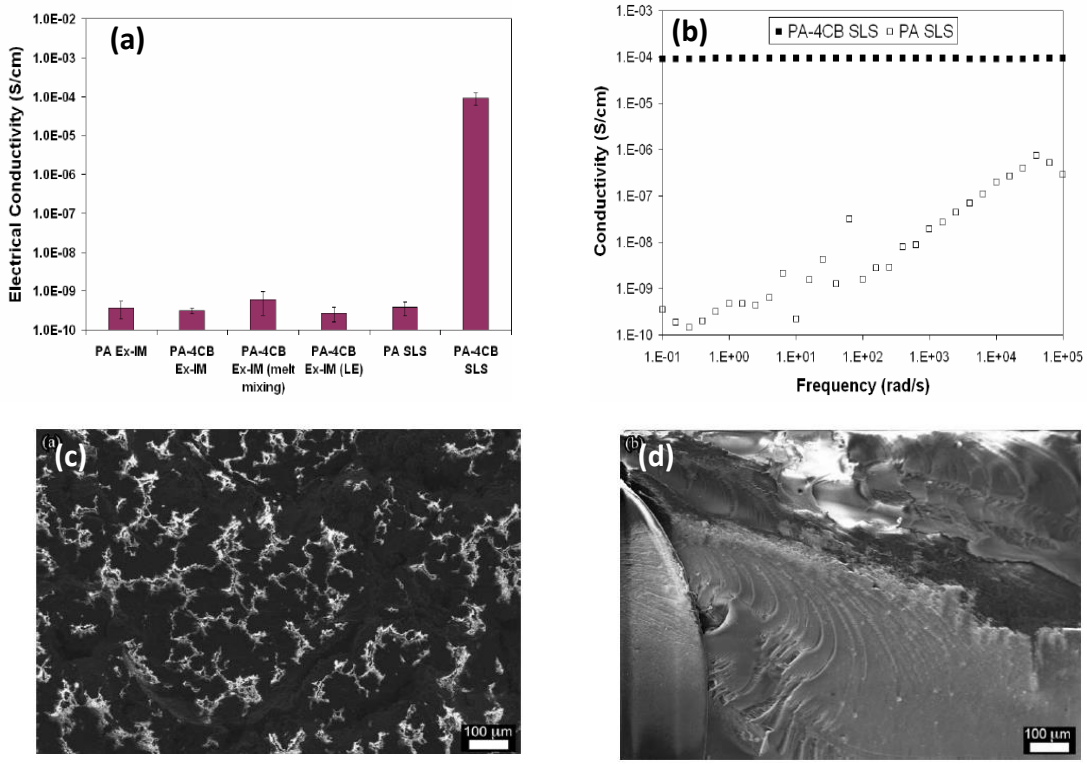

Figure 2.14. (a) Electrical conductivity of six systems at an alternating current (AC) frequency of 1 Hz. (Ex-IM: extrusion and injection moulding; LE: Laser irradiation); (b) variation of electrical conductivity with respect to the frequency of the AC voltage for the PA and PA/Carbon black for the SLS systems; (c) and (d) the fracture surfaces of carbon black/PA12 composites produced by the SLS process and injection moulding, respectively [101].

Electrically conductive graphite nanoplates (GNPs)-coated PA12 powders were investigated for the SLS system by Eshraghi *et al.* [156]. In Fig. 2.15 (a), the morphology of the graphite-coated PA12 powders indicated non-homogeneous dispersion, while the loading of 5 wt% GNPs in PA12 matrix surpassed the percolation threshold, achieving an increase in conductivity by three orders of magnitude than neat PA12. The composite conductivity (6.4×10^{-8} S/cm) was high enough for electrostatic dissipation. Chen *et al.* found d that nano-graphene platelets (NGPs)-reinforced PA11 was able to achieve conductivity in the upper region of the range for electrostatic

dissipation, while the state of exfoliation and dispersion of the NGP within the PA11 matrix was inadequate for improvements in the thermal stability and the electrical conductivity [25].

2.3.3 Mechanical properties

The mechanical properties such as the tensile modulus, tensile strength, flexural modulus and elongation at break are critical factors for evaluating the performances of engineering parts in automotive, aerospace and construction industries. Eshraghi *et al.* [157] demonstrated the sintering of the GNPs/PA12 powders with addition of 3 wt% and 5 wt% under different sets of laser parameters. The tensile modulus improved

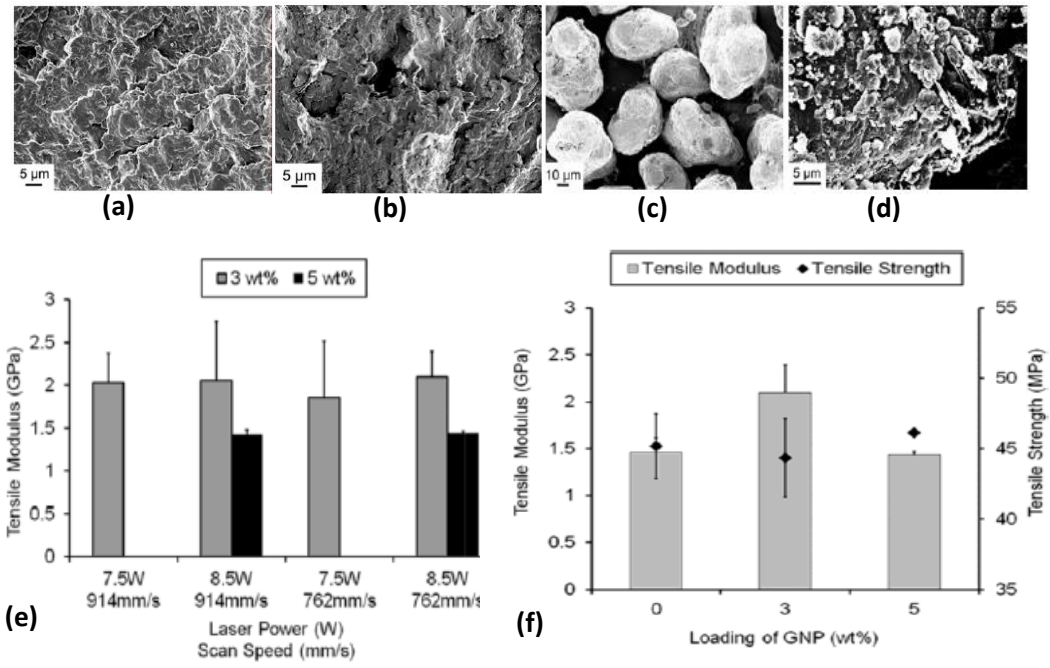

Figure 2.15. SEM images of surface morphologies of graphite/PA12 powers: (a) 3 wt% and (b) 5 wt%; (c) and (d) graphite/PA12 powders and surface morphology; (e) influences of process parameters on the tensile modulus and (f) tensile modulus and tensile strength of graphite/PA12 with the filler loadings of 0, 3 and 5 wt% [83].

slightly for a small loading as shown in Fig. 2.15 (f). However, the loading of GNPs in the PA12 matrix exhibited a compromise in the flexural modulus and strength when compared with the neat polymer. Although the GNPs are one type of strong micro-fibres, they exhibit poor adhesion with the polymer matrix, and their interfacial defects may induce crack propagation easily.

To improve the mechanical performance of laser-sintered composite parts, a resin infiltration step was introduced to fully fill resin into the cavities among sintered products and improve the surface adhesion between the polymer and fibres through chemical treatments as shown in Fig. 2.16 [36]. The carbon fibres (CFs) were coated with a layer of PA12 and then sintered to form highly porous 3D green parts of CFs/PA12 composites. Subsequently, the porous parts were merged into epoxy resin at an elevated temperature and the low-pressure environment. After the epoxy (EP) resin was infiltrated and cured, this method could yield the condensed composite with the ultimate tensile strength of 101.03 MPa and a flexural strength of 153.43 MPa. The modulus of CFs/PA12/EP was much higher than those of most of previously reported SLS materials. However, a trade-off between mechanical strength and elongation at break is still difficult to deal with for the microfiber-reinforced composites. Therefore, nano-reinforcements are attractive to toughen the composite, as they can improve both mechanical strength and ductility.

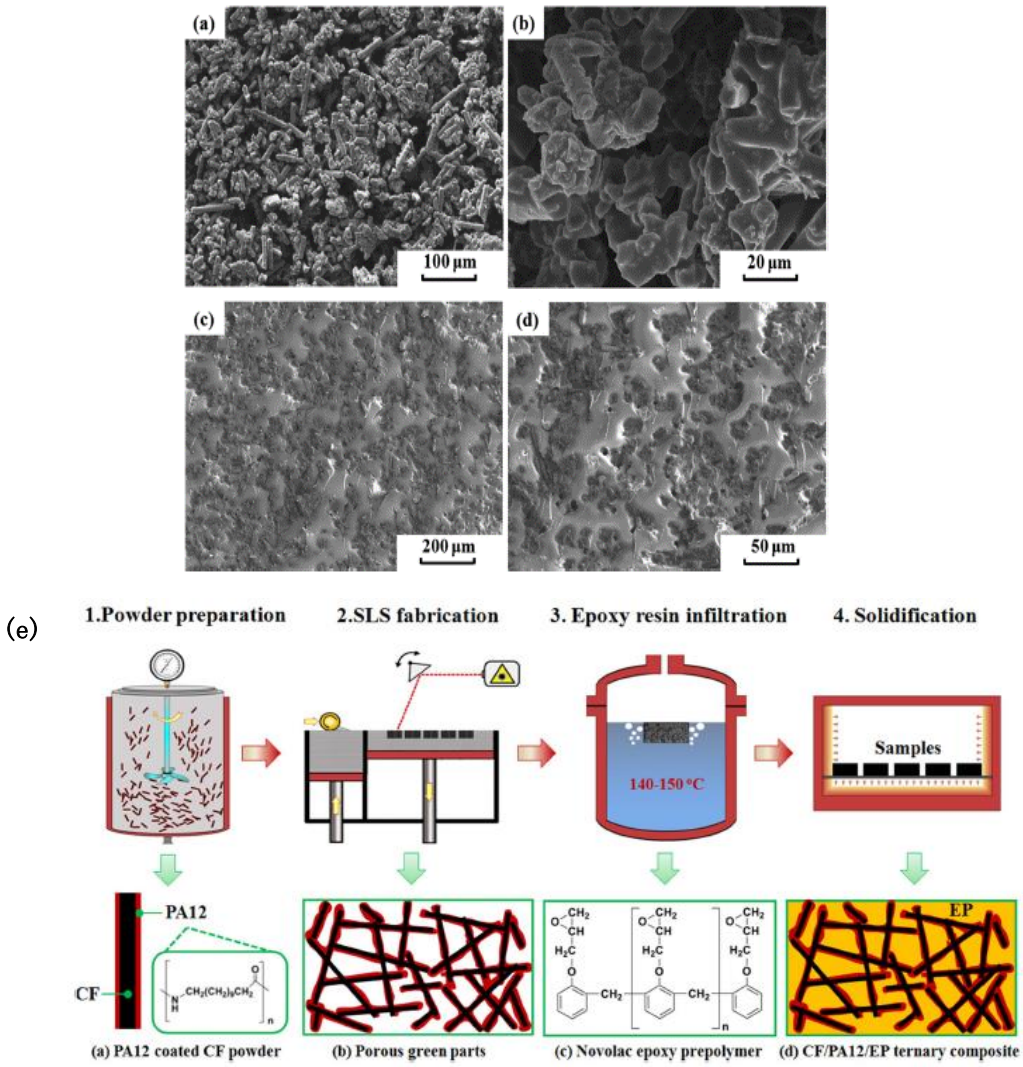

Figure 2.16. (a) and (b) the SEM images of the surfaces of the green parts via CFs/PA12; (c) and (d) the cross-sections of the CFs/PA12/EP ternary composite; (e) the illustration of the manufacturing process of the CFs/PA12/Epoxy composite [36]**.**

2.4 Design and fabrication of 3D structural composites

2.4.1 3D cellular structures

Lightweight cellular structures are an emerging class of high-performance structural materials with potential applications in high-stiffness panels, energy absorbers, catalyst supports and load supports [36-38, 158-160]. Different types of cellular structures, such as honeycombs [37], truss lattices and diamond lattices [159],

were successfully fabricated through AM techniques. The mechanical stiffness and strength of normal materials degrade substantially with a decreasing density because their structural elements bend under applied load [158]. However, the proper material formulation and the precise AM technique enable the fabrication of composite lightweight structures while maintaining high stiffness per unit mass.

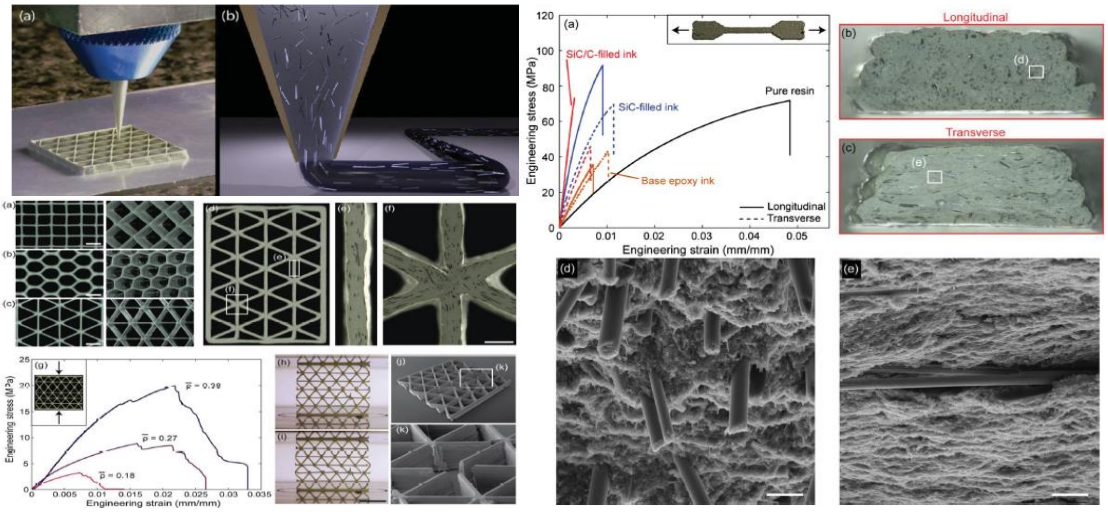

Figure 2.17. Manufacturing of lightweight cellular composite structures by the 3D extrusion printing method [37]**.**

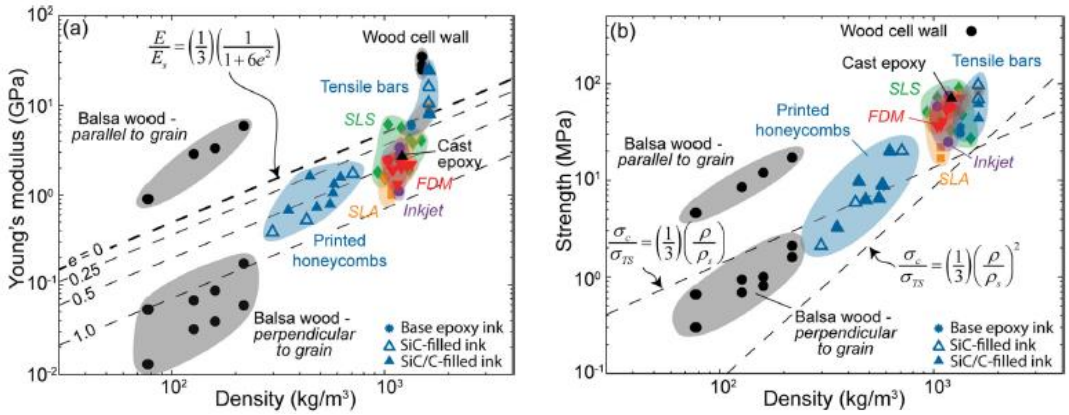

Figure 2.18. Ashby chart plots: (a) the compressive Young's modulus and (b) the compression strength versus the density of composite honeycombs printed by a 3D extrusion process compared with commercial polymers and polymeric composites as well as balsa wood and wood cell walls [37]**.**

Compton *et al.*[37] created the epoxy-based inks with addition of SiC and CFs which embodied the reological properties requied for the 3D extrusion method, and then printed the honeycomb structures with oriented fiber-fillered epoxy with excellent stiffness and strength per unit mass (Figs. 2.17 and 2.18). The extrusion process was able to control the alignment of multi-scale, high-aspect-ratio fibers to fabricate the hierarchical structures, which possess promissing mechanical stiffness, as compared with other AM techniques. This work demostrated an exemplinary study of the process-structure-property relationship in AM manufacturing. It is capable of inspiring an entirely new dimension to engineering design and manufacturing, where material composition, stiffness and toughness within a 3D structure can be digitally integrated with component design to achieve desirable performance.

2.4.2 3D auxetic structures

The term ‘auxetic’ originated from the Greek word ‘auxeis’ that means ‘to increase and grow. 3D mechanical metamaterials with the negative Poisson's ratio contract in the transverse directions in compressive loading regimes [161-164]. As the 3D auxetic lattices usually consist of networks of beams, multipods and rigid units, the conventional manufacturing methods are time-consuming and costly to fabricate such complex designs [162]. Different types of 3D auxetic structures have been proposed in design and mainly fabricated through AM techniques as shown in Fig. 2.19. The 3D dilatational elastic metamaterial fabricated through fused-deposition modelling shrank in transverse directions upon compression due to the rotational elements in structures [165, 166]. However, the flexibility of rotational nodes is quite limited in such design. The rational

designed complex structures such as soft metamaterials can be produced for effective protective and energy absorbing materials and acoustic dampers [163, 167]. However, only a few designs of 3D synthetic auxetic materials were fabricated and capable of maintaining their auxetic behaviour at large strains. A few AM techniques are able to print the suitable materials to satisfy the stringent requirements to sustain large strains and maintain high recoverability. A dual-material auxetic structure was designed and

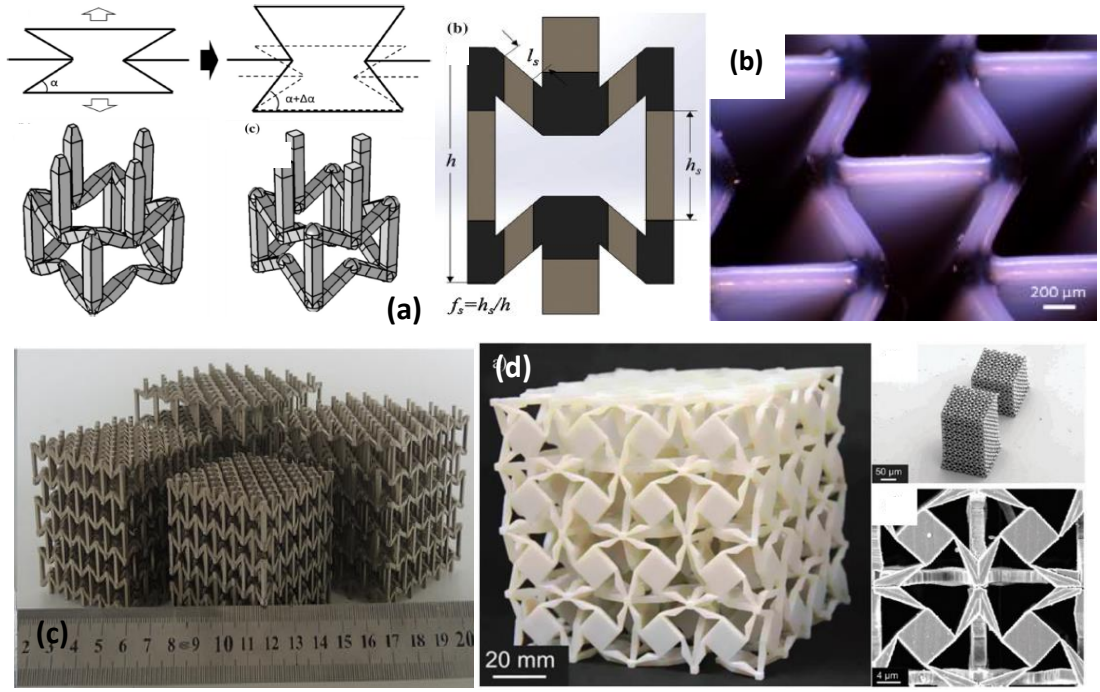

Figure 2.19. (a) Principle deformations of the unit design; (b) the dual-material auxetic lattice fabricated through inkjet printing [162]; (c) the 3D auxetic lattice printed by SLM and (d) a 3D dilatational elastic meta-material fabricated through FDM and SLM techniques [166].

then fabricated through an inkjet printing process (Fig. 2.19 (b-c)) [162]. The soft material portion was employed as flexible nodes, and the stiff material portion was used in the beams in the entire network.

Materials with the negative Poisson's ratio are not just limited to dilational

materials. A new group of 3D soft auxetic lattices were proposed by Babaee *et al.* [161]. Such structures were usually constituted by an array of soft spherical units, which could be arranged in periodical 3D patterns of simple cubic, body-centred cubic or face-centred cubic. The auxetic behaviours of this type of lattice structures under compression was modelled and analyzed due to buckling-induced instability of soft materials. Local buckling of spherical shells led to the responses of negative Poisson's ratio. The auxetic lattice structure or soft porous structures are also known to be capable of dissipating mechanical and acoustic energy subjected to strong impact or cyclic

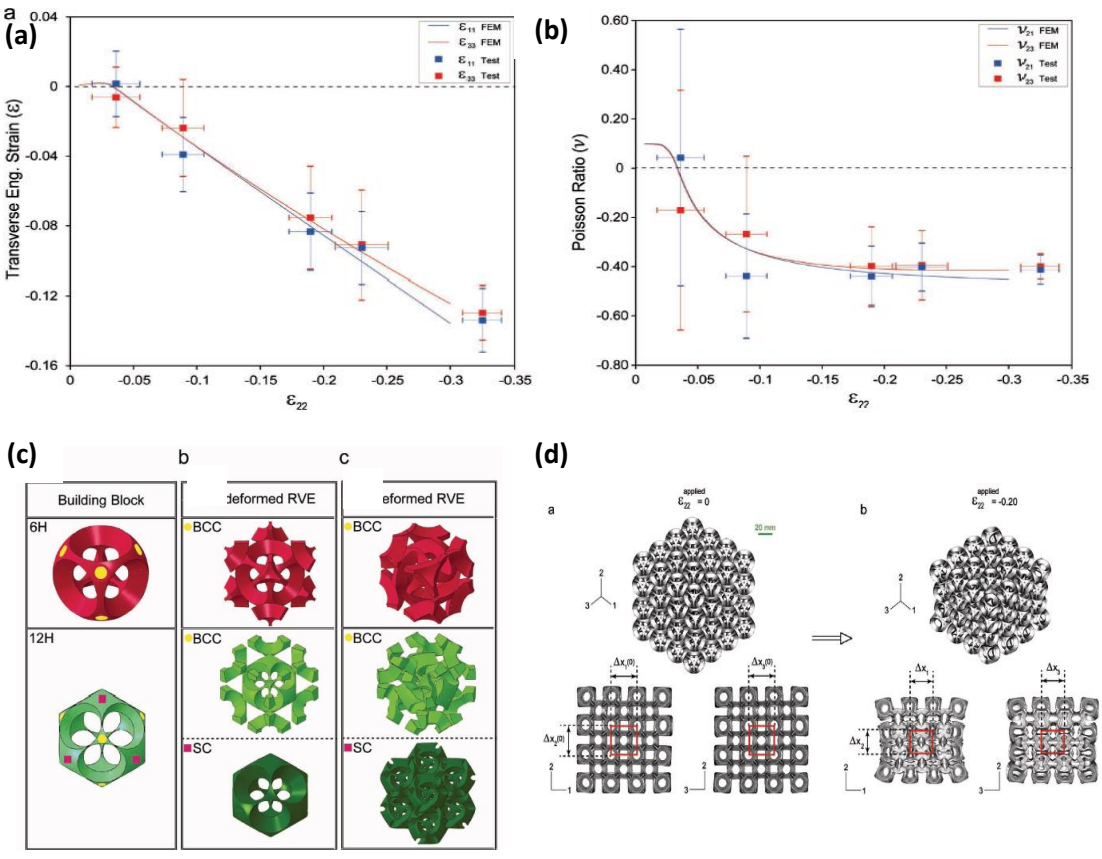

Figure 2.20. The experimental and simulation plots of (a) transverse engineering strain versus longitudinal strain and (b) the Poisson's ratio for *bcc*-6H design; (c) the building blocks of 6 holes and 12 holes' units and their under-formed or deformed configurations; (d) the X-ray profile of *bcc*-6H design upon compression [161].

loading [1]. The design features of unit configurations and 3D patterns may affect the capacity of energy absorption upon compression; meanwhile, the mechanical properties of materials and manufacturing techniques also influence the performances of lattice structures under cyclic l or impact loading.

The thermoplastics are usually used as building materials for the laser sintering process. The thermoplastic elastomers are soft and flexible and usually behave as vulcanized rubbers. Instead of the chemical cross-linked and vulcanized rubbers, the thermoplastic elastomers such as segmented-PU usually possess physical crosslinks and crystalline phases [23, 157-159]. Therefore, the development of the SLS system for desirable soft materials enables the manufacturing of 3D soft lattice structures for end-use applications such as actuators, mechanical dampers and biomedical devices. However, few numerical methods have been developed to simulate the behaviours of 3D soft complex structures as challenges are present in integrating the models of non-linear materials with those of 3D non-linear structures. In order to establish a model-guided design system for AM processes, it is necessary to provide a proper model to predict the mechanical behaviours and deformations to optimize different types of designs and select the optimal design for manufacturing.

Chapter 3 Formulation and development of polymeric nanocomposite powders

The colloidal method based on the latex technology has been reported to prepare electrically conductive carbon material/polymer composite with a low percolation threshold [34, 168]. This method can obtain the conductive bulky composites with segregated microstructure by drying the mixture of the aqueous dispersion of CNTs and polymer latex, in which CNTs can be self-aligned in the interstitial space among latex particles.

Surface modification has been revealed to be effective strategies to realize the multi-functionality of carbon nanomaterials and optimize their composite performance [40, 169]. The covalent and non-covalent functionalization of CNTs can be implemented to change their surface hydrophobicity and improve their dispersity in an aqueous solution. However, the covalent functionalization such as ionic doping and acid oxidation may induce localized defects on graphene walls, and the conventional non-covalent functionalization using amphiphilic long-tail surfactants such as sodium dodecyl sulfate (SDS) often creates interfacial barriers for electron or phonon transport. Thus, a proper selection of surface treatment is crucial to retaining the electrical and thermal performances of CNTs.

In this thesis research, a surfactant-facilitated latex technique has been proposed to coat carbon nanomaterials onto the surfaces of polymeric powders in a colloidal system under an elevated temperature. The composite polymeric powders can be obtained after they are filtrated and dried. The obtained powders can be further applied in powder-based AM and hot-moulding processes. The thermal and electrical conductance of

composites can be adjusted by varying the loading percentage of conductive fillers and selecting the types of surface functionalization. The surface treatment of nanofillers and the control of compositions and morphologies of the powders play a critical role in manufacturing composites with desirable microstructure and functional properties.

3.1 Material selection

Thermoplastic PA12 (PA2200 from EOS GmbH, Krailling, Germany) was employed as the polymeric matrix of the composite. PA12 had a melting point of 184 °C and the packing density of its powders was 0.45 g/cm^3. Another matrix material TPU powders (DESMOSINT X92, BASF Germany) had the packing density of 0.58 g/cm^3, and the melting pool of TPU ranged from 120 °C to 160 °C.

The diameter and length of MWCNTs were around 20-30 nm and greater than 5 μm, respectively. The precursor solution of MWCNTs had a weight ratio of 3% and purity greater than 95% (Nanostructured & Amorphous, USA). This precursor solution could be further diluted to a desirable concentration. With the facilitation of probe ultrasonicator (BRANSON Model 102C, USA) and the surface modification of sodium cholate hydrate (from C6445 SIGMA with purity > 99%). MWCNTs could be modified by cholate molecules and homogenously dispersed in deionized water. The sonication bath temperature was kept below 25 °C using ice water to prevent evaporation of the solution. The cholate ion-functionalized CNTs are conveniently named s-CNTs.

3.2 Composite powder development process

The fabrication of CNT/polymer nanocomposites consists of two major steps as

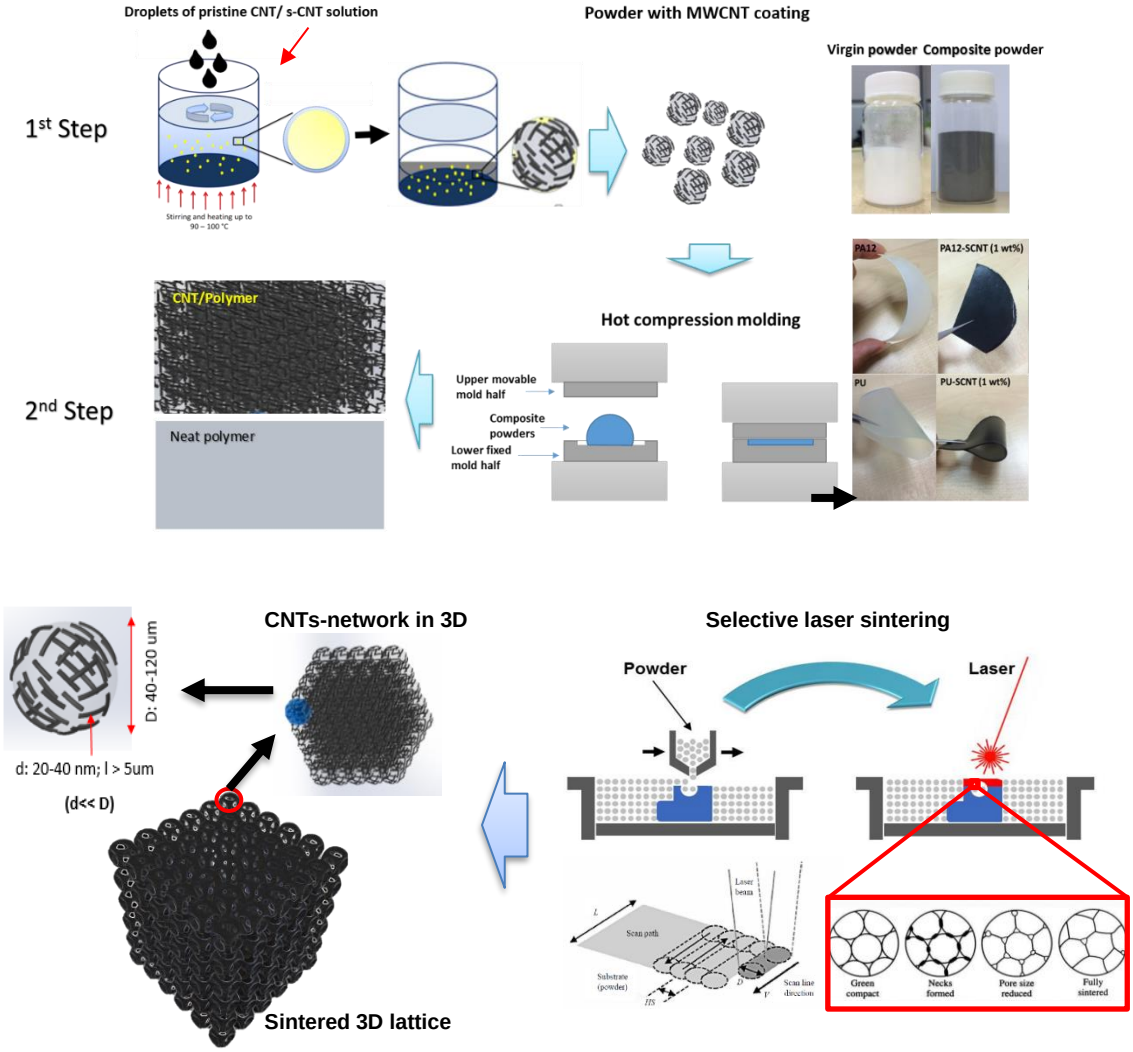

Figure 3.1. Schematic representations of the fabrication process of the MWCNT/polymer nanocomposite. In the first step, a surfactant-facilitated latex technique was applied to coat MWCNTs onto the polymeric powders. Note that the diameter of the polymeric powders was much larger than the thickness of the coating layer. In the second step, either bulky MWCNTs-reinforced nanocomposites were obtained through hot-compression or the powders were applied in the SLS process to fabricate the 3D composite structure with the reinforcement of CNTs.

illustrated in Fig. 3.1. PA12 and PU powders were dispersed into the aqueous suspension, which was then heated up to 90 °C and 70 °C for 30 min, respectively. Such suspension was a milky colloidal system at the elevated temperatures, and the surfaces of the polymeric powders were softened and activated. The pre-heated aqueous suspension of

MWCNTs was added into the milky powder suspension. This mixed suspension was stirred at 1200 rpm and kept heating for 30 min. The weight ratio of s-CNTs was controlled from 0 to 1 wt% in the composition. After the suspension was naturally cooled down, the polymer phase was separated from the water. The MWCNTs-coated polymeric powders were filtrated and dried. Afterward, the residual water absorbed by the polymer was evaporated through further drying in an oven at 70 °C. In the second step, the nanocomposite powders were hot-compressed at 200 °C and maintained at the pressure of 2 bars to form the CNTs/polymer composite sheets with the thickness of 1~2 mm. Another approach to obtain polymeric composite using these powders is to selectively melt and consolidate CNT/Polymer powders via SLS, which is discussed later in Chapter 4.

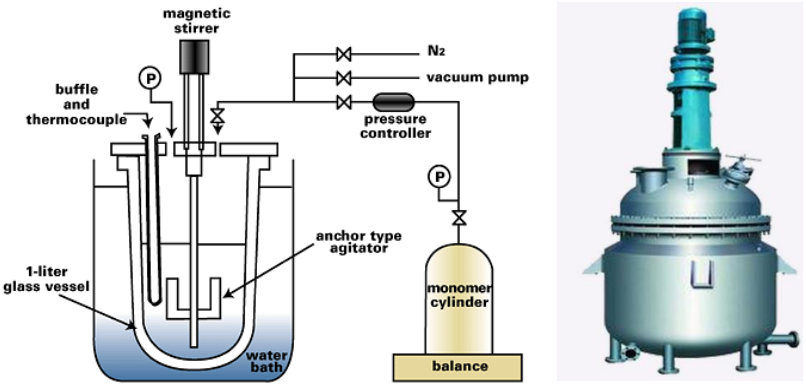

Figure 3.2. Schematic illustration of the solution-based reactor for composite powder preparation and the reaction with volume of 100 L [167].

To scale up the manufacturing process of composite powders, the solution-based reactor (100 L) has been developed to conduct the mixing and coating process [167]. The schematic illustration of reactor is shown in Fig. 3.2, with the vacuum pump and pressure controller to control the internal pressure and temperature. With the help of temperature and stirrer sensors, a feedback control system was established to monitor

the process conditions. The composite powders precipitated out after cooling and further filtered and dried in an oven.

3.3 Characterization of composite powders

The coating layer of CNTs was expected to achieve uniform assembly on the surface of polymer powders. The surface and powder morphology were characterized by SEM to evaluate the coating performance of pristine CNT and s-CNTs. In addition, dynamic thermal behaviours were evaluated by DSC to identify the melting and recrystallization manners, which significantly influence the sintering process and the dimensional accuracy of sintered parts.

As shown in Fig. 3.3, s-CNT/PA12 and s-CNT/PU possessed the uniform surface coverages of MWCNTs, which interconnect with each other to form a thin film. Such surface structure was desirable to build a 3D network of MWCNTs in the subsequent composite forming process. However, with an identical amount of loading, the pristine MWCNTs tended to agglomerate slightly. Thus, the surface coverage of pristine MWCNTs was not comparable with that of cholate ion-functionalized MWCNTs. Hence, sodium cholate certainly facilitated the coating of MWCNTs on powders effectively and prevented the agglomeration of MWCNTs as the loading increased. PA12 powders were of semi-spherical shape, which was desirable for powder deposition, while PU powders were of irregular shape with a broader size dispersity, which might also adversely impact on the coating quality because the surface energies of the powders varied over a wide size range.

DSC was employed to investigate the melting and recrystallization behaviours of

the polymers and their composites. These intrinsic thermal behaviours determined the specific process parameters of SLS and influenced the quality of sintered products. A sharp melting peak and a wide glass transition window were significant for the SLS polymeric materials. A sharp melting peak indicated the rapid melting process of the polymer under laser exposure. Besides, a wide process temperature range allowed the great processing adjustability, particularly during the optimization of other process conditions. This was because a small deviation of processing temperature would not have a significant influence on the dimension accuracy and mechanical properties. Therefore, the DSC characterization of the powders and the parametric analysis were an essential prerequisite of a successful sintering process.

The DSC curves in Figs. 3.4 and 3.5 show the energy release and absorption of PA12, CNT/PA12 and s-CNT/PA12 over the whole heating-cooling cycle from 25 °C to 250 °C at the rate of 10 °C/min. It can be observed that the melting point of s-CNT/PA12 dropped from 188 °C to 184 °C, with the addition of sodium cholate, modified MWCNTs into PA12. The narrow and smooth curves indicate that these composite powders easily melted as illustrated in Fig. 3.4, probably due to the factor that an improved surface coverage of MWCNTs could enhance the heat absorption and conduction within the polymer matrix. However, at 188 °C, PA12 and CNT/PA12 composites exhibited the sharp and broad absorption peaks. This observation implies that more heat was required to melt PA12 and CNT/PA12 than s-CNT/PA12, indicating the inefficient heat conduction and absorption in the polymer matrix.

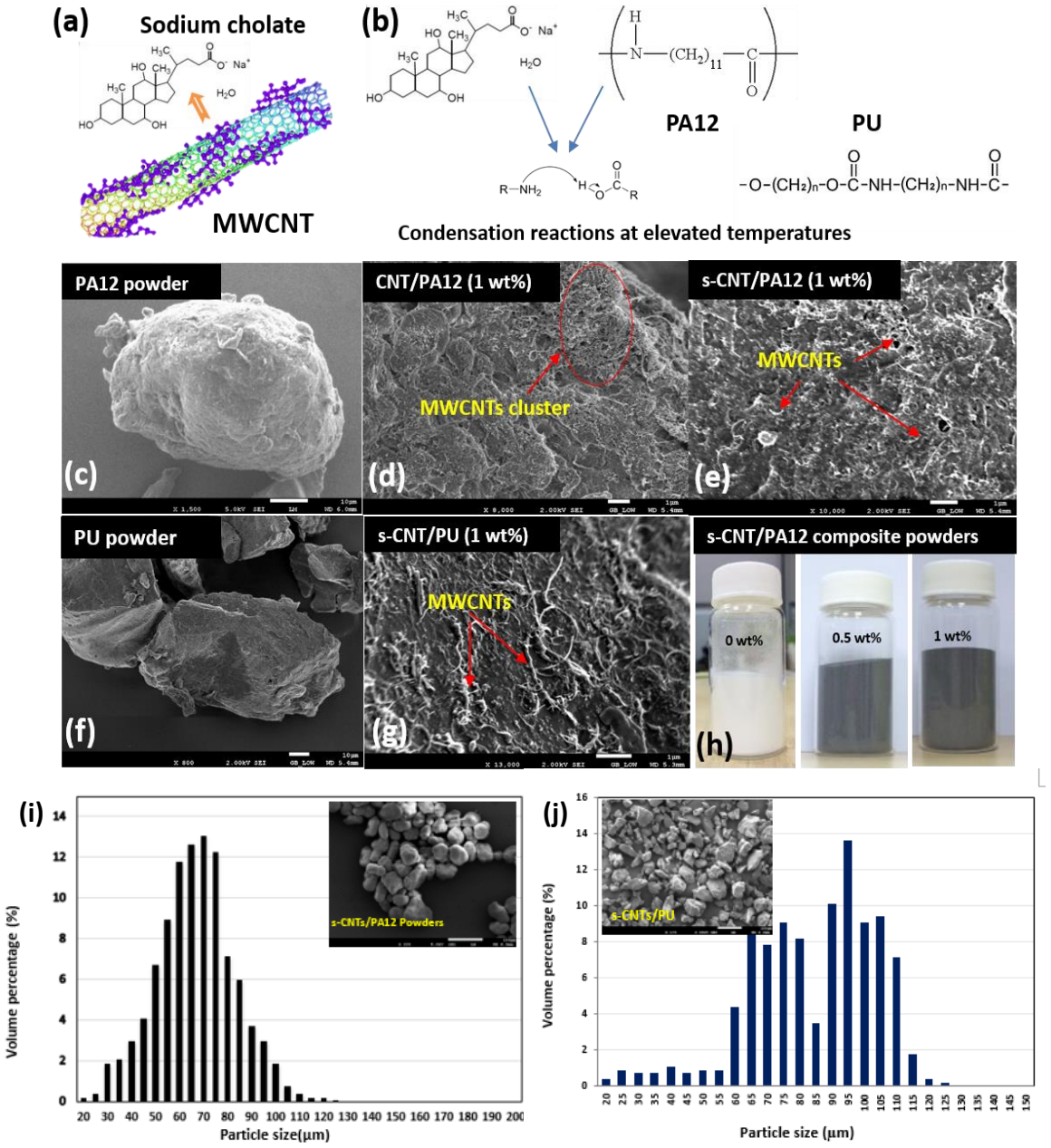

Figure 3.3. (a) Illustration of the cholate molecule attached to the sidewall of an MWCNT. (b) The covalent bond between the cholate and PA12. SEM images: (c) PA12 powder, (d) surface of the CNT/PA12 powder, (e) surface of s-CNT/PA12 powder, (f) PU powder, and (g) surface of the s-CNT/PA12 powder (scar bar: 1 μm). (h) Photos of PA12 and its nanocomposite powders. Powder size distributions: (i) s-CNT/PU and (j) s-CNT/PA12.

More specifically, as shown in Fig. 3.5, the recrystallization of s-CNT/PA12 was revealed by the sharp and narrow exothermal peaks, which initiated at 163 °C and

reached the ultimate point at 156.4 °C. Compared with that of s-CNT/PA12, the peaks of PA12 and CNT/PA12 were broad and present at a low-temperature range from 150.9 °C to 153.7 °C. These phenomena suggested that the induced MWCNTs could stimulate nucleation and accelerate crystal growth because the surfaces of MWCNTs might create a series of nucleation for crystal growth.

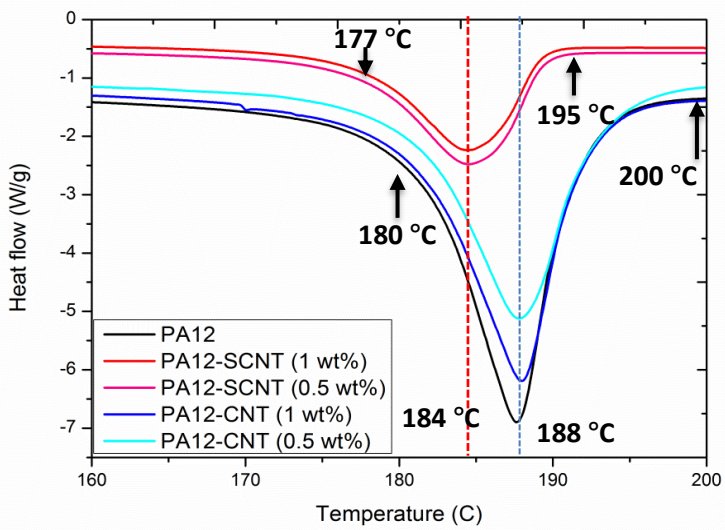

Figure 3.4. The melting curves from DSC for PA12, CNT/PA12, and s-CNT/PA12 nanocomposite powders at the heating rate of 15 °C/min.

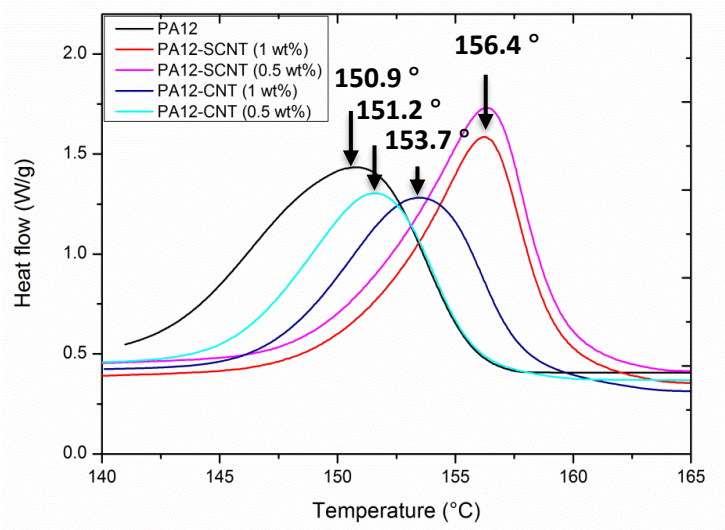

Figure 3.5. The recrystallization curves from DSC for PA12, CNT/PA12 and s-CNT/PA12 at the cooling rate of 15 °C/min.

On the other hand, the slight shifts of the melting peaks and recrystallization temperatures can cause the change of glass windows for the laser sintering process. For instance, s-CNT/PA12 had a melting point at 184 °C, which was lower than that of PA12, but the recrystallization temperature of s-CNT/PA12 was higher than that of PA12. Then, the glass window of s-CNT/PA12 was relatively narrow, compared with that of PA12. Therefore, the powder bed temperature of s-CNT/PA12 needed to drop several degrees centigrade; the chamber temperature also needed to be further modified to minimize the curling and warping during the cooling process.

The differences induced by cholate ion functionalized MWCNTs and their influences on the thermal behaviours of the composite powders were closely associated with the molecular structures and their interactions with MWCNTs. Molecular dynamic simulation [169] has revealed that cholate ion molecules, unlike conventional linear surfactants such as SDS, are rigid facial amphiphiles as shown in Fig. 3.6 (a) and possess a quasilinear, slightly bent but rigid steroid ring with a hydrophilic face (the hydroxyl group and the charged carboxylate group) and a hydrophobic face (the methyl group and the tetracyclic carbon backbone) residing back-to-back. As a result, this ring structure can effectively accommodate the curvature on the CNT wall and then enhance the dispersion stability of MWCNTs in aqueous solution (Fig. 3.6 (c) and (d)). Kiriya *et al*. reported that cholate ions could facilitate CNTs assembly on a flexible substrate via a roll-to-roll process. The obtained substrate with uniform CNT coating exhibited excellent electrical conductivity for thin-film transistors. It indicated that the network of cholate ion warped CNTs could offer an effective platform for electron transport in electrical devices.

The new types of composite powders such as s-CNT/PA12 and s-CNT/PU were

expected as feedstock materials in the SLS system to manufacture the advanced composite products with superior mechanical, thermal and electrical performances over the neat polymer products. The desired surface coating was achieved to further induce the formation of an interconnected network of MWCNTs within matrices. Therefore, the surface morphologies and coverages of MWCNTs on powders would significantly influence the internal distribution and configuration of MWCNTs in the subsequently produced nanocomposites.

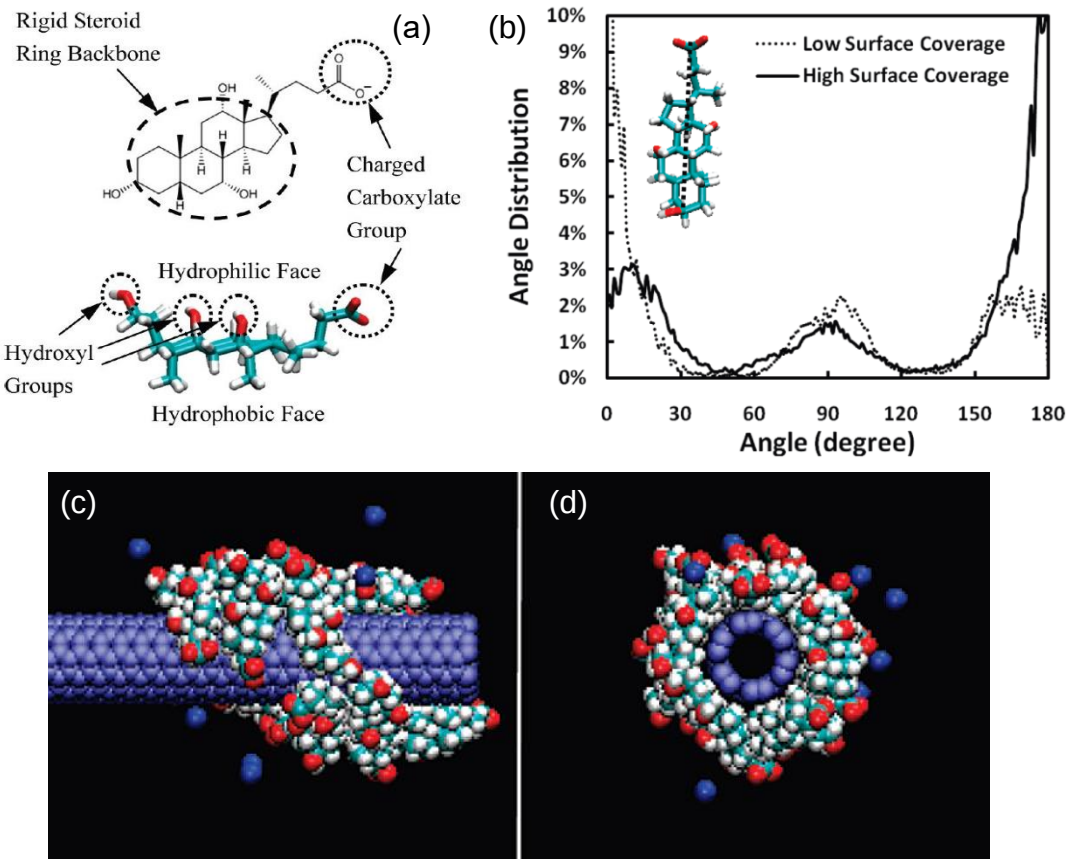

Figure 3.6. (a) Schematic and spatial chemical structures of sodium cholate, showing the rigid steriod-ring backbone, the hydrophobic and hydrophilic faces of the molecule, the hydroxyl group and the charged carboxylate group; (b) simulation distribution profiles of the angleΘ between the principle axis of the cholate ions and cylindrical axias of the CNT; (c) and (d) representative postequilibrium simulation snapshots of cholate ion warping around CNTs [170].

This method has the great advantage that polymer powders could achieve a uniform layer of networking nanocarbon fillers via CNTs at the low weight percentage range of 0.1-1%. In the hot-forming processes, the polymer composite comprises conductive fillers dispersed in the matrix material. Thereafter, the low percolation threshold of thermal or electrical conductivity can be achieved and the enhanced performance tends to saturate after the conductive fillers are sufficient to generate a continuous network in matrices.

On the other hand, such powders with uniform conductive coating are proper feeding materials with desirable configuration in a powder-fusion AM process because the surface layer of carbon nanofillers may contribute to heat absorption and conduction upon laser exposure. Meanwhile, the network of conductive fillers enables the formation of an electron pathway to overcome electrostatic agglomeration of particles. The manner of particles can avoid the caking and cluster effects in the powder deposition process. Therefore, the surfactant-facilitated latex technique offers a solution to prepare nanocomposite powders with tunable composition and configuration potentially applicable for the powder-based fusion process.

Chapter 4 Material evaluation and process optimization for selective laser sintering

The powder evaluation and process optimization methods have been proposed to determine the process parameters for the thermoplastic polymers and their composite powders. PA12 as a group of semi-crystalline thermoplastic and its composite CNT/PA12 are the most representative powders for laser sintering. Meanwhile, the dual-segment TPU has been newly introduced into the SLS system as its outstanding flexibility and wide industrial applications. The evaluation and optimization processes for TPU which is an amorphous phase-dominated matrix are also emphasized. The experimental-theoretical method has been utilized to fit the experimental results of temperature-dependent properties at different states and then these functions have been implemented to predict the energy absorption and consumption during sintering. Thus, the portable working range of the sintering parameters can be determined. The difference between semi-crystalline and amorphous thermoplastics is discussed and the influence of CNTs additives is also investigated.

4.1 Material evaluation

A systematic evaluation was conducted to analyze PA12, CNT/PA12 and TPU powders through measuring the powder flowability, powder size and distribution, and thermal transactions. The heat capacity and density in the three stages of powder phase, metastable melting phase and liquid phase were characterized and implemented into the theoretical model to predict the energy required for melting and decomposition. The laser absorbed by powders should be within the energy range from the melting to

decomposition of PA12, CNT/PA12 and TPU. The method of material evaluation and process optimization is cost effective and generally applicable for new material development in the SLS system.

The process development of SLS is mainly associated with the intrinsic chemical, thermal and rheological properties of the polymers and their physical behaviours in powder form, as illustrated in the schematic flowchart (Fig.4.1) where the critical material parameters influencing the SLS process and the relevant characterization methods are highlighted.

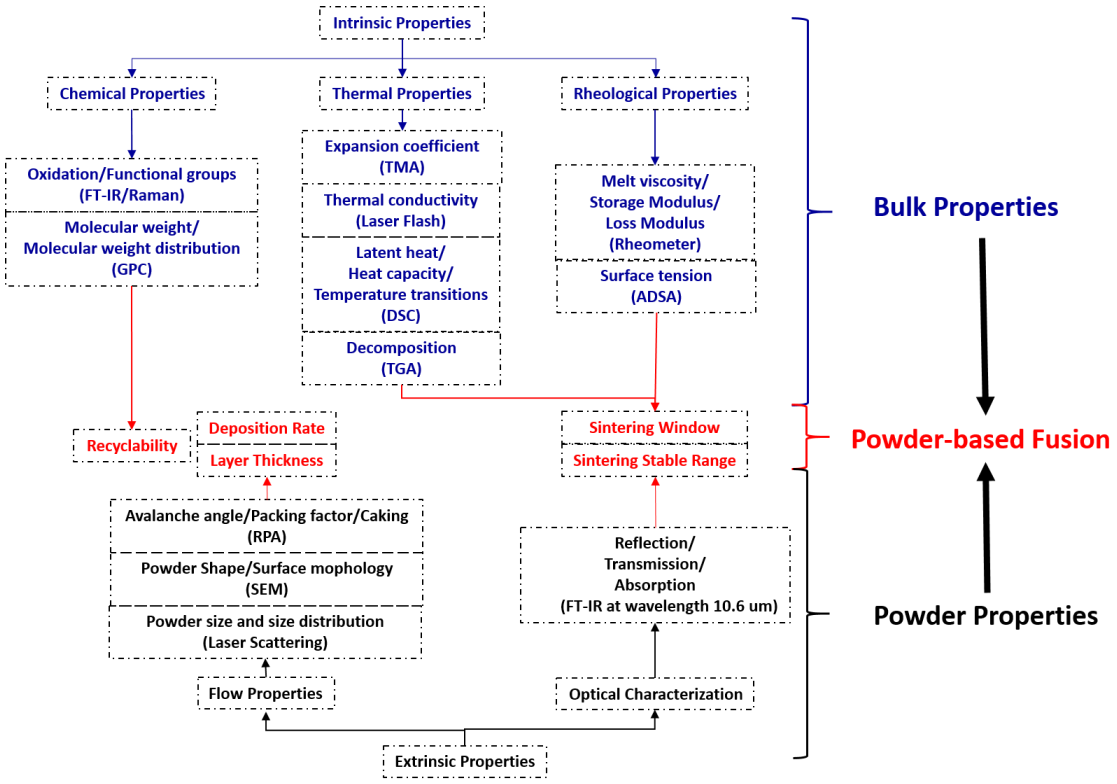

Figure 4.1. Illustration of a systematic method for new powder evaluation of the SLS system.

In order to determine the SLS process parameters, systematic material evaluation should be conducted to characterize the intrinsic properties of a polymer and the

extrinsic properties of its powders which are typically induced by the powder manufacturing process.

The intrinsic properties of the polymer including chemical, thermal and rheological properties are determined by its molecular structure and composition. Rheological testing can be employed to measure the melt viscosity and modulus as these melt behaviours can influence the status of coalescence powders. The differential scanning calorimetry (DSC) and thermogravimetric analysis (TGA) can be applied to identify the phase transition points of polymers. The melt surface tension of polymer can be measured using the axisymmetric drop shape analysis (ADSA). The Fourier transform infrared (FT-IR) or Raman spectroscopy can be used to analyze the chemical composition of polymers or their composites. Molecular weight and its distribution influencing recyclability of materials can be characterized by gel permeation chromatographe (GPC).

The two types of extrinsic properties via optical and flow properties of powders are significant to determine the process parameters of the SLS system. The flowability of powders is attributed to their morphology and size distribution, which can be characterized by scanning electron microscopy (SEM) and light scatter. The avalanche angle and packing factor measured by Revolution Powder Analyser (RPA) directly reflect the flow properties of powders. The light absorption and scattering at the specific wavelength of laser can be utilized to predict the heat absorption of powders induced by laser energy. Therefore, the effective method of process optimization for a new material consists of three steps: (i) powder characterization, (ii) powder feature analysis, and (iii) process parameter setting. This systematic methodology can guide the evaluation of

TPU powders and narrow the effective working range of laser energy required for the new material.

4.1.1 Powder properties

A field emission scanning electron microscope (FESEM) (JSM-7600F, JEOL Ltd., Tokyo, Japan) was used to characterize the surface morphologies of the polymeric nanocomposite powders with the e-beam power of 2-5 KV. In order to capture the network structure of CNTs within the polymer matrix after sintering, the optical microscopy (Olympus DP72, MA, 02453, USA.) was employed to investigate the microstructures of the sintered CNT/PA12 composites, which were properly ground and polished to achieve smooth and reflective surfaces. The shape and surface morphology of polymeric powders were also revealed through the SEM images.

The flowability of polymer powders was quantified through the flowability measurement conducted by RPA, based on the evaluated process conditions. The sample powders were placed inside the measurement drum. The instrument was run for 250 sets of avalanches or data points.

The light absorptivity of PA12, CNT/PA12 and TPU powders at 10.6 um wavelength was evaluated by FT-IR (PerkinElmer Spectrum One FTIR).

4.1.2 Bulk properties

During the transitions of solid powder melting metaphase-liquid phase, the critical thermal properties of the polymer powders change significantly. For instance, the changes of the heat capacity, density and melt viscosity of the polymer powders strongly

influence their heat absorption, melting and coalescence over the entire sintering process. Therefore, the concepts of the modified heat capacity and density were introduced to quantitatively evaluate the processaibility of PA12 and CNT/PA12 in laser sintering.

DSC was carried out using a Q200 DSC from TA Instruments under an air atmosphere. The PA12 and CNT/PA12 powders with the mass of 5 mg were encapsulated in a TA Tzero standard aluminum pan and loaded into DSC for heating-cooling loop testing. The thermal program for this experiment was as follows: cool rapidly to T = 25 °C, hold isothermally for 1 min, heat up with a rate of 10 °C/min to 250 °C, hold isothermally for 1 min, cool to T = 25 °C with a rate of 10 °C/min, hold isothermally and finally stop. This heating-cooling programming was conducted to identify the onset and offset of melting and recrystallization as well as the enthalpy changes during phase transitions. In addition, a modulated model of DSC was applied to characterize the modified heat capacity of PA12 and CNT/PA12 from powders to melt manners following the ASTM standard E1269-11 [23] and the modified heat capacities with respect to the three stages of powder phase, melting metaphase and liquid phase were calculated by [24]

$$C_P^* = C_P^p(T), T_{ms} > T\,, \tag{4.1}$$

$$C_P^* = C_P^P(T_{ms}) + \frac{\Delta H_m}{\sqrt{\pi (T_{mf} - T_{ms})^2}} \exp(-\frac{(T - T_{ms})^2}{(T_{mf} - T_{ms})^2}), T_{ms} < T < T_{mf}\,, \tag{4.2}$$

$$C_P^* = C_P^m(T), T > T_{mf}\,, \tag{4.3}$$

where T_{ms} and T_{mf} are the onset and offset points of melting, respectively. With the three stages from powder to metastable melting phase to fully melted phase, $C_P^P(T)$ is the

heat capacity of the material in powder form, which considers the influence of empty spaces among free-compacted powders; $C_P^m(T)$ is the heat capacity of material in a liquid phase; ΔH_{m} is the melting enthalpy.

In addition, a modulated model of DSC was applied to characterize the modified heat capacity of TPU upon its melting process following the ASTM standard E1269-11 [171]. The modified heat capacities C_{p}^* from the powder phase, melting metaphase and liquid phase were measured to behave as a functional of temperature.

As the amorphous polymer via TPU does not exhibit the critical phase change of melting, the concept of heat capacity in the melting stage $C_P^m(T)$ is not applicable for TPU powders. Therefore, a simplified function of temperature was utilized to describe the heat capacity of amorphous polymers and further predict the heat absorption of TPU. The function of temperature $C_P^m(T)$ can be obtained through proper experimental fitting based on the measured modulated heat capacity.

The volumetric changes of materials upon melting could be characterized through a novel method developed by Verbelen *et al.* [19]. The basic procedures of the method were as follows: (i) to build a special container and adapt it into a thermomechanical analyser (TMA) (Q400, TA instruments); ii) to disperse polymer or its composite powders into silicon oil and fill this mixture into the confined container; iii) to measure the difference of the volume expansion between pure silicon oil and the suspension of powders. The temperature-dependent specific volume of the polymer powders was measured at a heating rate of 0.5 °C/min. The instant density of the polymer powders was regarded as the reciprocal of the specific volume of material. Thus, the modified

densities $\rho^*(T)$ of PA12 and CNT/PA12 were temperature-dependent functions within the different stages of heating and could be obtained by

$$\rho^*(T) = \rho_P(T) = \frac{1}{V_P(T)}, T < T_{ms} \tag{4.4}$$

$$\rho^*(T) = \rho_m(T) = \frac{1}{V_m(T)}, T_{ms} < T < T_{mf} \tag{4.5}$$

$$\rho^*(T) = \rho_l(T) = \frac{1}{V_l(T)}, T > T_{mf} \tag{4.6}$$

where $\rho_p(T)$ and $V_P(T)$ are the modified density and specific volume of materials in powder form, respectively; $\rho_m(T)$ and $V_m(T)$ are these of the melting metaphase; $\rho_l(T)$ and $V_l(T)$ are these of the liquid phase.

Instead of measuring the critical changes of semi-crystalline polymers such as PA12 upon melting, TMA was utilized to characterize the coefficient of thermal expansion. The TPU powders gradually melted and expended upon melting, but the coefficient of thermal expansion remained as a constant.

Rheological dynamic measurements were performed at 200 °C in the strain-controlled DHR-Rheometer (TA-Instruments, USA), using the 25-mm diameter parallel plates. The powders were compressed into a cylinder (diameter in 25 mm and thickness in 2mm) by mechanical force. The specimens were tested in an oscillating dynamic mode, the frequency was varied from 100 to 0.1 rad/s, and the melt viscosities of PA12 and CNT/PA12 were characterized.

On the other hand, the melt viscoelastic storage modulus, loss modulus and loss factor of TPU were measured within the range from 100 °C to 200 °C. The specimens of TUP were tested in a dynamic mode, the frequency was varied from 100 to 0.1 rad/s

and the melt viscoelastic storage shear modulus and loss shear modulus were investigated at 180 °C.

Thermogravimetric analysis was conducted using TGA Q500 equipment (TA instrument, USA). For each run, the TGA results were acquired from approximately 15 mg TPU powders, which were heated from the room temperature to 650 °C under N_2 gas environment, in order to obtain decomposition of materials at an elevated temperature. The same procedure was conducted on PA 12 and CNT/PA12 powders.

4.1.3 Theoretical prediction

The critical parameters such as the laser power *p*, scanning speed *s* and hatch space *h* were monitored to control the sintering process because the energy input per unit area E_{area} and the volume E_{vol} from the laser are determined by

$$E_{area} = \frac{p}{hs}, \tag{4.7}$$

$$E_{vol} = \frac{p}{hsL}, \tag{4.8}$$

where *L* is the layer thickness.

The principles to determine the range of laser input energy were to evaluate the energy required for melting and decomposition of specific polymer powders. The energy per volume required for melting E_{mv} is defined by

$$E_{mv} = \rho^*(T)\phi\int_{T_b}^{T} C_p^* dT, T < T_{mf} \tag{4.9}$$

The energy absorption per volume E_{dv} within the stable sintering region (SSR) is described by

$$E_{dv} = E_{mv} + \rho_l(T)\int_{T_{mf}}^{T_{ds}} C_P^l(T)dT, T_{mf} < T < T_{ds} \tag{4.10}$$

SSR describes the optimum temperature range for successful laser sintering usually from the offset of melting T_{mf} to the onset of decomposition T_{ds}, which indicates the 1% weight loss from the TGA diagram [89].

The substitution of the modified density $\rho^*(T)$ into Eq. (4.9) results in

$$E_{mv} = \rho_p(T)\phi \int_{T_b}^{T_{ms}} C_P^P dT + \rho_m(T) \int_{T_{ms}}^{T_{mf}} C_p^* dT, T < T_{mf} \tag{4.11}$$

where ϕ is the packing factor of the polymer powders and T_b is the bed temperature of laser sintering. The modified density and heat capacity are the functions of temperature and used to predict the energy absorptions according to Eqs. (4.10) and (4.11).

In order to effectively sinter polymer powders and prevent polymer degradation or decomposition, the input laser energy should satisfy the following relationship:

$$E_{mv} < E_{vol}\alpha_{critical} < E_{dv} \tag{4.12}$$

where E_{vol} is the laser energy per volume, and $\alpha_{critical}$ is the critical heat absorptivity of polymer powders exposed to laser heat. This relationship can be applied to evaluate the heat absorptivity in corporation with experimental observations, and employed to predict the proper process parameters so that sufficient energy for melting can be induced and the heating temperature can remain within SSR.

4.2 Process optimization

4.2.1 PA12 and CNT/PA12 composites

In this section, the proposed method was used to predict the laser energy input range and narrow the working range of laser parameters to effectively optimize sintering. The reinforcement mechanism of CNTs within the sintered PA12 matrix was investigated

through analysing the thermal influences of the CNTs, the microstructures and mechanical properties of the sintered composite parts.

4.2.1.1 Evaluation of CNT/PA12 powders

The size and morphology of composite powders were investigated (Fig. 4.2). It was found that the particle size was mainly within a narrow range of 60-70 μm, which was consistent with that of the neat PA12 (PA2200) reported in the literature [171, 172]. This was because the thickness of the CNT coating was extremely thin, compared with the diameter of the polymeric powders. The original near-spherical shape of the polymer powders was retained and such shape and morphology of these powders exhibited proper flowability and were preferable in the layer-by-layer deposition [4, 5]. Furthermore, the CNTs were able to assemble uniformly onto the surface of the polymer powders and form a network structure as shown in Fig. 4.2 (d).

The melting and recrystallization of materials were studied using DSC as the melting peaks coud provide important indications on the sinterability of the materials. PA12 showed a very sharp melting peak with high enthalpy of fusion because of the high crystal perfection of virgin powders [173]. It also indicated that the energy trigger of melting was required to be strong and fast, as this was the unique advantage of the laser energy. In comparison, CNT/PA12 showed a relative smooth peak and a low melting point, which indicated the improved heat conductance and efficiency of fusion. This observation implied that the requirement of thermal energy input from laser could be reduced and the fully melting of CNTs-introduced composite could be easily achieved.

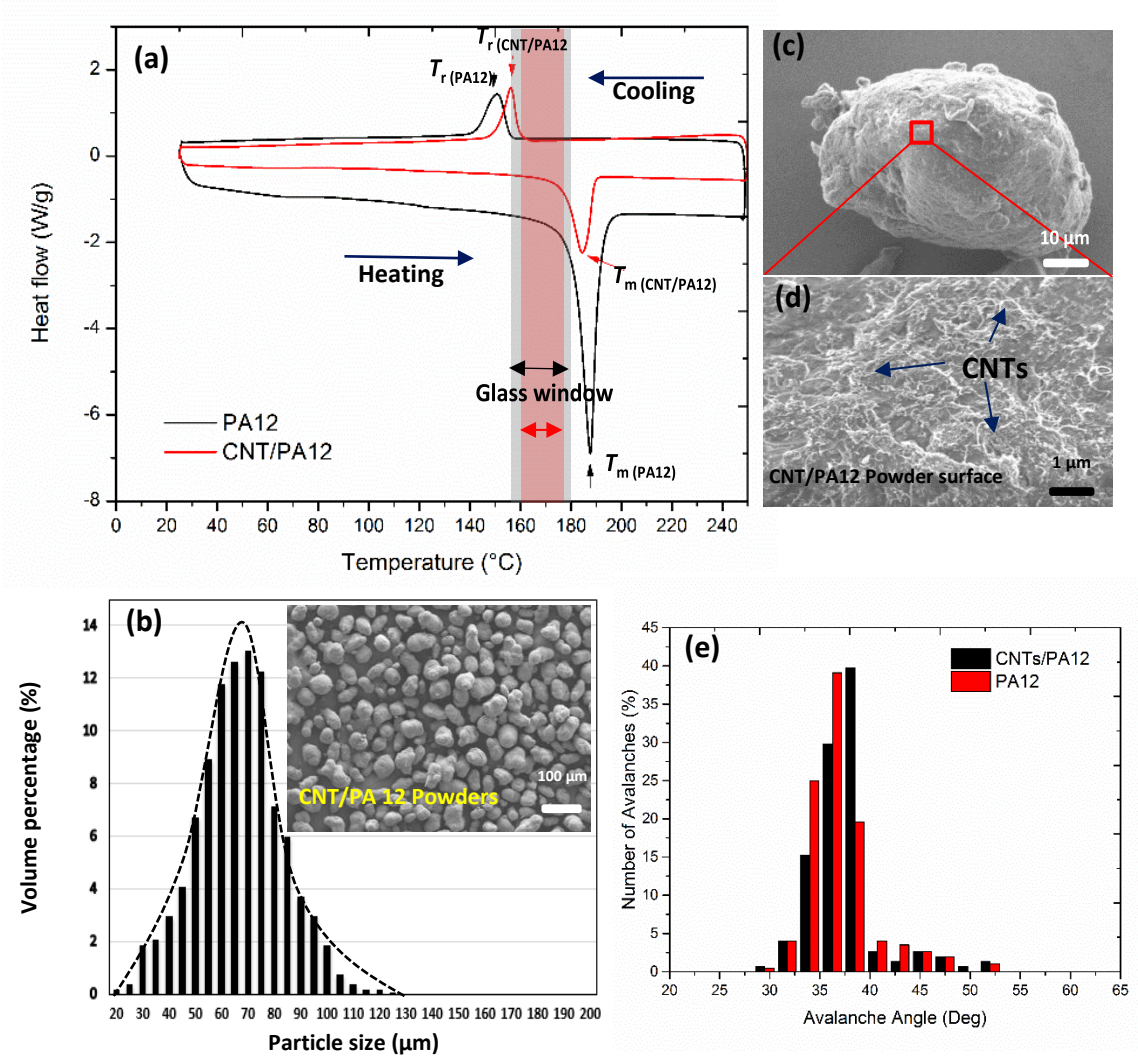

Figure 4.2. (a) DSC diagrams of PA12 and CNT/PA12 upon heating and cooling at the rate of 10 °C/min; (b) size distribution of PA12 and CNT/PA12 (0.5 wt%); SEM images: (c) composite powders and (d) the surface layer of CNTs which are light network structure; (e) avalanche angle graph indicating the required average angle to start and maintain the flow of the PA12 and CNT/PA12 powders.

The recrystallization peak of CNT/PA12 was relatively sharp and narrow compared with that of PA12 because the CNTs could act as a nucleating agent and accelerate the crystallization process [172]. However, the onset of recrystallization of PA12 was at a lower temperature than that of its composite and the broad peak of PA12 indicated its gradual crystallization kinetics.

In general, the process temperatures such as pre-heating temperature T_b and chamber temperature T_c are roughly determined based on the DSC heating-cooling cycle. The glass window is within the temperature range of the melting and crystallization onsets. The T_b should be set within the glass window and just below the melting onset, and T_c be set below the recrystallization offset. Since the polymers for the laser sintering process experience the transitions from the powder form to liquid phase to solid form, the critical temperature transitions are crucial for quantitatively evaluating the energy input for heating or melting. The specific heat of PA12 and CNT/PA12 in powder form and liquid form are plotted as the functions of temperature (Fig. 4.3).

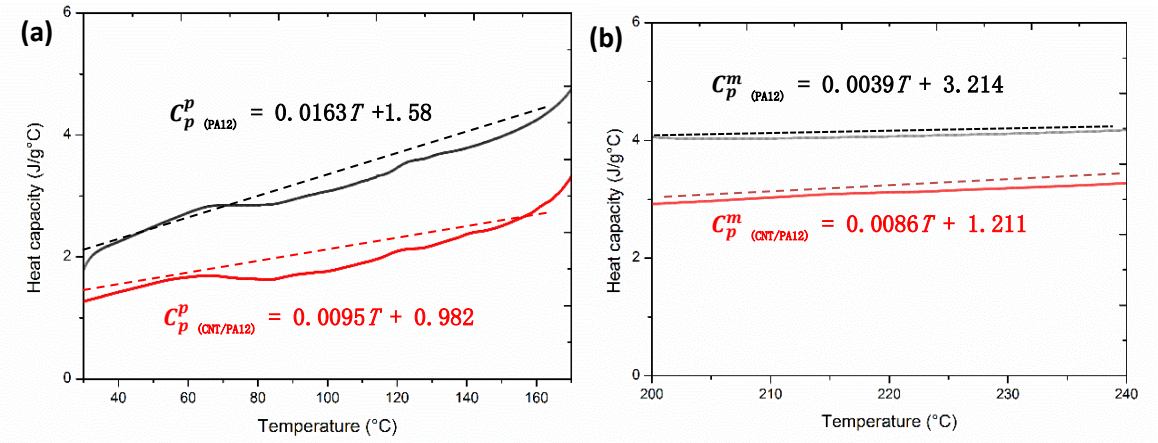

Figure 4.3. Specific heat of PA12 and CNT/PA12 at (a) the powder phase and (b) the liquid phase.

In this study, the glass window of CNT/PA12 was evaluated by the DSC analysis and it was relatively narrower than that of PA12. The DSC heating-cooling curves were also utilized to obtain the onset, offset and absolute enthalpy values of melting and recrystallization of PA12 and CNT/PA12 for further quantitative evaluation (Table 4.1).

Table 4.1. Material parameters for PA12 and CNT/PA12 powders

	PA12	CNT/PA12
Powder specific heat C_p^p (J/g °C)	0.0163*T*+1.58	0.0095*T*+0.98
Melt specific heat C_p^m (J/g °C)	0.0039*T*+3.21	0.0086*T*+1.21
Melting peak T_m (°C)	187.66	184.46
Enthalpy of melting ΔH_m (J/g)	107.2	90.85
Recrystallization peak T_r (°C)	150.90	156.22
Enthalpy of recrystallization ΔH_r (J/g)	50.04	46.11
Packing fraction ϕ	0.445	0.44
Thermal conductivity K_p (W/mK)	0.12 (± 0.04)	0.25 (± 0.08)
Onset melting temperature T_{ms} (°C)	180.93	177.21
Onset recrystallization temperature T_{rs} (°C)	155.70	159.22
Glass window width (GW) (°C)	25.23	17.99
Stable sintering region (SSR) (°C)	198 ~ 360	187 ~ 402
Melt viscosity at 0.1 rad/s η (Pa·s)	1.4 x10^3	5.4x10^3

The proper fusion of powder particles is crucial to obtaining fully condensed parts through laser sintering. The viscous sintering of polymer powders can be described by a simplified model [66, 104, 174]:

$$\frac{x^2}{R} = \frac{2\Gamma}{3\eta_0} t, \tag{4.13}$$

where x and R are the necking and particle radii, respectively; Γ and η_0 are the surface tension and and zero-shear viscosity of the polymer melt, respectively; t is the sintering time.

Although this simple model is limited to perfectly spherical powders at the initial stage of sintering, the extended models [174] have revealed that the shear viscosity is critical for judging material sinterability as compared with the surface tension, which is only a weak function of temperature.

The investigation into melt viscosity of a polymer and its composite was applied to

analyse the post-condensation and coalescence behaviours in laser sintering. The advantage of using melt viscosity to evaluate these behaviours, rather than direct molecular weight measurements such as gel permeation chromatography, is that the changes in molecular weight and influences of additives as a function of time and temperature can be directly determined [173].

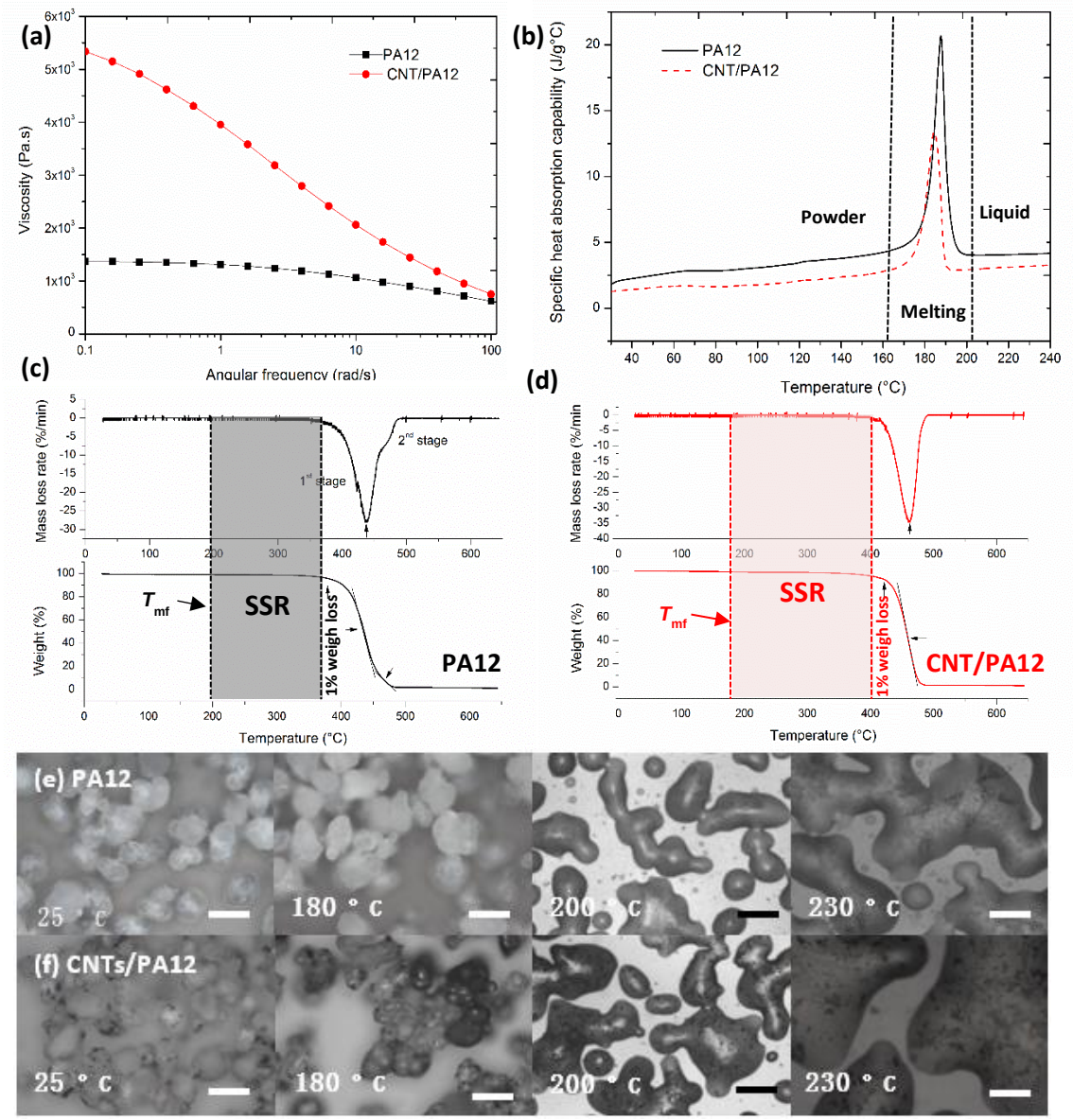

Figure 4.4. (a) Melt viscosity of PA12 and CNT/PA12 at 200 °C; (b) specific heat absorption of PA12 and CNT/PA12 over the process temperature range; (c) and (d) TGA plots of decomposition processes of PA12 and CNT/PA12; (e) and (f) optical images of the fusion process of PA12 and CNT/PA12 powders (the scale bar: 100 μm).

The oscillatory measurements were conducted to obtain the melt viscosity of PA12 and CNT/PA12 through varying the frequency from 0.1 to 100 rad/s (Fig. 4.4 (a)). Since the typical polymers are shear-thinning materials, their viscosities increase as the applied angular frequency increases above a certain rate. However, the melt viscosity of PA12 was not sensitive to frequency change, and a plateau phenomenon was observed at the low frequency range (<1 rad/s).

The melt viscosity of CNT/PA12 significantly decreased as the angular frequency increased. The composites exhibited the high melt viscosity at the low frequency range, especially at zero frequency, compared with the neat PA12. Such observations indicated that CNT/PA12 might require enough time to fuse and coalesce even though the laser could fully melt the powders. Therefore, the powder fusion under the pressure-free condition was captured through an optical microscopy to observe the powder coalescence of PA12 and CNT/PA12 (Figs. 4.4 (e) and (f)). CNT/PA12 started to fuse at 180 °C, but PA12 still retained the solid state.

When the temperature increased above the melting point of powders, these powders were melted and gradually merged together. Fortunately, although the melt viscosity of CNT/PA12 was higher than that of PA12 at the pressure-free condition, the composite powders could fuse easily when they are fully melted at elevated temperature. Thus, the addition of CNTs with 0.5 wt% did not cause adversely effects during the powder coalescence.

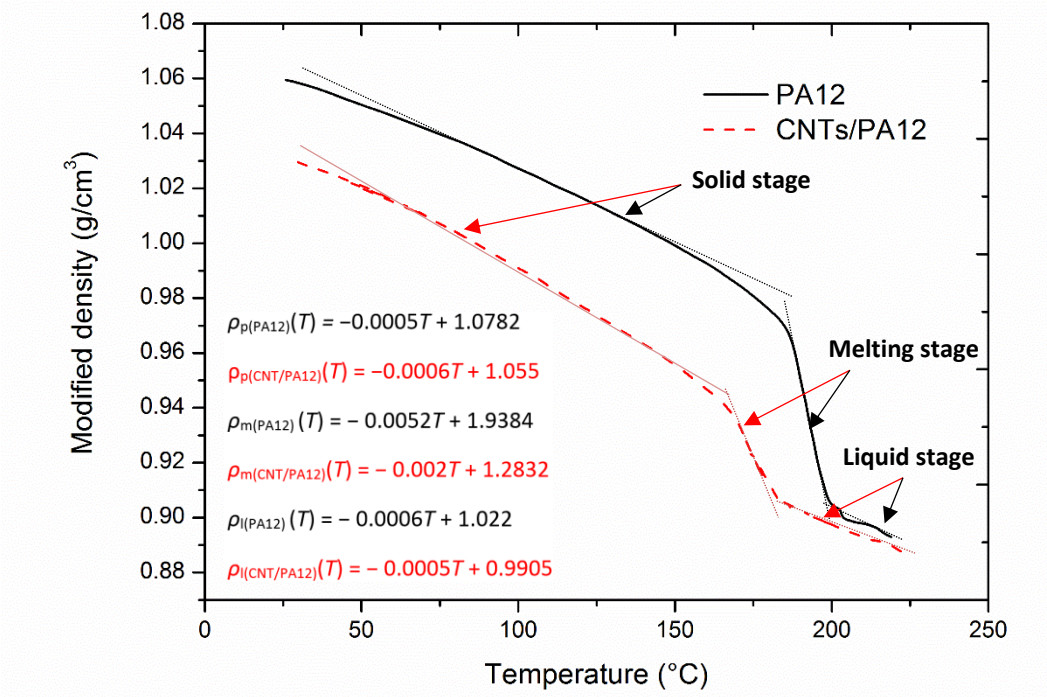

Figure 4.5. Increasing temperature from 25 to 225 °C, the modified densities of PA12 and CNT/PA12 exhibit the linear relationships with temperature in three stages via the solid, melting and liquid state.

To determine the SSR of laser sintering, the DSC and TGA analysis were combined to determine the offset of melting and onset of decomposition of materials. Usually, a polymer with a wide SSR via optimum temperature range is preferable for laser sintering process. As shown in Fig. 4.4s (c) and (d), CNT/PA12 exhibited a wider range of SSR than PA12.This observation indicated that the stable sintering was easily controlled and the decomposition of polymer composite could be prohibited even though the local temperature increased dramatically. Meanwhile, the temperature range of SSR could be implemented to quantitatively predict the energy required before decomposition using Eq. (4.10).

Conventionally, the dilatometric properties are measured to investigate the potential of warping and shrinkage of the sintered parts, as the specific volume of the polymers

behaves as a function of temperature upon the heating-cooling process [173]. In this work, in order to exactly predict the energy required for melting and decomposition, the reciprocal of the specific volume was applied to evaluate the modified density, which was introduced to describe the trends of density change of PA12 and CNT/PA12 upon heating. Fig. 4.5 plots the linear functions of densities in the three stages of materials used in laser sintering.

The thermal behaviours relevant to the sintering process are summarized in Table 4.1. The majority of temperature-dependent properties were characterized and discussed. The packing factor ϕ represents the effectiveness of powders occupying a specific volume in the deposition process. The detailed measurement procedures were reported elsewhere [174] and the packing factors of PA12 and CNT/PA12 powders were evaluated by Peyre *et al.* [172]. The experimental measurements conducted by Bai *et al.* revealed that the thermal conductivities of PA12 and CNT/PA12 powders were the weak functions of temperature, and the influences of temperature on thermal conductivities were negligible in the theoretical evaluation [3].

4.2.1.2 Enhancements of CNTs in the PA12 matrix

The CNT coating could enhance the PA12 matrix in two aspects: i) the facilitation of heat absorption and conduction during laser sintering; and ii) the reinforcement on mechanical properties of the sintered polymeric composites. The experimental observations and theoretical prediction were discussed as follows.

Using the experimental-theoretical approach, the energy required for melting unit mass or volume were evaluated as listed in Table 4.2. The value of E_{mv} of PA12 agreed

with the predicted result of Vasquez *et al*. [89], while E_{dv} was slightly higher , due to the fact that a wide SSR was obtained in current work (Table 4.2).

Table 4.2. Evaluation of the energies required for melting and absorbed before polymer degradation with respect to the specific mass and volume and the thermal conductivities of the PA12 and CNT/PA12 parts.

Energy Parameter	PA12	CNT/PA12
Mass energy for melt E_{mm} (J/g)	189.51	167.07
Volume energy for melt E_{mv} (J/mm^3)	0.072	0.064
Mass energy before decomposition E_{dm} (J/g)	688.96	767.52
Volume energy before decomposition E_{dv} (J/mm^3)	0.555	0.606
Thermal conductivity K_o (W/mK)	0.15 (±0.05)	0.45 (±0.09)

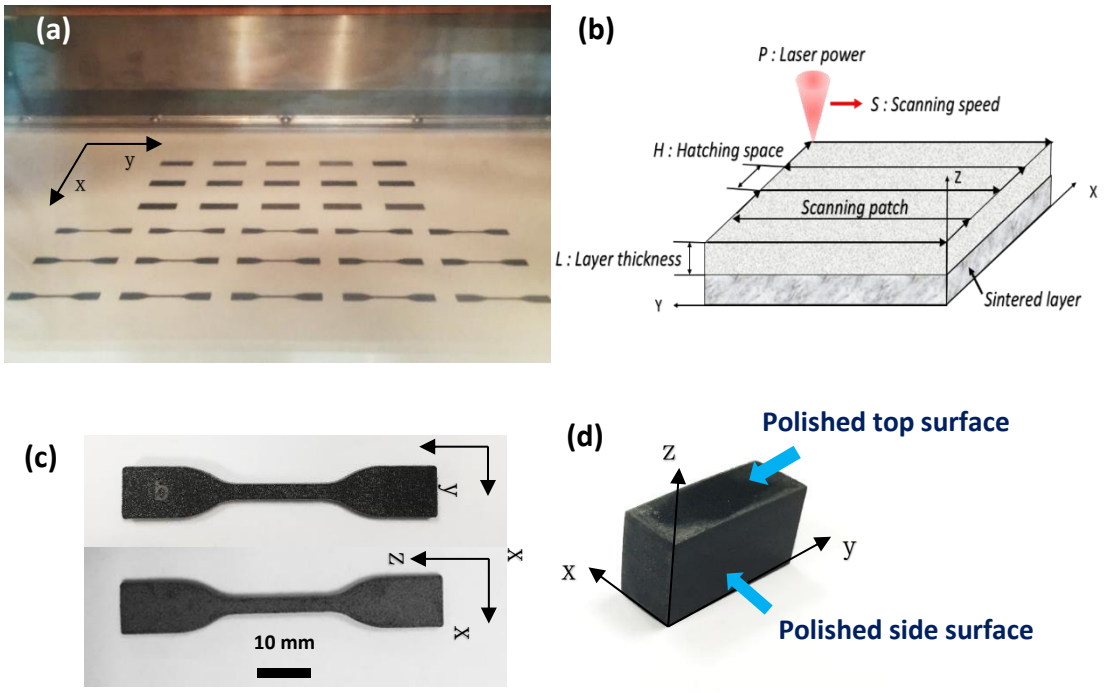

Figure 4.6. (a) Building platform of the EOS P395 machine with the *X*-*Y* plane attached; (b) schematic illustration of the critical parameters in the laser sintering process; (c) micro tensile specimens (ASTM D638, type IV) produced in the *X*-*Y* and *X*-*Z* planes; (d) polished specimen for microstructure characterization in the *X*-*Y* (top surface) and *Y*-*Z* (side surface) planes.

The theoretical analysis showed that CNT/PA12 required less energy to melt and

consumed more energy till decomposition than PA12. This evaluation revealed that CNTs assisted the polymer melting and resulted in the ease of sintering, which could improve the effectiveness of laser sintering. Meanwhile, the improved thermal conductivity of the composite powders also positively accelerated the thermal conduction within the polymer matrix and increased the penetration length of the laser source through the powder bed [66], possibly resulting in the full melting of polymeric powders and the minimization of interlayer delamination.

Fig. 4.7 shows the microstructures of the sintered PA12 and CNT/PA12 from the X-Y and X-Z cross-sections. It is observed that CNTs-coating was remained on the powder boundaries and formed a secondary phase to be embedded into the polymer matrix. The composite powders were fully sintered with random shapes on the X-Y plane, while the composite powders were melted and formed many menisci, which were condensed to stack together, as observed from the X-Z plane (Fig. 4.7 (c)). This indicated that the composite powders were fully melted and the molten polymer tended to spread within the confided space, and the formation of the menisci was driven by gravity and surface tension at the liquid state. However, in Figs. 4.7 (b) and (d), the PA12 powders remained semi-spherical shape and non-molten polymers were also shown on the X-Z cross-section. This revealed that PA12 powders were just partially melted to sinter and exhibited a weak tendency to fully fuse together. Although the composites exhibited an increased melt viscosity with a limited melt flow capability compared with neat polymer (Fig. 4.2 (a)), the improved state of melting enabled the enhancement of the coalescence and fusion of composite powders.

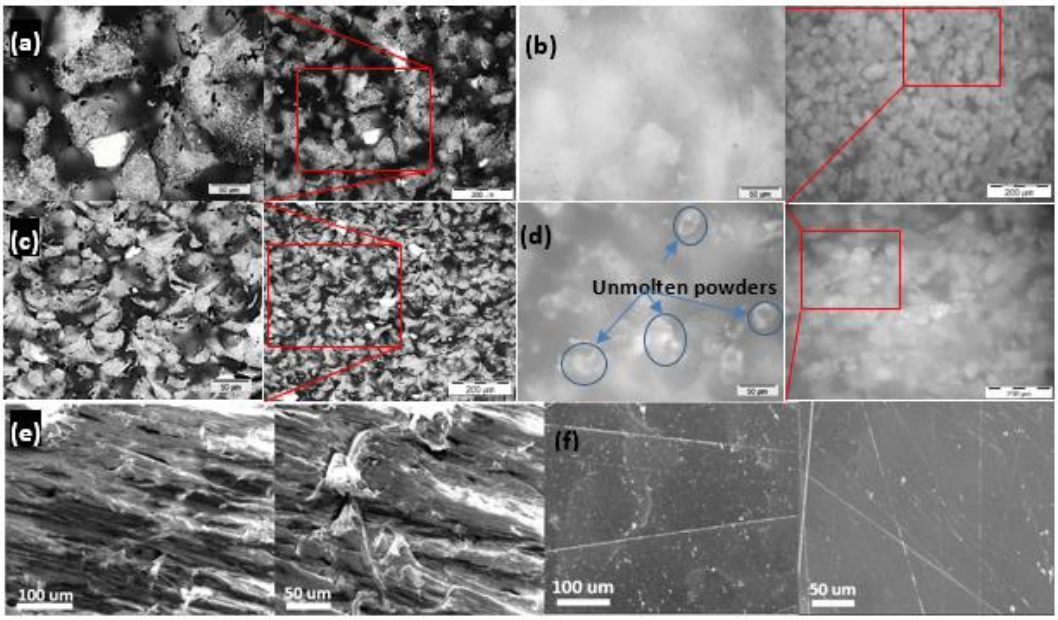

Figure 4.7.Optical images of microstructures: (a) CNT/PA12 and (b) PA12 from the X-Y plane; (c) CNT/PA12 and (d) PA12 from the X-Z plane. SEM images of the surface structures: (e) CNT/PA12 and (f) PA12 through mechanical grinding and polishing.

The partially melted state of virgin polymer powders induced inferior melt flowability and adverse coalescence of the powders. The surface morphologies showed the cross-sections of the sintered CNT/PA12 and PA12 after sand grinding: the composite exhibited very rough surface due to the fact that CNT bundles were bonded with the polymer and too stiff to remove, while the surface of PA12 was smooth and flat (Figs. 4.7 (e) and (f)).

The relationship of melting and degradation energy with laser energy (Eq. (4.12)) was applied to evaluate the heat absorption and predict the proper range of the energy input by laser expressed as $E_{mv} < E_{vol}\alpha_{critical} < E_{dv}$,where $\alpha_{\text{critical}}\, E_{\text{vol critical}}$ is the total energy absorbed to just fully melt polymer powders upon laser sintering. A greater value of α_{critical} reveals that more heat is absorbed when specific powders are being exposed to laser scanning. The critical value of E_{vol} is the minimum value of the

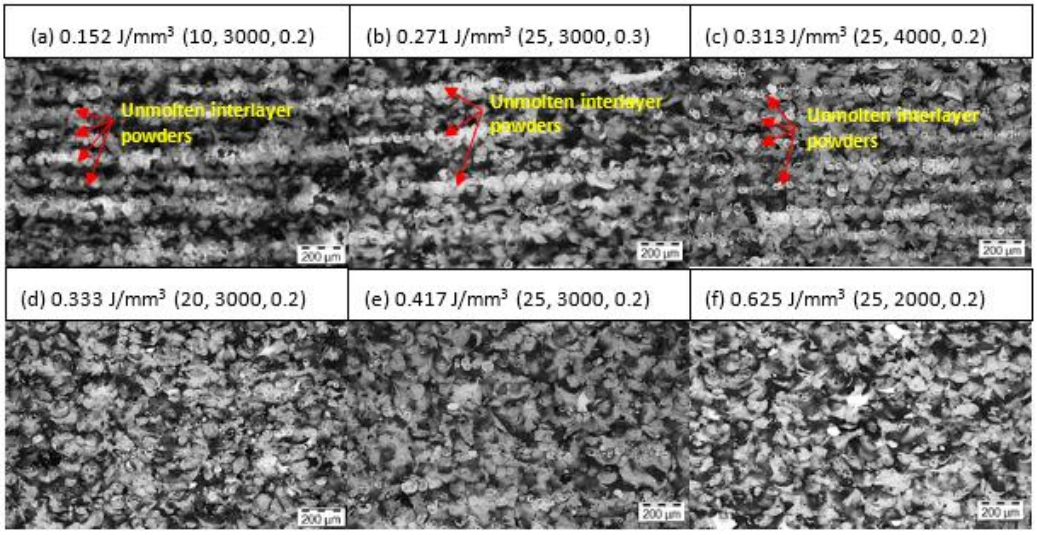

Figure 4.8. The microstructures of the CNT/PA12 parts sintered upon varied laser input energy in the X-Z plane. Note the power (W), scanning speed (mm/s), and hatching space (mm).

laser energy to fully melt for specific powders. Grewell *et al.* investigated that a maximum of 20 % of infra-red laser energy was possibly absorbed by neat PA [175], and therefore the minimum energy input from laser E_{vol} to possibly fully melt PA12 powders started with a value around 0.356 J/mm^3 ($E_{\mathrm{mv}}/20\%$). A set of laser parameters are listed in Table 4.3, in which the energy input of laser E_{vol} was 0.333 J/mm^3 corresponding to the sintered structures of PA12 and CNT/PA12 in Fig. 4.8. The ratios of $E_{\mathrm{mv}}/E_{\mathrm{vol}}$ for PA12 and CNT/PA12 were 19.4 % and 21.8 %, respectively. Based on microstructure characterization, it can be concluded that the $\alpha_{\mathrm{critical(CNTs/PA12)}}$ was higher than the value of 0.218, but $\alpha_{\mathrm{critical(PA12)}}$ was much lower than 0.194 due to the fact that the large number of partially melted PA12 powders were observed. This reveals that the portion of the laser energy absorbed by PA12 was much less than 20% in the SLS process because the light transmission, reflection and scattering of the powders strongly dissipated the laser energy.

Table 4.3. The sets of process parameters for the laser sintering of CNT/PA12 powders.

Set	Fixed parameters	Varied parameters					
1	*s*:3000 (mm/s), h: 0.2 (mm)	*p* (W)	10,	15,	20,	25,	30
2	*p*: 25 (W), *h*:0.2 (mm)	s (mm/s)	2000,	2500,	3000	3500,	4000
3	*p*:25 (W), *s*:3000 (mm/s)	*h* (mm)	0.2,	0.25,	0.3,	0.35,	0.4

The microstructures of the sintered CNT/PA12 parts under the different sets of laser energies were characterized from the X-Z plane to investigate the critical heat absorptivity $\alpha_{\mathrm{critical}}$. As observed in Fig. 4.9, the critical energy input was between 0.313 and 0.333 J/mm^3 because the unmolten interlayer powders indicated the state of the heat absorption by CNT/PA12. Thus, the $\alpha_{\mathrm{critical}}=E_{\mathrm{mv}}/E_{\mathrm{vol\ critical}}$ was around 0.22, revealing that 22% of the laser energy input was absorbed by the composite powders to effectively melt and sinter the polymer.

The CNTs-coated PA12 was within the extended SSR, resulting in an increased E_{dv}, and then $E_{\mathrm{vol}} = E_{\mathrm{dv}}/\alpha_{\mathrm{critical}}$ could be estimated to be around 2.75 J/mm^3, which was the energy required to induce polymer decomposition during the sintering process of CNT/PA12. Nevertheless, such a laser energy density is extremely high and rarely used in commercially available SLS machines. As shown in Fig. 4.9, the mechanical properties tended to saturate once the polymer powders were fully melted and coalesced before being decomposed. Thus, the PA12 decomposition is not a critical issue causing inferior performances, and the insufficient melting-induced voids or interlayer delaminations are more essential for the mechanical properties of materials.

Fig. 4.9 shows that the tensile modulus and elongation at break of the sintered CNT/PA12 specimens in both X-Y and X-Z planes tended to saturate when the laser

energy input was above the critical energy per unit volume $E_{\text{vol critical}}$, the minimum energy required to fully melt the composite powders as evaluated above. However, if the laser energy input was lower than $E_{\text{vol critical}}$, the mechanical performances dropped significantly due to the insufficient melting as shown in Fig. 4.8.

Another type of enhancements of CNTs on the mechanical aspect are shown in Table 5, in which the tensile strength and elongation at break both increased by 31.8 % and 37.54 %, respectively, compared with the neat PA12. Impressively, the toughness increased dramatically by 84.9 % and the tensile moduli remained the same. In comparison, the ball-milled CNT/PA12 composite powders for laser sintering were reported to increase the ultimate strength and flexural modulus by 9.3% and 31.5%, respectively, but the elongation at break dropped by 18% [176]. The glass and ceramic fillers were also introduced to improve the mechanical stiffness of the sintered polymeric composite, but scarifying ductility under tension [177-180]. It is known that the critical shortcoming of sintered polymeric composites is the poor ductility due to the weak interfacial adhesion and micro-defects induced by fillers.

The results of the CNTs-coated PA12 parts via laser sintering reveal that the nanofillers simultaneously enhance the strength and ductility of the sintered polymeric composites. As observed in Figs. 4.7 (a) and (c), the CNTs-coating layer remained at the powder boundaries, and then the CNTs formed a 3D network within the matrix due to the unique pressure-free and superfast heating-cooling process of laser sintering. As a secondary phase in the PA12 composite, the CNTs framework enabled the strengthening of the polymer matrix by preventing intermolecular movement of the polymer chains under loading.

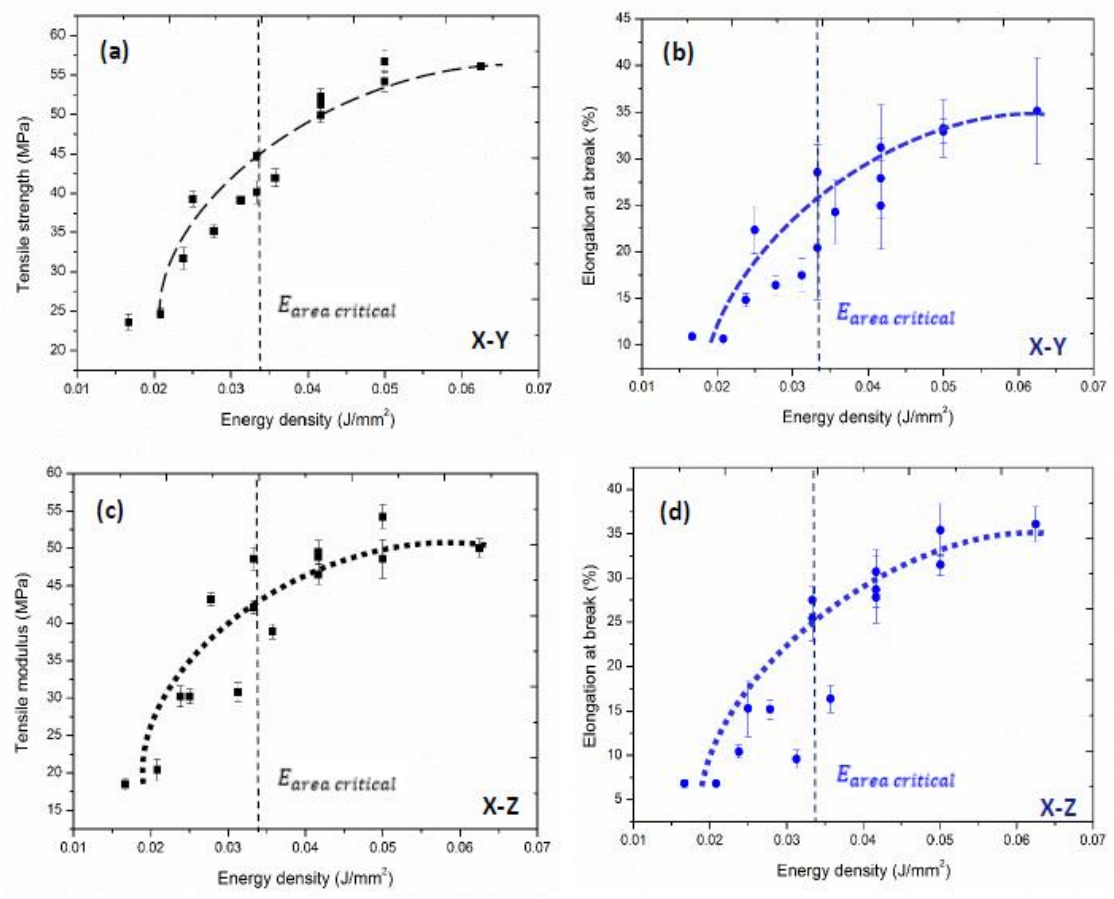

Figure 4.9. Energy density influences on (a) the tensile strength and (b) the elongation at break of the specimens in the X-Y plane; (c) tensile strength and (d) elongation at break of specimens in the X-Z plane.

Meanwhile, the CNTs facilitated the heat absorption and promoted the melting process of polymers to minimize the presence of pores in the composites. Fig. 4.7 indicates that the CNT/PA12 (0.5 wt%) demonstrated an excellent melting and fusion state and CNTs remained at the powder boundaries. In contrast, the unmolten phase of PA12 was observed in the neat polymer specimens and inevitable voids existed. The pores usually cause crack initiation leading to weak ductility of laser-sintered parts. Such a strengthening mechanism is helpful to overcome the limited ductility of laser-sintered parts and improve the strength and toughness.

Table 4.4. SLS parameters for PA12 and CNT/PA12 powders.

Process parameter	**Value**
Laser power *p* (W)	40
Scanning speed s (mm/s)	4000
Hatching spacing *h (mm)*	0.3
Bed temperature T_b (°C)	174
Chamber temperature T_c (°C)	130
Layer thickness *L* (μm)	100
Laser beam diameter *d* (mm)	0.42

Table 4.5. Comparison of the mechanical properties of laser sintered specimens PA12 and CNT/PA12 with a loading of 0.5wt% CNTs.

	Tensile modulus (MPa)	Tensile strength (MPa)	Elongation at break (%)	Toughness (J/mm^3)
PA12	1291 (± 12.1)	44 (± 1.3)	24 (± 0.8)	10.18 (± 0.9)
CNT/PA12	1301 (± 14.5)	68 (± 2.4)	33 (± 2.4)	18.86 (± 1.8)
Enhancement	0.8%	45.8%	37.5%	84.9%

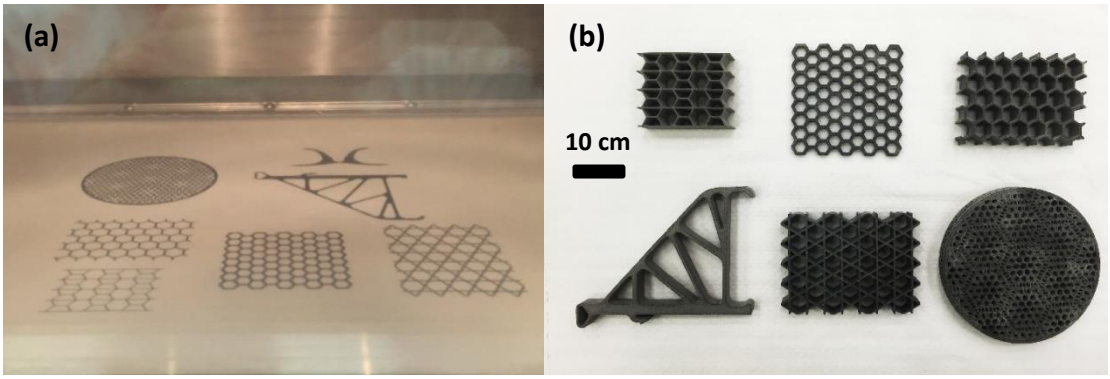

Figure 4.10. (a) The building platform of EOS P395 with the dimension of 34×34×60 cm); (b) Light-weight CNT/PA12 parts with complex geometries manufactured by SLS.

The optimized set of parameters (*p*: 25 W, *s*: 2500 mm/s, *h*: 0.2 mm and *L*: 0.1 mm) was successfully applied to print the 3D complex lightweight structures using

CNT/PA12 composites. These truss, honeycomb and kagome lattices, which are widely used lightweight engineering structures, are demonstrated in Fig. 4. 10.. The composite powder deposition and sintering are not barriers to the production of complex 3D structures in the full dimension of a machine building platform.

4.2.2 Thermoplastic polyurethane

In this work, a systematic evaluation was conducted to analyse TPU powders through measuring the powder flowability, powder size and distribution, and thermal transactions. The onset and offset of melting were effectively identified through rheological testing, as the TPU did not exhibit a critical melting point upon heating. Through implementing the energy gap between melting and decomposition to predict the effective energy input from laser, this thermal model could predict the proper ranges of the laser parameters, which were further applied for process optimization, rather than empirical optimization based on an iteration of trial and error builds.

4.2.2.1 TPU powder evaluation

In the pre-sintering steps, the powder evaluation usually includes the measurements of size distribution, flowability, endo- and exothermal and rheological properties of polymer powders as illustrated in Figs. 4.11 and 4.12. The size range determines the minimum layer thickness upon deposition, and the proper flowability of powders ensures a uniform deposition of each layer. It is observed that the irregular TPU powders were with a relatively wide size distribution from 60 to 110 μm (Fig. 4.11(a)).

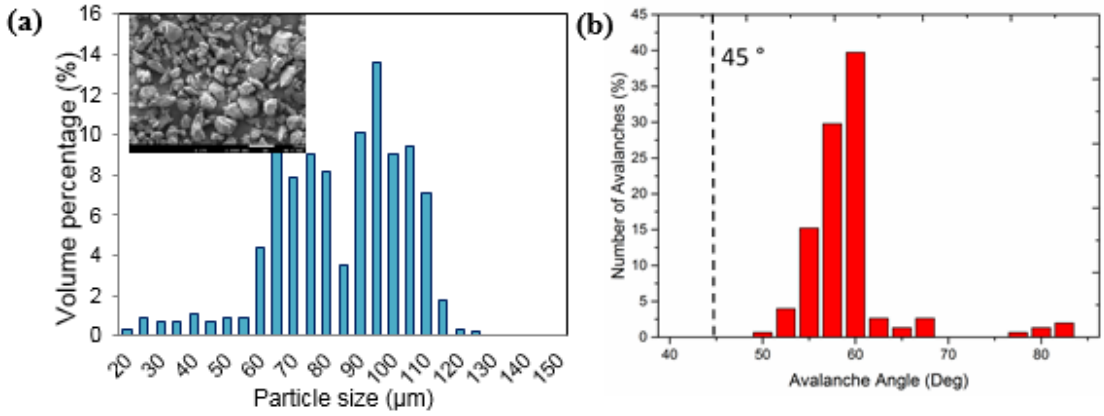

Figure 4.11. (a) Size distribution of the TPU powders; (b) avalanche angle graph indicating the required average angle to start and maintain the flow of the powders.

The avalanche angle of the TPU powders was much higher than 45°, below which the powders could flow properly to be deposited during the printing process. Such inferior flow behaviour is not preferable in the SLS process because it may adversely affect the layer-by-layer deposition. Fortunately, these irregular TPU powders could still be deposited uniformly in the EOS P395 system, even though their flowability was not comparable with that of semi-spherical polymer powders [4].

Compared with semi-crystalline polymers such as polyethylene and polyamides (PA 12 and PA 11), the duel-segment TPU are mainly consisting of the amorphous phase with no critical melting point. Additionally, the thermal behaviours of TPU powders have been analysed to determine the process parameters, as these critical transitions during the cycle of heat absorption and release are the essential indicators to predict the parameter ranges of laser sintering [4, 5, 90].

DSC is a standard approach to determine the glass transition temperature T_g, the melting point T_m and the recrystallization temperature T_r, which are significant for predicting the working temperature ranges of the powder bed and removal chamber.

Usually, polyurethanes are composed of the soft and stiff segments, and the T_g of TPU can be tailored by controlling the composition of each segment. TPU elastomers can be flexible at room temperature because the soft and amorphous phases are predominant. As illustrated in Fig. 4.12, the TPU powders exhibited two glass transitions of T_g' and T_g''. The soft segments had a low T_g' at - 4 °C and no critical melting point, while the hard segments showed a high T_g'' at 101 °C. However, the melting of the TPU powders occurred at the temperature ranging from 120 °C to 180 °C. Meanwhile, the recrystallization peak was located at 72.74 °C and the entire recrystallization ranged from 78 °C to 62 °C. These observations indicated that the soft segments were amorphous structures and the hard segments were semi-crystalline structures.

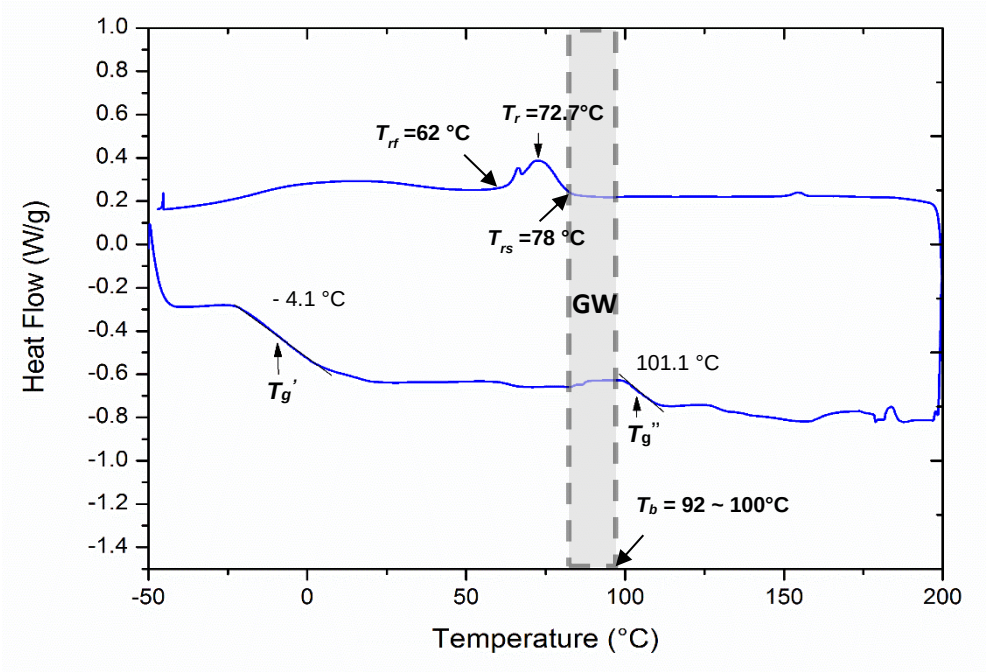

Figure 4.12. The endo- and exothermal heat flow of the TPU powders was characterized upon heating and cooling from –50 °C to 200 °C at the rate of 10 °C/min. Two glass transition temperature points and the onset and offset of recrystallization temperature were indicated. The glass window (GW) for bed temperature control was identified.

The semi-crystallized hard segments experience dramatic phase change and volume

shrinkage during recrystallization [62]. Thus, the removal chamber temperature needs to be set just below the offset of recrystallization to secure a stable arrangement of polymer segments after solidification and minimize the dimensional shrinkage of printed parts.

The sintering window is defined as the temperature difference between the initial crystallization and melting temperatures which can be used to evaluate the SLS processability of polymers. However, the melting temperature of TPU was not obvious, and thus the rheological testing was employed to investigate the melting behaviour of the TPU powders through measuring the storage and loss moduli over the melting range. Polymer behaves in a solid manner within the temperature range, where the storage modulus is higher than the loss modulus. In contrast, the loss modulus is higher than the storage modulus at the liquid state. Therefore, as illustrated in Fig. 4.13, the melting transition of TPU occurred at 150 °C, and the onset and offset of melting were around 131 °C and 171 °C, respectively.

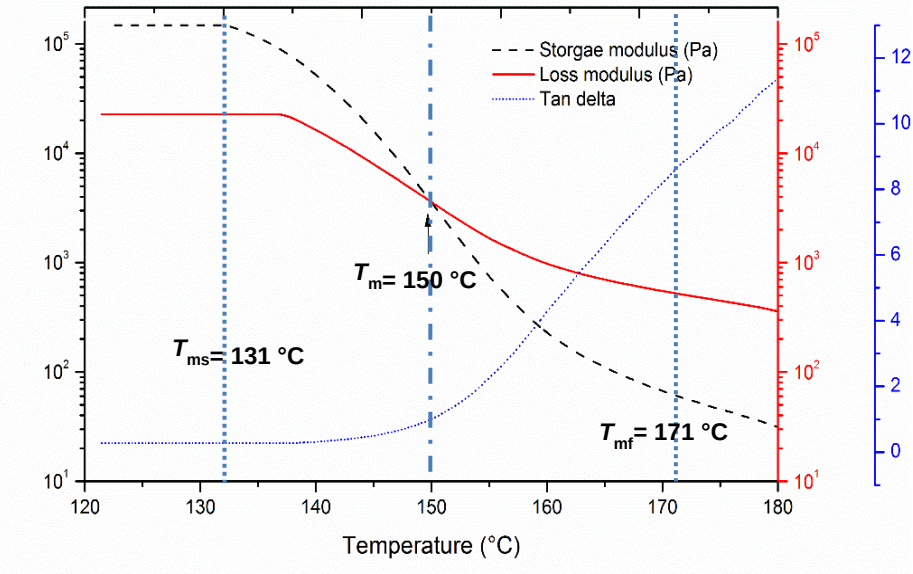

Figure 4.13. Rheological testing diagram of the TPU powders from – 50 °C to 200 °C at the cooling and heating rate of 10 °C/min under the angular frequency of 1 rad/s.

Additionally, Fig. 4.14 shows that the decomposition of TPU started from 242 °C and two stages of decomposition were observed due to the presence of dual-segments. Thus, the SSR was identified via the range between the offset of melting and the onset of decomposition, as given in Fig. 4.14 (b). This process stable window between 171°C and 242°C was relatively narrow, compared with that of PA12 from 198 °C to 360 °C [4].The energy input from the laser needed to be precisely controlled to maintain the process temperature within the SSR.

Fig. 4.15 shows that the melt viscosity of TPU exhibited a plateau at the low frequency range (< 1 rad/s) but dropped dramatically when the angular frequency increased above 1 rad/s at an isothermal condition around 180 °C. The zero-shear melt viscosity had a strong impact on the state of coalescence, as revealed by the Frenkel's relation (Eq. 4.13). This function reveals that the melt viscosity is a critical factor to

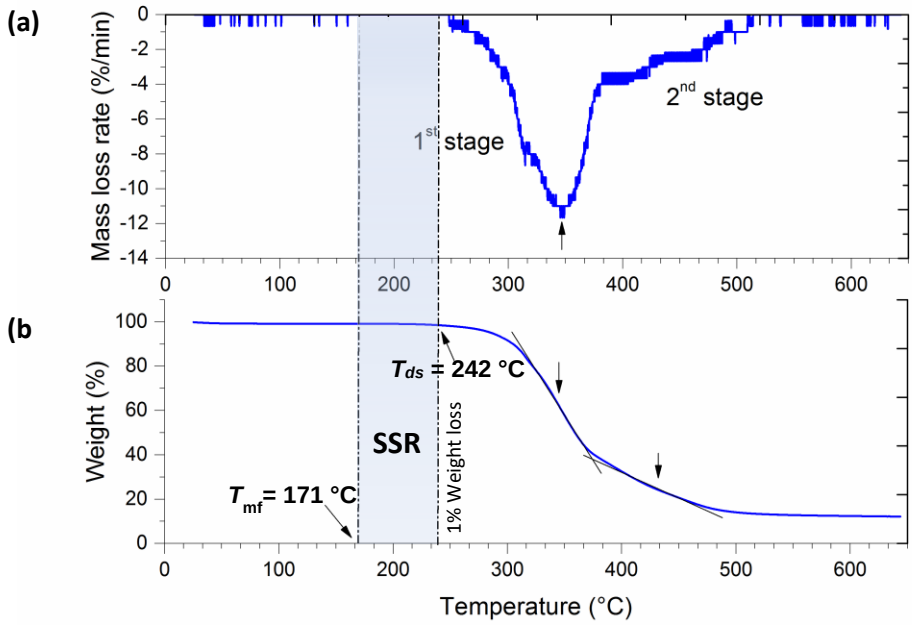

Figure 4.14. TGA plots of (a) the mass loss rate and (b) the weight ratio of TPU decomposition started from 25 °C to 600 °C. The SSR was indicated between the offset of melting and the onset of decomposition.

judge the sinterability of powders as compared with the surface tension, which is weakly affected by temperature change. It also indicates that the increase of fusion time helpsto overcome the insufficient coalescence caused by the undesirable morphology of the powders and their relatively high zero-shear viscosity [92, 174]. At a low angular frequency range (< 1 rad/s), TPU has the melt viscosity of 1.03×10^3 Pa.s, which is close to that of PA12 (1.4×10^3 Pa.s) [4]. Thus, the melt viscosity of TPU should not limit the full fusion of powders thermodynamically.

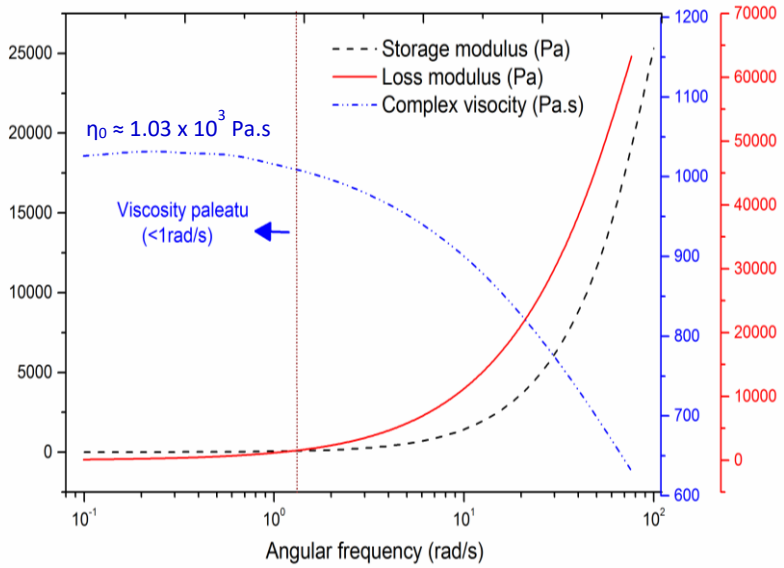

Figure 4.15. Storage and loss moduli of the fully melted TPU and its melt viscosity over the angular frequency range from 0.1 to 100 rad/s at the temperature of 180 °C.

Additionally, the modulated specific heat C_p^* of TPU over the temperature range from the powder phase to melting metaphase to liquid phase was characterized and fitted, as shown in Fig. 4.16. The values of C_p^*, were further applied to evaluate the energy absorptions at the stages of melting and decomposition using Eqs. (4.1) and (4.2). The material parameters that determine the range of process parameters are summarized in Table 4.6. The adverse effects such as unfavourable powder morphology and size

distribution, narrow SSR and weak flowability need to be taken into consideration when the process parameters are monitored for optimization

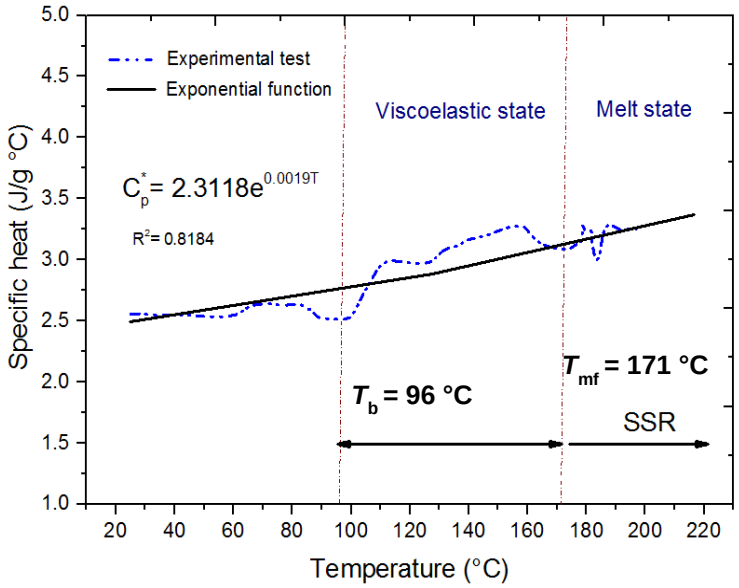

Figure 4.16. The plot of temperature-dependent specific heat of the TPU powders from the powder phase to melting metaphase to liquid phase.

Table 4.6. Material properties of the TPU powders

Material properties	**Value**
Specific heat C_p^* (J/g °C)	$2.31e^{0.0019T}$
Melting temperature T_m (°C)	150
Recrystallization peak T_r (°C)	78
Enthalpy of recrystallization ΔH_r (J/g)	46.11
Modified density ρ^* (g/cm^3)	1.2
Packing fraction ϕ	0.48
Onset melting temperature T_{ms} (°C)	131
Offset melting temperature T_{mf} (°C)	171
Onset recrystallization temperature T_{rs} (°C)	78
Offset recrystallization temperature T_{rf} (°C)	62
Glass window width (GW) (°C)	17.99
Stable sintering region (SSR) (°C)	171 ~ 242
Melt viscosity η at 0.1 rad/s (Pa·s)	1.03×10^3
Light absorptivity α at 10.6 μm (%)	18

Note: T is the instant temperature of the polymer powders or melts during the sintering process

4.2.2.2 Process optimization

According to material properties listed in Table 4.6, the cooling chamber temperature was set at 60 °C just below the recrystallization range as suggested. The powder bed temperature was 92 °C to 100 °C just below the T_g'' as observed in a powder deposition process. This was because the polymer powders tended to agglomerate with a caking effect once the bed temperature increased to be above 103 °C. Table 4.7 lists the results obtained through the evaluation of the energies required for melting and decomposition.

The critical tensile properties such as tensile stress and elongation at break of the laser-sintered specimens are shown in Fig. 4.17, corresponding to the different combinations of process parameters. The energy densities of each set of parameters were labelled on the diagrams. According to the predicted effective range of E_{vol}, the input laser energy was sufficient to fully melt the powers when it was above the level of 0.4 J/mm^3, and the obtained elongation strain approaching 500% demonstrated the qualification of being used to construct3D soft metamaterials to sustain large strains.

Table 4.7. Evaluation of E_{mm}, E_{mv}, E_{dm} and E_{dv} for the TPU powders and prediction for the effective range of E_{vol} corresponding to SSR of TPU.

Energy parameter	**Value**
Mass energy for melt E_{mm} (J/g)	119.5
Volume energy for melt E_{mv} (J/mm^3)	0.068
Mass energy before decomposition E_{dm} (J/g)	192.3
Volume energy before decomposition E_{dv} (J/mm^3)	0.231
Energy input range of laser E_{vol} (J/mm^3)	0.378 – 1.283

Table 4.8. Laser sintering parameters in the EOS P395 system.

Process parameter	Value
Laser power p (W)	8, 10, 12,14
Scanning speed s (mm/s)	3000, 4000
Hatching spacing h (mm)	0.1
Bed temperature T_b (°C)	96
Chamber temperature T_c (°C)	60
Layer thickness h (μm)	100

Usually, the tensile strength and elongation at break decrease as the scanning speed increases or the laser power decreases. The scanning speed determines the duration of exposure time for powders to be sintered, and the laser power indicates the thermal energy input onto the powder bed in unit time. The tensile strength considerably decreases when the scanning speed increases from 3000 mm/s to 4000 mm/s, and thus a lower scanning speed is preferable to controlling the coalescence among powders. The SLS process only undergoes the internal driving force of melting flow without the external force for the coalescence.

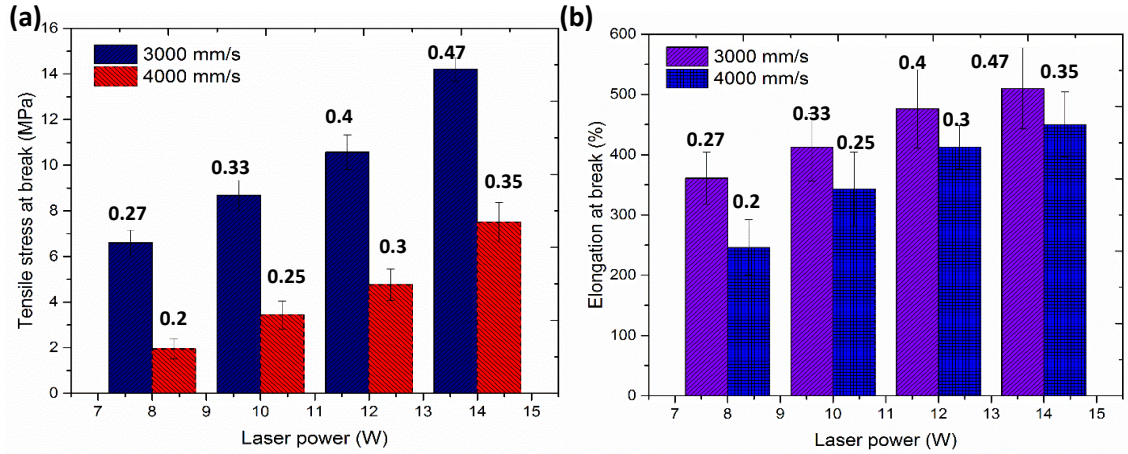

Figure 4.17. Evaluations of the SLS specimens fabricated using different sets of process parameters: (a) the tensile stress at break and (b) the elongation at break. The volumetric energy densities of different combinations are indicated in the unit of J/mm^3.

In Figs. 4.18 (a)-(c), the SEM images show that the gases trapped among the interspace of powders were difficult to remove. The sintered parts show that the powders could not fuse fully in the inter-plane (X-Y plane) and out-plane (Z axis) direction when the input laser energy was below 4 J/mm^3. However, in the out-plane direction, the interlayer voids were still present even though the laser power increased to 0.4 J/mm^3. This was mainly due to the poor heat penetration of the laser, as the TPU powders were closely packed and weakly thermal conductive. If the exposure time to laser is extremely short at a fast scanning speed, the instant coalescence among powders is limited by the fusion kinetics as explained in Frenkel's theory of sintering [4, 174]. Therefore, the scanning speed could even be further reduced from 3000 mm/s and correspondingly the laser power needed to increase slightly to secure sufficient thermal energy for melting.

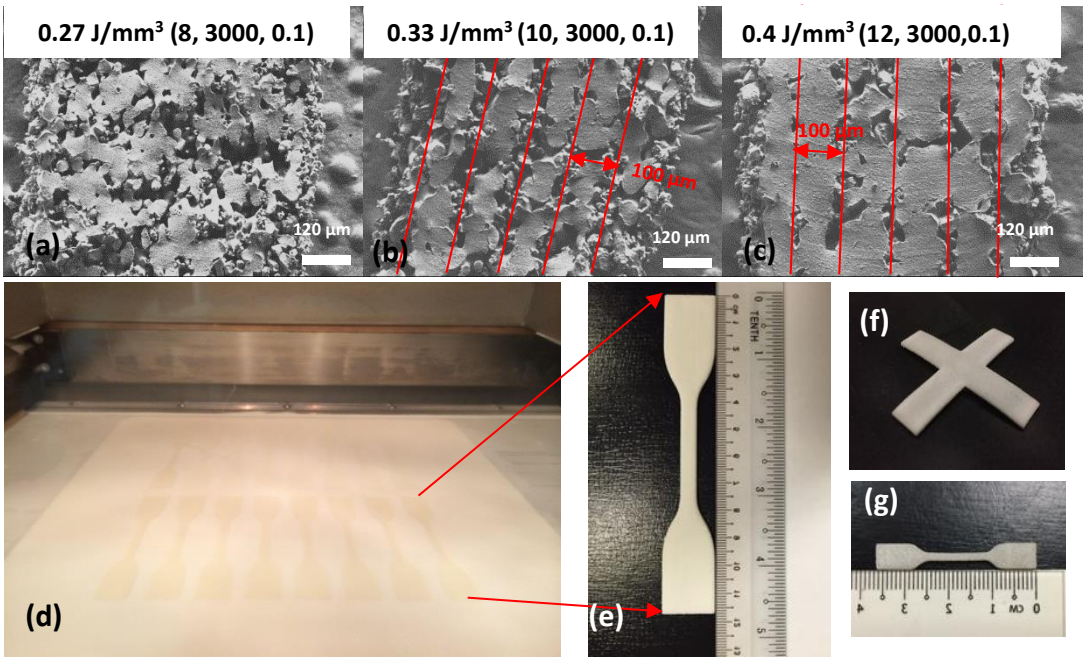

Figure 4.18. The cross-sections of the TPU specimens sintered using various laser powers: (a) 8 W, (b) 10 W and (c) 12 W (the bed temperature: 96 °C, scanning speed: 3000 mm/s and hatching space: 0.1 mm); (d) the building bed of laser sintering within the heating chamber; (e) the dog-bone tensile bar (ASTM D638 Type IV) for tensile testing; (f) and (g) the printed samples for warping and elongation testing.

On the other hand, it was observed that the powders started to decompose with smoky dusts once the laser powder increased above 15 W, even though the input laser energy per volume was still lower than the upper limit of 1.283 J/mm^3. As the laser heat distribution followed a Gaussian profile, the localized temperature upon the powder bed was higher than the onset of decomposition 242 °C. Therefore, reducing the scanning speed is an effective way to improve the fusion of powders and print soft and flexible metamaterials.

The efficient scanning pattern to produce complex geometries includes the selection of the hatching space, scanning contour and edge. The basic scanning methods for the EOS P395 system are shown in Fig. 4.19. For a precise printing approach, double contours are effectively chosen to smooth surface of printed products, double edges are selected to improve the accuracy of shape features, and the proper hatching space is helpful to avoid overheating or decomposition of polymeric powders.

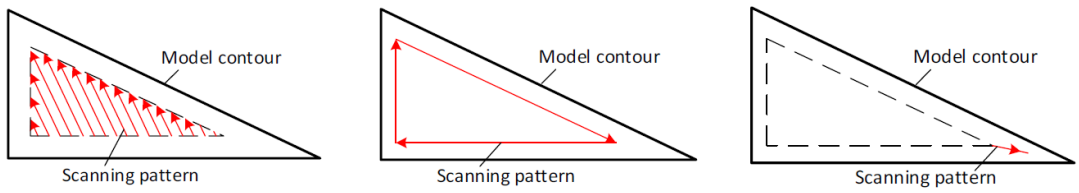

Figure 4.19. Basic scanning methods for in the EOS P395 machine.

A few sets of optimal process parameters were obtained for printing 3D complex geometries, as listed in Table 4.9. These sets can minimize the degradation of polymers under heating and maintain the acceptable mechanical strength and outstanding ductility and flexibility of TPU. For instance, they were employed to produce the auxetic lattice

structures for energy dissipation purpose, as discussed later in Chapter 6.

Table 4.9. The optimized process parameters for TPU to produce products of complex geometries.

Process parameter		**Value**
Laser power p (W)	Hatching	12
	Contour 1, Contour 2	14,14
	Edge 1, Edge 2	14,14
Scanning speed s (mm/s)	Hatching	2000
	Contour 1, Contour 2	3000
	Edge 1, Edge 2	3000
Hatching spacing h (mm)		0.1
Bed temperature T_b (°C)		96
Chamber temperature T_c (°C)		60
Layer thickness L (μm)		100

Chapter 5 Electrical and thermal properties of laser-sintered nanocomposite products

The aerospace industry is a typical industrial sector that would benefit from AM techniques, and nowadays has a significant share of AM parts (16.6 %) in the market. However, this industry imposes very stringent requirements on the material properties of aerospace components, especially in terms of lightweight, continuous operation temperature, electrical conductivity and thermal stability as well as mechanical properties [181]. So far, intensive research works have been conducted to develop high-performance polymers or polymeric composites which could be processed in the SLS system to produce electrical anti-static, robust and lightweight components.

Carbon fibers-reinforced PA12/epoxy [36] and PEEK [182] have been prepared by the SLS process, and exhibited outstanding mechanical strength and Young's modulus. The carbon black/PA12 composite has been sintered by laser and exhibited relatively high electrical conductivity in the range of 10^{-6} to 10^{-4} S/cm with the addition of 1-4 wt% [101, 124]. However, several drawbacks are present in currently available composite materials obtained by adding carbon short fibers or carbon black. For instance, A post-infiltration process was required to overcome the weakness of brittle and porous carbon fiber/PA12 composite [36]. Besides, it is extremely challenging to achieve anti-static and anti-EMI polymer composites with the desirable mechanical strength and toughness using polymer-based AM techniques. In this thesis research, , carbon nanomaterials, especially MWCNTs, are proposed as reinforcements in laser-sinterable polymers to simultaneously improve their mechanical strength and

toughness as well as electrical and thermal performances..

5.1 Composite fabrication

The composite architectures in this work were manufactured by the s-CNT reinforced polymeric composite powders as illustrated in Fig. 5.2. The powders were composed of two parts: the polymeric core such as PA12 and PU and the outer layer of the s-CNT network embedded onto the core. Such a configuration is critical for fully utilizing CNTs to enhance the laser absorption of powders [3] and form a 3D interconnected CNT network among sintered composite parts [4]. The surface layer of carbon nanomaterials usually behaves as heat absorbers to enhance light energy absorption and subsequently facilitate the powder sintering process. Meanwhile, these CNT fibers can be distributed among powder boundaries and formed strong networking within the polymer matrices. For instance, the CNT network could help to reinforce the mechanical properties, electrical and thermal conductivities at a small addition of 0.1 to 1 wt% loading of CNTs [53].

Fig. 5.1 illustrates the building chamber and laser scanning system of the SLS process. The layer of powders was deposited onto the X-Y plane and then sintered by the laser heat to form solid bulk composites. The structure was built along the Z-axial through the layer-by-layer bottom-up method. Thus, the product may exhibit anisotropic properties along the X-Y plane and X-Z plane. In this work, a layer of MWCNTs were coated onto the powder surface, and such a powder configuration could induce a unique distribution of reinforcements within a polymer matrix as shown in Fig. 5.1. The investigation of the process-structure-property relationship for laser

sintered composites is critical for developing novel composite materials with proper electrical and thermal properties.

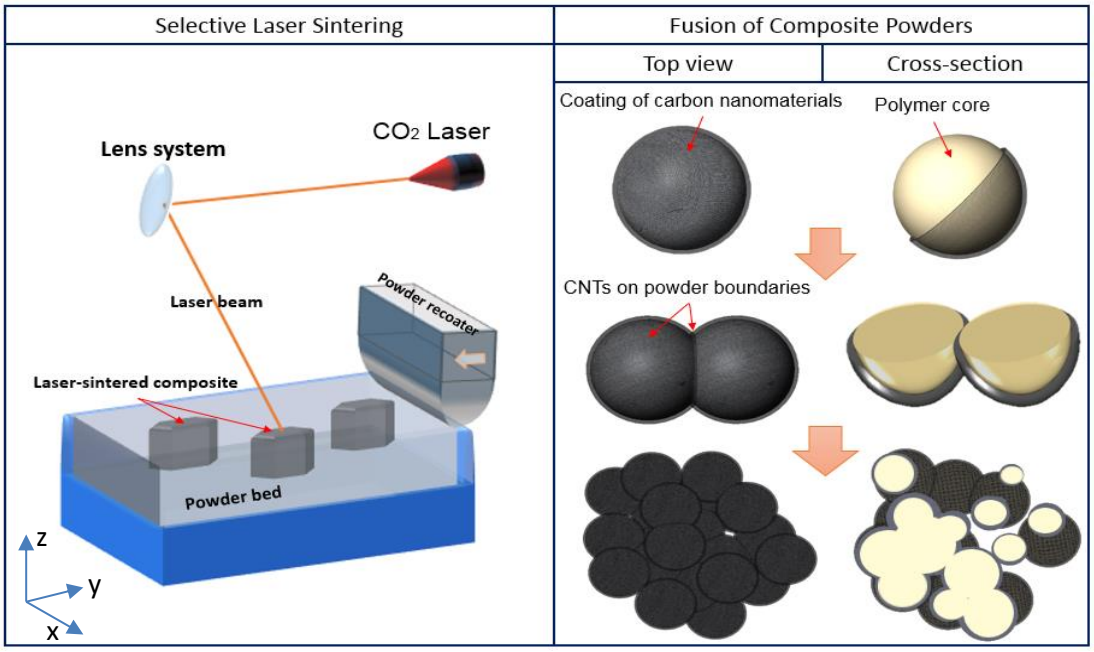

Figure 5.1. Illustration of the system of selective laser sintering and the fusion of composite powders from the top view and cross-section.

To achieve the positive performances, the powder preparation stage needed to overcome the nanomaterial agglomeration and weak interfacial interactions between the MWCNTs and polymer. It was proposed to employ a steroid-based surfactant (sodium cholate) as surface functionalization to facilitate the assembly of thin-layer CNTs on the powder surface to enhance the affinities between the polymers and MWCNTs. Figs. 5.2 (a) and (b) show that a uniform layer of s-CNTs covered the surface of PA12 and PU powder surface and these CNTs were entangled with each other at the loading of 1 wt%. FTIR spectroscopy was used to investigate the intra/intermolecular bonds for polymer chains and the interfacial bonds between polymer chains and surfactants. It was observed that after s-CNTs were coated onto the

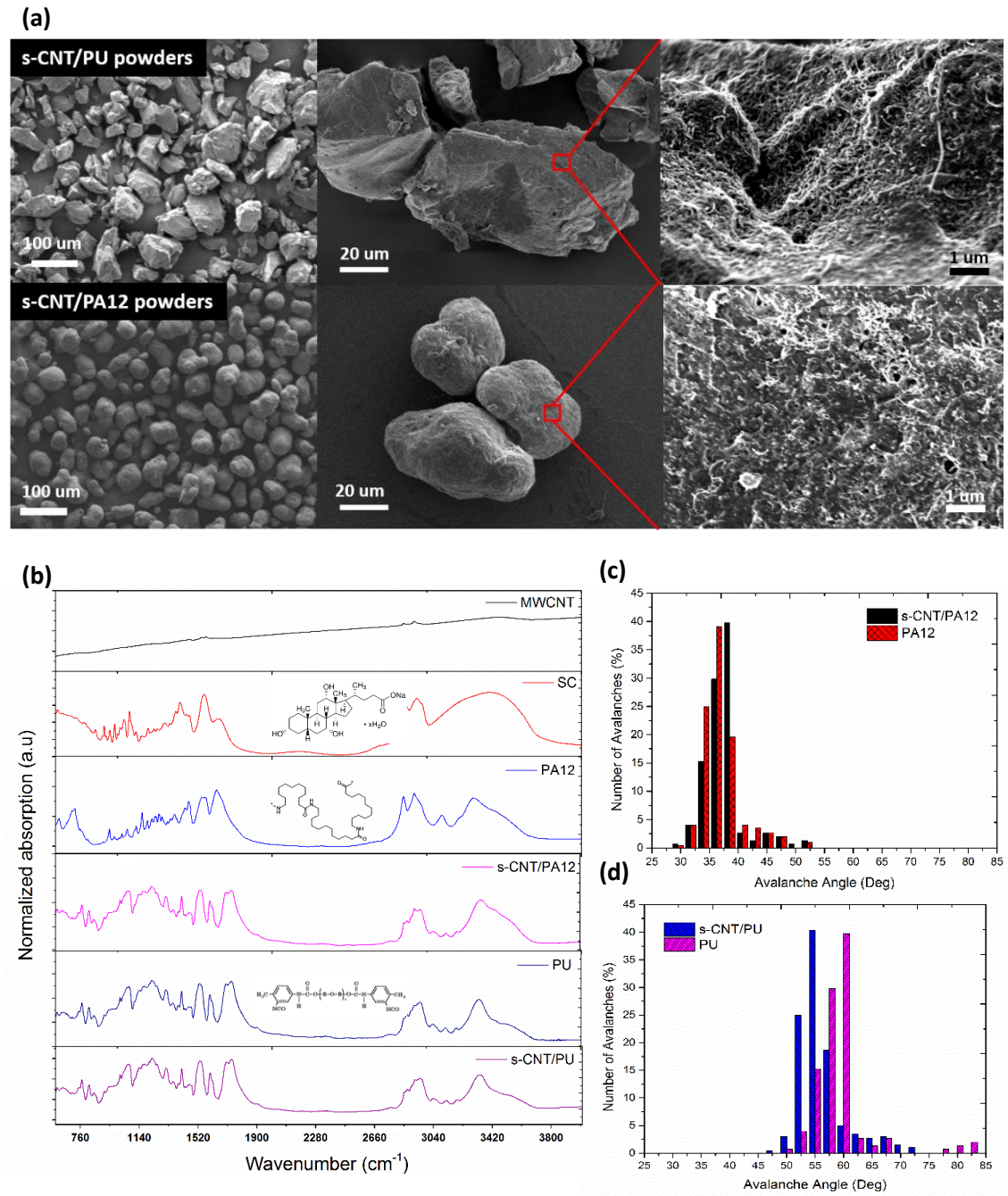

Figure 5.2. (a) SEM micrographs of s-CNT/PU, s-CNT/PA12 powders and the surface morphologies of the CNT coating. (b) FT-IR scattering spectra of MWCNTs, sodium cholate hydrate (SC), PU, PA12, s-CNT/PA12 and s-CNT/PU powders. The avalanche angle distribution of (c) PA12 and s-CNT/PA12 and (d) PU and s-CNT/PU powders.

surface of the powders, the absorption peak of PA12 at 3094 cm^{-1} was eliminated. This peak indicated the fermi-resonance of N-H stretching with an overtone amide II, and

the elimination of the peak might be due to the fact that the surface NH_2- groups reacted with COOH- groups on the cholate molecules at an elevated temperature. Thus, the sodium cholate molecules functioned as an interfacial layer to bond the polymer and pristine MWCNTs to facilitate the assembly of MWCNTs on the surface of polymeric powders. The PU and s-CNT/PU spectra demonstrated no significant difference and so did the PA12 and s-CNT/PA12 spectra. The results of spectra indicated that the amount of sodium cholate molecules absorbed onto composite powders was much lower than the original addition of this surfactant. This was because the saturated portion of surfactant molecules was removed with the waste water. Usually, the saturated quantity of surfactants was used for this composite powder preparation process to ensure the uniform assembly of MWCNTs onto the surface of polymers.

Furthermore, the proposed method for composite powder preparation enabled the retention of the original size and size distribution of polymer powders and improved the flowability. The avalanche angle is the critical indicator to justify the flowability of polymer powders for the use of sintering materials. As shown in Figs. 5.2 (c) and (d), the avalanche angles of PA12 and s-CNT/PA12 powders were distributed within the range of 30° to 50°, a preferable range of flowability for the SLS system. The avalanche angle of the PU powders was around 55° to 65°, which was much higher than that of the s-CNT/PU powders. It indicated that the thin layer of s-CNTs coating might function as an anti-static layer to avoid the static clusters of polymer powders. Therefore, the composite powders could be easily deposited uniformly during the laser sintering process. The sets of process parameters regarding PA12, PU and their composite powders are summarized in Table 5.1.

Table 5.1. The laser sintering parameters for PA12, PU, s-CNT/PA12 and s-CNT/PU powders.

Process parameter	**PA12**	**s-CNT/PA12**	**PU**	**s-CNT/PU**
Laser power p (W)	25	20, 25	12	8, 10, 12
Scanning speed s (mm/s)	3000	3000	3000	3000
Hatching spacing h (mm)	0.2	0.2, 0.3	0.1	0.1
Bed temperature T_b (°C)	174	174	96	108
Chamber temperature T_c (°C)	130	130	60	72
Layer thickness h (μm)	100	100	100	100

Fig. 5.3 demonstrates the intake manifold and inlet manifold components in the car engine, the auxetic lattices and the cellular lattices fabricated by the laser sintering of s-CNT/PA12 (0.5 wt%). The carbon/polymer composites possess unique advantages of lightweight, outstanding specific strength and impact toughness. Thus, they are proposed as alternative materials to replace aluminum alloys and steels and applied to fabricate the mechanically inferior components in automotive and aerospace industries. Meanwhile, the powder-based 3D printing technique via the SLS process offers a facile and economic method to manufacture engineering parts with complex geometries, avoiding the development of moulding and tooling equipment.

To meet the industrial requirements in thermal, electrical and mechanical aspects, the functionalized CNTs were introduced to prepare composite powders with unique core-shell configuration as shown in Fig. 5.2. It was observed that the polymeric composites with a small addition of s-CNTs exhibited significant improvements in mechanical toughness and strengthen as well as thermal stability.

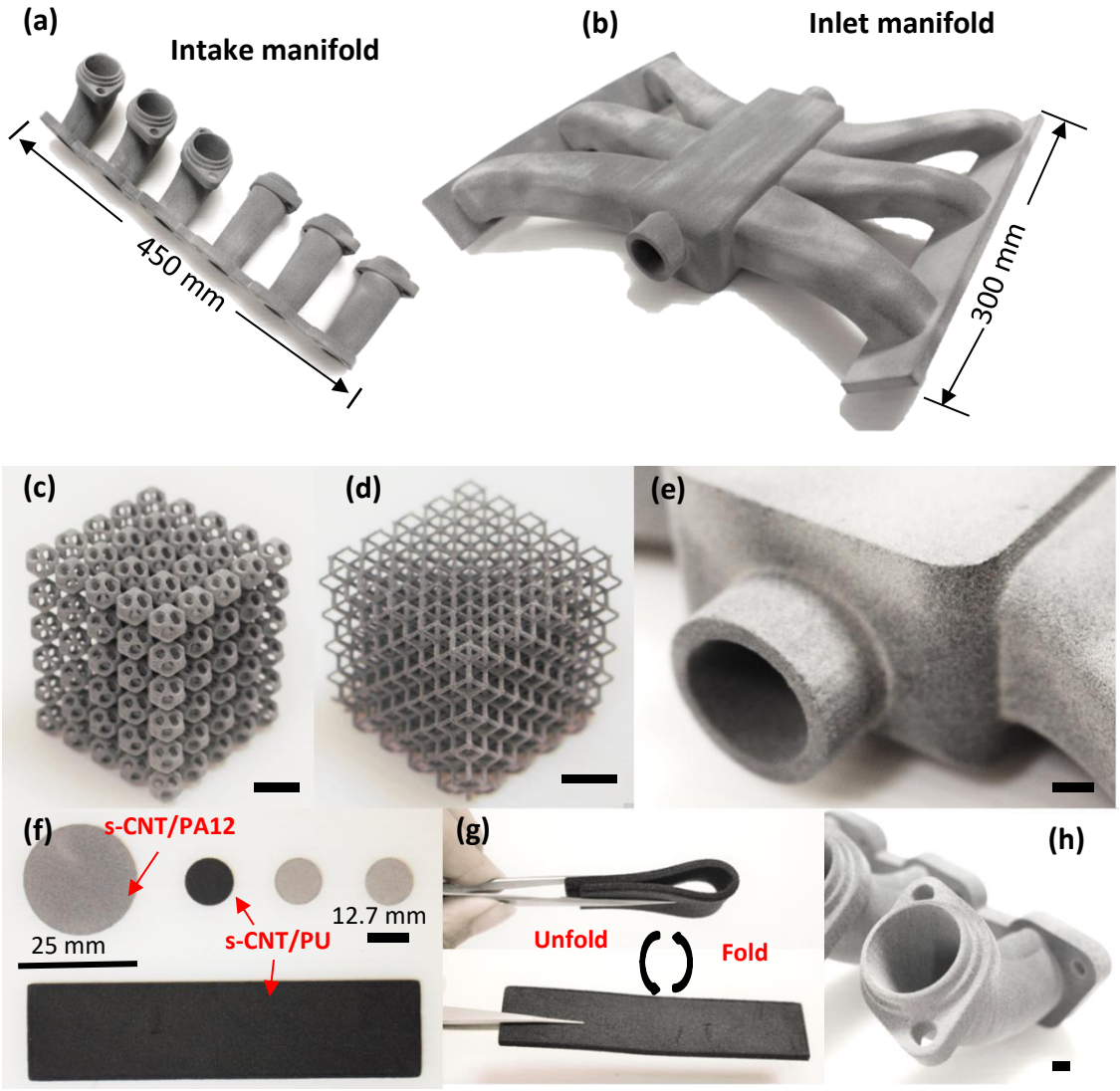

Figure 5.3. Engineering parts for automotive applications: (a) intake manifold and (b) inlet manifold manufactured by laser-sintering the s-CNT/PA12 composite; lightweight composite structures: (c) auxetic lattice and (d) cellular lattice; (e) and (h) surface finishing and features of the s-CNT/PA12 composite; (f) the laser-sintered s-CNT/PA12 and s-CNT/PU samples for electrical and thermal measurements; (g) the demonstration of flexible and foldable laser-sintered s-CNT/PU composites.

As illustrated in Fig. 5.3, the dimensional accuracy of the sintered parts was well controllable. The engineering parts were configured precisely by the laser beam and their features consisted of all the geometrical information provided by the computer-added design model.

Despite the enhancements in the mechanical aspect, this research was focused on improving the electrical and thermal performances of laser-sintered composites and investigating the underlying relationship of the process-structure-properties. As the layer of s-CNT coating was designed to embed into polymer matrix and form a network in the polymeric composite after laser sintering, the interconnected CNTs were capable of conducting electron or phonon to improve the electrical and thermal conductivities. However, the distribution and microstructure of the composites are strongly dependent on the manufacturing process and original feeding powders.

5.2 Electrical conductivity

The direct current (DC) conductivity of composites are highly concentration-dependent as shown in Fig. 5.4 (a). The DC conductivity of the laser-sintered composites significantly increased by a few orders of magnitude (over 10^{-5} S/cm) when the filler content approached 0.5 wt%. Additionally, the laser-sintered composites exhibited much higher electrical conductivity than the hot-compressed composites at the identical weight ratio. Meanwhile, the s-CNT/PU composites possessed great enhancement in the DC conductivity as compared with the s-CNT/PA12 composites. The DC electrical measurements were conducted on the cylindrical samples in parallel with the X-Y and X-Z planes. Fig. 5.4 (b) shows the strong improvement of electrical conductivity in the PA12 and PU composites along two building directions after the addition of s-CNTs.

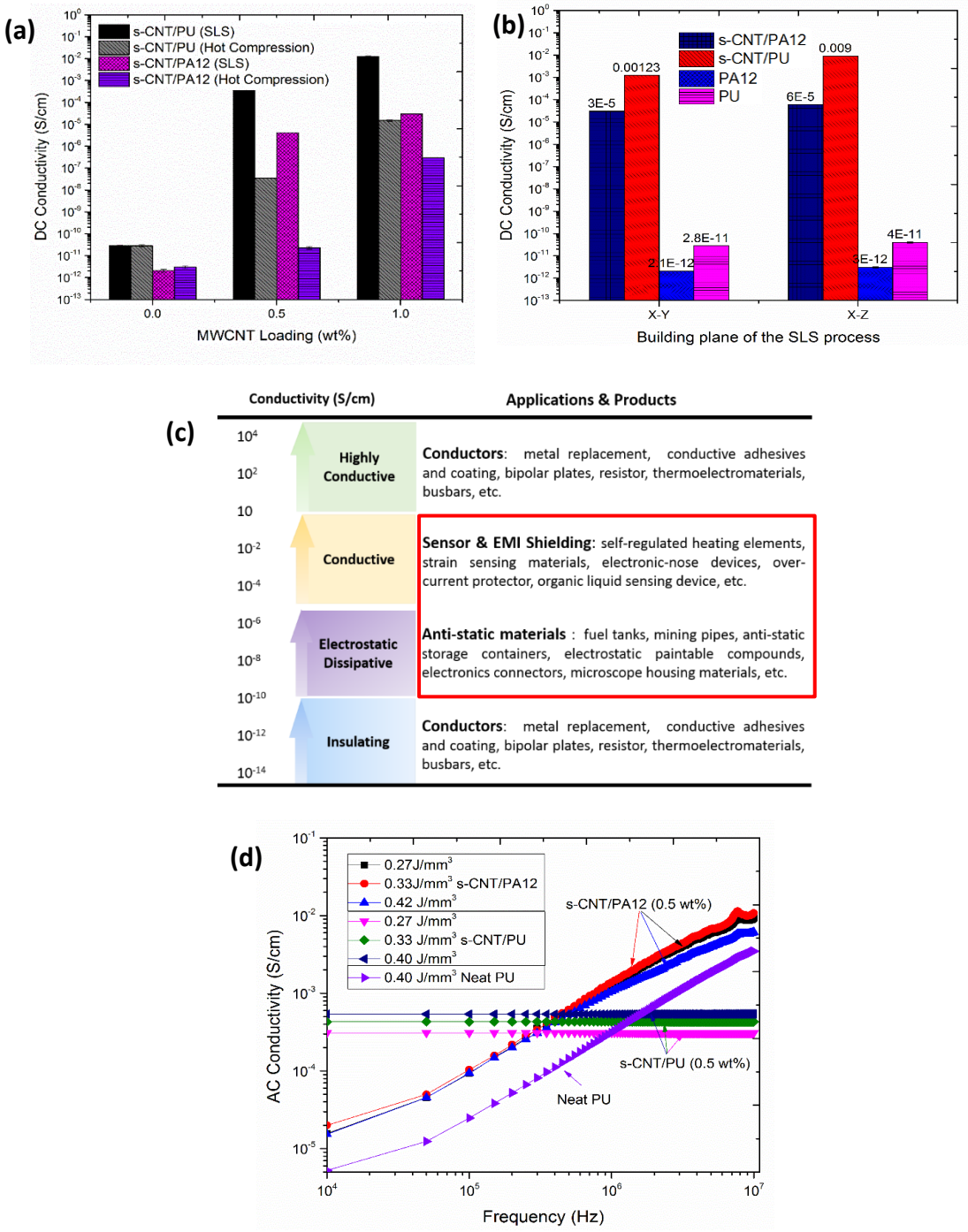

Figure 5.4. (a) Comparison of the DC conductivities of the laser-sintered composite and hot-compressed composite; (b) influence of the building directions (X-Y and X-Z plane) on the DC conductivities of PA12, PU and their composites; (c) the AC conductivities of the s-CNTs-reinforced composite produced with different laser energy inputs; (d) exemplary applications of materials from the insulating to conductive range.

These composite materials approached the electrostatic dissipative (10^{-10}~10^{-6} S/cm) and conductive (10^{-6}~ 10^{0} S/cm) ranges, and thus could be potentially employed to fabricate anti-static components, sensors and EMI shielding elements as illustrated in Fig. 5.4 (c).

The alternating current (AC) conductivity tests were conducted on a series of laser sintered s-CNT/PA12 and s-CNT/PU (0.5 wt%) samples, which were prepared by increasing the laser energy from 0.27 to 0.42 J/mm^3. This range of energy inputs was set within the sintering stable range of each material [4]. Fig. 5.4 (d) shows that the electrical conductivity of s-CNT/PA12 (0.5 wt%) increased from 10^{-5} to 10^{-2} S/cm as a function of the frequency ranging from 10^4 to 10^7 Hz. In contrast, the laser-sintered s-CNT/PU (0.5 wt%) exhibited a frequency-independent conductivity (above10^{-4} S/cm) up to 10^{-7} Hz. This indicated a transition from an insulating to conductive regime after the addition of s-CNTs at 0.5 wt% for the PU composites. However, with an identical loading of fillers, the s-CNT/PA12 could not achieve fully conductive performance. Additionally, once the laser energy input was sufficient to melt the polymers, such an energy input was a minor factor influencing the conductivity of the composites as compared with the loading ratio of the s-CNT addition.

The electrical conductivity of s-CNT/PA12 and s-CNT/PU dramatically increased by several orders of magnitude when the initially conducting channels were formed at a small loading range of s-CNTs from 0.5 to 1 wt%. Such observation indicated that the laser-sintered polymeric composites exhibited ultralow percolation behaviors, which was mainly due to the formation of the networks of CNTs among the powder boundaries to provide conductive paths for free electrons. However, the PU and PA12

showed different percolation thresholds after they were processed by laser sintering. To understand the underlying mechanism of electrical enhancement for the laser-sintered composites, the process-structure-properties relationship needed to be further investigated.

5.2.1 Microstructure

The microstructures of laser-sintered s-CNT/PA12 composites were investigated by optical microscopy and TEM, as the s-CNT/PA12 composites were a type of hard materials which could be polished and sliced precisely for advanced characterization. Instead, the soft s-CNT/PU composites were not able to be polished, and thus the SEM and Micro-CT (computed tomography) were employed to investigate their internal microstructures.

In Figs. 5.5 (a) and (b), within the X-Y building plane, the cross-section of s-CNT/PA12 shows that a layer of s-CNT coating remained at the powder boundaries and formed interconnected networks within the polymer matrix after laser sintering. The composite powders were fully melted and formed many menisci, which were condensed stacking together, as observed from the Y-Z plane (Fig. 5.5 (d)). The secondary phase of the s-CNTs was distributed among the boundaries of these menisci as well. The TEM images demonstrate the s-CNTs morphologies at the boundary region of the powders (Figs. 5 (c) and (f)). It was observed that the s-CNTs were entangled with each other and the interfacial medium were present at the CNT-CNT interfaces.

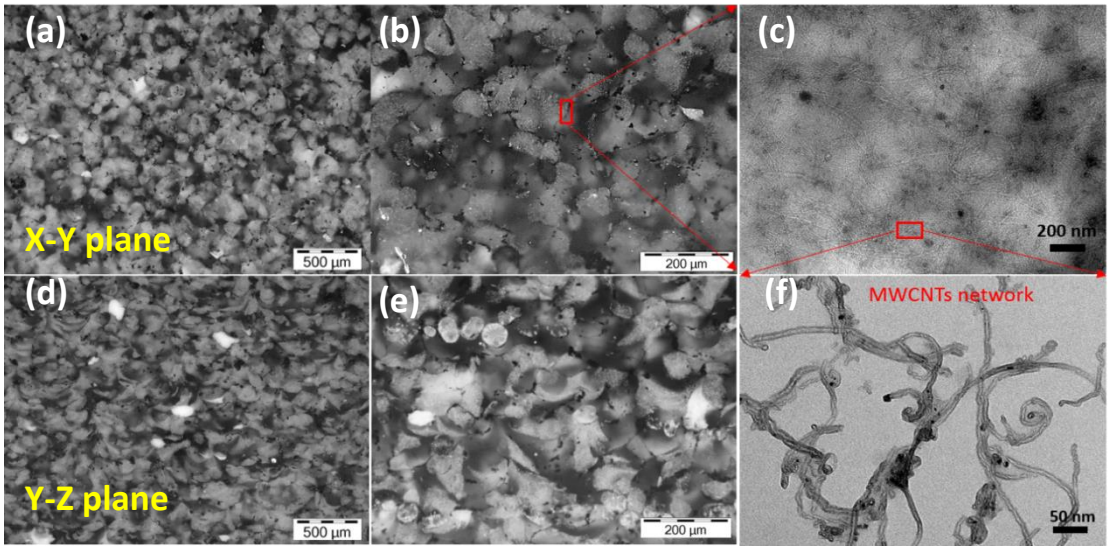

Figure 5.5. Morphology of s-CNT/PA12 with 0.5 wt% addition: (a-b) and (d-e) the optical images of the polished cross-section of s-CNT/PA12 in the X-Y and Y-Z building plane, respectively; (c) and (f) the TEM images of MWCNT networks around the powder boundaries in different magnifications.

In Fig. 5.6, the SEM images of s-CNT/PU composites show the layer-by-layer and segregated microstructures in the Y-Z and X-Y cross-sections, respectively. Additionally, large voids were present among the interlayer region, and the layer of s-CNT coating was mainly located at the surface of the polymer matrix and formed good connections.

Micro-CT as a non-destructive method was employed to investigate the spatial configurations and define the internal structures of the polymer matrix, pores, and filler distribution. The variation of density within a composite structure exhibits different absorption properties of X-ray and its image contrast can be used to identify the distribution of the polymer matrix and pores in 3D space. Additionally, the distribution of pore size and phase content within a selected volume can be quantitatively evaluated through Micro-CT scanning and reconstruction of the 3D objects.

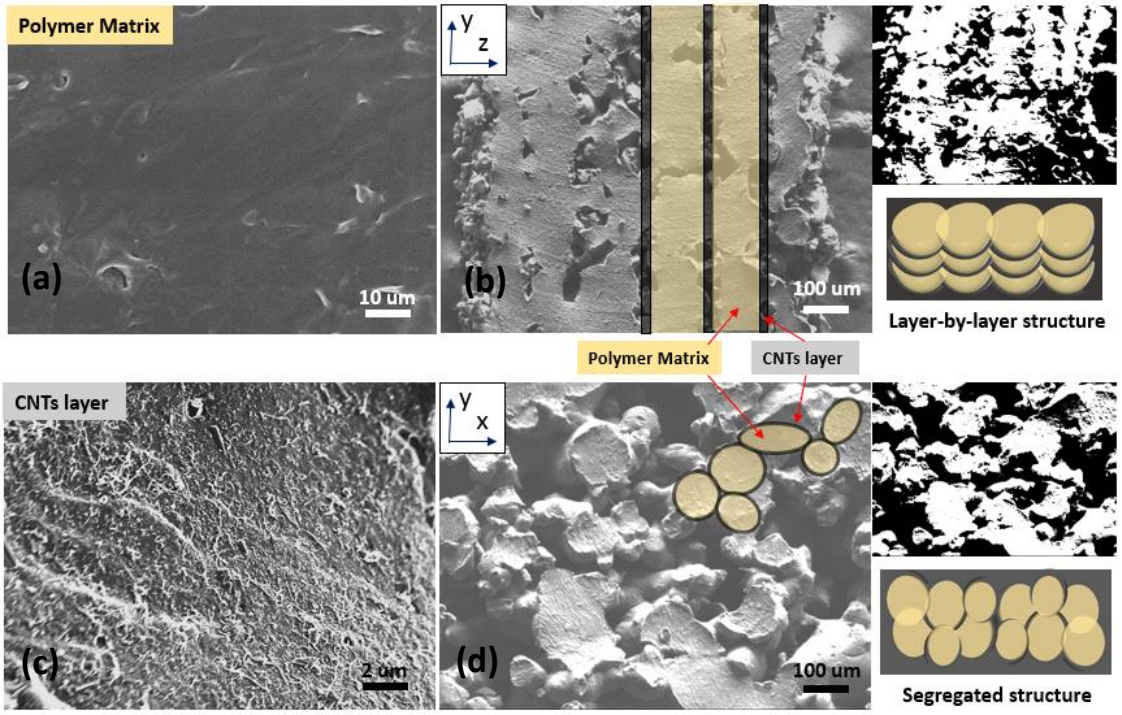

Figure 5.6. SEM micrographs of the laser-sintered s-CNT/PU (1 wt%) composite on the cross-sections of the X-Y and X-Z planes: (a) the PU matrix and (b) the layer-by-layer structures along the building direction (Z-axial); (c) the s-CNT network covering the surface of 3D connected-porous polymer structures and (d) the segregated structures observed on the X-Y building plane**.**

5.2.2 Porosity

Fig. 5.7 illustrates the distribution and volume percentage of the polymer matrix and pores in a representative s-CNT/PU sample, and the variation of pores is coded with colour spectrum. It shows that the pores took the volume percentage up to 21.89% and formed 3D connected and open channels. From the cross-sections of the X-Y and X-Z planes, the interlayer space exhibited higher porosity than the inner layer matrix. Thus, the conductive path via a s-CNT network covered the entire surface of the open channels within this highly porous composite. Instead, the CNT network formed among powder boundaries in the fully condensed s-CNT/PA12 composite. Therefore, the difference between of the conductivities of PU and PA12 composites was mainly

induced by the morphologies of the conductive path among the polymeric matrix. In the porous PU

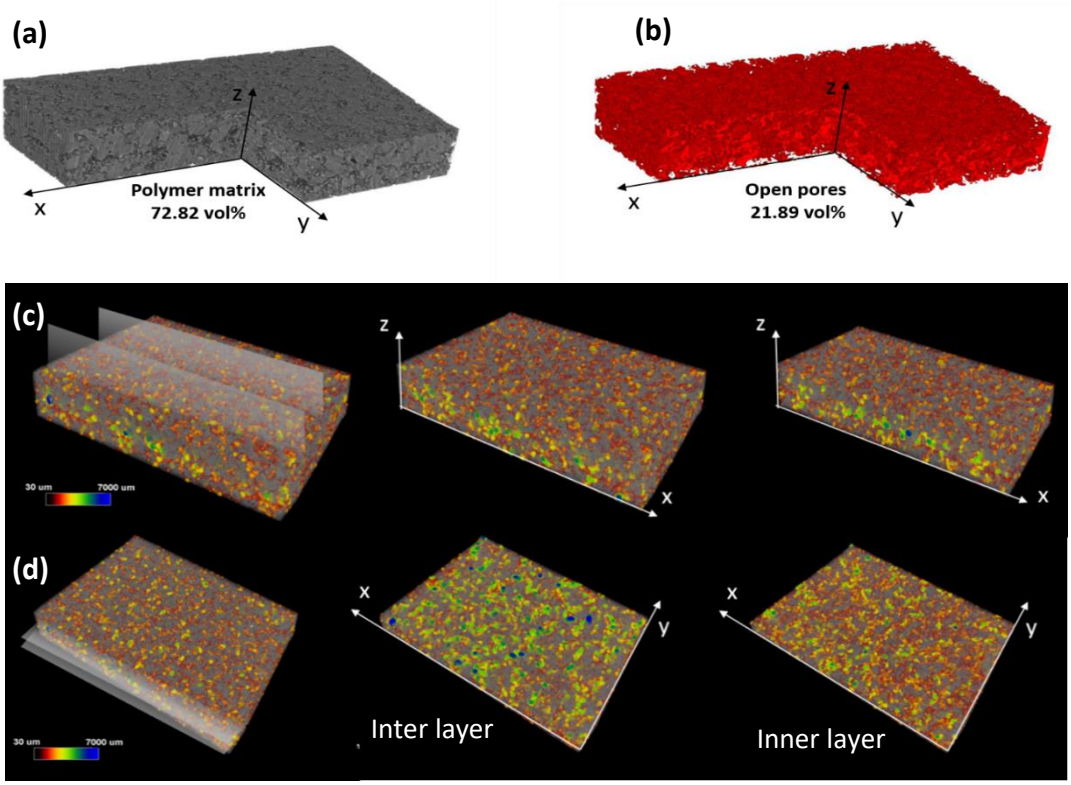

Figure 5.7. Porosity characterization of the s-CNT/PU composite measured by high-resolution Micro-CT scanning. The space within the rectangular sample was occupied by (a) the polymer matrix and (b) the distribution of 3D connected pores. (c) and (d) The distribution of pores on the X-Z and X-Y cross-sections, respectively.

composites, the surface s-CNT layer covering open channels were much effective to conduct electrons, as compared with the CNT network embedded within the condensed PA12 composites. Therefore, the laser-sintered highly porous polymeric matrix with conductive CNT networks can function as flexible conductive components or be filled with a second phase to obtain a new composite with tunable modulus, strength and chemical reactivity for tissue engineering.

5.3 Thermal properties

As polymers are mainly insulating, the electrical and thermal performances of their composites rely on the formation of conductive networks through incorporating fillers. In general, the formation of a segregated structure in polymeric composites remains the most promising strategy to achieve low percolation thresholds. The latex technology [168], *in-situ* synthesis [33, 183], dry mixing [169] and hot sintering are conventional methods for forming a segregated composite structure with conductive paths. As compared with these conventional methods, the laser sintering of s-CNT coated polymer powders can offer the unique advantages of engineerable microstructures at the micro-scale and complex geometries at the macro-scale. The micro-arrangements of conductive fillers can be tailored by changing their type size, and various thermoplastic polymers can be introduced into such laser sintering systems to form 3D objects with unlimited design and manufacturing freedom.

To further investigate the underlying mechanisms of the net effect on the thermal conductivity of the MWCNTs-reinforced polymeric composite, systematic experiments were conducted to explain the contributions of various factors to the enhancement of thermal conductivity. The pristine MWCNTs and s-CNTs were used as fillers to prepare hot-compressed composites; the s-CNTs-coated polymer powders were applied in laser sintering and hot-compression. The effective thermal enhancement of the polymeric nanocomposite is attributed to a net-effect of several factors, including the distribution and functionalization of MWCNTs, the interface scattering of polymeric chain-MWCNT, and the phonon propagation along MWNCTs and through the interfaces of CNTs. The previous studies reported that MWCNTs could

impact on the dynamic recrystallization of semi-crystalline polymers, such as PA, PU and polyethylene, and change the crystallinity and grain size of the crystals. Consequently, the orientation and alignment of the polymer chains could increase the thermal conductivity of the polymeric matrix [150, 151]. Further, the surface modification could be introduced to the suspension of MWCNTs to improve their dispersion properties and their uniformity within the matrix [126]. However, the influences of surface modification on the thermal and electrical conductivities of polymeric composites remain unclear[126]. Surface functionalization could also possibly induce face defects or impurities, which limit phonon propagation and enhance the scattering and damping of phonon modes [145]. Nevertheless, the most recent researches have demonstrated that covalent bonds or hydrogen bonds are able to enhance the phonon transportation between polymers and carbon lattices or among aligned polymer chains [147, 152, 153].

Fig.5.8 shows that the thermal conductivity of laser-sintered s-CNT/PA12 increased from 0.21 to 0.40 $WK^{-1}m^{-1}$ as the s-CNTs were added from 0 to 0.5 wt%. However, once the thermal percolation threshold was achieved, the thermal conductivity of the laser-sintered specimens became saturated. For the s-CNT/PU composites, the laser-sintered composite with highly porous micro-channels showed poor thermal conduction at ambient temperature because the highly porous structures easily dissipated thermal energy to prohibit phonon propagation.

The laser-sintered s-CNT/PA12 specimens showed slight enhancement on their thermal conductivity as compared with hot-compressed ones. This observation was mainly due to the laser sintering process-induced microstructures and defects in the

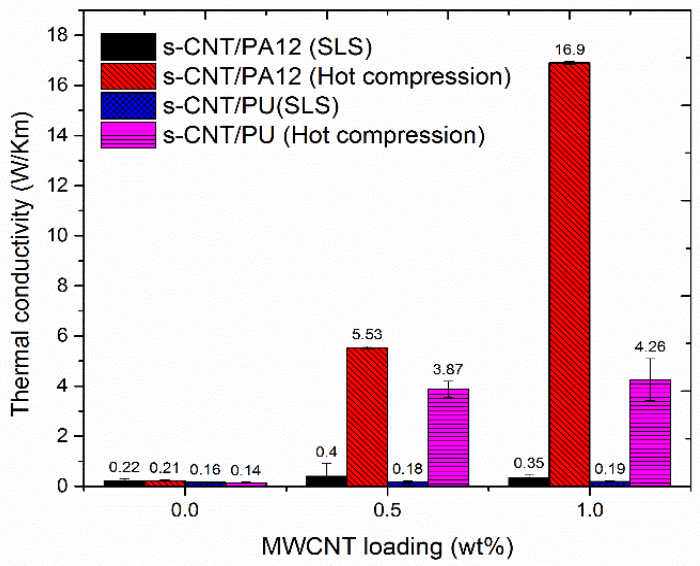

Figure 5.8. Thermal conductivities of s-CNT-reinforced PA12 and PU manufactured by the SLS and hot compression processes.

matrix. Firstly, laser sintering was a pressure-free process, which was hard to achieve a fully condensed polymer matrix, and thus the interfacial affinities of CNT-CNT and CNT-polymer were limited. Secondly, the thermal decomposition interval of cholic acid and CNTs were 200 to 400 °C [184] and 450 to 900 °C [185], respectively. The stable sintering region of PA12 was 184 to 420 °C. The process temperature upon laser scanning was predicted in the range of 200 to 300 °C [3]. Thus, the laser energy might cause the partial decomposition of surfactant via cholic acid, which might create the interfacial defects of the CNT-polymer and CNT-CNT. Thirdly, in Table 5.2, the Micro-CT results revealed that the closed and open pores were inevitable, and they could scatter the phononic wave and prevent phonon migration. Thereafter, the weakening of the thermal conductivity in the laser-sintered specimens was mainly associated with the loose packing of CNTs, interfacial defects and the presence of voids.

Fig. 5.9 (a) shows that the thermal conductivity of CNT/PA12 demonstrated a

slightly linear increase from 0.2 to 0.25 $Wm^{-1}K^{-1}$ with an increasing loading of MWCNTs (Fig. 5.9). Such observation agreed with the prediction of the series model, which suggested that the intrinsic resistances of polymers predominately determined the high series resistance of composites, thus leading to a poor improvement on the thermal conductivity through adding CNTs [147].

Table 5.2. The properties of laser-sintered PA12, PU and s-CNTs reinforced composites.

	PA12	PU	s-CNT/PA12 (0.5 wt%)	s-CNT/PA12 (1 wt%)	s-CNT/PU (1 wt%)
Closed porosity (%)	0.63	8.41	0.006	1.21	0.5
Open porosity (%)	0	5.78	0	0	21.89
Density (g/cm^3)	1.02	0.91	1.14	1.15	0.75
Thermal diffusivity (mm^2/s)	0.08	0.07	0.19	0.18	0.11

Note that the Micro-CT scanning resolution is 6.7 μm for the above characterizations.

In contrast, the s-CNTs-reinforced polymeric nanocomposites exhibited a substantial enhancement of the thermal conductivity as the s-CNTs loading increased. The thermal conductivities of s-CNT/PU and s-CNT/PA12 increased from 0.14 to 4.3 $Wm^{-1}K^{-1}$ and from 0.20 to 16.9 $Wm^{-1}K^{-1}$, respectively, within the low loading range of 0~1 wt%. These observations indicated extremely small percolation thresholds for s-CNT/PU and s-CNT/PA12 composites. Meanwhile, the measured thermal conductivities were comparable with or much greater than those of the other previously reported MWCNTs-reinforced polymeric nanocomposites, in which MWCNTs were functionalized and distributed randomly or aligned as summarized in Fig. 5.9. The s-CNT/polymers, s-CNT/PA12 and s-CNT/PU nanocomposites exhibited much greater enhancement (by the factors of 83 and 20 for neat PA12 and PU, respectively) in

thermal conductivity than the CNT/PA12 and CNT/PU nanocomposites with an identical weight fraction of MWCNTs. Impressively, the thermal conductivity of s-CNT/PA12 (K_C ~ 0.2-16.9 $Wm^{-1}K^{-1}$) increased more rapidly with the weight fraction than that of s-CNT/PU (K_C ~ 0.14-4.6 $Wm^{-1}K^{-1}$). Such dramatic increases in experiments were predicted by the percolation theory, which suggests breakthrough in the electrical or thermal conductivity once the MWCNTs form conductive pathways for electron or acoustic phonon transport [186]. This theory assumes the perfection of CNT-CNT interfacial thermal energy transport.

Thus far, few experimental studies have reported the thermal threshold phenomena and the exact weight fraction of the thermal conductive threshold because there are difficulties in controlling the heat conduction. In the polymeric composite systems, the s-CNTs-reinforced PA12 nanocomposites indicated an extremely low percolation threshold around 0.1 wt% and possessed the outstanding isotropic thermal conductivity in the small weight fraction range (0~1 wt%), compared with other types of MWCNTs-reinforced polymeric composites. However, in order to establish a theoretical model to explain and predict the thermal conductivity, multi-scale modelling is required. For instance, a molecular dynamics simulation model can be applied to predict the interfacial resistances of CNT-CNT, polymer-CNT, and polymer-surfactant-CNT, and the predicted results can be further implemented into the composite percolation model or series model. Meanwhile, the distribution and morphology of the CNT networks should be considered in the theoretical model because the manufacturing process and original powder morphologies also influence the internal distribution of CNTs within the polymeric matrix as illustrated in Figs. 5.10 (c), (f) and (i).

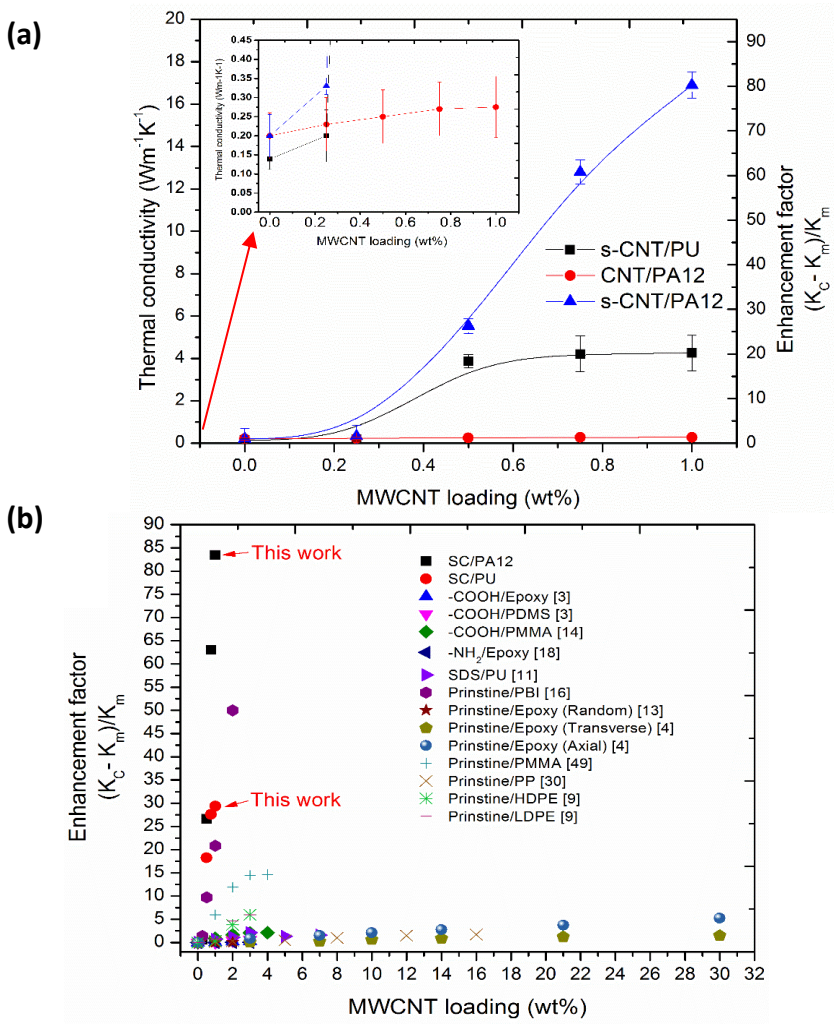

Figure 5.9. (a) Thermal conductivities of the s-CNT/PU, CNT/PA12 and s-CNT/PA12, with the MWCNT loading range from 0 to 1 wt%. Note that the thermal conductivity of CNT/PA12 slightly increased from 0.2 to 0.25 Wm-1K-1 with a positive linear relationship with the increasing weight fraction of MWCNTs. (b) Comparison of the thermal conductivities of MWCNT/polymer nanocomposite with different functional groups. The thermal conductivity enhancement factors of nanocomposite with respect to the neat polymer is given by K_c-K_m)/K_m.

5.3.1 Microstructure and rheological properties

The transmission optical micrographs in Fig. 5.10 indicate the internal distribution and configuration of MWCNTs embedded within the medium at the micro-scale. The pristine MWCNTs were bundled and randomly distributed or misaligned in the

polymeric matrix, and such behaviour usually induced the deviations of the theoretical prediction from the experimental results. However, the s-CNTs maintained the film structures within the PA12 matrix after the composite powders were hot-compressed.

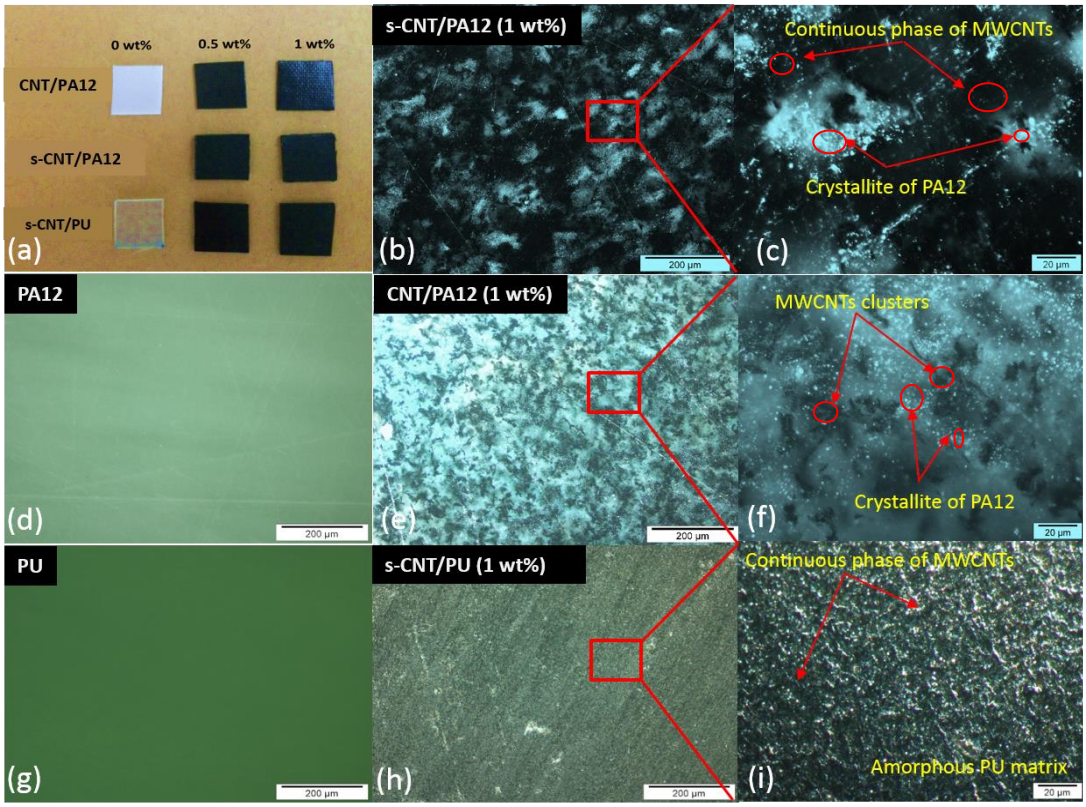

Figure 5.10. (a) Photograph of the testing specimens of PA12, PU, and their composites. Transmission optical micrographs: (b) s-CNT/PA12 (1 wt. %); (d) neat PA12; (e) and (f) CNT/PA12 (1 wt. %); (g) neat PU; (h) and (i) s-CNT/PU (1 wt. %). Note that the dark and light regions were the CNT phase and PA12 matrix, respectively.

The 3D-interconnected framework of MWCNTs was formed to facilitate the phonon propagation along the thermal conductive pathways. Meanwhile, numerous nucleation sites were created, and the crystalline grains of small size grew among the interspaces of the MWCNT framework in the s-CNT/PA12 and s-CNT/PA12 bulk composites. The overlaps and connected junctions of CNT-CNT were characterized by

TEM (Fig. 5.11 (d)), demonstrating the CNT film structure within the matrix.

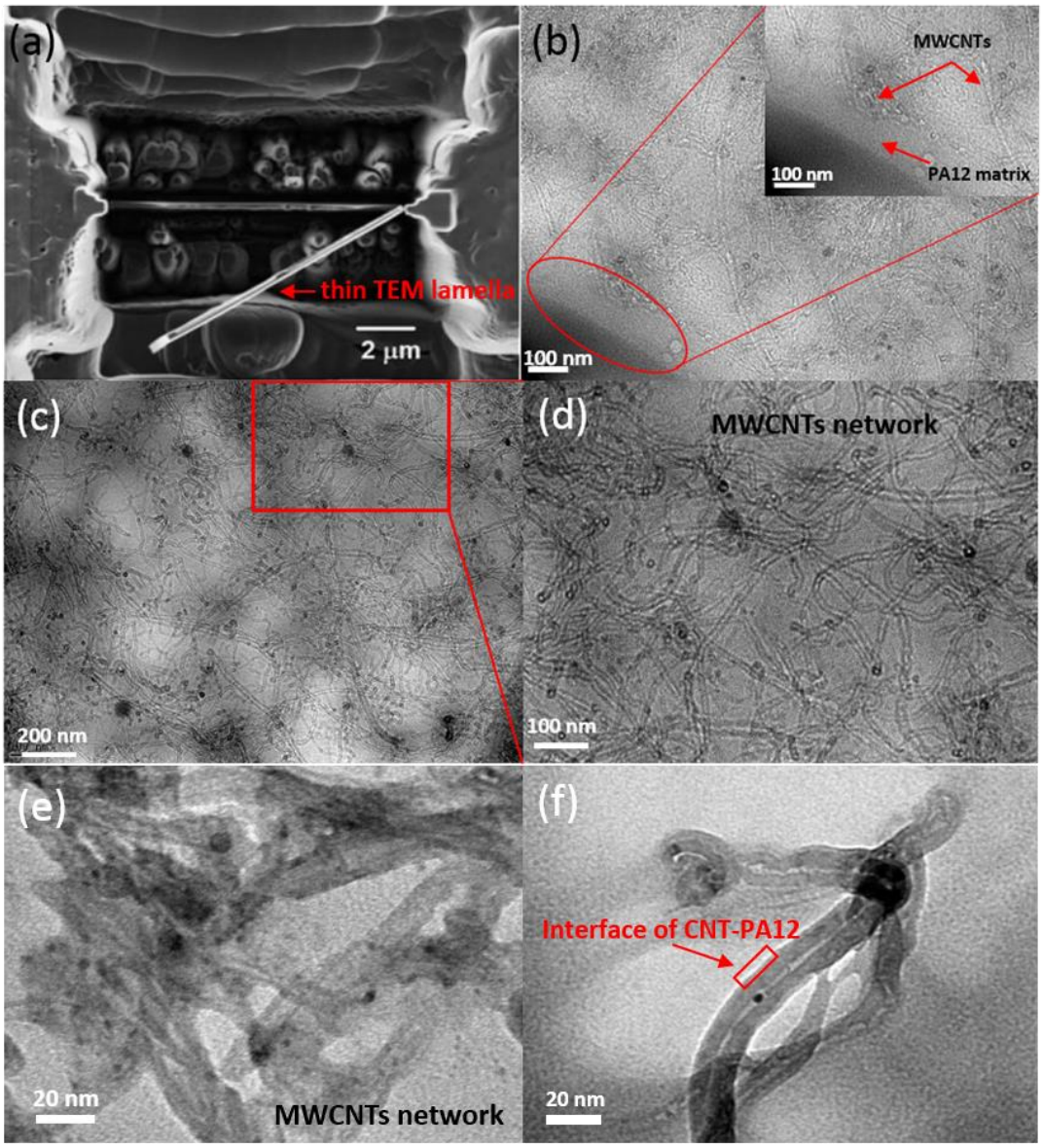

Figure 5.11. (a) TEM sample preparation through focused ion beam (FIB) and the thin lamella sample prepared by ion milling at the intensive white-spot region. (b), (c), (d), (e) and (f) TEM images of the MWCNTs networks within the PA12 matrix through the hot-compression process with different magnifications.

As the amorphous structure was predominant in the s-CNT/PU composite, PU remained in the rubbery state at room temperature. Therefore, even after grinding and polishing, the MWCNTs-network of s-CNT/PU (Figs. 5.10 (h) and (i)) was not

observed as clearly as s-CNT/PA12 (Figs. 5.10 (b) and (c)) through the transmission optical micrographs.

The TEM images in Fig. 5.11 reveal the interconnected s-CNT network structures within the PA12 composites at the nanoscale. The s-CNTs were well dispersed and randomly connected to form a film-like network in the thin lamella. It was also shown that the polymer phase strongly adhered with individual MWCNTs. Apparently, no boundary gap, distorted MWCNTs, and their clusters were present in these s-CNT/PA12 (1 wt%) specimens, which exhibited a dramatic increase of the thermal conductivity by a factor of over 80.

The melt rheological properties of the PA12, CNT/PA12, and s-CNT/PA12 sheet composites were further investigated to study the microstructure-performance relationship by adding MWCNTs into PA12. Generally, the addition of fillers leads to an increase in the melt complex viscosity η^* of the polymer [66]. The filled polymer possesses a relatively high viscosity at low shear rates, but yielding may occur with the increased concentration of fillers [66]. Linearly monodispersed polymer melts exhibit a classical linear viscoelastic behaviour as the storage modulus and the loss modulus obey $G' \approx \omega^2$ and $G'' \approx \omega$, respectively, where ω is the angular frequency.

However, at 200 °C, the storage moduli G' and the loss moduli G" of PA12 and its composites were not proportional to ω^2 and ω. As listed in Figs. 5.12 (a) and (b), the powers of the angular frequency corresponding to G' and G" of PA12 were slightly less than 2 and 1, respectively, because of the polydispersity of the polymer chains. The powers of the angular frequency in s-CNT/PA12 were the lowest among the three specimens because the reinforcement of s-CNTs with the polymer chains was stronger

than that of CNTs with the polymer chains and inter-molecular interaction of PA12.

In Fig. 5.12 (d), the Cole-Cole plots of G' versus G" indicate the frequency-dependent transition from the fluid-like to solid-like state, when G' was higher than G" [187]. The transition of s-CNT/PA12 was notable at the relatively low frequency of 1 rad/s, compared with those of CNT/PA12 and PA12 at 4 and 10 rad/s, respectively. The melted s-CNT/PA12 had a high dynamic modulus mainly because the uniformly interconnected MWCNTs hindered the movement of the polymer chains and strong interfacial interactions existed between the polymer matrix and MWCNTs.

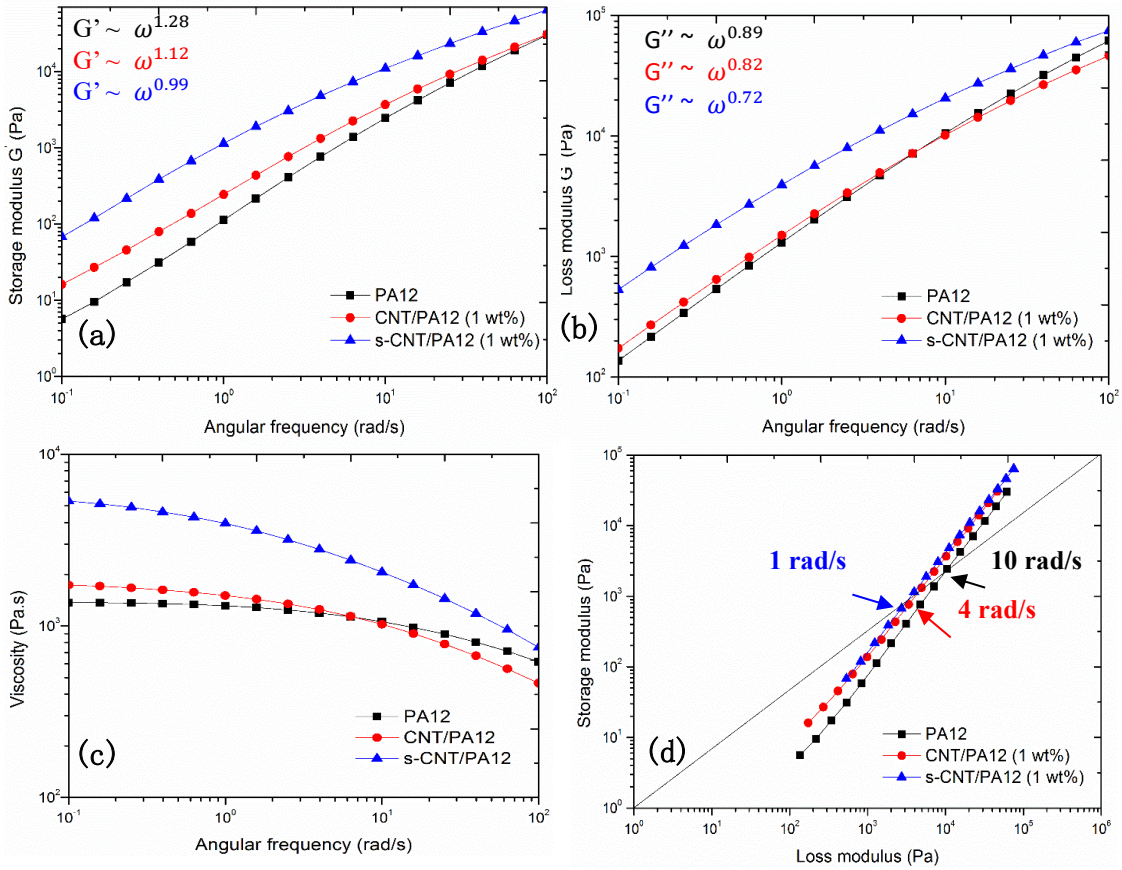

Figure 5.12. Comparisons of PA12, CNT/PA12 (1 wt%) and s-CNT/PA12 (1 wt%) with respect to the angular frequency from 0.1 to 100 rad/s at 200 °C: (a) storage modulus, (b) loss modulus, (c) viscosity, and (d) Cole-Cole plots of the storage modulus versus loss modulus.

It is widely accepted that a Newton fluid demonstrates nearly invariant complex viscosity η^*. Fig. 5.12 (c) shows that the η^* of PA12 exhibited a plateau of the flow regime at a low angular frequency less than 10 rad/s, and the pristine CNTs-reinforced PA12 demonstrated similar rheological properties as neat PA12. However, the η^* of s-CNT/PA12 showed a strong dependence on the angular frequency over the flow regime. At 100 rad/s, the addition of s-CNTs into neat PA12 could significantly improve its storage modulus and loss modulus by 200% and 25%, respectively. Although CNT/PA12 and s-CNT/PA12 had the same weight fraction of MWCNTs, the η^* of s-CNT/PA12 was much higher than that of CNT/PA12 at the low shear rate range (angular frequency less than 10 rad/s), within which the non-Newtonian behaviour was remarkable in s-CNT/PA12. These observations were mainly attributed to the internal network-like microstructures of s-CNTs, which greatly restrained the motion of the long molecule chains in melted bulk composites.

Therefore, the quantitative rheological measurements strongly resorted to the observations of optical micrographs and TEM images. The enhanced rheological properties of s-CNT/PA12 were attributed to the unique microstructures via a 3D interconnected network of MWCNTs, which was induced by the improved coating uniformity of MWCNTs on the polymeric powders. The cholate molecules wrapped around MWCNTs and adhered with PA12, and such morphologies could significantly improve the dispersion of MWCNTs and enhance the coupling between MWCNTs and the surrounding polymeric matrix after hot-compressing. In contrast, the pristine MWCNTs inevitably aggregated with the non-uniform coverage on the powder surfaces, leading to the poor 3D distribution and thermal conductive performance of

bulk CNT/PA12 composites.

5.3.2 Crystallinity and kinetics of crystallization

The crystallinity of the thermoplastics and the existence of the crystalline phases around CNTs also influence the thermal conductivity of a composite. When s-CNTs were added into PA12, its melting point dropped from 188 °C to 184 °C. The narrow and smooth curves indicate that such a composite could easily melt because the improved 3D morphology of MWCNTs was able to enhance the heat absorption and conduction within the polymeric matrix. However, PA12 and CNT/PA12 melted at 188 °C and exhibited the sharp and broad absorption peaks, which indicated the inefficient heat conduction and absorption in the polymeric matrix.

In Fig. 5.13 (a), compared with the recrystallization curves of PA12 and CNT/PA12, those of s-CNT/PA12 are sharp and narrow, indicating the imitation of recrystallization at a relatively high temperature of ~163 °C The recrystallization peaks of s-CNT/PA12 around 156.4 °C were higher than those of PA12 and CNT/PA12 in the range of 150.9-153.7 °C. In Fig. 5.13 (c), the dynamic crystallization processes show that the crystallization of the polymer melt became rapid with the addition of MWCNTs; especially s-CNT/PA12 had the highest crystallization rate. The degree of crystallinity at time *t* is defined by

$$X(t) = \frac{X_C(t)}{\Delta H_\infty} = \frac{\int_0^t \frac{dH(t)}{dt} t}{\Delta H_\infty} = \frac{\Delta H_t}{\Delta H_\infty} \tag{5.1}$$

where $\mathrm{d}H(\mathrm{t}))/\mathrm{dt}$ is the rate of heat evolution; ΔH_t is the heat generated at time *t*; ΔH_∞ is the total heat corresponding to fully crystallized PA12, which is taken as 245

J/g [188].

The accelerated recrystallizations of PA12 were associated to the well-distributed s-CNTs, which could create numerous heterogeneous nucleation sites for the PA12 polymer chains. This was because the energy barrier of heterogeneous nucleation rather than homogeneous nucleation of crystals could be easily overcome. Consequently, polymer crystals grew from the dense nuclei on the MWCNT surfaces and then were confined between the adjacent phases as shown in Figs. 5.10 (c) and (f) and Fig. 5.11 (b). Thus, the grain size range of the crystals decreased, which was also observed in the studies by Cai *et al.*[144] and Li *et al.* [143, 188].

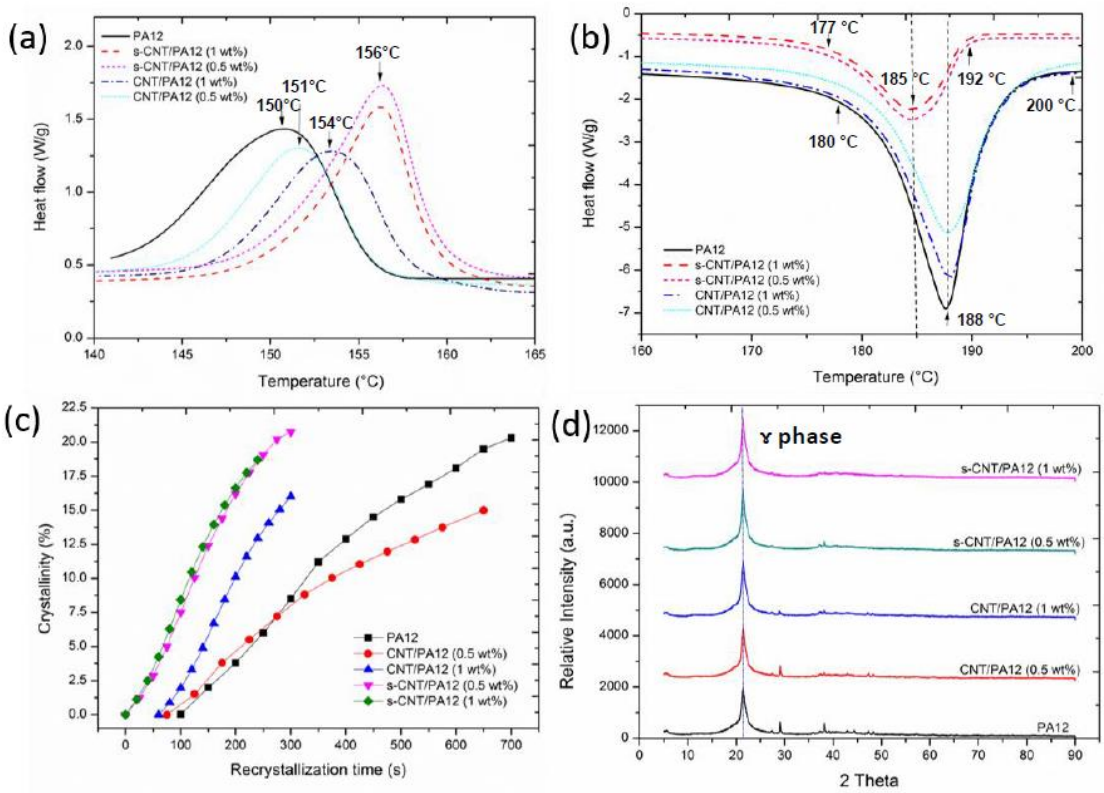

Figure 5.13. Comparisons of PA12, CNT/PA12 and s-CNT/PA12: (a) DSC recrystallization curves for at the cooling rate of 15 °C/min; (b) DSC melting curves at the heating rate of 15 °C/min; (c) the dynamic crystallinity over the time range of the recrystallization process; (d) the wide-angle X-ray diffraction patterns.

However, the addition of CNTs did not significantly increase the crystallinity ratio of PA12, and the CNT/PA12 nanocomposite possessed an even lower crystallinity ratio than the neat PA12, as illustrated in Figs. 5.13 (c) and (d). The contribution of crystallites around the CNTs was to effectively eliminate phonon scattering at the CNT-polymer interfaces, which had a much more positive impact on the thermal conductivity of the nanocomposite than the crystallinity change of the polymer. However, such impact could only enhance the thermal conductivity no larger than 5 times [144], indicating a minor contribution to the remarkable increase up to 80 times.

5.3.3 Functionalization of MWCNTs

The effects of functionalization on the thermal properties of the CNT/polymer nanocomposite were essentially those on the interfacial interactions of CNT-CNT and CNTs-polymer. The previous research works about the enhancement of the effective thermal conductivity of CNTs-reinforced nanocomposites are summarized in Fig. 5.9 (b). The lateral π-stacking [152] and the axial carbon-carbon covalent bonds [140] induced the distinct thermal diffusivities along the transverse and axial directions respectively, resulting in the anisotropic phonon transportation. However, for the randomly networked MWCNTs within the polymeric matrix, the increased phonon scatterings were present at CNT junctions, non-bonded interfaces between CNTs-polymers and surface imperfections of CNTs, leading to the poor conductance of bulky composites.

A possible way of improving the interfacial strength is to alter the type of interactions from van der Waals forces to covalent bonds, which have been

experimentally and theoretically proved to facilitate phonon transport at CNT-polymer interfaces and CNT-CNT lateral boundaries [152, 189]. Therefore, the covalent functionalization of MWCNTs was proposed to enhance the interfacial coupling of CNT-polymer through chemical treatments via functionalizing MWCNTs with –COOH or $–NH_2$ [147, 190]. Balandin *et al.* observed that the thermal conductivity of polymeric nanocomposites with functionalized CNTs was affected in the presence of MWCNTs and that the covalent functionalization increased the coupling of CNTs and the polymeric matrix, but caused the formation of defects that impeded the phonon transport at the outer layers of MWCNTs [145]. Non-covalent surfactants such as sodium dodecyl sulfate (SDS) and sodium dodecylbenzene sulfonate (SDBS) generally stabilize CNTs in an aqueous solution; they can form cylindrical micelles around individual CNTs and their hydrophobic tails usually adopt a wide range of orientations with respect to CNTs. Such structureless and adsorbed layer of surfactants was reported to inhibit the heat transport at CNT-CNT and CNT-polymer interfaces with the equilibrium thermal resistance on the order of 10^{-8} m^2 K/M [144, 146, 191].

Raman spectroscopy is an effective method to characterize the functional groups of polymers and the degree of order for the functionalized MWCNTs. Fig. 5.14 (a) shows that the amide I peak appeared at 1635 cm^{-1}. The shifts located at 1295, 1364 and 1436 cm^{-1} were associated to the twisting, wagging and bending of CH_2, respectively [192]. For CNT/PA12, the D-band appeared around 1360 cm^{-1} corresponding to the defects of sp^3-hybridized carbons at the boundaries of CNTs and the disorder-induced modes. However, the D-band of s-CNTs slightly shifted to 1367

cm^{-1}, while the G-band of pristine CNTs and s-CNTs were both located around 1584 cm^{-1}, which was attributed to the planar vibration of sp^2-hybridized carbons along the CNT walls [193]. The I_D/I_G ratio (~ 1.15) of s-CNTs in PA12 dropped slightly as compared with that of pristine CNTs (I_D/I_G ~ 1.18). In this work, the change of the I_D/I_G ratio was partly ascribed to the surface disorder of CNTs and ring coupling between cholate molecules and their outmost walls.

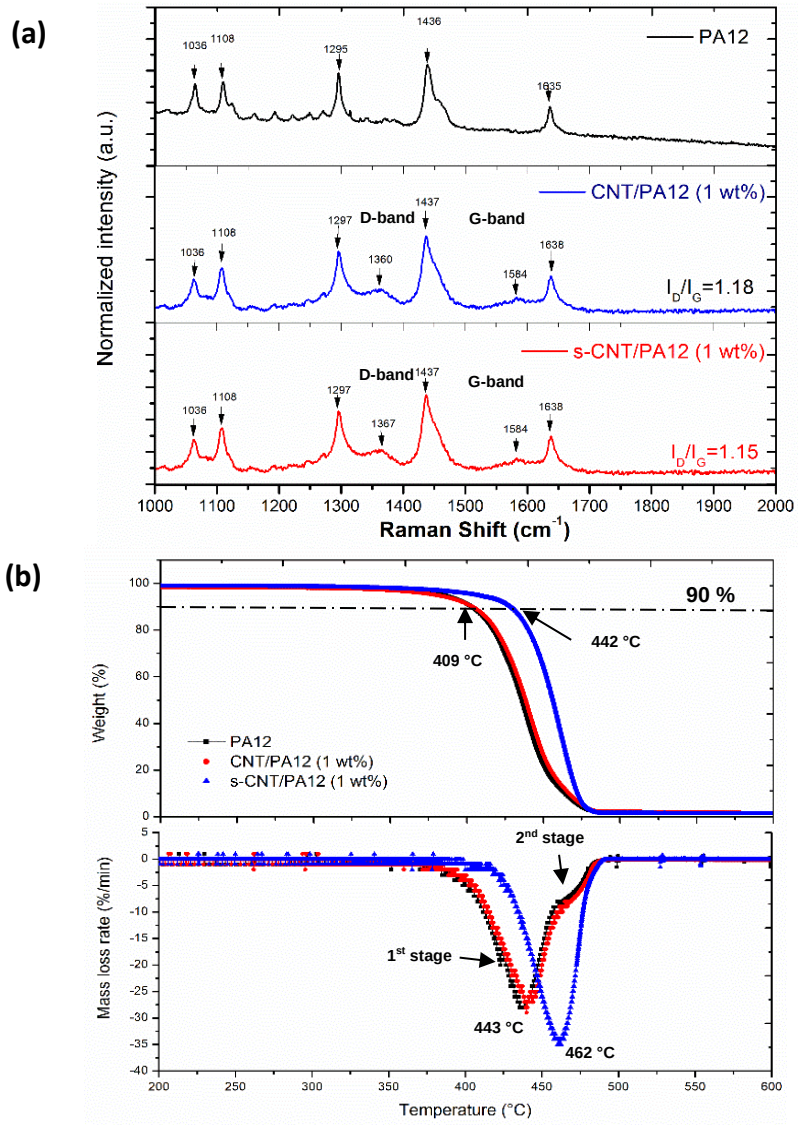

Figure 5.14. (a) Raman spectra from 1000 to 2000 cm-1 and (b) weight in % and mass loss rate of PA12, CNT/PA12, and s-CNT/PA12 composites through hot-compression.

The thermogravimetric analysis (TGA) under the N_2 gas was performed to investigate the influences of the functionalized MWCNTs on the thermal stability of PA12, which was related to the interfacial interactions between polymers and fibers, the intermolecular bonding among polymer chains and the high aspect ratio of MWCNTs. It can be seen from Fig. 5.14 (b) that neat PA12 and CNT/PA12 both showed a weight loss of about 10 % around -409 °C and a two-stage decomposition process in which the first and second stage mass loss peaks appeared at 443 °C and 462 °C, respectively. After PA12 was fully decomposed, the remained weights were quantitatively consistent with the fractions of CNTs in CNT/PA12 and s-CNT/PA12. However, the s-CNTs stabilized the matrix against the first stage of degradation at such a low mass fraction of 1 wt%, mainly due to the fact that the s-CNT network captured the thermal radical easily and effectively transported thermal energy between the s-CNTs and the polymer chains to prevent chemical decomposition of PA12.

Compared with covalent-functionalized and non-covalent-functionalized MWNCTs (Fig. 5.9 (b)), the cholate molecules helically wrapping around MWCNTs maintained their structure at the CNT-polymer interfaces due to the following factors: (i) the strong interactions between the rings and the graphene sidewalls of MWCNTs [194], (ii) the cooperative stabilization through hydrogen bond networks between adjacent molecules, and (iii) the strongly interfacial connections induced by condensation of carboxylic groups and the surface chemical groups of polymers such as PA12 (Fig. 5.15).

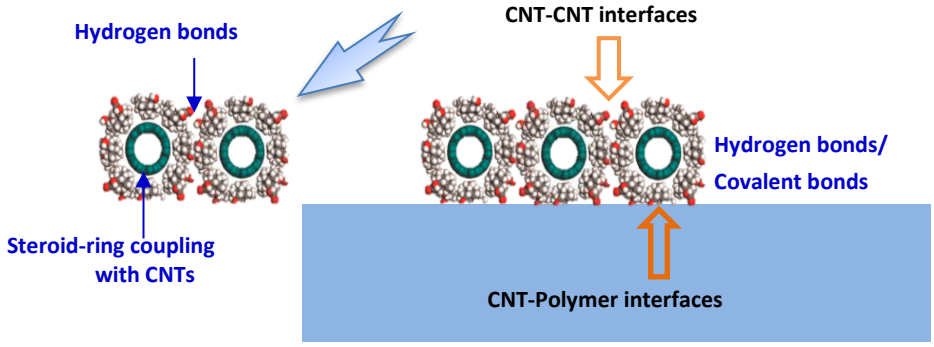

Figure 5.15. Illustration of the interfacial interactions of CNT-CNT and CNT-polymer in s-CNT/PA12 nanocomposites.

With the assistance of sodium cholate, MWCNTs were stacking on each other and bonding with polymers via a thin but effective bridging layer as a "molecular phonon coupler" to mitigate phonon scattering. Lin *et al.* reported that the interfacial phonon coupler layer could improve the thermal conductivity of the MWCNTs/mating substrate interface by almost two orders of magnitude [195]. The pristine MWCNTs assembled onto the polymer surfaces with separation distance at the nanoscale, i.e. the regime where the van der Waals force dominated. However, such "contacts" with the mating substrate were not permanent or binding, and these interactions were non-efficient to migrate phonon transport compared with π-stacking or covalent bonds [140, 196]. Therefore, in this study, the inter-layer of sodium cholate molecules were able to form pressed contact assembly, which was proposed to effectively address the issue of reducing the interfacial thermal resistance. Meanwhile, the non-covalent functionalization, particular for sodium cholate, would not cause surface defects on the side walls of MWCNTs, thus avoiding the surface imperfections-induced phonon scattering.

Chapter 6 Laser-sintered 3D lattice structures for energy absorption

. Lightweight cellular composites fabricated by AM processes exhibit the outstanding specific strength and Young's modulus. These structural materials also offer the advantages for the potential applications in catalyst supports, vibration damping, heat management, energy absorption, etc. By controlling the material composition and architecture in multi-scale, the structural materials are able to achieve remarkable mechanical properties. Laser-sintered CNT/PA12 composites can show an significant enhancement of mechanical toughness, and have the potential to be applied for the impact shock energy absorption. TPUs are of great interest for the applications in soft actuators, smart devices, energy storage devices, dampers and minimally invasive biomedical devices [197, 198].

6.1 Mechanical properties of laser-sintered materials

To investigate the effects of CNTs-reinforcement within the laser-sintered PA12, the compression and tensile measurements were conducted to study the mechanical enhancements. On the other hand, TPU is a viscoelastic polymer and exhibits time-temperature-dependent behaviors under the tensile or compressive loading. Therefore, the factors of elongation and strain rates should be taken into account in the experiment design.

6.1.1 s-CNT/PA12 composites

The tensile and compression specimens of s-CNT/PA12 composites were fabricated

by the set of optimized parameters given in Chapter 3 and the specimens of PA12 were manufactured by the commercial set of parameters from the EOS company. , The tensile stress-stain curves in Fig. 6.1 (a) show that the tensile strength of s-CNT/PA12 ($\sigma_t = 68$ MPa) was much higher than that of PA12 ($\sigma_t = 45$ MPa). The elongation at break increase from 28% to 33% after the addition of s-CNTs at 0.5 wt%. Thus, the s-CNT/PA12 composites exhibited impressive improvement in the mechanical toughness as compared with the neat PA12.

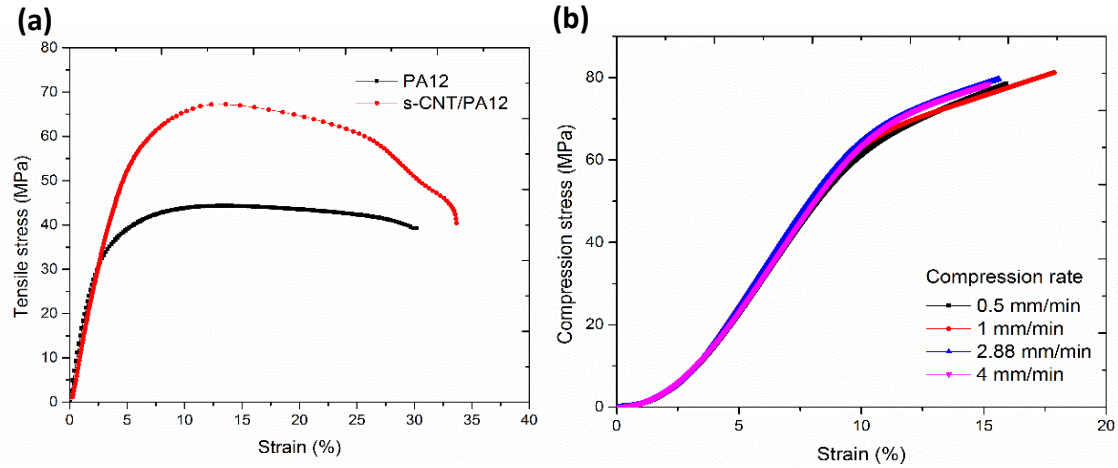

Figure 6.1. (a) Uniaxial tensile stress-strain curves for the laser-sintered PA12 and s-CNT/PA12 tensile bars; (b) the uniaxial compressive strain-stress curves for s-CNT/PA12 corresponding to varied compression rates.

Usually, a polymer exhibits viscoelastic behaviours due to the matrix arrangement of intrinsic macromolecules. Thus, the strain rate-dependent compression behaviours of the laser-sintered s-CNT/PA12 composites were investigated (Fig. 6.1 (b)). Under the ambient temperature, it was observed that the compression yield strengths and strain-stress curves were independent of the applied strain rate (0.5 to 4 mm/min). Therefore, the viscoelastic property of the s-CNT/PA12 composite is negligible when it is used for the energy absorption design.

The manufacturing technology often limits the material composition and mechanical performance of 3D-printied composites. Usually, the carbon fibers-reinforced composites manufactured by fused deposition, inkjet printing or direct writing methods are stiff and brittle. The printed 3D composite lattice structures exhibit outstanding specific strength and Young's modulus. However, such brittle materials are not faviorable for energy absorption or damping purposes in mechanical applications.

The laser-sintered s-CNT/PA12 composite exhibits significant increases in the tensile strength, compression yield strength and elongation at break up to 68 MPa, 70 MPa and 33%, respectively. This composite possesses the tough and ductile manners upon tensile and compressive loading. Due to the tough and ductile behaviours as compared with other 3D-printed polymers or composites, this type of s-CNT/PA12 composite is proposed for the use of manufacturing energy absorption structures, such as hard-foam structures.

6.1.2 Thermoplastic polyurethane

The auxetic foams composed of highly porous thermoplastic polyurethane (TPU) exhibit an attractive behaviour of withstanding a large volume reduction upon the cyclic compressive loading. In this work, the TPU powders were used to manufacture artificial foam structures such as auxetic lattices, while the energy dissipation of the soft TPU auxetic lattices such as soft foam structures wasinvestigated.

In Fig. 6.2, the strain-stress curves under different elongations show that the laser-sintered TPU specimens could be elongated up to 300% without breaking and these specimens had high recoverability after the extension ratios were changed. Meanwhile,

the viscoelastic behaviours were investigated through varying the compression rates. The lower the strain rate was applied; the higher the compression modulus was observed. Additionally, a large compression deformation up to 25% was observed and the compression specimens still exhibited strong recoverability. Such a soft and ductile polymer is preferable to construct the soft and recoverable structures for damping or energy dissipation purpose.

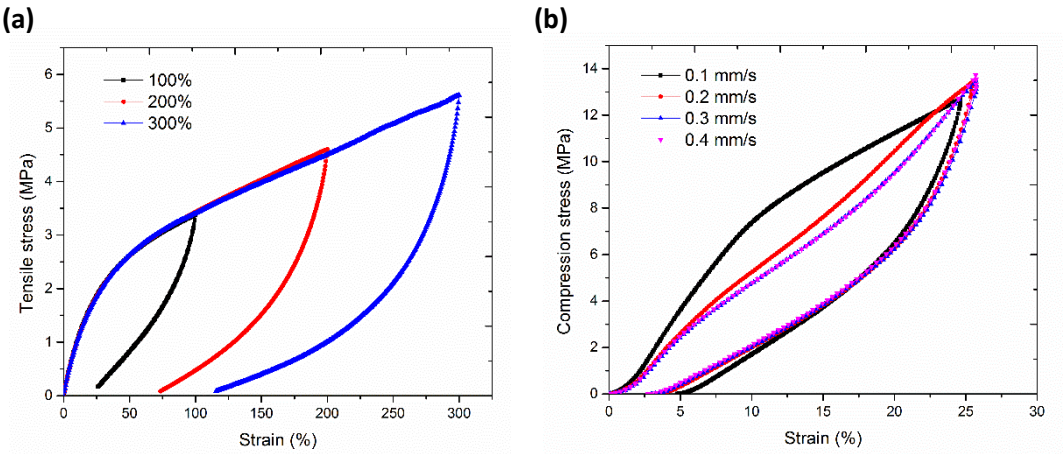

Figure 6.2. (a) The tensile strain-stress curves for laser-sintered TPU tensile bars corresponding to different elongations; (b) the uniaxial compressive stress-strain curves for laser-sintered TPU specimens with varied compression rates.

6.2 Design of 3D lattice structures for laser sintering

Lattice structures have functional roles beyond the highly porous or hollow structures. Their unit blocks are often regularly and periodically patterned in 3D. The length scale can vary throughout the lattice volume to tailor its properties, especially its density and stiffness in distinct locations. Cellular lattices including auxetic lattices are most representative groups in 3D lattice designs. Cellular lattices are known to have their low density and high specific stiffness, and among them the auxetic lattices exhibit unusual deformation behaviour, such as the negative Poisson's ratio, and are able to

deform in a large elongation or compression strain.

6.2.1 Truss structures

Among a number of 3D cellular lattice designs, three types of representative truss structures are selected for investigation of the mechanical performance of laser-sintered composite structures. They are diamond-truss, octet-truss and dode-truss, which have unique 3D patterns and deformation behaviours.

The diamond truss originates from the nature diamond atomic structure, consisting of two interpenetrating face-centred-cubic (*fcc*) Bravais lattices, displaced along the body diagonal of the cubic cell by one quarter of the length of the diagonal. The unit cell within a conventional cubic cell of diamond truss is as shown in Fig. 6.3. Five repeating units along an axis were applied for constructing a 3D lattice for manufacture (Fig. 6.3). Diamond is known as the hardest material in nature due to the unique atomic package in 3D, and therefore this packaging configuration draws intensive attentions to produce ultra-stiff lightweight structures.

Octet-truss is a typical group of the stretch-dominated lattice. The geometric configuration of unit cell of octet-truss was proposed by Deshpande *et al* [160]. This type of periodic structure usually satisfies Maxwell's criterion for static determinacy. The criterion in 3D is given by b-3j+6≥0, where b and j are the numbers of the struts and nodes, respectively, in the unit cell. As a stretching-dominated lattice, the octet-truss structures often fail due to plastic yielding or elastic buckling of the struts. They show an outstanding strength (or stiffness) to weight ratio, which approaches half the theoretical maximum values for isotropic void materials [160]. These attractive

behaviours make octet-truss structures as the alternatives of metallic foams [199].

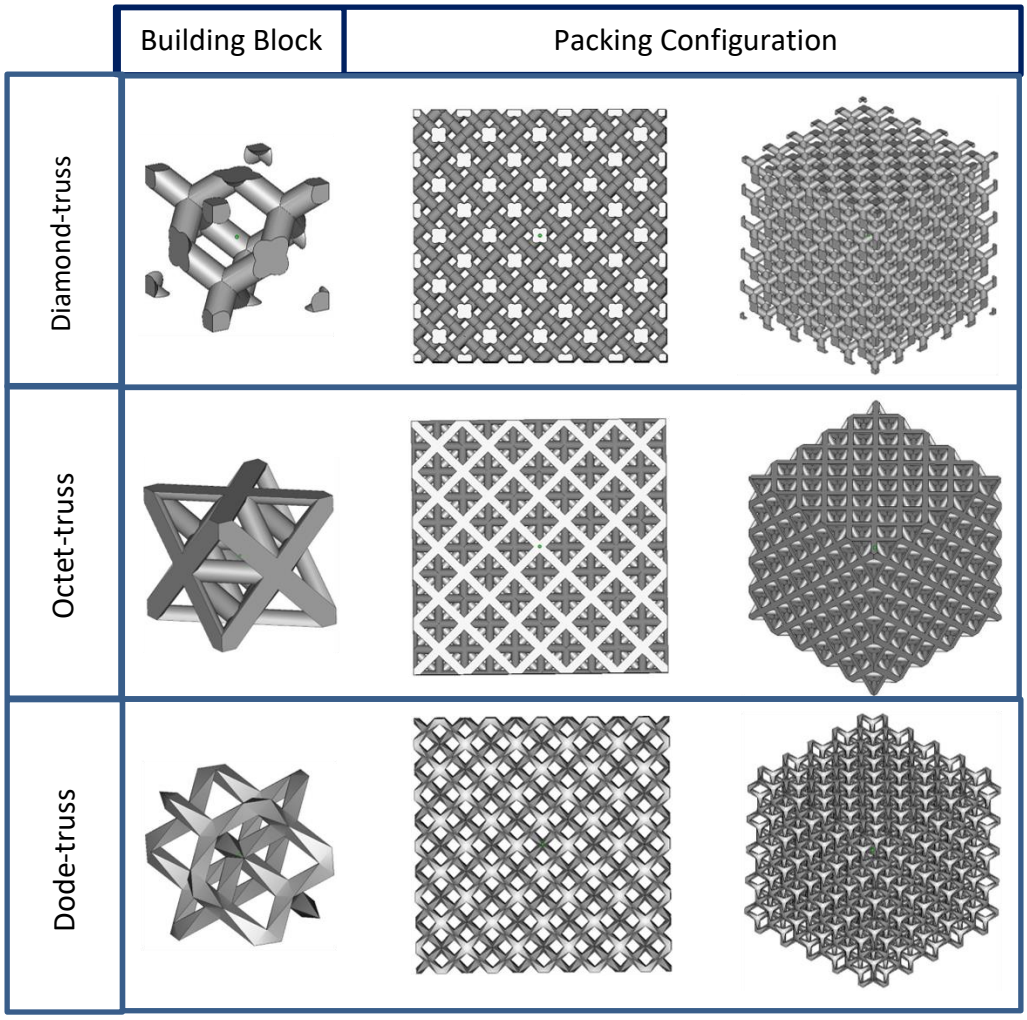

Figure 6.3. The building blocks and 3D configurations of three types of representative cellular lattices: diamond-truss, octet-truss and dode-truss.

The category of dode-truss structures is attractive due to its elastic and post-elastic responses like the elastomeric bearings with the alternating rigid layers and soft rubber layers. This category of lattice exhibits low shear moduli and may be able to stop or dramatically attenuate shear waves. Such deformation behaviours enable the dode-truss to simultaneously show the soft and stiff deformation modes. Considering the post-elastic response, the dode-truss structure is investigated on the acceptable energy

dissipation capacity and supplemental damping performance.

6.2.2 Auxetic structures

3D mechanical metamaterials with the negative Poisson's ratio contract in the transverse directions under longitudinal compressive loading regimes, seemingly opposite to the natural laws of material deformation [161-164]. Such auxetic behaviours are observed in the natural foams [100, 200, 201], cubic elemental metals [202], synthetic kagome lattice structures [164], interlocked cellular structures [203], chiral honeycombs [204] and bucklicrystals [161], which exhibit attractive mechanical properties such as shear resistance, impact resistance [205] and extraordinary capability of energy dissipation [163, 167, 206]. The rational topology optimization of auxetic structures enables design of the 3D architectures with tuneable negative Poisson's ratio and mechanical stiffness [161, 207, 208].

Babaee *et al.* designed a new group of 3D metamaterials (also called Bucklicrystals) and investigated the buckling-induced auxetic behaviour of the infinite units in Bucklicrystals using non-linear finite element analysis [161]. In these designs, elastomeric spherical shells with 6 or 12 holes are arranged periodically to construct 3D body-centre-cubic (*bcc*) and simple-cubic (*sc*) structures. The two types *bcc*-6H, *bcc*-12H and *sc*-12H. The spherical shells with 6 holes or 12 holes are arranged periodically to construct 3D *bcc* and *sc* structures.

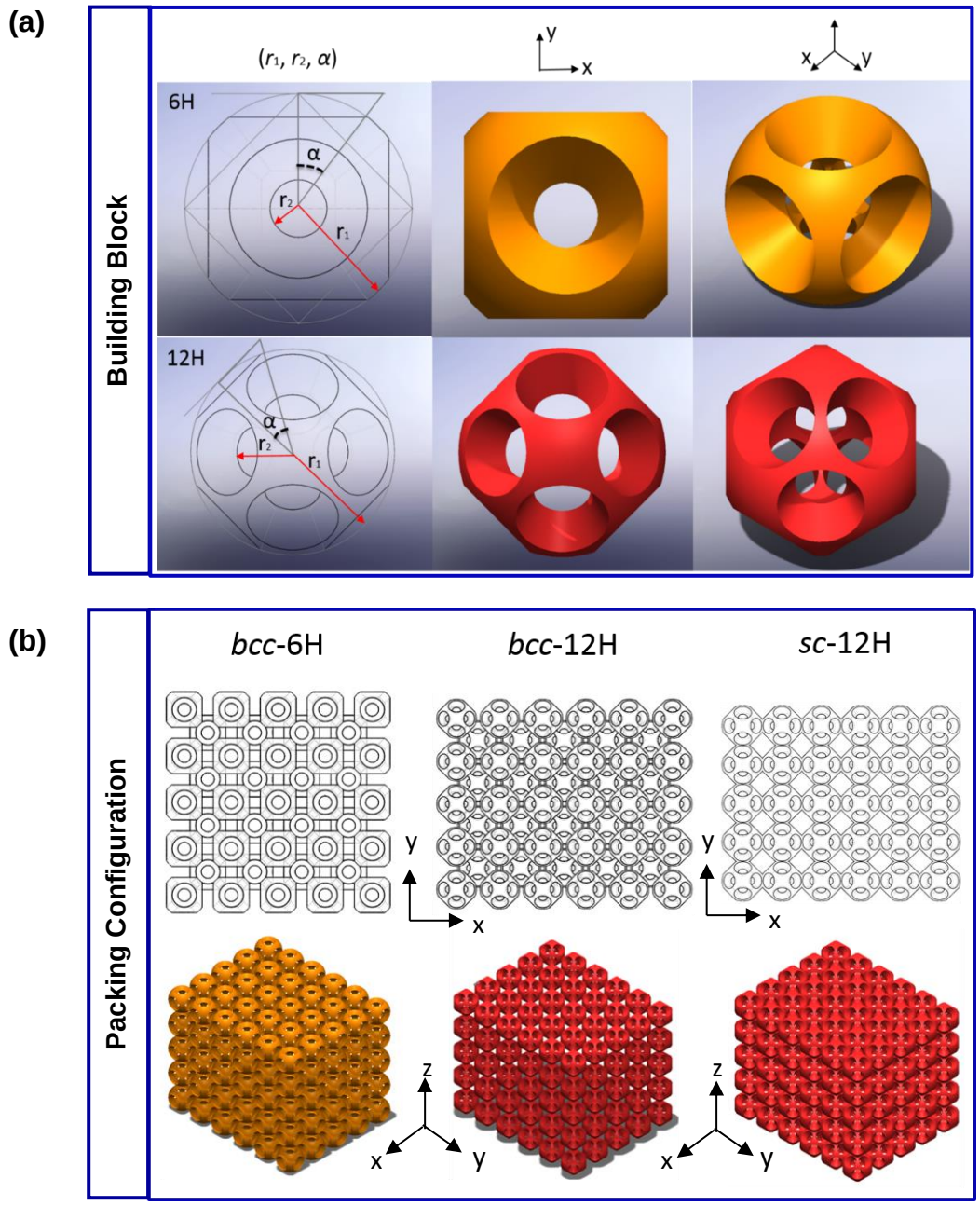

Figure 6.4. 3D auxetic lattices via Bucklicrytal are designed through assembling the 6-H and 12-H units in the cubic crystal systems of *bcc* and *sc*. The parameters r_1, r_2 and α are monitored to change the porosity and shell thickness of each unit. The three samples of *bcc*-6H, *bcc*-12H and *sc*-12H possess the porosity of 60%.

Under compressive loadings, the 3D periodic, soft and porous structures buckle and the connecting nodes rotate, leading to the shrinkage of the entire volume of lattice

structures. Buckling-induced large deformations require that the Bucklicrystals consist of soft and highly ductile materials, as the localized regions (e.g., the connected nodes and beams) experience the extremely large local strains.

The dimensions of building blocks including the inner diameter r_1, outer diameter r_2 and projection angle α determine the porosity and shell thickness of each unit and the configurations of an assembled structure in the cubic crystal systems. A trade-off exists between the optimal structure strength and the maximum strain deformation when the dimensional factors are being modified. In this work, the parameters of r_1, r_2 and α in 6-hole and 12-hole units were monitored to achieve the identical porosity, and the size and dimensional accuracy of printed lattices were mainly limited by the laser process.

For a spherical shell, the outer radius r_1 and inner radius r_2 are two important geometric parameters, as indicated in Fig. 6.4 (a). The porosity of a spherical shell is controlled by both radii, defined as

$$\phi = 1 - \frac{V_u}{V_s} \tag{6.1}$$

where V_u and V_s are the volumes of the spherical shell and solid sphere, respectively. The distance l between the centres of two adjacent shells is the parameter to govern the packing configuration. The global porosity of the lattice structures can also be defined as

$$\phi_g = 1 - \frac{V_l}{V} \tag{6.2}$$

where V_l is the total volume of lattice structure and V is the volume of the cuboid containing the specific lattice. This porosity of lattice is different from that of the spherical shells due to the varied packing configurations.

6.3 Energy absorption and dissipation

Energy absorption and dissipation capabilities of materials are critical performance factors to determine the end-use applications for protective packaging, actuation, damping and impact protection. Two types of energy absorption behaviours were observed under the impact loading condition as shown in Fig. 6.5. Usually, plastic or elastic foams behave as the type-I plot with a flat-topped load-displacement curve. In contrast, stiff truss or honeycomb structures exhibit the type-II plot with an initial peak load followed by a 'steeply falling' curve. For the identical energy absorption capability, the foam-like structures always contribute a lower peak force and the energy is absorbed as the cell walls bend plastically, buckle or fracture, but the peak stress is limited by the long and flat plateau of the strain-stress curve. Such energy absorption performances are favourable for the impact or compression protection, which must absorb the kinetic energy of the impact or static loading while keeping the peak stress below the threshold that causes injury or damages. The desirable energy absorption structures often undergo a large deformation at a constant stress value and then absorb large energies with a small increase in the peak stress.

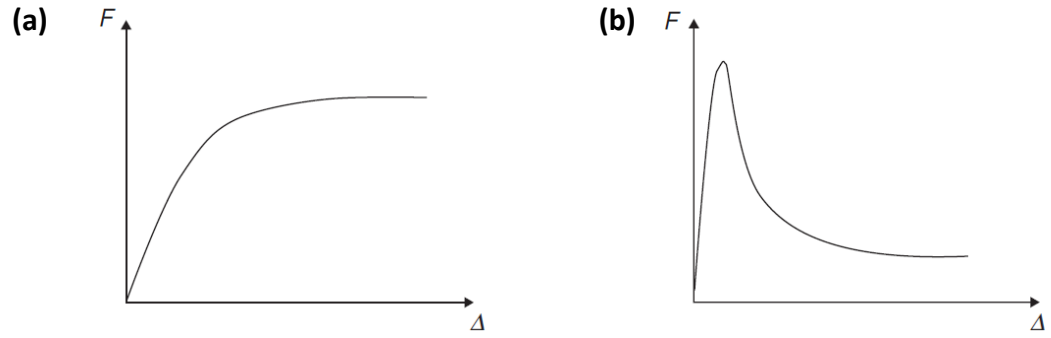

Figure 6.5. Two types of structures: (a) type I with a flat-topped load-displacement curve; (b) type II with an initial peak load followed by a 'steeply falling' curve [209].

Two categories of structural lattices are able to display the flat-topped loaded-displacement curves. One is the elastomeric foam-like structures and the other is the plastic foam-like structures, with their energy absorption diagram shown in Figs. 6.6 and 6.7, respectively. The energy absorption capability is usually indicated by the energy per unit volume W/E_s versus peak stress σ_p/E_s, which is a density-dependent function. The density of each lattice structure has a σ_p , and the best enegry absorption performance corresponding to this structure is given by the shoulder on its energy curve diagram. In Fig. 6.6, the heavy line shows the envelope of these shoulder points. This line often indicates the relationship between the absorbed energy W and the peak stress σ_p for the optimum of lattice density and loading at certain strain-rate and temperature [209].

In addition, the strain-stress deformations of elastomeric foams demonstrated in Fig. 6.6 are classified into two types according to open-cell and closed-cell foam-like structures. The deformation of open-cell elastomeric foams is dominated by bending and buckling of the cell walls, and thus the linear-elastic portion of the curve is followed by a horizontal plateau at the stress level of σ_{el}^*, which can be retained till the densification strain ε_D as shown in Fig. 6.6 (a). On the other hand, the closed-cell foam-like structures are deformed by bending, buckling and stretching of the cell walls. At a lower density range of structures, the peak stress σ_p/E_s and the energy per unit volume W/E_s are independent of the density increase, as the energy absorption is dominated by compression of the encapsulated gas or liquid within the cells. When the relative density of the structure increases to be above 0.1, the energy absorption capability is positively associated to it (Fig. 6.7).

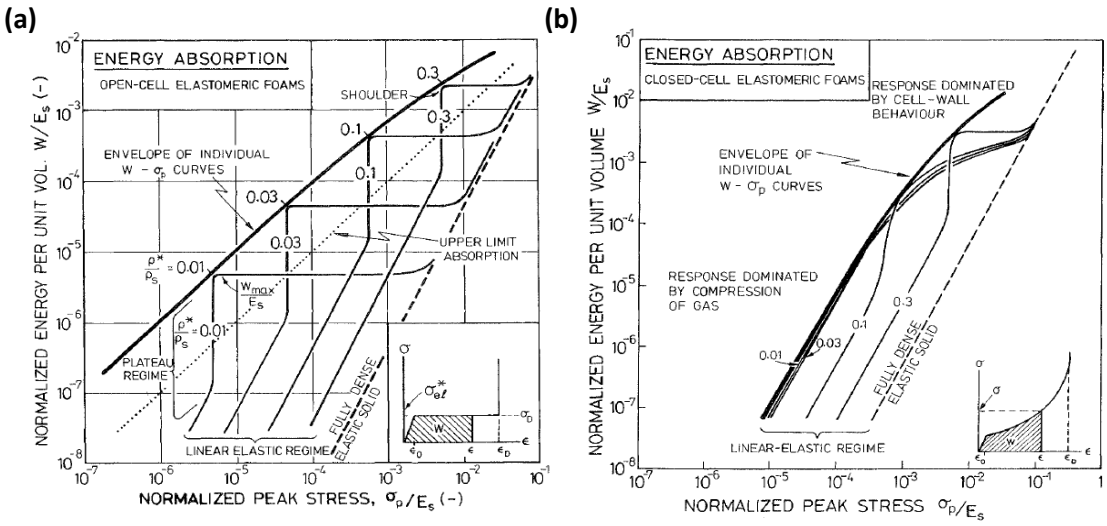

Figure 6.6. (a) The modelling of the energy-absorption diagram for open-cell elastomeric foams. The envelope line has a slope close to 1 at low stresses, falling to 0.85 at high stress. Viscous dissipation caused by the expulsion of pore fluid displaces the envelope to the right. (b) The modelling of the energy-absorption diagram is for closed-cell elastomeric foams. At high densities, compression of the gas in the cells becomes dominant ($p_0/E_s = 6.7\times10^{-4}$, corresponding to p_0 = 1 atmosphere and E_s=150 MN/m^2, for polyethylene) [209].

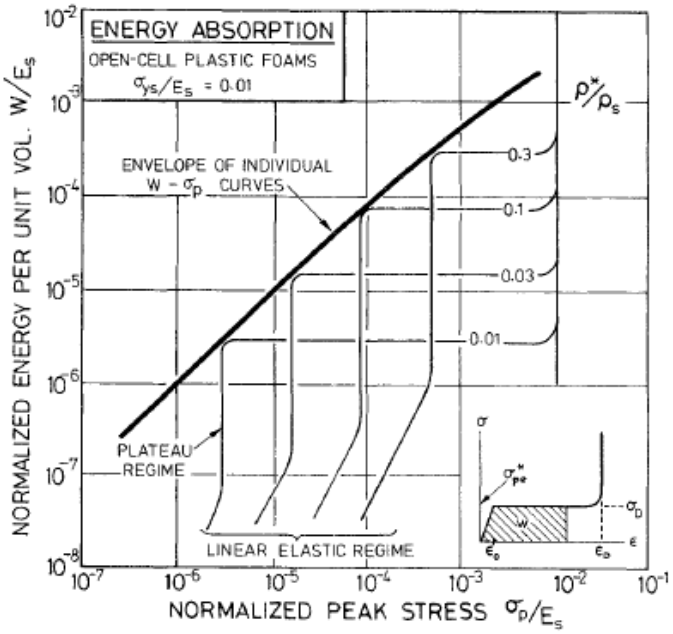

Figure 6.7. The modelling of the energy absorption diagram for plastic foams ($\sigma_{ys}/E_s = 0.01$) [209].

For the category of plastic foam-like structures, they behave as the open-cell plastic foams, whose deformation are caused by bending and stretching of the cell walls. The plastic foam-like structues are usually stiff and strong (Fig.6.7), and the linear-elastic regime energy is stored in the bending of the cell walls. As the strain increases, the plateau is also the important part of the strain-stress curve. In the regime, the energy is absorbed at a constant stress σ_{pl}^{*} as indicated in Fig.6.7.

6.3.1 Energy absorption

The laser-sintered s-CNT/PA12 composite exhibits strong toughness, and it can be a desirable candidate material to construct the plastic foam-like structures and optimze the energy absorption capability of structures. Therefore, s-CNT/PA12 powders were employed as original feeding materials to build the two groups of 3D structures.

The static compression tests were conducted on the 3D composite structures with a relative low strain rate of 6 mm/min. The strain-stress curves and energy-absorption diagrams were plotted, and the work done on each lattice corresponded to the area under its strain-stress curve. The densification strain of each lattice is identified at the strain with the $E_{\max} = \int_0^{\varepsilon} \frac{\sigma(\varepsilon)\mathrm{d}\varepsilon}{\sigma}$ [13]. The investigation of the static compression can provide guidance for the energy absorption capability of each type of lattices and their deformation behaviours under a certain loading conditions.

6.3.1.1 Truss lattices

The strain-stress curves of the dode-truss structures started with a linear-elastic regime and subsequently continued with a plateau regime, which was controlled by plastic collapse of the open-cell plastic foam. In the linear regime, the energy was stored

in the bending of struts, and then the plateau of the strain-stress curve ended abruptly at the densification strain ε_D. In the structure evolution of the deformation patterns of the dode-truss (Fig. 6.8 (a)), it was observed that the struts were stretched when the nodes tended to have plastic collapse.

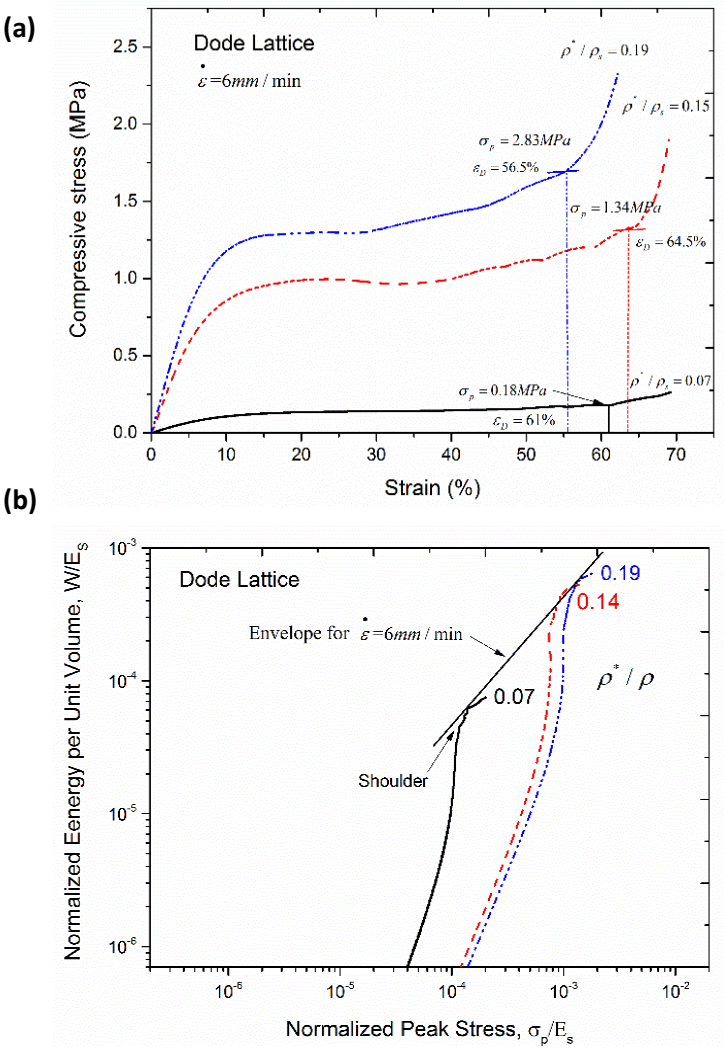

Figure 6.8. (a) The strain-stress curves of the dode-truss structures with different relative densities; (b) the experimental energy absorption diagram of energy per unit volume (W/E_s) versus peak stress (σ_p/E_s) for these dode-truss structures.

Upon the plateau regime, the energy absorption significantly increased while the applied stress gained a slight increase. The shoulder point of each energy-absorption

diagram suggested the optimum energy absorption per unit volume when the specific lattice sustained its maximum stress value ε_D. When the density was lower, the energy-absorption capability was significantly improved by increasing the density of the dode-truss. The dode-truss composed of the s-CNT/PA12 composite can offer an alternative solution for artificial plastic foams with the controllable stiffness, strength and energy-absorption capability.

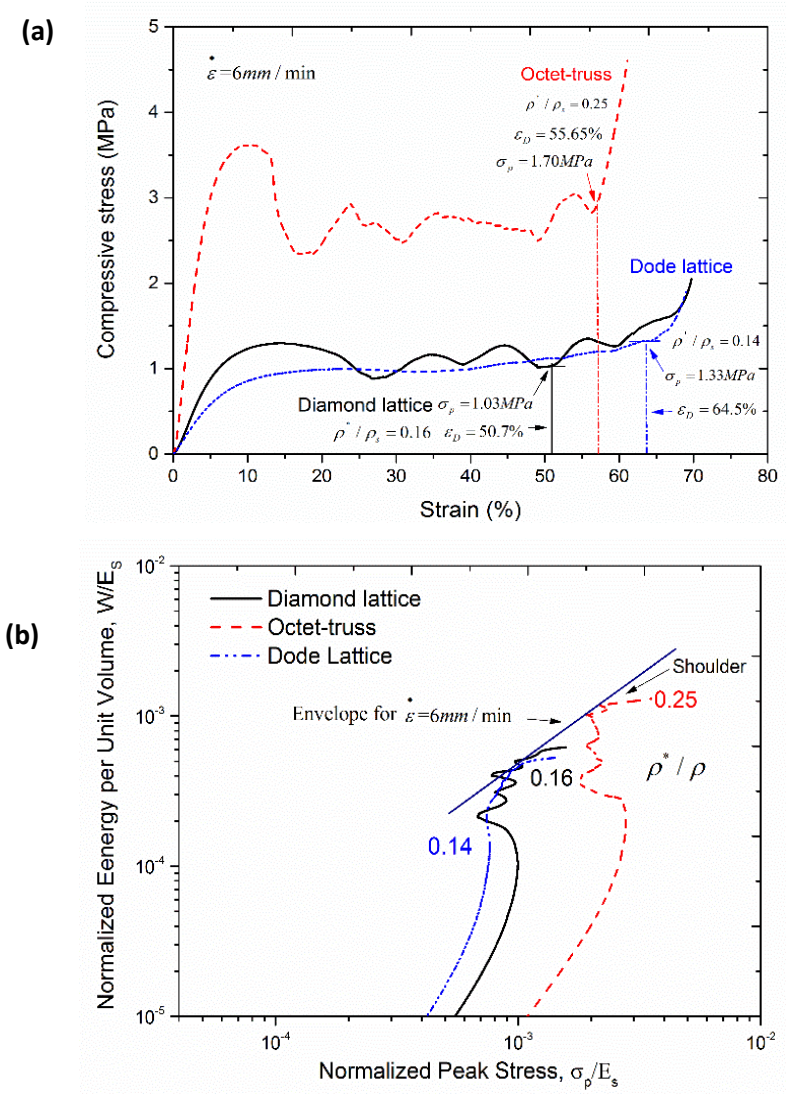

Figure 6.9.(a) The strain-stress curves of the diamond-truss, octet-truss and dode-truss upon static compression; (b) the experimental energy absorption diagram of energy per unit volume (W/E_s) versus peak stress (σ_p/E_s) for the diamond-truss, octet-truss and dode-truss.

As compared with the dode-truss structures, the diamond-truss and octet-truss showed the progressive deformation behaviour. In Fig.6.9 (a), the strain-stress curves of octet-truss and diamond-truss structures showed that the lattices approached a maximum compressive stress in the elastic regime, and then the strain-stress curve fluctuated within a large deformation strain until approaching the densification strain. The failure mechanism of the stretch-dominated lattice demonstrated that the critical shear failure occurred at the weak junctions of struts and subsequently the stress intensive range transferred to adjacent junctions.

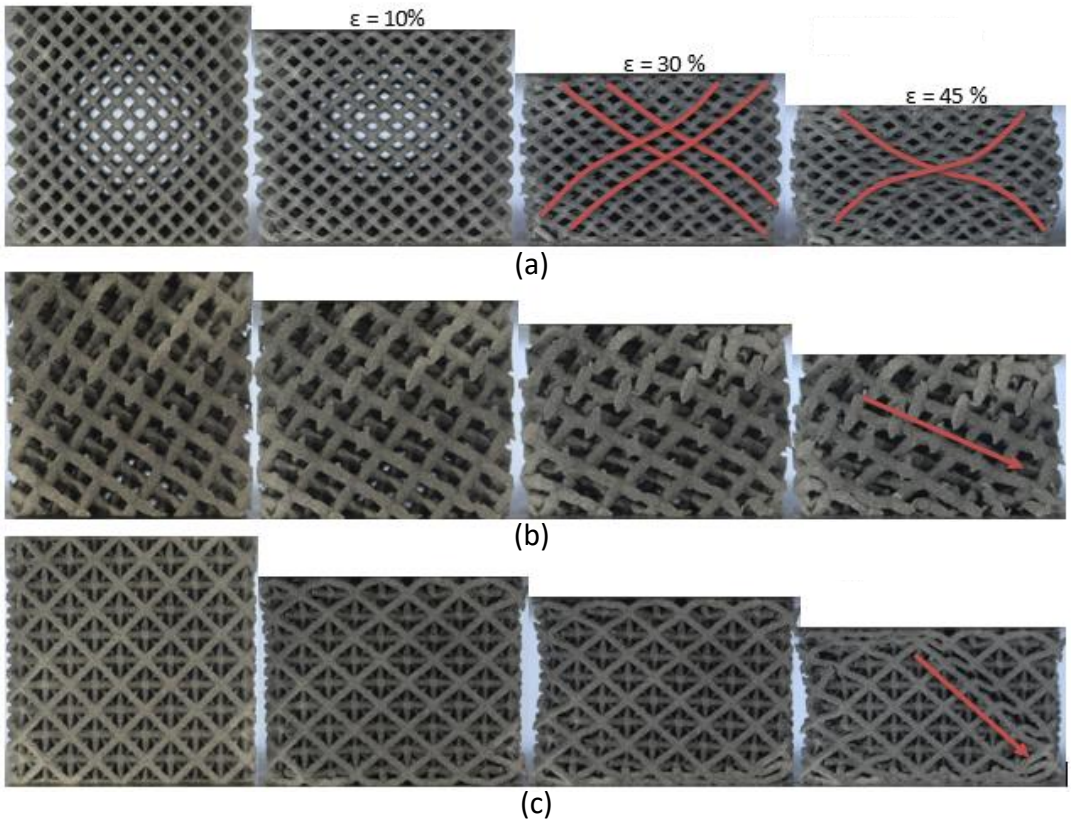

Figure 6.10. The optical images of the evolution of the deformation patterns for (a) dode-truss, (b) diamond-truss and (c) octet-truss under a static compression condition.

Meanwhile, the remaining trusses continued to carry load until their levels of compressive stress abruptly increased at the densification strains. Therefore, the

fluctuation of strain-stress curve of diamond-truss shows that this lattice sustained loading and absorbed energy during a progressive deformation process. The progressive energy absorption could be observed from the energy-absorption diagrams of the diamond-truss and octet-truss. However, the energy absorption per volume of stretch-dominated truss was not smoothly changing with the increase of applied stress. Therefore, such structures are not recommended as engineerable cellular lattices for energy absorption.

In summary, for the three groups of truss structures, the dode-truss (Fig. 6.10) exhibits the desirable deformation behaviour as the open-cell plastic foam. Such lattice design can be further customized for energy absorption corresponding to the applied stress and the expected energy absorption capability.

6.3.1.2 Auxetic lattices

For this group of auxetic lattices, the auxetic behaviour is dominated by the buckling-induced node rotation [161]. At the same time, the bending and stretching of the spherical shell units also retain the external loading and absorb energy during compression.

The strain-stress curves of auxetic *bcc*-12H lattices show that the compressive stresses significantly increased as the lattices were statically compressed. Especially, the dense lattice ($\rho^*/\rho \sim 0.33$) experienced a dramatic hardening effect when undergoing a large deformation. However, the energy-absorption capability can not be optimized due to the linear increasing behaviour of the compressive stress. As a result, no critical

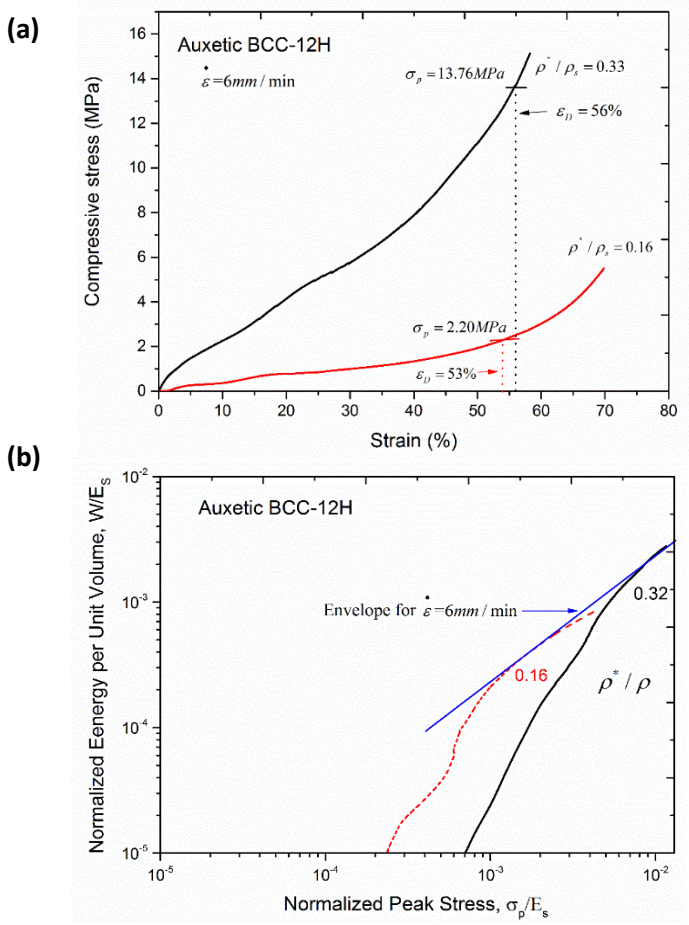

Figure 6.11.(a) The strain-stress curves of auxetic *bcc*-12H lattices upon static compression. (b) the experimental energy-absorption diagram of energy per unit volume W/E_s versus peak stress σ_p/E_s for the auxetic *bcc*-12H lattices.

shoulder of energy-absorption curves could be observed, and the increase of normalized energy per unit volume (W/E_s) was linearly proportional to the increase of compressive stress (σ_p/E_s). Thus, there is no optimal choice for the design of structure (*bcc*-12H) corresponding to a specific applied stress.

On the other hand, it is worthly to note that the buckling-induced axuetic behaviour was clearly observed through characterizing the evolution of deformation patterns. In Fig. 6.12, the denser lattice ($\rho^*/\rho \sim 0.33$) showed a critical negative Poisson's effect and deformed uniformaly due to the deforamtion dominated by buckling and bending of

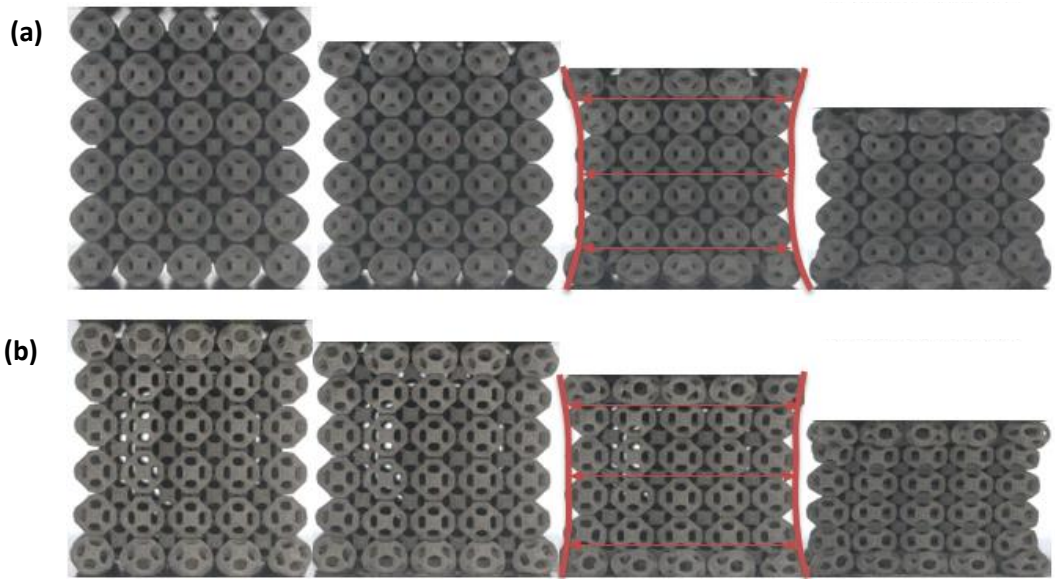

Figure 6.12. The optical images of the evolution of the deformation patterns for auxetic *bcc*-12H lattices with the relative densities of (a) 0.33 and (b) 0.16.

building blocks, whereas the lighter lattice ($\rho^*/\rho \sim 0.16$) showed the localized bending fractures at the top and bottom layers and its negative Poisson's effect was not as obvious as the denser one. The densitification of the denser lattice was mainly caused by buckling and bending, resulting in a significant increase of compressive stress upon a static loading.

In Fig. 6.13, the strain-stress curves of *sc*-12H lattices show a linear-elastic regime and continue with a plateau regime, which can retain the compressive stress with a slight increase but optimize the energy absorption capability of the lattices upon deformation. Therefore, the critical shoulders can be observed on the energy-absorption curves, which is the optimal choice of energy-absorption corresponding to the specific design. In addition, the localized fracture of the lighter *sc*-12H lattice ($\rho^*/\rho \sim 0.12$) is observed in Fig. 6.13 (b). The bottom layer of building block started to fracture due to bending failure of the spherical shell. Then, the layer-by-layer fracture occurred when

the structure sustained the compressive stress above a certain level.

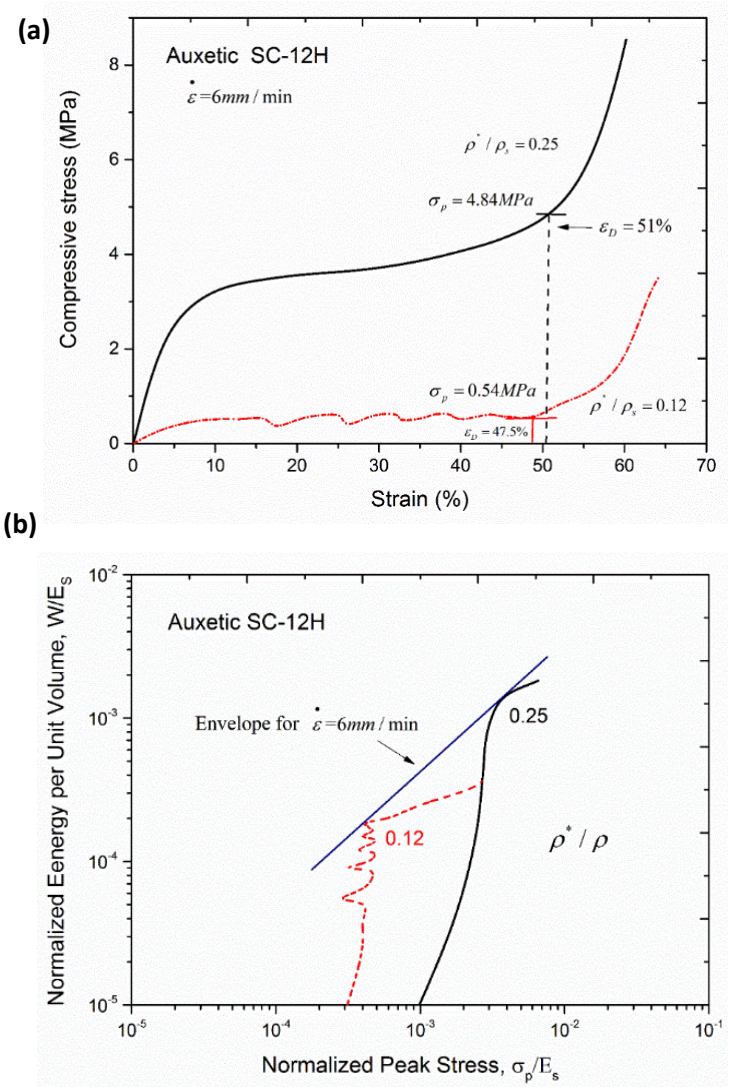

Figure 6.13. (a) The strain-stress curves of auxetic *sc*-12H lattices upon static compression; (b) the experimental energy-absorption diagram of energy per unit volume (W/E_s) versus peak stress (σ_p/E_s) for the auxetic *sc*-12H lattices.

Therefore, the progressive failure behaviours can be observed from the fluctuation of strain-stress curves. However, the deformation of the denser *sc*-12H lattice ($\rho^*/\rho \sim$ 0.25) was uniform and each building block also deformed due to bending of spherical shells. Such deformation behaviour wasalso observed during the compression of the

open-cell plastic foam and the dode-truss, which are proposed as the desirable candidate structures for energy absorption.

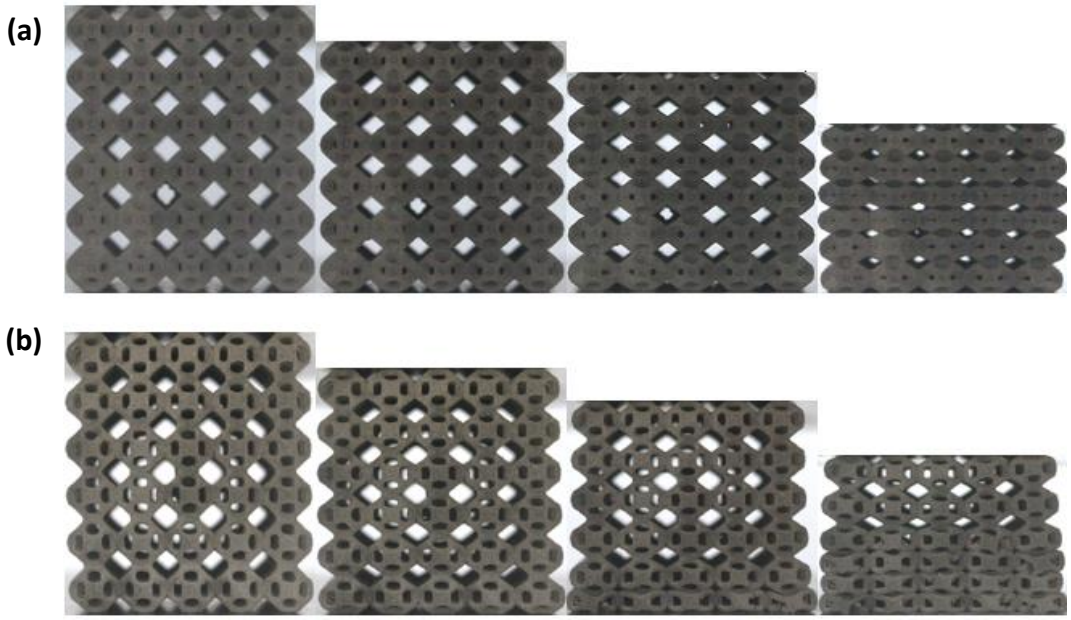

Figure 6.14. The optical images of the evolution of the deformation patterns for auxetic *sc*-12H lattices with the relative densities of (a) 0.25 and (b) 0.12.

As compared with the auxetic lattices of *bcc*-12H and *sc*-12H, the auxetic lattice of *bcc*-6H exhibited the impressive densification stress of 19.49 MPa and energy-absorption profile (Fig. 6.15). With a similar relative density ($\rho^*/\rho \sim 0.3$), the *bcc*-6H lattice showed much higher energy unit per volume (W/E_s) than the *bcc*-12H lattice, and a critical shoulder of the energy-absorption curve occurred for the *bcc*-6H lattice. This critical shoulder provides a useful indicator to determine the optimal level of applied stress and energy-absorption capability.

The evolution of the deformation patterns shows that the entire volume of this lattice shrank in the horizontal plane. The negative Poisson's ratio is a critical effect due to the buckling of *bcc*-12H lattices with the relative density of 0.3. The spherical shells

and the post-buckling effect of the lattice can sustain loading and keep absorbing energy. The strain-stress profiles demonstrate a deformation behaviour as closed-cell elastomer foams (Fig. 6.6 (b)). Therefore, the *bcc*-6H lattice possesses the high potential for the future impact protection and damping application due to its outstanding capability of energy absorption as compared with other designs.

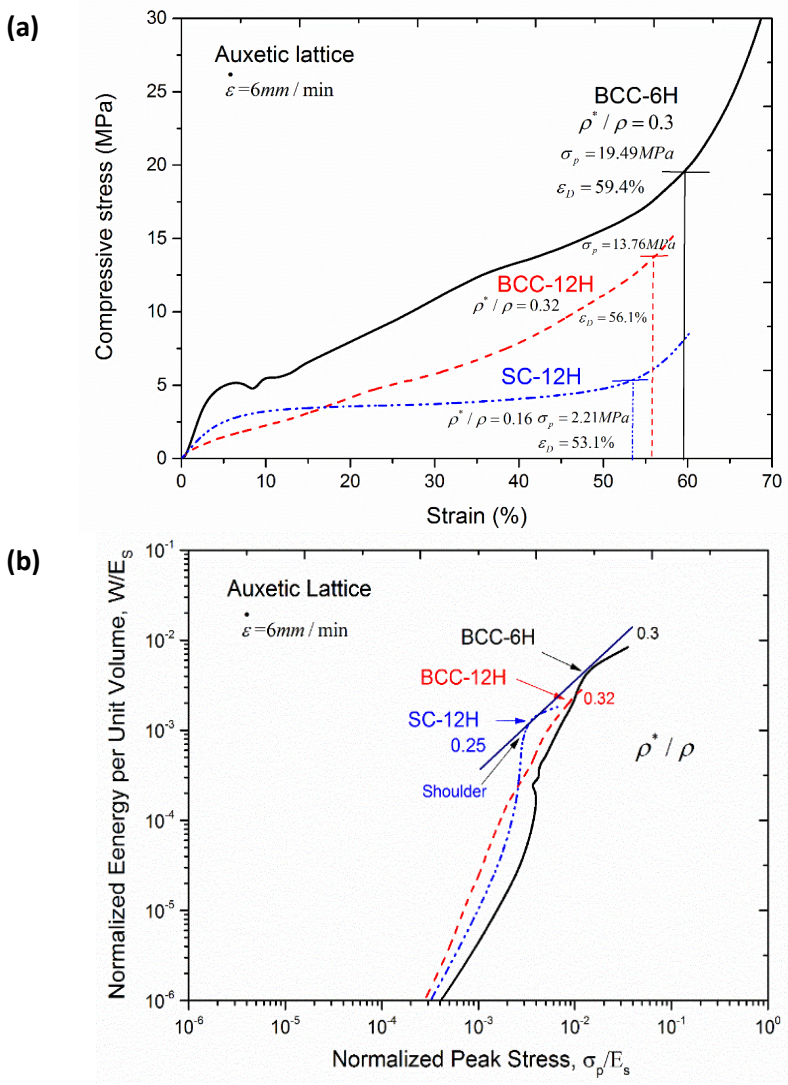

Figure 6.15. (a) The strain-stress curves of the auxetic *bcc*-6H, *bcc*-12H and *sc*-12H lattices upon static compression; (b) the experimental energy-absorption diagram of energy per unit volume (W/E_s) versus peak stress (σ_p/E_s) for the auxetic *bcc*-6H, *bcc*-12H and *sc*-12H lattices.

Figure 6.16. The optical images of the evolution of the deformation patterns for auxetic *bcc*-6H lattices with the relative densities of 0.3.

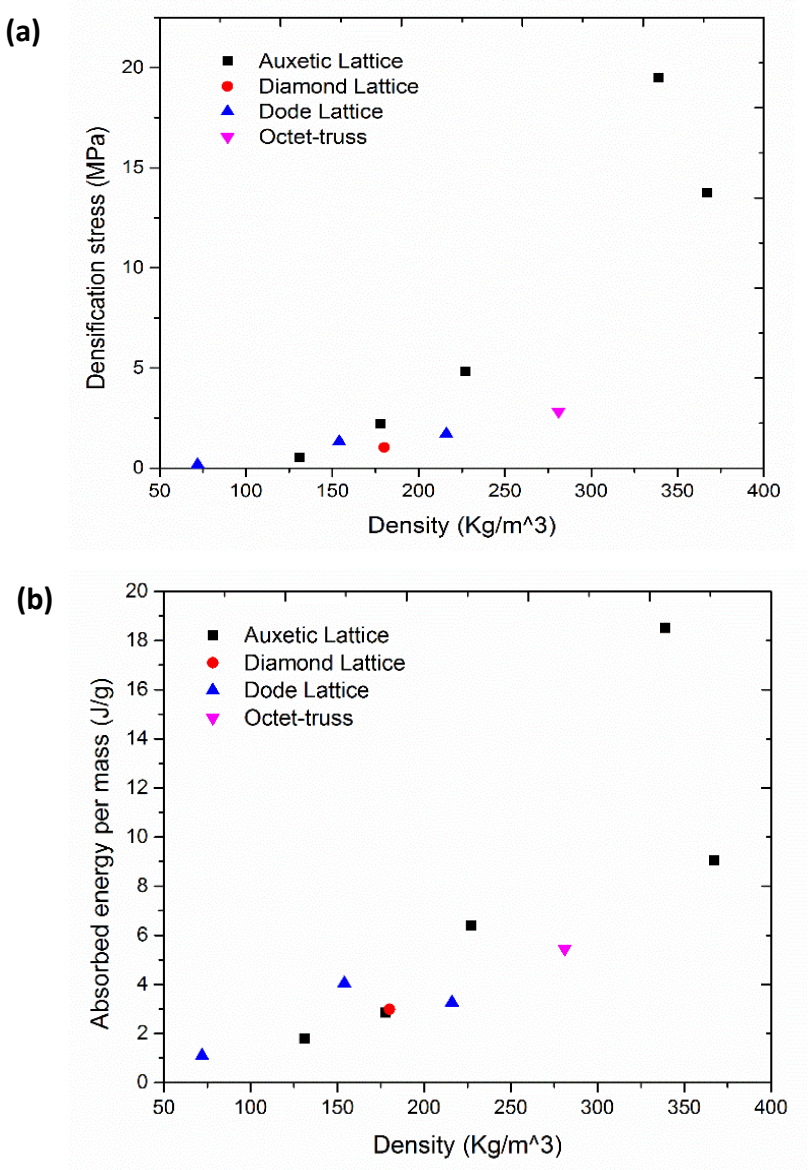

Figure 6.17. (a) The diagram of densification stress of various lattices versus lattice density. (b) The diagram of absorbed energy per mass versus lattice density.

The energy absorbed by unit gram and the densification stress of the investigated truss and auxetic structures are demonstrated in Fig.6.17. The diagram of densification stress versus lattice density shows that the densification stresses of auxetic lattices were dramatically enhanced by strengthening their densities, as compared with that of truss lattices. Thus, the absorbed energy per mass of the auxetic lattice significantly increased as the density increased.

6.3.1.3 Design charts

To illustrate the mechanical performances of the laser-sintered 3D composite lattices, the Ashby charts of compressive strength and gravimetric energy versus density are plotted to compare the properties of auxetic and truss lattices with other 3D-printed materials or structures (Fig.6.18).

In Fig.6.18 (a), the laser-sintered s-CNT/PA12 lattices exhibit a similar strength versus density performance as the SiC reinforced composites, which are printed by a direct writing technology as reported by Compton and Lewis [179]. As compared with the wood or honeycomb structures, the auxetic lattices have the merits of isotropic mechanical strength and their deformations are also induced by the entire structural buckling and post-buckling effects. Therefore, the tough and ductile s-CNT/PA12 composite could offer its auxetic lattices with high potential for energy absorption purpose.

In Fig. 6.18 (b), the auxetic lattices can cover a wide range of gravimetric energies within a relatively narrow change of density as compared with the truss lattices. It is worthy to note that the energy-absorption capability of s-CNT/PA12 auxetic lattices is

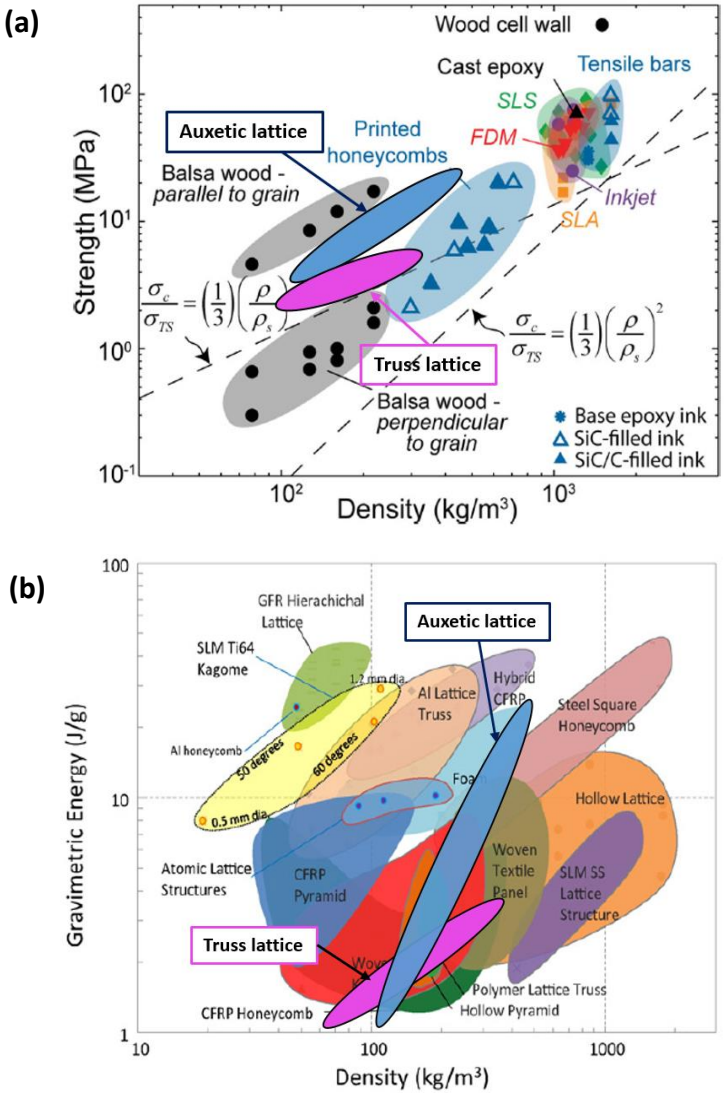

Figure 6.18. (a) The compression strength of 3D-printed lattices by the direct writing and SLS as compared with that of bulky materials [1]; (b) the energy-absorption capability of s-CNT/PA12 composite lattices as compared with other most advanced metallic and composite designs [158].

comparable with those of the stainless-steel lattices, hybrid CFRP, and aluminum alloy lattices. Only the titanium alloy lattices printed by SLM or EBM can exhibit the better energy-absorption performance than the auxetic s-CNT/PA12 lattices. As a small loading of CNTs (<1 wt%) is applied in the s-CNT/PA12 composite development, the manufacturing of the s-CNT/PA12 composite lattices by SLS is much cost-effective than

the fabrication of titanium alloy or other metallic lattices by SLM or EBM. The CNTs-reinforced composites can be an alternative material in 3D printing to substitute the costly metallic parts for energy absorption.

In Fig. 6.19, the Ashby charts of compressive strength for the conventional materials are demonstrated and the coverages of auxetic and cellular lattices are noted with the blue and red regions, respectively. It can be observed that the laser-sintered composite lattices are distributed within the overlapped ranges of composite and porous structures, such as foam and honeycomb structures, which is commonly used as lightweight materials in aerospace and automobile industries. Moreover, 3D printing technology offers the freedom of design and manufacturing, and it is possible to tailor and control the energy absorption and specific strength through the topology of structures and the optimization of material selection.

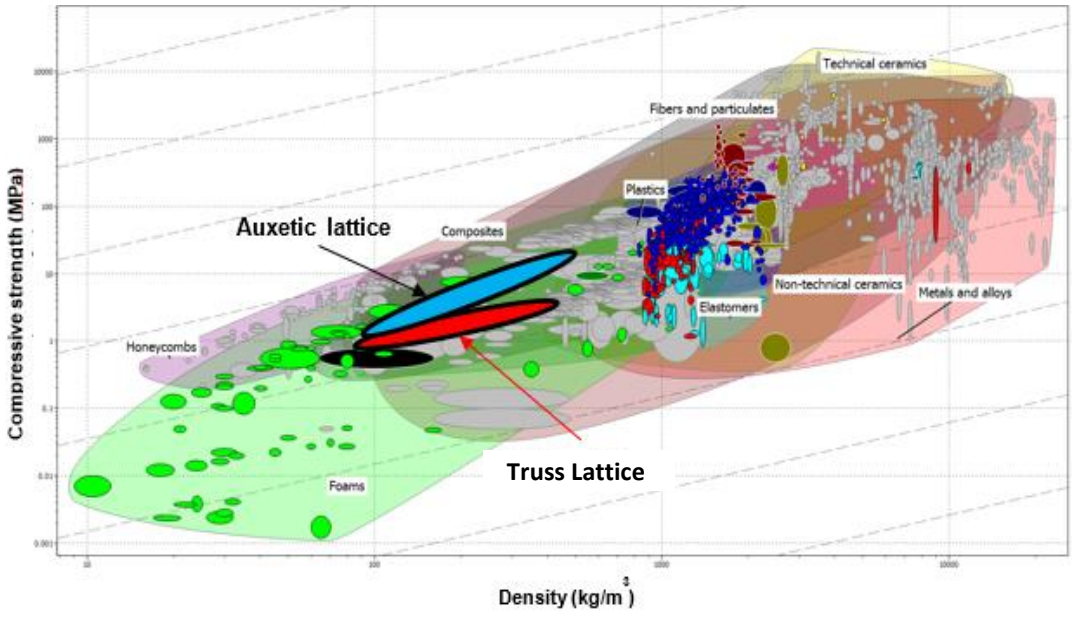

Figure 6.19. The compressive strength versus density for auxetic and truss lattices with s-CNT/PA12 composites as plotted in an Ashby chart to compare with other convetional materials. Material properties are obtained from the Softewere CES Edupack 2014 (Granta Design), and the laser-sintered lattices are indicated by red (truss lattice) and blue (axuetic lattice) regions.

Impact protection is one of the beneficial usages from energy absorption. Herein, the representative nanocomposite lattices were investigated and their energy absorption capability under static loading was evaluated. This work is helpful to selecting the group of functional lattices which has large potential for further impact energy absorption. The underlying mechanism of impact absorption of lattice materials is a complicated system. Firstly, the deformation modes of the lattices, such as bending-, stretching- and buckling-dominated ones, determine their suitability for energy absorption. Secondly, the failure modes of the lattices such as progressive fractures and continuous plastic yielding are highly dependent on the structural design, loading rate and constitutive materials. Thirdly, the fabrication defects create the localized weakness and vary with the process parameters and feeding materials. Inevitable voids and anisotropic mechanical properties are usually observed in laser-sintered products. This work serves to provide a comparison of energy absorption capability diagrams for truss-lattices and auxetic-lattices under static loading and to experimentally prove the advantage of auxetic lattices in energy consumption and guide the future structural design and optimization for impact energy absorption.

6.3.2 Energy dissipation

The elastomeric foams composed of highly porous TPU exhibit an attractive behaviour of withstanding a large strain upon cyclic compressive loading. Therefore, the laser-sintered TPU lattices could be a type of artificial foam, which may possess the energy-absorption capability for protective packaging and mechanical energy dampers. The deformation and energy dissipation behaviours of the soft 3D auxetic TPU

structures are investigated.

The laser-sintered TPU auxetic structures are shown in Fig. 11 (a-c) corresponding to the designs of *bcc*-6H, *sc*-12H and *bcc*-12H. The basic units were printed in 3D to form Bucklicrystals with a negative Poisson's ratio, and the *bcc*-6H lattice was uniaxially compressed to investigate its buckled configurations as shown in Fig. 6.20 (d). The deformation of *bcc*-6H array was captured by taking photos every 5 s at the applied normal strain rate of 1 mm/s, and the recovery of structure was also investigated upon release of the applied vertical displacement. The lateral boundaries of the laser-sintered TPU structure bent inwards, showing a clear indication of negative Poisson's ratio. Both transverse strains ε_{xx} and ε_{yy} decreased, indicating that the structure contracts in both lateral boundaries. The Poisson's ratios are calculated from the engineering strains as $\nu_{ij} = -\varepsilon_{ii}/\varepsilon_{jj}$. The evolutions of ν_{xz} and ν_{yz} are plotted as the functions of ε_{zz} as shown in Fig. 6.20 (f). Initially, both Poisson's ratios decreased gradually till $\varepsilon_{zz} = -0.01$, and then dramatically dropped and reached the value of $\nu \approx -0.6$ and plateau at $\varepsilon_{zz} = -0.02$. This demonstrated that the laser-sintered Bucklicrystal could maintain the auxetic behavior over a wide range of deformation.

The corresponding compressive strain-stress curve indicates that the structural transformations induced by instabilities occurred when the Bucklicrystal was compressed at the various levels of strains.

Such 3D soft auxetic lattices possess high potential applications in damping, energy dissipation and mechanical actuation. The cyclic loading and unloading of the *sc*-12H structure was conducted to investigate its compressive behaviour and recoverability. The lattice structure underwent a softening effect over the first cycle, and became slightly

compliant from second cycle onwards. The recovery curves followed the same path regardless of loading cycles. The residual strain of the entire *sc*-12H structure maintained at 2~3 %, which was much lower than the instant recoverable strain of the laser-printed neat PU in dog-bone shape [5]. Therefore, the strain-stress loops exhibited

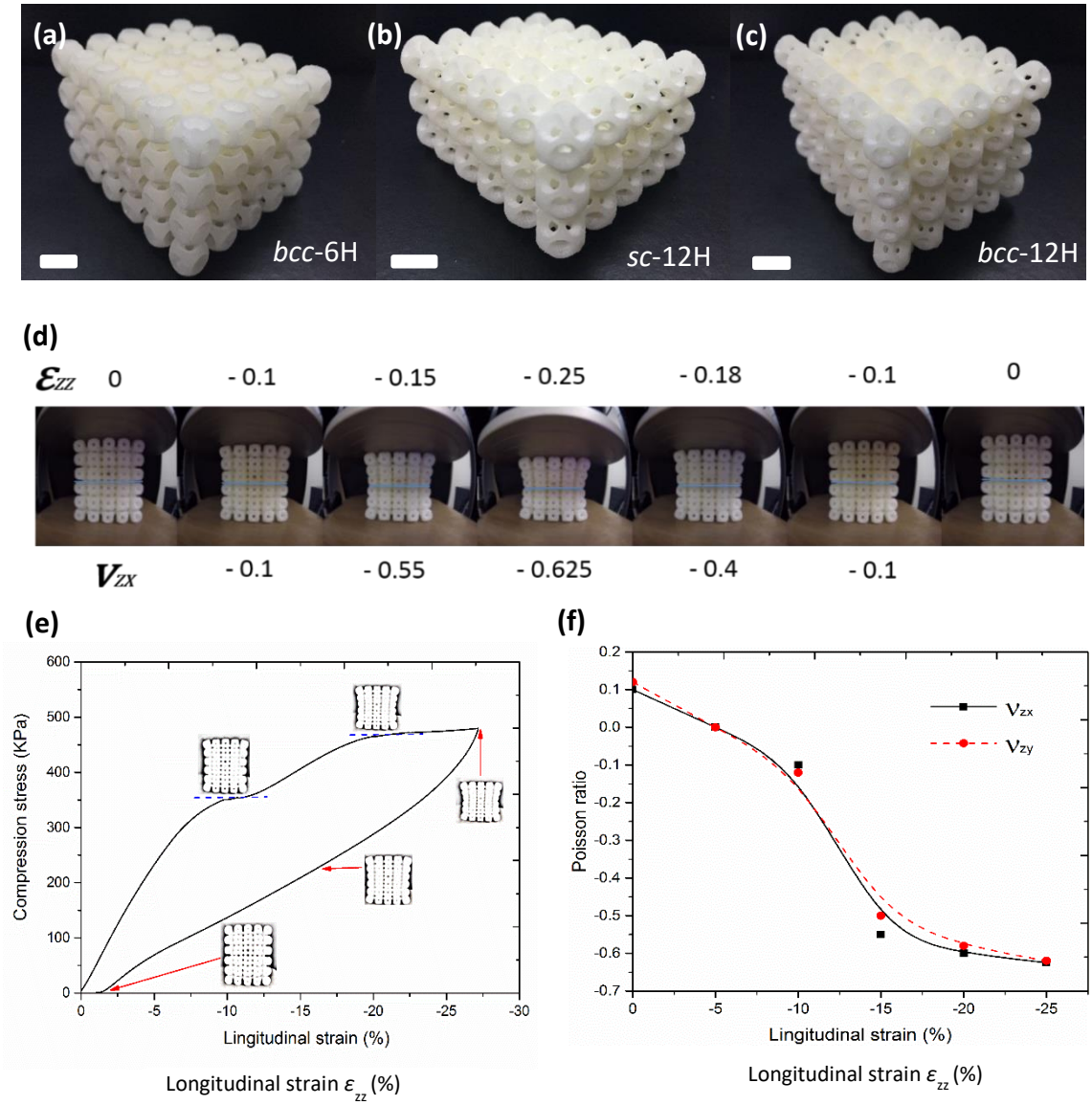

Figure 6.20. 3D complex auxetic lattices: (a) *bcc*-6H, (b) *sc*-12H and (c) *bcc*-12H (The scale bars are 1 cm); (d) the photos of the progressive deformation of *bcc*-6 hole structures; (e) the compression-relaxation strain-stress curve and (f) two Poisson's ratios of ν_{xz} and ν_{yz} versus the longitudinal strain ε_{zz} of *bcc*-6H structure.

highly recoverable and repeatable behaviors, as the TPU retained the elastomeric properties even after being constructed into the complex 3D geometries by laser sintering. The energy dissipation of each cycle could be predicted through a hyper-elastic model with the Mullins effect as investigated by Shen *et al.* [210], which considered the softening effect at the first loop and predicted the cycling compression-relaxation behaviours in energy aspects. Therefore, a proper model integrated with the non-linear behaviours of the material and structure can effectively guide a new generation of 3D design for AM, and the systematic selection and evaluation process of materials are beneficial to the process development and optimization of the manufacturing technique.

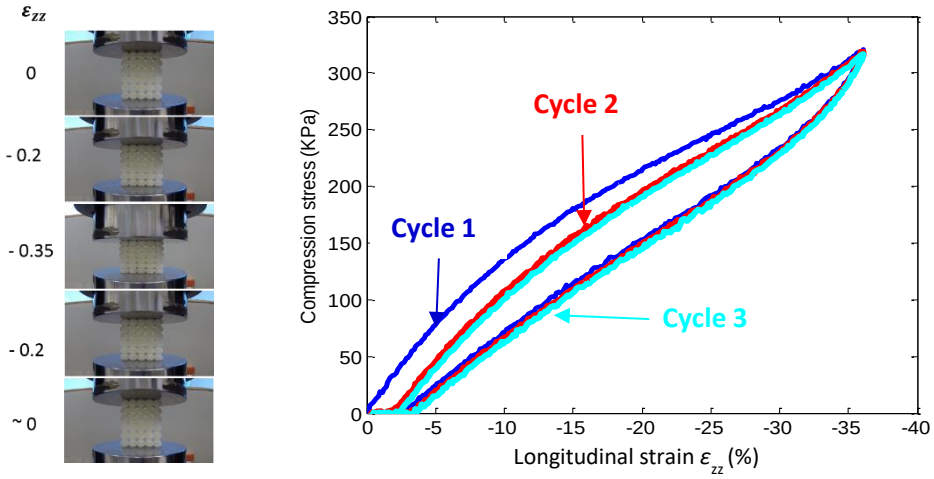

Figure 6.21. The 3 cycles of strain-stress curve for the *sc*-12H of lattice structure upon the loading and unloading at a strain rate of 1 mm/s.

Chapter 7 Conclusions and recommendations

A systematic methodology has been proposed toward innovative formulation and manufacturing of polymeric composite powders and their optimization for the SLS process. The investigation of energy absorption and dissipation of functional design was conducted by the integration of the advantages of composite materials with those of lightweight structures.

7.1 Conclusions

This thesis research has studied the formulation and approach of manufacturing of MWCNTs-reinforced polymeric powders and the effective process optimization of the SLS system. Through the design and development of the 3D auxetic and cellular lattices, the potential application of energy absorption of the CNT/PA12 and TPU materials has been explored by the repeated compressive testing. These studies would offer important guidance for the new type of material development for the SLS system and take the advantages of both materials and structures to optimize the performance for a specific functional application.

The surfactant-facilitated latex technique has been employed to uniformly coat a layer of functionalized CNTs on the surface of the polymeric powders. This method could retain the original geometric configuration of the neat polymeric powders, and these composite powders could maintain similar flowability as the original polymeric ones. The CNTs-coated polymeric powders could be applied in different types of powder-based manufacturing processes, such as powder injection moulding and SLS to

fabricate composite parts or components.

The systematic material evaluation and process optimization have been conducted on the CNTs-coated PA12 and TPU powders. The polymer properties and powder behaviours played significant roles in determining the behaviour of the polymer and its composite powders upon laser sintering. The fundamental thermal, rheological and optical properties have been measured to predict the thermal absorption and fusion behaviours of powders. A simplified theoretical model has been proposed to predict the effective working range of the input laser energy through identifying the stable sintering range of each type of powders. It has been helpful to narrow down the working range of the laser energy and effectively identify the set of parameters for optimization purposes in the new material development. Additionally, it was observed that the mechanical properties of the laser-sintered polymer and its composites were positively correlative to the effectiveness of sintering. The strength and Young's modulus of laser-sintered PA12, CNT/PA12 and TPU tended to saturate when the input laser energy per volume has above the energy required to fully melt the polymer in unit volume. For TPU, the stable range was quite narrow as compared with PA12, and the overheating of the laser energy might cause the degradation of its polymer chains, leading to adverse effects on its mechanical properties.

The electrical and thermal conductivities of CNTs-reinforced polymeric composites have been systematically characterized, and the underlying enhancement mechanisms of CNTs within thermoplastics that were manufactured by different techniques such as SLS and hot-moulding have been investigated through microstructure characterization, thermal and rheological measurements. The CNTs-reinforced TPU and PA12

composites fabricated by laser sintering exhibited significant enhancements of electrical conductivity as compared with the hot-moulded composites. However, the hot-moulded CNT/polymer composites showed much higher thermal conductivities than the laser-sintered composites. Such phenomena indicated that electrical and thermal conductions of CNTs within the polymer matrix highly depended on the manufacturing processes, as the different microstructures induced by the manufacturing processes result in the different electrical and thermal enhancement mechanisms. Therefore, it was worthy to note that the SLS process could induce CNT/PA12 and CNT/TPU composites with segregated microstructures at an ultra-small weight loading, and such composites were approaching the conductive range of materials for the anti-static applications.

The energy absorption capability of the CNT/PA12 composites and soft TPU lattices have been investigated through the comparison of different types of designs such as cellular and auxetic structures. The laser-sintered CNT/PA12 composites showed excellent enhanced mechanical strength and toughness as compared with the neat PA12, leading to the inspiration that this tough composite material can be applied to construct 3D lattice structures for destructive energy absorption purpose. In addition, the soft TPU materials were applied to print the non-destructive auxetic lattices which behaved as dampers or mechanical actuators over cyclic loading. The energy absorption capability of the soft TPU lattices was evaluated to provide guidance for the design of wearable products such as the insoles of shoes and protective clothes.

In summary, a systematic research methodology for AM techniques has been developed based on the framework of the material-process-design-application. This approach for the SLS process is rooted in the manufacturing process of composite

powders, develops the composite powders for the laser-sintering process, and then purposely utilizes the functionality of laser-sintered polymer or its composite for the structure designs that couples the advantages of both materials and structures. Meanwhile, this method is generally applicable to different types of AM techniques by integrating the merits of advanced materials and functional designs, which may produce the products with unpredictable performances and open a new window for future manufacturing system integration.

7.2 Recommendations

A comprehensive study of MWCNTs-reinforced polymeric materials for the SLS process has been conducted, and the systematic research methodology of the material development and process optimization has been demonstrated to fabricate the 3D lattice structures for the energy absorption purpose. However, there are still many hurdles ahead before the nanocomposite materials could match the stringent requirements and be widely applicable in the aerospace and automobile applications. Furthermore, the efforts required to develop and customize the new type of materials are still labour intensive and expensive. Based on the research works achieved, potential future researches are recommended as follows.Powdering technology for composite materials plays a key role in engineering the microstructure and configuration of powders. The primary process to manufacture the composite powders can affect the microstructures of the subsequently produced products. Coating the powders with nanoparticles can produce a unique composite with the segregated microstructures, which is highly beneficial for the electrical conductivity of a composite. On the other hand, if the fillers

can be embedded into the polymeric powders, the fillers can be uniformly and homogeneously distributed within the polymer matrix to reinforce the mechanical properties significantly. Therefore, the different approaches to manufacturing polymeric powders can achieve the desirable microstructures, and then the composite powders could be utilized to fabricate the composite products with superior performances for the end-use industrial applications. Hence, the future study can focus on the combination of various manufacturing processes for formulating new materials and achieving desirable microstructures of composite powders.

A theoretical modelling of the laser scanning process will provide effective guidance for process parameter optimization. An accurate prediction of temperature distribution upon scanning and dynamic fusion state of powders can offer a computational solution for process parameters in the experimental design instead of the empirical optimization of processing parameters, which is based on an iteration of trial and error builds. Such a computational method can be generally applicable to predicting the sintering behaviours of various types of polymeric materials, once the fundamental thermal, optical and rheological properties of polymeric powders are characterized and implemented into the theoretical model. Thus, the combination of theoretical and experimental methods will minimize time and material cost, especially for non-recyclable polymers.

The laser-sintered structural composites have attractive applications in mechanics and acoustics. AM techniques offer the design and manufacturing freedom to fabricate customized products for end-use applications. The design principles derived from material and structure mechanics suggested that the products manufactured by the SLS process are possible to achieve a digitized mapping of energy absorption for impact

protection purpose. Meanwhile, the micro to macro scale of laser-sintered structures can induce acoustic response corresponding to the respective range of wavelengths. Therefore, the tunable and engineerable 3D complex products could offer the solution to control or modify the sound propagation for the applications in building construction and interior decoration.

AM techniques will become the mainstream technologies in the high-end manufacturing for high value-added production of components or products. The whole chain of feeding material, manufacturing process and product design will be integrated to establish an industrial system of engineering.

References

[1] Chua CK, Leong KF. 3D Printing and Additive Manufacturing: Principles and Applications. 5th Edition, World Scientific Publishing 2017.

[2] Ligon SC, Liska R, Stampfl J, Gurr M, Mülhaupt R. Polymers for 3D Printing and Customized Additive Manufacturing. Chemical Reviews. 2017;117:10212-90.

[3] Bai J, Goodridge R, Yuan S, Zhou K, Chua C, Wei J. Thermal Influence of CNT on the Polyamide 12 Nanocomposite for Selective Laser Sintering. Molecules. 2015;20:19041.

[4] Yuan S, Bai J, Chua C, Wei J, Zhou K. Material evaluation and process optimization of CNT-coated polymer powders for selective laser sintering. Polymers. 2016;8:370.

[5] Yuan S, Bai J, Chua CK, Zhou K, Jun W. Characterization of creeping and shape memory effect in laser sintered thermoplastic polyurethane. Journal of Computing and Information Science in Engineering 2016;16:041007.

[6] Gaikwad S, Tate J, Theodoropoulou N, Koo J. Electrical and mechanical properties of PA11 blended with nanographene platelets using industrial twin-screw extruder for selective laser sintering. Journal of Composite Materials. 2012.

[7] Lao SC, Yong WY, Nguyen K, Moon TJ, Koo JH, Pilato LA, et al. Flame-retardant polyamide 11 and 12 nanocomposites: processing, morphology and mechanical properties. Journal of Composite Materials. 2010.

[8] Fanselow S, Emamjomeh SE, Wirth KE, Schmidt J, Peukert W. Production of spherical wax and polyolefin microparticles by melt emulsification for additive manufacturing. Chemical Engineering Science. 2016;141:282-92.

[9] Hao L, Savalani M, Zhang Y, Tanner K, Harris R. Selective laser sintering of hydroxyapatite reinforced polyethylene composites for bioactive implants and tissue scaffold development. Proceedings of the Institution of Mechanical Engineers, Part H: Journal of Engineering in Medicine. 2006;220:521-31.

[10] Rimell JT, Marquis PM. Selective laser sintering of ultra high molecular weight polyethylene for clinical applications. Journal of Biomedical Materials Research. 2000;53:414-20.

[11] Verbelen L, Dadbakhsh S, Van den Eynde M, Strobbe D, Kruth JP, Goderis B, et al. Analysis of the material properties involved in laser sintering of thermoplastic polyurethane. Additive Manufacturing. 2017;15:12-9.

[12] Yuan S, Shen F, Bai J, Chua CK, Wei J, Zhou K. 3D soft auxetic lattice structures fabricated by selective laser sintering: TPU powder evaluation and process optimization. Materials & Design. 2017;120:317-27.

[13] Bates SRG, Farrow IR, Trask RS. 3D printed polyurethane honeycombs for repeated tailored energy absorption. Materials & Design. 2016;112:172-83.

[14] Raasch J, Ivey M, Aldrich D, Nobes DS, Ayranci C. Characterization of polyurethane shape memory polymer processed by material extrusion additive manufacturing. Additive Manufacturing. 2015;8:132-41.

[15] Şirin K, Doğan F, Çanlı M, Yavuz M. Mechanical properties of polypropylene (PP) + high-density polyethylene (HDPE) binary blends: Non-isothermal degradation kinetics of PP + HDPE (80/20) Blends. Polymers for Advanced Technologies. 2013;24:715-22.

[16] Hao L, Savalani MM, Zhang Y, Tanner KE, Harris RA. Selective laser sintering of hydroxyapatite reinforced polyethylene composites for bioactive implants and tissue scaffold development. Proceedings of the Institution of Mechanical Engineers, Part H: Journal of Engineering in Medicine. 2006;220:521-31.

[17] Martin JP. An investigation of the microstructure and properties of a cryogenically mechanically alloyed polycarbonate- poly(ether ether ketone) system: State University 2001.

[18] Plummer K, Vasquez M, Majewski C, Hopkinson N. Study into the recyclability of a thermoplastic polyurethane powder for use in laser sintering. Proceedings of the Institution of Mechanical Engineers Part B Journal of Engineering Manufacture. 2012.

[19] Tan KH, Chua CK, Leong KF, Cheah CM, Gui WS, Tan WS, et al. Selective laser sintering of biocompatible polymers for applications in tissue engineering. Bio-Medical Materials and Engineering. 2005;15:113-24.

[20] Yuan M, Diller TT, Bourell D, Beaman J. Thermal conductivity of polyamide 12 powder for use in laser sintering. Rapid Prototyping Journal. 2013;19:437-45.

[21] Liu B, Bai P, Li Y. Post treatment process and selective laser sintering mechanism of polymer-coated Mo powder. Open Materials Science Journal. 2011;5:4.

[22] Shi Y, Chen J, Wang Y, Li Z, Huang S. Study of the selective laser sintering of polycarbonate and postprocess for parts reinforcement. Proceedings of the Institution of Mechanical Engineers, Part L: Journal of Materials Design and Applications. 2007;221:37-42.

[23] Yan C, Shi Y, Yang J, Liu J. Preparation and selective laser sintering of nylon-12 coated metal powders and post processing. Journal of Materials Processing Technology. 2009;209:5785-92.

[24] Athreya SR. Processing and characterization of carbon black-filled electrically conductive nylon-12 nanocomposites produced by selective laser sintering. United State: Georgia Institute of Technology; 2010.

[25] Chen DZ, S. C. Lao, J. H. Koo, M. Londa, and Z. Alabdullatif. Powder processing and properties characterization of polyamide 11-graphene nanocomposites for selective laser sintering. In Proc 2010 solid freeform fabrication symposium. Austin, TX, USA2010. p. 2.

[26] D. Z. Chena, S. C. Lao, J. H. Koo, M. Londaa, Alabdullatif Z. Powder processing and properties characterization of polyamide 11-graphene nanocomposites for selective laser sintering. Proc 2010 solid freeform fabrication symposium, Austin, TX, August 2010.

[27] Shuai C, Feng P, Cao C, Peng S. Processing and characterization of laser sintered hydroxyapatite scaffold for tissue engineering. Biotechnol Bioproc E. 2013;18:520-7.

[28] Sinha Ray S, Okamoto M. Polymer/layered silicate nanocomposites: a review from preparation to processing. Progress in Polymer Science. 2003;28:1539-641.

[29] Bourell DL, Manthiram A, Marcus HL. Selective laser sintering using nanocomposite materials. Google Patents; 1995.

[30] Smalley RE, Dresselhaus MS, Dresselhaus G, Avouris P. Carbon nanotubes: synthesis, structure, properties, and applications: Springer Science & Business Media; 2003.

[31] Balandin AA. Thermal properties of graphene and nanostructured carbon materials. Nature Materials. 2011;10:569-81.

[32] Berber S, Kwon YK, Tomanek D. Unusually high thermal conductivity of carbon nanotubes. Physical review letters. 2000;84:4613-6.

[33] Ding P, Zhuang N, Cui X, Shi L, Song N, Tang S. Enhanced thermal conductive property of polyamide composites by low mass fraction of covalently grafted graphene nanoribbons. Journal of Materials Chemistry C. 2015;3:10990-7.

[34] Wu C, Huang X, Wang G, Lv L, Chen G, Li G, et al. Highly conductive nanocomposites with three-dimensional, compactly interconnected graphene networks via a self-assembly process. Advanced Functional Materials. 2013;23:506-13.

[35] Song K, Zhang Y, Meng J, Green E, Tajaddod N, Li H, et al. Structural polymer-based carbon nanotube composite fibers: understanding the processing–structure–performance relationship. Materials. 2013;6:2543.

[36] Zhu W, Yan C, Shi Y, Wen S, Liu J, Wei Q, et al. A novel method based on selective laser sintering for preparing high-performance carbon fibres/polyamide12/epoxy ternary composites. Scientific Reports. 2016;6:33780.

[37] Compton BG, Lewis JA. 3D-Printing of Lightweight Cellular Composites. Advanced Materials. 2014;26:5930-5.

[38] Bauer J, Schroer A, Schwaiger R, Kraft O. Approaching theoretical strength in glassy carbon nanolattices. Nature Materials. 2016;15:438-43.

[39] Lin D, Nian Q, Deng B, Jin S, Hu Y, Wang W, et al. Three-dimensional printing of complex structures: man made or toward nature. ACS Nano. 2014;8:9710-5.

[40] Chang CM, Liu YL. Electrical conductivity enhancement of polymer/multiwalled carbon nanotube (MWCNT) composites by thermally-induced defunctionalization of MWCNTs. ACS Applied Materials & Interfaces. 2011;3:2204-8.

[41] Chen Y, Zhao Y, Liang Z. Solution processed organic thermoelectrics: towards flexible thermoelectric modules. Energy & Environmental Science. 2015;8:401-22.

[42] Dong L, Makradi A, Ahzi S, Remond Y, Sun X. Simulation of the densification of

semicrystalline polymer powders during the selective laser sintering process: Application to Nylon 12. Polym Sci Ser A. 2008;50:704-9.

[43] Natarajan B, Lachman N, Lam T, Jacobs D, Long C, Zhao M, et al. The evolution of carbon nanotube network structure in unidirectional nanocomposites resolved by quantitative electron tomography. ACS Nano. 2015.

[44] Kim JH, Lee S, Wajahat M, Jeong H, Chang WS, Jeong HJ, et al. Three-dimensional printing of highly conductive carbon nanotube microarchitectures with fluid ink. ACS Nano. 2016;10:8879-87.

[45] Pang H, Xu L, Yan D, Li Z. Conductive polymer composites with segregated structures. Progress in Polymer Science. 2014;39:1908-33.

[46] Spitalsky Z, Tasis D, Papagelis K, Galiotis C. Carbon nanotube–polymer composites: Chemistry, processing, mechanical and electrical properties. Progress in Polymer Science. 2010;35:357-401.

[47] Punetha VD, Rana S, Yoo HJ, Chaurasia A, McLeskey Jr JT, Ramasamy MS, et al. Functionalization of carbon nanomaterials for advanced polymer nanocomposites: A comparison study between CNT and graphene. Progress in Polymer Science. 2017;67:1-47.

[48] Kenry, Lim CT. Nanofiber technology: current status and emerging developments. Progress in Polymer Science. 2017;70:1-17.

[49] MacDonald E, Wicker R. Multiprocess 3D printing for increasing component functionality. Science. 2016;353.

[50] Han Z, Fina A. Thermal conductivity of carbon nanotubes and their polymer nanocomposites: A review. Progress in Polymer Science. 2011;36:914-44.

[51] Zhu W, Yan C, Shi Y, Wen S, Liu J, Shi Y. Investigation into mechanical and microstructural properties of polypropylene manufactured by selective laser sintering in comparison with injection molding counterparts. Materials & Design. 2015;82:37-45.

[52] Versavaud S, Régnier G, Gouadec G, Vincent M. Influence of injection molding on the electrical properties of polyamide 12 filled with multi-walled carbon nanotubes. Polymer. 2014;55:6811-8.

[53] Yuan S, Bai J, Chua CK, Wei J, Zhou K. Highly enhanced thermal conductivity of thermoplastic nanocomposites with a low mass fraction of MWCNTs by a facilitated latex approach. Composites Part A: Applied Science and Manufacturing. 2016;90:699-710.

[54] Yu W, Fu J, Chen L, Zong P, Yin J, Shang D, et al. Enhanced thermal conductive property of epoxy composites by low mass fraction of organic–inorganic multilayer covalently grafted carbon nanotubes. Composites Science and Technology. 2016;125:90-9.

[55] Koerner H, Liu W, Alexander M, Mirau P, Dowty H, Vaia RA. Deformation–morphology correlations in electrically conductive carbon nanotube—thermoplastic polyurethane nanocomposites. Polymer. 2005;46:4405-20.

[56] Yang. S, Leong. K. F, Du. Z, K. CC. The design of scaffolds for use in tissue engineering. part II. rapid prototyping techniques. Tissue Engineering. 2002;8:11.

[57] Yang. S, Leong. K. F. , Du. Z, K. CC. The design of scaffolds for use in tissue engineering. part I. traditional factors. Tissue Engineering. 2001;7:10.

[58] Childs THC, Tontowi AE. Selective laser sintering of a crystalline and a glass-filled crystalline polymer: Experiments and simulations. Proceedings of the Institution of Mechanical Engineers, Part B: Journal of Engineering Manufacture. 2001;215:1481-95.

[59] Shahzad K, Deckers J, Zhang ZY, Kruth JP, Vleugels J. Additive manufacturing of zirconia parts by indirect selective laser sintering. J Eur Ceram Soc. 2014;34:87-95.

[60] Wen SF, Yan CZ, Wei QS, Zhang LC, Zhao X, Zhu W, et al. Investigation and development of large-scale equipment and high performance materials for powder bed laser fusion additive manufacturing. Virtual and Physical Prototyping. 2014;9:213-23.

[61] Shahzad K, Deckers J, Boury S, Neirinck B, Kruth J-P, Vleugels J. Preparation and indirect selective laser sintering of alumina/PA microspheres. Ceramics International. 2012;38:1241-7.

[62] Goodridge RD, Tuck CJ, Hague RJM. Laser sintering of polyamides and other polymers. Progress in Materials Science. 2012;57:229-67.

[63] Berretta S, Ghita O, Evans KE. Morphology of polymeric powders in Laser Sintering (LS): From Polyamide to new PEEK powders. European Polymer Journal. 2014;59:218-29.

[64] Schmidt M, Pohle D, Rechtenwald T. Selective laser sintering of PEEK. CIRP Annals - Manufacturing Technology. 2007;56:205-8.

[65] Schultz J, Martin J, Kander R, Suchicital C. Selective laser sintering of nylon 12-PEEK blends formed by cryogenic mechanical alloying. Proceedings SFF Symposium, Austin (TX), USA2000. p. 119-24.

[66] Bai J, Goodridge RD, Hague RJM, Song M, Okamoto M. Influence of carbon nanotubes on the rheology and dynamic mechanical properties of polyamide-12 for laser sintering. Polymer Testing. 2014;36:95-100.

[67] Paggi RA, Beal VE, Salmoria GV. Process optimization for PA12/MWCNT nanocomposite manufacturing by selective laser sintering. Int J Adv Manuf Technol. 2013;66:1977-85.

[68] Yan CZ, Hao L, Xu L, Shi YS. Preparation, characterisation and processing of carbon fibre/polyamide-12 composites for selective laser sintering. Composites Science and Technology. 2011;71:1834-41.

[69] Yan CZ, Shi YS, Yang JS, Liu JH. An organically modified montmorillonite/nylon-12 composite powder for selective laser sintering. Rapid Prototyping Journal. 2011;17:28-36.

[70] Goodridge RD, Shofner ML, Hague RJM, McClelland M, Schlea MR, Johnson RB, et al. Processing of a Polyamide-12/carbon nanofibre composite by laser sintering. Polymer Testing. 2011;30:94-100.

[71] Wang JH, Bai PK, Zhang ZL, Li YX. Processing and characterization of core-shell PA12/Silica composites produced by selective laser sintering. Advanced Materials Research. 2011;160:756-61.

[72] Jain PK, Pandey PM, Rao PVM. Selective laser sintering of clay-reinforced polyamide. Polymer Composites. 2010;31:732-43.

[73] Chung H, Jee H, Das S. Selective laser sintering of PCL/TCP composites for tissue engineering scaffolds. Journal of Mechanical Science and Technology. 2010;24:241-4.

[74] Kenzari S, Bonina D, Dubois JM, Fournée V. Quasicrystal–polymer composites for selective laser sintering technology. Materials & Design. 2012;35:691-5.

[75] Bae DH, Lee SW, Lee DY, Moon SM, Bae SJ. Fabrication methods of metal/polymer/ceramic matrix composites containing randomly distributed or directionally aligned nanofibers. Google Patents; 2011.

[76] Bai PK, Wang WF. Selective laser sintering mechanism of polymer-coated molybdenum powder. T Nonferr Metal Soc. 2007;17:543-7.

[77] O'Neill W, Sutcliffe CJ, Morgan R, Landsborough A, Hon KKB. Investigation on multi-layer direct metal laser sintering of 316L stainless steel powder beds. CIRP Annals - Manufacturing Technology. 1999;48:151-4.

[78] Song YA, Koenig W. Experimental study of the basic process mechanism for direct selective laser sintering of low-melting metallic powder. Cirp Annals 1997 Manufacturing Technology. 1997;46:127-30.

[79] Chung H, Das S. Functionally graded Nylon-11/silica nanocomposites produced by selective laser sintering. Materials Science and Engineering: A 2008;487:251-7.

[80] Cheah CM, Chua CK, Leong KF, Chua SW. Development of a tissue engineering scaffold structure library for rapid prototyping. part 1: investigation and classification. Int J Adv Manuf Technol. 2003;21:291-301.

[81] Chua CK, Leong KF, Tan KH, Wiria FE, Cheah CM. Development of tissue scaffolds using selective laser sintering of polyvinyl alcohol/hydroxyapatite biocomposite for craniofacial and joint defects. Journal of Materials Science: Materials in Medicine. 2004;15:1113-21.

[82] Wiria F, Leong K, Chua C, Liu Y. Poly- ε-caprolactone/hydroxyapatite for tissue engineering scaffold fabrication via selective laser sintering. Acta Biomaterialia. 2007;3:1-12.

[83] Kim HC, Hahn HT, Yang YS. Synthesis of PA12/functionalized GNP nanocomposite powders for the selective laser sintering process. Journal of Composite Materials. 2012.

[84] De Rosa C, Auriemma F, Di Girolamo R, Ruiz de Ballesteros O, Pepe M, Tarallo O, et al. Morphology and mechanical properties of the mesomorphic form of isotactic polypropylene in stereodefective polypropylene. Macromolecules. 2013;46:5202-14.

[85] Salmoria G, Klauss P, Zepon K, Kanis L. The effects of laser energy density and particle

size in the selective laser sintering of polycaprolactone/progesterone specimens: morphology and drug release. Int J Adv Manuf Technol. 2013;66:1113-8.

[86] Yan C, Shi Y, Yang J, Liu J. Investigation into the selective laser sintering of styrene–acrylonitrile copolymer and postprocessing. Int J Adv Manuf Technol. 2010;51:973-82.

[87] Foroozmehr A, Badrossamay M, Foroozmehr E, Golabi Si. Finite element simulation of selective laser melting process considering optical penetration depth of laser in powder bed. Materials & Design. 2016;89:255-63.

[88] Riedlbauer D, Drexler M, Drummer D, Steinmann P, Mergheim J. Modelling, simulation and experimental validation of heat transfer in selective laser melting of the polymeric material PA12. Computational Materials Science. 2014;93:239-48.

[89] Vasquez M, Haworth B, Hopkinson N. Methods for quantifying the stable sintering region in laser sintered polyamide-12. Polymer Engineering & Science 2013;53:1230-40.

[90] Berretta S, Evans KE, Ghita O. Predicting processing parameters in High Temperature Laser Sintering (HT-LS) from powder properties. Materials & Design. 2016;105:301-14.

[91] Measuring the Angle of Repose of Free-Flowing Mold Powders. West Conshohocken, PA: ASTM International; 2000.

[92] Yu CL, Gao DP, Xu CB, Tang NB, Zhao T. Interpretation of Frenkel's theory of sintering considering evolution of activated pores: I. Confirmation of the time constant. Science of Sintering. 2014;46:141-7.

[93] Schmid M, Amado A, Wegener K. Polymer powders for selective laser sintering (SLS). AIP Conference Proceedings. 2015;1664:160009.

[94] Schmidt J, Sachs M, Blümel C, Winzer B, Toni F, Wirth K-E, et al. A novel process route for the production of spherical LBM polymer powders with small size and good flowability. Powder Technology. 2014;261:78-86.

[95] Cardon L, Deckers J, Verberckmoes A, Ragaert K, Delva L, Shahzad K, et al. Polystyrene-coated alumina powder via dispersion polymerization for indirect selective laser sintering applications. Journal of Applied Polymer Science. 2013;128:2121-8.

[96] Chunze Y, Yusheng S, Jinsong Y, Jinhui L. A nanosilica/nylon-12 composite powder for selective laser sintering. Journal of Reinforced Plastics and Composites. 2009;28:2889-902.

[97] Maeda K, Childs THC. Laser sintering (SLS) of hard metal powders for abrasion resistant coatings. Journal of Materials Processing Technology. 2004;149:609-15.

[98] Martinoni R. Powder compositions and methods of manufacturing articles therefrom. Google Patents; 2010.

[99] Bellet RJ, Broyer E, Bekker AY, Lace MA. Method of compressively molding articles from resin coated filler materials. Google Patents; 1987.

[100] J. P. Kruth, P. Mercelis, J. Van Vaerenbergh, L. Froyen, Rombouts M. Binding mechanisms

in selective laser sintering and selective laser melting. Rapid Prototyping Journal. 2005; 11 10.

[101] Athreya SR, Kalaitzidou K, Das S. Processing and characterization of a carbon black-filled electrically conductive Nylon-12 nanocomposite produced by selective laser sintering. Materials Science and Engineering: A. 2010;527:2637-42.

[102] Nelson JC, Vail NK, Barlow JW, Beaman JJ, Bourell DL, Marcus HL. Selective laser sintering of polymer-coated silicon carbide powders. Industrial & Engineering Chemistry Research. 1995;34:1641-51.

[103] I. Gibson, Shi D. Material properties and fabrication parameters in selective laser sintering process. Rapid Prototyping Journal. 1997;3:7.

[104] Bai JM, Goodridge RD, Hague RJM, Song M. Improving the mechanical properties of laser-sintered polyamide 12 through incorporation of carbon nanotubes. Polymer Engineering & Science. 2013;53:1937-46.

[105] Shi Y, Li Z, Sun H, Huang S, Zeng F. Development of a polymer alloy of polystyrene (PS) and polyamide (PA) for building functional part based on selective laser sintering (SLS). Proceedings of the Institution of Mechanical Engineers, Part L: Journal of Materials Design and Applications. 2004;218:299-306.

[106] J.P. Krutha, G. Levyb, F. Klockec, Childsd THC. Consolidation phenomena in laser and powder-bed based layered manufacturing. CIRP Annals - Manufacturing Technology. 2007;56:29.

[107] R.S. Evans, D.L. Bourell, J.J. Beaman, Campbell MI. SLS materials development method for rapid manufacturing. Sixteenth Solid Freeform Fabrication Symposium2005. p. 184–96.

[108] Ramesh C. Crystalline Transitions in Nylon 12. Macromolecules. 1999;32:5704-6.

[109] Murthy NS. Hydrogen bonding, mobility, and structural transitions in aliphatic polyamides. Journal of Polymer Science Part B: Polymer Physics. 2006;44:1763-82.

[110] Salmoria GV, Leite JL, Paggi RA. The microstructural characterization of PA6/PA12 blend specimens fabricated by selective laser sintering. Polymer Testing. 2009;28:746-51.

[111] Zia KM, Bhatti HN, Ahmad Bhatti I. Methods for polyurethane and polyurethane composites, recycling and recovery: A review. Reactive and Functional Polymers. 2007;67:675-92.

[112] J. S. Tate, J. Massingill, P. Patel, Konga S. Enhancement in mechanical properties by improving fiber/matrix adhesion in bio-based polyurethane/E-glass composites. International SAMPE Symposium and Exhibition Long Beach, CA, USA: S. Konga; 2008.

[113] Mazzoli A, Moriconi G, Pauri MG. Characterization of an aluminum-filled polyamide powder for applications in selective laser sintering. Materials & Design. 2007;28:993-1000.

[114] Zhang Z, Breidt C, Chang L, Friedrich K. Wear of PEEK composites related to their

mechanical performances. Tribology International. 2004;37:271-7.

[115] Bao WS, Meguid SA, Zhu ZH, Meguid MJ. Modeling electrical conductivities of nanocomposites with aligned carbon nanotubes. Nanotechnology. 2011;22:485704.

[116] Hussain F, Hojjati M, Okamoto M, Gorga RE. Review article: polymer-matrix Nanocomposites, processing, manufacturing, and application: an overview. Journal of Composite Materials. 2006;40:1511-75.

[117] Tan KH, Chua CK, Leong KF, Cheah CM, Cheang P, Abu Bakar MS, et al. Scaffold development using selective laser sintering of polyetheretherketone–hydroxyapatite biocomposite blends. Biomaterials. 2003;24:3115-23.

[118] Shishkovsky I, Scherbakov V. Selective laser sintering of biopolymers with micro and nano ceramic additives for medicine. Physics Procedia. 2012;39:491-9.

[119] Kruth J-P, Wang X, Laoui T, Froyen L. Lasers and materials in selective laser sintering. Assembly Automation. 2003;23:357-71.

[120] Exner H, Regenfuss P, Hartwig L, Klötzer S, Ebert R. Selective laser micro sintering with a novel process. Fourth International Symposium on Laser Precision Microfabrication: International Society for Optics and Photonics; 2003. p. 145-51.

[121] Wang XC, Laoui T, Bonse J, Kruth JP, Lauwers B, Froyen L. Direct selective laser sintering of hard metal powders: experimental study and simulation. Int J Adv Manuf Technol. 2002;19:351-7.

[122] H. H. Tang, M. L. Chiu, H. C. Yen. Slurry-based selective laser sintering of polymer-coated ceramic powders to fabricate high strength alumina parts. J Eur Ceram Soc. 2011;31:1383-8.

[123] Lao SC, Koo JH, Moon TJ, Londa M, Ibeh CC, Wissler GE, et al. Flame-retardant polyamide 11 nanocomposites: further thermal and flammability studies. Journal of Fire Sciences. 2011;29:479-98.

[124] Athreya SR, Kalaitzidou K, Das S. Microstructure, thermomechanical properties, and electrical conductivity of carbon black-filled nylon-12 nanocomposites prepared by selective laser sintering. Polymer Engineering & Science. 2012;52:12-20.

[125] Pandey G, Thostenson ET. Carbon Nanotube-Based Multifunctional Polymer Nanocomposites. Polymer Reviews. 2012;52:355-416.

[126] Kiriya D, Chen K, Ota H, Lin Y, Zhao P, Yu Z, et al. Design of surfactant–substrate interactions for roll-to-roll assembly of carbon nanotubes for thin-film transistors. Journal of the American Chemical Society. 2014;136:11188-94.

[127] Lee JU, Huh J, Kim KH, Park C, Jo WH. Aqueous suspension of carbon nanotubes via non-covalent functionalization with oligothiophene-terminated poly (ethylene glycol). Carbon. 2007;45:1051-7.

[128] Xie Y, Soh A. Investigation of non-covalent association of single-walled carbon nanotube

with amylose by molecular dynamics simulation. Materials Letters. 2005;59:971-5.

[129] Petrucci RH, Herring FG, Madura J, Bissonnette C. General chemistry : principles and modern applications2017.

[130] Baumann FE, Monsheimer S, Grebe M, Christoph W, Schiffer T, Scholten H. Laser-sintering powder with titanium dioxide particles, process for its preparation, and moldings produced from this laser-sintering powder. Google Patents; 2004.

[131] Reisenauer C, Kirschniak A, Drews U, Wallwiener D. Anatomical conditions for pelvic floor reconstruction with polypropylene implant and its application for the treatment of vaginal prolapse. European Journal of Obstetrics & Gynecology and Reproductive Biology. 2007;131:214-25.

[132] W. Y. Zhou, M. Wang, W. L. Cheung, Ip WY. Selective laser sintering of Poly(L-Lactide)/Carbonated hydroxyapatite nanocomposite porous scaffolds for bone tissue engineering. In: Eberli D, editor. Tissue Engineering: InTech; 2010. p. 524.

[133] Piorkowski DT, McClements DJ. Beverage emulsions: recent developments in formulation, production, and applications. Food Hydrocolloids. 2014;42, Part 1:5-41.

[134] Bai J, Goodridge RD, Hague RJM, Song M. Improving the mechanical properties of laser-sintered polyamide 12 through incorporation of carbon nanotubes. Polymer Engineering & Science. 2013;53:1937-46.

[135] Bittner B, Kissel T. Ultrasonic atomization for spray drying: a versatile technique for the preparation of protein loaded biodegradable microspheres. Journal of Microencapsulation. 1999;16:325-41.

[136] Cai D, Jin J, Song M. Process. Google Patents; 2009.

[137] Zhang W, Dehghani SA, Blackburn R. Carbon based conductive polymer composites. J Mater Sci. 2007;42:3408-18.

[138] Kim P, Shi L, Majumdar A, McEuen P. Thermal transport measurements of individual multiwalled nanotubes. Physical review letters. 2001;87:215502.

[139] Nan CW, Shi Z, Lin Y. A simple model for thermal conductivity of carbon nanotube-based composites. Chem Phys Lett. 2003;375:666-9.

[140] Prasher RS, Hu X, Chalopin Y, Mingo N, Lofgreen K, Volz S, et al. Turning carbon nanotubes from exceptional heat conductors into insulators. Physical review letters. 2009;102:105901.

[141] Marconnet AM, Yamamoto N, Panzer MA, Wardle BL, Goodson KE. Thermal conduction in aligned carbon nanotube–polymer nanocomposites with high packing density. ACS Nano. 2011;5:4818-25.

[142] Haggenmueller R, Guthy C, Lukes JR, Fischer JE, Winey KI. Single wall carbon nanotube/polyethylene nanocomposites: thermal and electrical conductivity. Macromolecules. 2007;40:2417-21.

[143] Li L, Li CY, Ni C, Rong L, Hsiao B. Structure and crystallization behavior of Nylon 66/multi-walled carbon nanotube nanocomposites at low carbon nanotube contents. Polymer. 2007;48:3452-60.

[144] Cai D, Song M. Latex technology as a simple route to improve the thermal conductivity of a carbon nanotube/polymer composite. Carbon. 2008;46:2107-12.

[145] Gulotty R, Castellino M, Jagdale P, Tagliaferro A, Balandin AA. Effects of functionalization on thermal properties of single-wall and multi-wall carbon nanotube–polymer nanocomposites. ACS nano. 2013;7:5114-21.

[146] Bryning M, Milkie D, Islam M, Kikkawa J, Yodh A. Thermal conductivity and interfacial resistance in single-wall carbon nanotube epoxy composites. Applied Physics Letters. 2005;87:161909.

[147] Gojny FH, Wichmann MH, Fiedler B, Kinloch IA, Bauhofer W, Windle AH, et al. Evaluation and identification of electrical and thermal conduction mechanisms in carbon nanotube/epoxy composites. Polymer. 2006;47:2036-45.

[148] Ivanov I, Puretzky A, Eres G, Wang H, Pan Z, Cui H, et al. Fast and highly anisotropic thermal transport through vertically aligned carbon nanotube arrays. Applied Physics Letters. 2006;89:223110.

[149] Zeng Y, Liu P, Du J, Zhao L, Ajayan PM, Cheng H-M. Increasing the electrical conductivity of carbon nanotube/polymer composites by using weak nanotube–polymer interactions. Carbon. 2010;48:3551-8.

[150] Datsyuk V, Trotsenko S, Reich S. Carbon-nanotube–polymer nanofibers with high thermal conductivity. Carbon. 2013;52:605-8.

[151] Singh V, Bougher TL, Weathers A, Cai Y, Bi K, Pettes MT, et al. High thermal conductivity of chain-oriented amorphous polythiophene. Nature nanotechnology. 2014;9:384-90.

[152] Luo T, Lloyd JR. Enhancement of thermal energy transport across graphene/graphite and polymer interfaces: a molecular dynamics study. Advanced Functional Materials. 2012;22:2495-502.

[153] Kim GH, Lee D, Shanker A, Shao L, Kwon MS, Gidley D, et al. High thermal conductivity in amorphous polymer blends by engineered interchain interactions. Nature Materials. 2015;14:295-300.

[154] Ma PC, Siddiqui NA, Marom G, Kim JK. Dispersion and functionalization of carbon nanotubes for polymer-based nanocomposites: A review. Composites Part A: Applied Science and Manufacturing. 2010;41:1345-67.

[155] Bauhofer W, Kovacs JZ. A review and analysis of electrical percolation in carbon nanotube polymer composites. Composites Science and Technology. 2009;69:1486-98.

[156] Eshraghi S, Das S. Mechanical and microstructural properties of polycaprolactone scaffolds with one-dimensional, two-dimensional, and three-dimensional orthogonally oriented porous architectures produced by selective laser sintering. Acta Biomaterialia.

2010;6:2467-76.

[157] Eshraghi S, Karevan M, Kalaitzidou K, Das S. Processing and properties of electrically conductive nanocomposites based on polyamide-12 filled with exfoliated graphite nanoplatelets prepared by selective laser sintering. International Journal of Precision Engineering and Manufacturing. 2013;14:1947-51.

[158] Ullah I, Brandt M, Feih S. Failure and energy absorption characteristics of advanced 3D truss core structures. Materials & Design. 2016;92:937-48.

[159] Zheng X, Lee H, Weisgraber TH, Shusteff M, DeOtte J, Duoss EB, et al. Ultralight, ultrastiff mechanical metamaterials. Science. 2014;344:1373-7.

[160] Deshpande VS, Fleck NA, Ashby MF. Effective properties of the octet-truss lattice material. Journal of the Mechanics and Physics of Solids. 2001;49:1747-69.

[161] Babaee S, Shim J, Weaver JC, Chen ER, Patel N, Bertoldi K. 3D soft metamaterials with negative Poisson's ratio. Advanced Materials. 2013;25:5044-9.

[162] Wang K, Chang Y-H, Chen Y, Zhang C, Wang B. Designable dual-material auxetic metamaterials using three-dimensional printing. Materials & Design. 2015;67:159-64.

[163] Shim J, Shan S, Kosmrlj A, Kang SH, Chen ER, Weaver JC, et al. Harnessing instabilities for design of soft reconfigurable auxetic/chiral materials. Soft Matter. 2013;9:8198-202.

[164] Wu G, Cho Y, Choi I-S, Ge D, Li J, Han HN, et al. Directing the deformation paths of soft metamaterials with prescribed asymmetric units. Advanced Materials. 2015;27:2747-52.

[165] Zheng X, Smith W, Jackson J, Moran B, Cui H, Chen D, et al. Multiscale metallic metamaterials. Nature Materials. 2016;15:1100-6.

[166] Tiemo B, Robert S, Michael T, Muamer K, Graeme WM, Martin W. On three-dimensional dilational elastic metamaterials. New Journal of Physics. 2014;16:033032.

[167] Lazarus A, Reis PM. Soft actuation of structured cylinders through auxetic behavior. Advanced Engineering Materials. 2015;17:815-20.

[168] Regev O, ElKati PNB, Loos J, Koning CE. Preparation of conductive nanotube–polymer composites using latex technology. Advanced Materials. 2004;16:248-51.

[169] Ye L, Ye C, Shi X, Zhao H, Xie K, Chen D, et al. Block-assembling: a new strategy for fabricating conductive nanoporous materials from nanocomposites based on a melt-miscible crystalline/crystalline blend and MWCNTs. Journal of Materials Chemistry C. 2015;3:8510-8.

[170] Lin S, Blankschtein D. Role of the Bile Salt Surfactant Sodium Cholate in Enhancing the Aqueous Dispersion Stability of Single-Walled Carbon Nanotubes: A Molecular Dynamics Simulation Study. The Journal of Physical Chemistry B. 2010;114:15616-25.

[171] Danley RL. New heat flux DSC measurement technique. Thermochimica Acta. 2003;395:201-8.

[172] Scholten H, Christoph W. Use of a nylon-12 for selective laser sintering. Google Patents; 2001.

[173] Verbelen L, Dadbakhsh S, Van den Eynde M, Kruth J-P, Goderis B, Van Puyvelde P. Characterization of polyamide powders for determination of laser sintering processability. European Polymer Journal. 2016;75:163-74.

[174] Ristić MM, Milosević S. Frenkel's theory of sintering. Science of Sintering. 2006;38:7-11.

[175] Grewell D, Rooney P, Kagan VA. Relationship between optical properties and optimized processing parameters for through-transmission laser welding of thermoplastics. Journal of Reinforced Plastics and Composites. 2004;23:239-47.

[176] Salmoria GV, Paggi RA, Lago A, Beal VE. Microstructural and mechanical characterization of PA12/MWCNTs nanocomposite manufactured by selective laser sintering. Polymer Testing. 2011;30:611-5.

[177] Chung H, Das S. Processing and properties of glass bead particulate-filled functionally graded Nylon-11 composites produced by selective laser sintering. Materials Science and Engineering: A 2006;437:226-34.

[178] Lee G. Selective laser sintering of calcium phosphate materials for orthopedic implants [Ph.D.]. Ann Arbor: The University of Texas at Austin; 1997.

[179] Yi X, Tan Z, Yu W, Li J, Li B, Huang B, et al. Three dimensional printing of carbon/carbon composites by selective laser sintering. Carbon. 2016;96:603-7.

[180] Francis V, Jain PK. Experimental investigations on fused deposition modelling of polymer-layered silicate nanocomposite. Virtual and Physical Prototyping 2016;11:109-21.

[181] Pozegic TR, Anguita JV, Hamerton I, Jayawardena KDGI, Chen JS, Stolojan V, et al. Multi-functional carbon fibre composites using carbon nanotubes as an alternative to polymer sizing. Scientific Reports. 2016;6:37334.

[182] Fischer S, Pfister A, Galitz V, Lyons B, Robinson C, Rupel K, et al. A high-performance material for aerospace applications: development of carbon fiber filled PEKK for laser sintering. Proceedings of the 26th Annual International Solid Freeform Fabrication. Austin (TX), USA2016.

[183] Sahoo NG, Rana S, Cho JW, Li L, Chan SH. Polymer nanocomposites based on functionalized carbon nanotubes. Progress in Polymer Science. 2010;35:837-67.

[184] Shopova N, Milkova T. Thermochemical decomposition of cholic acid and its derivatives. Thermochimica Acta. 1995;255:211-20.

[185] Mahajan A, Kingon A, Kukovecz Á, Konya Z, Vilarinho PM. Studies on the thermal decomposition of multiwall carbon nanotubes under different atmospheres. Materials Letters. 2013;90:165-8.

[186] Zhang G, Xia Y, Wang H, Tao Y, Tao G, Tu S, et al. A percolation model of thermal

conductivity for filled polymer composites. Journal of Composite Materials. 2010;44:963-70.

[187] Xiao Y, Wang W, Lin T, Chen X, Zhang Y, Yang J, et al. Largely enhanced thermal conductivity and high dielectric constant of poly(vinylidene fluoride)/boron nitride composites achieved by adding a few carbon nanotubes. The Journal of Physical Chemistry C. 2016;120:6344-55.

[188] Ellis B, Smith R. Polymers: A Property Database. 2 ed: CRC Press; ; 2009.

[189] Aitkaliyeva A, Chen D, Shao L. Phonon transport assisted by inter-tube carbon displacements in carbon nanotube mats. Scientific Reports. 2013;3.

[190] Blackburn JL, Engtrakul C, McDonald TJ, Dillon AC, Heben MJ. Effects of surfactant and boron doping on the BWF feature in the Raman spectrum of single-wall carbon nanotube aqueous dispersions. The Journal of Physical Chemistry B 2006;110:25551-8.

[191] Di Crescenzo A, Ettorre V, Fontana A. Non-covalent and reversible functionalization of carbon nanotubes. Beilstein J Nanotechnol. 2014;5:1675-90.

[192] Fang X, Chunze Y, Yat-Tarng S, Hong C, Yongde X, Yanqiu Z. Ultra-toughened nylon 12 nanocomposites reinforced with IF-WS 2. Nanotechnology. 2014;25:325701.

[193] Blackburn JL, Engtrakul C, McDonald TJ, Dillon AC, Heben MJ. Effects of Surfactant and Boron Doping on the BWF Feature in the Raman Spectrum of Single-Wall Carbon Nanotube Aqueous Dispersions. The Journal of Physical Chemistry B. 2006;110:25551-8.

[194] Oh H, Sim J, Ju SY. Binding affinities and thermodynamics of noncovalent functionalization of carbon nanotubes with surfactants. Langmuir : the ACS journal of surfaces and colloids. 2013;29:11154-62.

[195] Lin W, Zhang RW, Moon KS, Wong CP. Molecular phonon couplers at carbon nanotube/substrate interface to enhance interfacial thermal transport. Carbon. 2010;48:107-13.

[196] Lin W, Xiu Y, Jiang H, Zhang R, Hildreth O, Moon K-S, et al. Self-assembled monolayer-assisted chemical transfer of in situ functionalized carbon nanotubes. Journal of the American Chemical Society. 2008;130:9636-7.

[197] Robertson J, Torbati A, Rodriguez ED, Mao Y, Baker RM, Qi HJ, et al. Mechanically Programmed Shape Change in Laminated Elastomeric Composites. Soft Matter. 2015;11:5754-64.

[198] Matteo B, Fabrizio S. Vibration transmissibility and damping behaviour for auxetic and conventional foams under linear and nonlinear regimes. Smart Materials and Structures. 2013;22:084010.

[199] Suard M. Characterization and optimization of lattice structures made by Electron Beam Melting: Grenoble Alpes; 2015.

[200] Lakes R. Foam Structures with a Negative Poisson's Ratio. Science. 1987;235:1038-40.

[201] Zach R, Roderic SL. Cosserat elasticity of negative Poisson's ratio foam: experiment. Smart Materials and Structures. 2016;25:054004.

[202] Baughman RH, Shacklette JM, Zakhidov AA, Stafstrom S. Negative Poisson's ratios as a common feature of cubic metals. Nature. 1998;392:362-5.

[203] Wang X, Li X, Ma L. Interlocking assembled 3D auxetic cellular structures. Materials & Design. 2016;99:467-76.

[204] Mousanezhad D, Babaee S, Ebrahimi H, Ghosh R, Hamouda AS, Bertoldi K, et al. Hierarchical honeycomb auxetic metamaterials. Scientific Reports. 2015;5:18306.

[205] Olly D, Leon F, Terry S, Andrew A, Tom A. Quasi-static characterisation and impact testing of auxetic foam for sports safety applications. Smart Materials and Structures. 2016;25:054014.

[206] Nicolaou ZG, Motter AE. Mechanical metamaterials with negative compressibility transitions. Nature Materials. 2012;11:608-13.

[207] Clausen A, Wang F, Jensen JS, Sigmund O, Lewis JA. Topology optimized architectures with programmable poisson's ratio over large deformations. Advanced Materials. 2015;27:5523-7.

[208] Xin R, Jianhu S, Arash G, Hongqi T, Yi Min X. A simple auxetic tubular structure with tuneable mechanical properties. Smart Materials and Structures. 2016;25:065012.

[209] Gibson LJ, Ashby MF. Cellular Solids: Structure and Properties. 2 ed. Cambridge: Cambridge University Press; 1997.

[210] Shen F, Yuan S, Guo Y, Zhao B, Bai J, Qwamizadeh M, et al. Energy absorption of thermoplastic polyurethane lattice structures via 3D printing: modeling and prediction. International Journal of Applied Mechanics. 2016;08:1640006.